Development of Porous Thin Film based Multiparametric Glucose Sensors

Thesis Submitted for the Degree of Doctor of Philosophy (Science)

To

Jadavpur University

By

Deeparati Basu

Under the Joint Supervision of

Prof. Jayoti Das

&

Dr. Syed Minhaz Hossain

Department of Physics
Jadavpur University
Kolkata 700032, India

2022

Dedicated

To

My Family

CERTIFICATE FROM THE SUPERVISORS

This is to certify that the thesis entitled *"**Development of Porous Thin Film based Multiparametric Glucose Sensors**"* submitted by Ms. ***Deeparati Basu*** who got her name registered on 28th April, 2015 for the award of ***Ph.D. (Science) degree*** of Jadavpur University, is absolutely based upon her own work under the joint supervision of Prof. Jayoti Das and Dr. Syed Minhaz Hossain and that neither this thesis nor any part of it has been submitted for either any degree/diploma or any other academic award anywhere before.

Jayoti Das
20/04/2022

[Prof. Jayoti Das]

Signature of the Supervisor &

date with official seal

Dr. Jayoti Das
Professor
Department of Physics
Jadavpur University
Kolkata - 700 032

Syed Minhaz Hossain
20/04/2022

[Dr. Syed Minhaz Hossain]

Signature of the Supervisor &

date with official seal

Dr. S. M. Hossain
Associate Professor
Department of Physics
Indian Institute of Engineering Science and Technology, Shibpur
Howrah-711 103, INDIA

List of Publication

Journal

1. **Deeparati Basu**, Kaustav Sen, Syed Minhaz Hossain, and Jayoti Das. "Influence of pore diameter on physical and sensing properties of free-standing Chitosan-Silica Nanocomposite membrane." *Journal of Porous Materials* 28, no. 5 (**2021**): 1595-1607. DOI: https://doi.org/10.1007/s10934-021-01079-z (***Impact factor: 2.49***)

2. **Deeparati Basu**, Tanusree Sarkar, Kaustav Sen, Syed Minhaz Hossain, and Jayoti Das. "Multi-Parametric optical glucose sensor based on surface functionalized nano-porous silicon." *IEEE Sensors Journal* 18, no. 24 (**2018**): 9940-9947. DOI: 10.1109/JSEN.2018.2872846 (***Impact factor: 3.3***)

3. Kaustav Sen, **Deeparati Basu**, Syed Minhaz Hossain, and Jayoti Das. "Calcium selective optical sensor based on calmodulin functionalized porous silicon." *Applied Physics: A* 127, no. 10 (**2021**): 1-8. DOI: https://doi.org/10.1007/s00339-021-04869-z (***Impact factor: 2.54***)

4. Tanusree Sarkar, **Deeparati Basu**, Nandini Mukherjee, and Jayoti Das. "Comparison of glucose sensitivity of nano and macro porous silicon." *Materials Today: Proceedings* 5, no. 3 (**2018**): 9798-9803. DOI: https://doi.org/10.1016/j.matpr.2017.10.169 (***Impact factor: 1.24***)

5. **Deeparati Basu**, Syed Minhaz Hossain and Jayoti Das. “Chitosan-silica nanocomposite porous thin film based multi-parametric optical glucose sensor: Effect of surface functionalization.” Communicated to *Journal of Physics D: Applied Physics*, 2022

6. **Deeparati Basu**, Syed Minhaz Hossain, and Jayoti Das. “Label-free optical biosensor methods and materials: Progress in the last decade.” Communicated to *Optical and Quantum Electronics*, 2022.

7. **Deeparati Basu**, Syed Minhaz Hossain, and Jayoti Das. “Automated optical multiparametric bio-analyte detection system: Design, development and noise analysis.” Communicated to *Instrumentation Science and Technology*, 2022.

8. **Deeparati Basu**, Jayoti Das, and Syed Minhaz Hossain. “Effect of etching parameters on sensing performance of porous silicon thin film based optical biosensor.” Communicated to *Silicon*, 2022.

Conference

9. **Deeparati Basu**, Jayoti Das, Syed Minhaz Hossain, “Design and Development of Multi-parametric Optical Measurement System for Biosensing Application”, In *2021 International Conference on Innovative Research in Engineering and Technology (ICIRET organised by IFERP)*, pp. 5, IFERP Explore, **2021**, ISBN: 978-93-92105-07-4

10. **Deeparati Basu**, Kaustav Sen, Syed Minhaz Hossain, and Jayoti Das. "Instrumentation and Development of Grating Coupler Sensor for Cost-effective and Precision Measurement of Biomolecules." In *2019 10th International Conference on Computing, Communication and Networking Technologies (ICCCNT)*, pp. 1-4. IEEE, **2019**. DOI: 10.1109/ICCCNT45670.2019.8944788

11. Kaustav Sen, **Deeparati Basu**, Arnesh Sen, Syed Minhaz Hossain, and Jayoti Das. "Automated detection of profile axis angle of human finger for quantitative digital clubbing diagnosis." In *2019 10th International Conference on Computing, Communication and Networking Technologies (ICCCNT)*, pp. 1-4. IEEE, **2019**. DOI:10.1109/ICCCNT45670.2019.8944519

12. Kaustav Sen, Arnesh Sen, **Deeparati Basu**, Syed Minhaz Hossain and Jayoti Das. "Automated Technique Based on Image Processing for Accurate Diagnosis of Finger Clubbing," In *2018 IEEE SENSORS Conference*, **2018**, pp. 1-4, DOI: 10.1109/ICSENS.2018.8589695.

Preface

Biosensors are a special category of sensors that detect the presence and concentration of biological analytes. After the discovery of first biosensor in 1962 (Enzyme electrode for glucose detection by Leland C. Clark) many research groups took interest in the field and from then onwards new innovations and constant improvements in existing methods and materials have contributed to immense advancement in pathological diagnosis these days.

Among different types of biosensors based on transduction method, optical biosensors have become a leading field of research due to their high sensitivity and precision measurement capability. Also, they are least affected by external electromagnetic noises which makes them a suitable choice for real-time monitoring of bio-analytes in wearable sensors. Label-free optical techniques like Surface Plasmon Resonance, Interferometry, Fiber Optic sensors, Ring Resonators etc. are being studied extensively for the last two decades due to their precision, accuracy and robustness. Multiparametric measurement systems i.e., systems that monitor several sensor parameters simultaneously, is a comparatively new field in optical biosensor research. Multiparametric systems are in general way better in terms of selectivity and reliability than their single parametric counterparts. Most of the label-free optical biosensors reported up until now are single parametric in nature. So, the thesis focuses on developing a label-free optical multiparametric system which is capable of monitoring five interlinked optical parameters (Transmittance, Reflectance, Internal Scattering, Surface Scattering and Absorption) simultaneously. Image processing was found to be a convenient and cost efficient method

for extracting different optical parameter information from transmitted and reflected spot images. An automated image acquisition and analysis system has been developed in this thesis based on MATLAB image processing environment which provides information about all the interlinked parameters as well as some non-interlinked parameters (RGB channel information) simultaneously. Such system has immense potential in the field of multiparametric optical biosensing.

Often precision optical structures for interferometry or ring resonator arrangements require costly and complex fabrication methods. So, cost efficient and easy to fabricate thin film structures has been chosen as biosensor platform. Also, proper choice of biosensor material depends on some vital properties like biocompatibility, low toxicity, good absorption capability, large biomolecular interaction space etc. and consideration of all these properties has led to two distinct types of porous thin film samples for biosensor measurements in multiparametric optical setup. Porous Silicon (PS) is well known for its biocompatibility, low toxicity and large surface to volume ratio which allows increased interaction space with biomolecules, thus increasing sensitivity of PS based sensors. PS thin film on silicon substrate can be fabricated easily and cost effectively by standard electrochemical etching procedure. Also, variation of etching parameters or preparation parameters can modulate characteristics of the PS films. Thus, a detailed investigation on effect of preparation parameters on the structure and properties of PS thin films has been performed and optimization of PS thin film structures for biosensing application has been presented in this thesis. As PS samples are optically non-transparent in visible spectra, only reflected spot image information could be utilized in multiparametric measurement setup. So, to utilize all five interlinked parameters obtained from transmitted and reflected spot images, semi-transparent polymer based thin films were considered. Chitosan is a synthetic biopolymer having unique properties like biocompatibility, anti-bacterial and antifungal properties, wound healing property etc. Chitosan thin film is optically transparent and controlled addition of Silica Nanoparticle (SiNp) can modulate the refractive index of Chitosan Silica Nanocomposite (CSNC) thin films. Also, hot NaOH etching of composite thin film can induce pores in the structure producing a sponge like polymer composite network which increases surface to volume ratio of the CSNC thin films significantly. Physiochemical properties of the film can be controlled by simply varying SiNp size which changes pore

diameter and morphology of the thin films. Detailed investigation on the effect of different pore size in physiochemical properties of CSNC thin films have been presented and optimization of the films for biosensing application has been carried out in this thesis.

Diabetes mellitus is a metabolic disorder which affects millions of people worldwide and if left untreated, causes heart, kidney, nerve, eye damage and in extreme cases death also. There has been a lot of research going around the world on glucose sensors for early detection and continuous monitoring of glucose level in human body fluids. So, multiparametric optical measurement of glucose might be a promising field of research with significant importance. The main aim of the thesis is thus set to multiparametric optical detection of glucose level in pathological range using PS and CSNC thin film sensors. Surface functionalization is a crucial step in any biosensor fabrication as it aids selective attachment of bio-analytes on sensor surface thus reducing background noise generated by complex solution and increasing selectivity of the sensor significantly. For selective binding of glucose molecules, the thin film sensors were functionalized with Glucose Oxidase (GOX) enzyme. GOX is basically a catalyst that aids the conversion of glucose molecules into Gluconic acid crystals which are clustered around GOX sites on the sensor surface changing the optical properties of the sensor. As PS thin film sample morphology aids GOX attachment, simple physisorption process is used to produce GOX functionalized PS sensors. On the other hand, CSNC thin films required chemisorption process of surface functionalization where GOX molecules are attached to CSNC surface via Glutaraldehyde crosslinking chains. Both PS and CSNC thin film glucose sensors were analysed in terms of different biosensor characteristics like sensitivity, selectivity, response time, stability etc. and finally a comparison between the two glucose sensors has been presented in the final chapter of the thesis.

Acknowledgements

It is extremely difficult to express my sincere gratitude towards all those who have supported, assisted and motivated me in this long journey. Though it is a pleasure to mention and thank all these people, but mare words are insufficient to express my appreciation towards them.

First, I would like to sincerely thank my first supervisor Prof. Jayoti Das (Department of Physics, Jadavpur University) for her invaluable guidance and thoughtful advices. Her expertise has helped me immensely to formulate research problem and methodology. Most of all she inspired me to think freely which helped immensely in finding out of the track solutions. She was always there to assist in my technical as well as non-technical problems and was like a second guardian without whom it was impossible for me to complete this thesis.

I am also extremely thankful to my second supervisor Dr. Syed Minhaz Hossain (Department of physics, IIEST Shibpur) for his expert advices and vast resources. I am truly grateful for his immense help in optical instrument development and many other fields of research, without which my work would have been incomplete. His guidance and motivation have influenced me deeply which helped me to understand the value of productive research.

I would like to acknowledge Prof. Nabin Baran Manik (Department of Physics, Jadavpur University) for supporting and motivating me throughout this long period. I would also like to thank Prof. Sukhen Das (Department of Physics, Jadavpur University) for his immense technical support. A special thanks to Prof. Sanat Karmakar (Department of Physics, Jadavpur University) and Prof. Sanjay Kumar (Department of Physics, Jadavpur University) who has provided technical support time to time. Also, I am grateful to Prof. Partha Pratim Ray (Department of Physics, Jadavpur University) and Prof. Brajadulal Chattopadhay (Department of Physics, Jadavpur University) for helping me in crucial moments. I would like to specially thank Prof. Debiprashad Bhattacharya (Retired from Department of Physics, Jadavpur University) for his insightful words and advices which have motivated me in passionate research and I wish to acknowledge my deepest respect towards him.

I would like to acknowledge Department of Science and Technology (DST), India for providing Inspire Fellowship throughout the tenure of my research. The financial support helped me immensely in uninterrupted research work.

I would like to thank my colleagues Tanusreedi, Kaustav, Arnesh and Mintu for their support and assistance. Dheeraj, Pabitrada, Animesh, Chandradi, Rituparnadi and almost everyone in department of physics in Jadavpur University was extremely helpful for which I am truly grateful. Special thanks to Sudipta, Sayari, Anupamda in Department of Physics, IIEST Shibpur for helping me numerous times despite of their busy schedule.

Finally, I would like to take the opportunity to acknowledge my family for their constant support through thick and thin. I am grateful to Baba (Mr. Praloy Kumar Basu) and Ma (Mrs. Tandra Basu) for their unconditional love and experienced advices which made my life a lot better. I would like to especially thank Dada (Debanjan Basu) for motivating and

inspiring me in this long journey. His warm presence and cheerful personality have always lifted me up from the deepest frustrations. I love you all very much and wish to thank you for everything you have done for me.

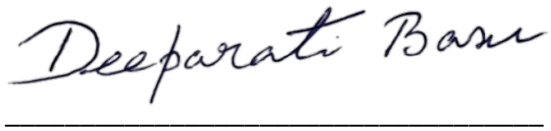

Deeparati Basu

(Index No.: 56/15/Phys./23)

SRF, Department of Physics
Jadavpur University
Kolkata 700032, India

Date: 21.04.2022

Place: Jadavpur

Contents

Chapter 1

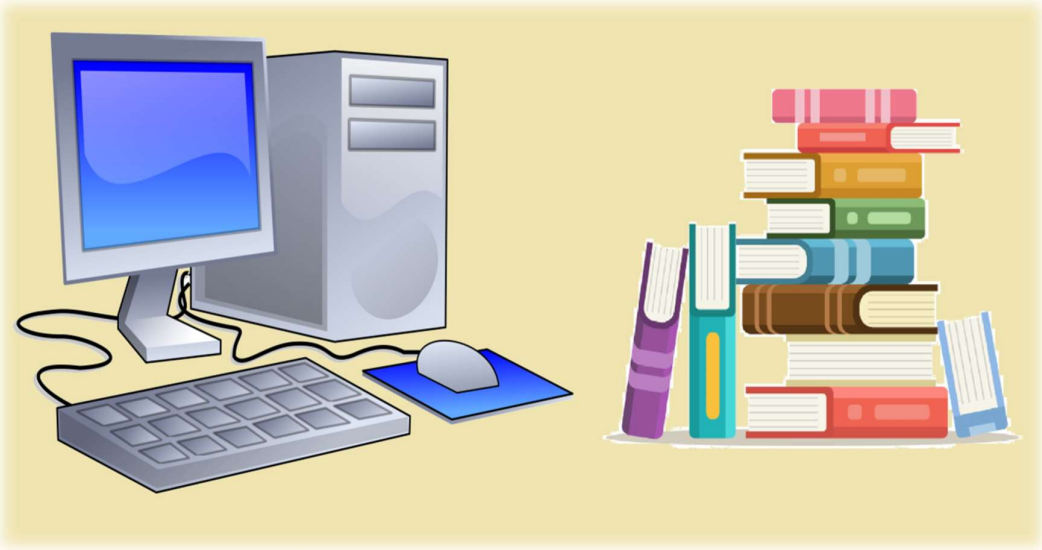

Chapter 1

Literature Review and Scope of Work

1.1. A Brief Introduction to Biosensors

Sensors have always been a topic of great interest as they have the ability to detect changes inside a system or surrounding environment. Sensors have a wide range of applications; for example, physical sensors measure physical parameters like temperature, pressure, displacement, stiffness etc., while chemical sensors measure concentration of different chemical substances called analyte. In this section, a special type of sensor called biosensor is introduced and their basic structure, types and fields of application have been presented.

1.1.1. What Is Biosensor?

Biosensors either contain a biological element or can detect biological analytes both qualitatively and quantitatively. It is hard to put an exact definition of a biosensor because, a canary bird in cage can also be considered as a biosensor, as they were vastly used by the miners to determine the presence of toxic gases. According to I. Palchetti and M. Mascini 'any physical (thermometer) or chemical sensor (microelectrode implanted in animal tissue) operating in biological samples can be considered as *Biosensor*' [1]. Also, a sensor which consists of a biological element and a physicochemical detector can also act as a biosensor, whether it detects a biological sample or not and this is also the recent definition of a biosensor [2]. According to IUPAC, biosensor is 'A device that uses specific biochemical reactions mediated by isolated enzymes, immunosystems, tissues, organelles or whole cells to detect chemical compounds usually by electrical, thermal or optical signals'[3].

1.1.2. History of Biosensor

From the very beginning, living beings like animals, plants all have biological sensors within them. For example, sunflowers are living solar tracking system and almost every plant has optical sensors within them. Human beings themselves are loaded with all kind of sensors. Eyes operate as optical sensors, ears as acoustic sensors, nose and tongue as chemical sensors, skin as pressure and temperature sensor etc. and there are numerous other sensors stuffed inside every living being. These sensors inside living body are purely biological.

From the point of view of research and discovery, the very first biosensor was invented by Leland C. Clark for glucose detection. He was considered as the father of biosensor and in 1962, he demonstrated glucose detection by amperometric enzyme electrodes [4]. Influenced by his work many researchers took interest in the field of biosensors and in 1969, Guilbault and Montalvo discovered first potentiometric biosensor using urease immobilized ammonia electrodes to detect urea [5]. In 1975, Yellow Springs Instruments launched first commercial glucose biosensor [6]. Then came the fibre optic pH sensor in 1982 which was found suitable for glucose measurement [7] and in the same year, first fibre optic-based implantable glucose sensor was discovered [8]. The journey has been long since then; different new approaches were invented for precision and accurate

measurements. Optical techniques, amperometry, immunoassay, chromatography and many other techniques are being investigated everyday for further improvement of biosensor performance. Currently nanotechnology has been introduced to produce biocompatible nanostructures like porous membranes, thin films, composites etc. which have improved sensitivity of the biosensor systems remarkably [9]. Today research in biosensors is not limited to a narrow field but has combined principles of basic science i.e., physics, chemistry, biology with electronics, nanotechnology, applicatory medicines etc. and has formed a huge interdisciplinary area of research.

1.1.3. Biosensor Structure

As we have discussed before, a biosensor can detect and measure presence of different types of physical, biological or chemical elements. The subject of interest, which a biosensor detects, is called analyte. Analytes can be chemical or biochemical substances. Complex biochemical substances like cells, antigens, DNA, RNA, virus, bacteria, living microorganism etc. can act as analyte for a specific biosensor. Simple chemical compounds that require constant monitoring for the diagnosis of common health problems like glucose, uric acid, sodium, potassium, calcium etc. are also analytes.

So, what should be the sequence of a biosensor design for human health monitoring? First, disease specific biomarkers or target molecules are pin pointed and their normal and abnormal pathological range is studied. These biomarkers will be the analyte for the designed biosensor system. Then a particular biochemical compound that has affinity towards that analyte is selected. For example, antigen and antibody has affinity towards each other which means if some immunoglobulin (IgG) antibody is added in a complex solution containing anti Immunoglobulin (IgG) antigen, it will only selectively bind to its antigen sites. These bonds are generally weak non-covalent bonds like hydrogen bonds, Van der Waals forces, electrostatic and hydrophobic interactions [10]. So, the elements which selectively bind target analyte from a complex solution are called capturing agents and they are implanted on the biosensor surface by surface functionalization process. These surface functionalized capturing agents are called Bio-receptors of a biosensor system.

Now, with the help of bio-receptors, target analytes can successfully interact with the biosensor avoiding most of the background noises generated by complex solution. The

next step is to choose a transducer. Transducers are devices which convert one form of energy to another. In biosensors, different types of problem specific material are used and the capturing agents are immobilized on them. These materials may be anything from porous structures, membranes, thin films etc. and their choice is solely dependent on the requirement of biosensor sensitivity. Transducers made from these unique materials are the core of a biosensor device and almost all the properties of the device are controlled by them. Introduction of analyte molecules on the biosensor surface changes some physiochemical properties like electrical, optical, mechanical etc. of this base material. As a result, the transducer generates some change in their output signal which is recorded and sometimes further processed for reliable measurement.

Often signal processing is required for increasing system accuracy, noise reduction and calibration of the transducer output. In many cases also, signal processing block is optional.

A schematic diagram of the building blocks of a biosensor is given in figure 1.1.

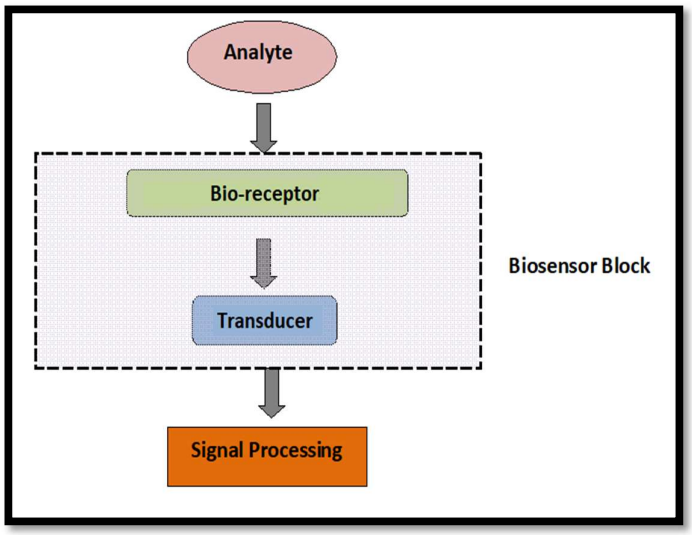

Fig.1.1. Schematic diagram of a biosensor

1.1.4. Classification

Biosensors can be classified in three different ways based upon choice of bio-receptors, transducers and sensing material. A brief chart of biosensor classification is provided in figure 1.2.

Bio-receptors or biorecognition elements may range from enzyme, antibody, cell, DNA/RNA, microorganisms to biomimetics [11]. As bio-receptors enhance selectivity of a sensor significantly; their proper choice can provide noise-free, accurate results for problem specific applications. Classification based on transducers is mainly divided into three classes optical, electrical and mechanical. Optical transducers will be discussed in details in section 1.2. Briefly there are many optical techniques available like Surface Plasmon Resonance (SPR), Interferometry, Fibre Optical arrangements, Optical Waveguide Lightmode Spectroscopy (OWLS), Chemiluminescence, Fluorescence etc. for high precision measurements [12-14]. Electrical transducers are well known for their rapid response [15]. Amperometry, Potentiometry, Conductometry etc. produces direct electrical signal which is desirable for many small size, compact, wearable sensors [15-18]. Mechanical sensors like Piezoelectric, Cantilever Resonance, Surface acoustic wave etc. are robust in nature and they are being investigated a lot recently [19]. Mechanical biosensors have the potential to measure change in mass, surface stress, interaction force, displacements, viscoelasticity etc. in cellular and subcellular regions [19, 20]. Sensor material is also equally important for achieving high sensitivity and accuracy of a biosensor. Development in nanotechnology has provided a good range of nanostructured materials with large interaction space and high sensitivity [9]. There has been remarkable development in the field of photonic crystal, liquid crystal, molecularly imprinted polymers etc. which are being utilised vastly in biosensor devices [21-25].

1.1.5. Application

Biosensors are used widely in different fields like healthcare, environmental monitoring, industrial process control, military, defence and many more. In medical industry, they are used extensively in disease detection, drug discovery, artificial tissue, bone, organ engineering etc [26]. They provide detailed insight in the field of biomolecule and their interaction study [26]. Their vast application in fermentation control and analysis of beverages and quality control in food production industry is also well known [27]. In environmental study, they take part in pollution and toxicity analysis of water and soil [28]. Plant pathology and soil quality analysis is essential in agriculture which is monitored by

biosensors for better production [29]. Biosensors have become an inevitable tool in forensic science and military applications nowadays [30].

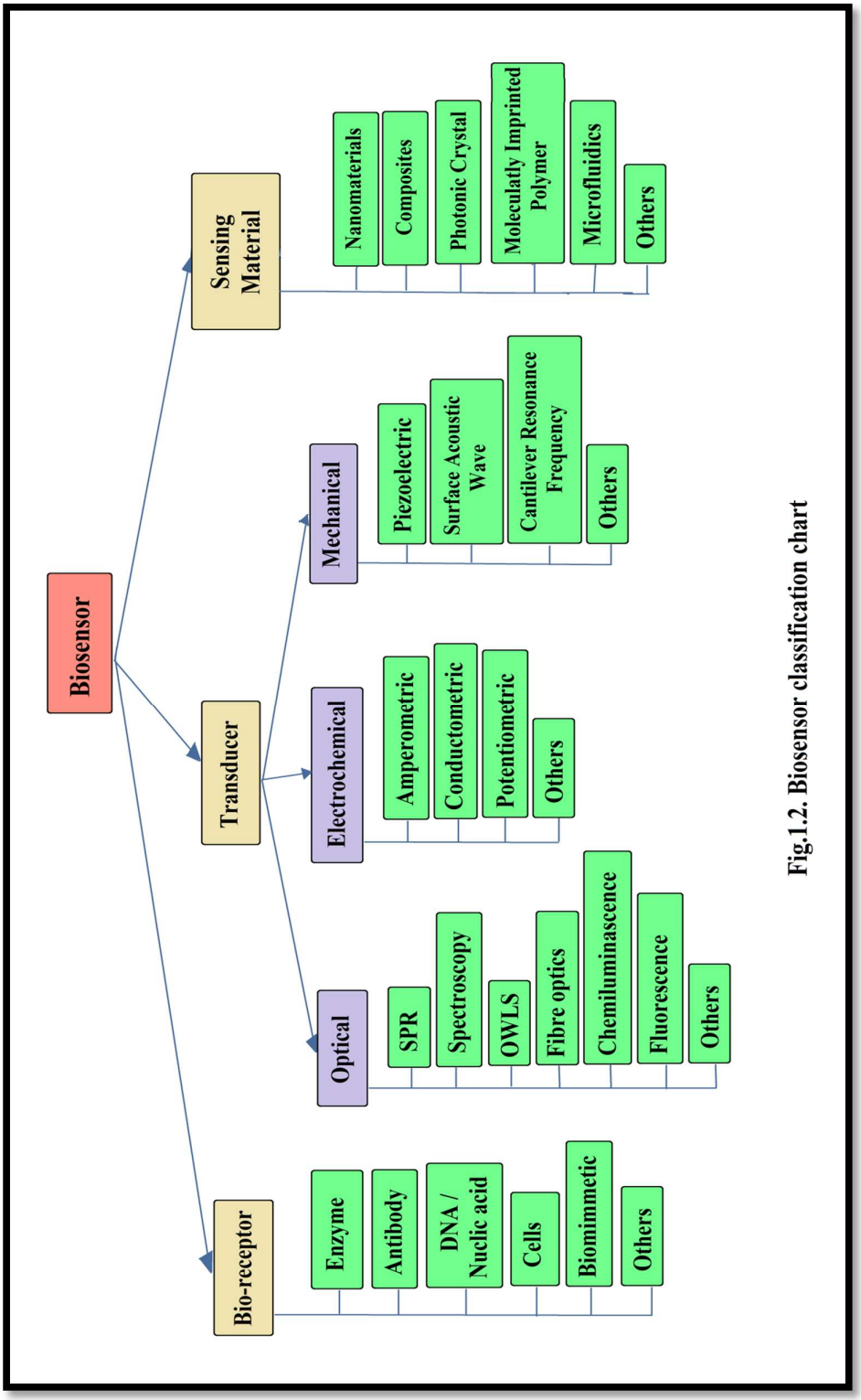

Fig.1.2. Biosensor classification chart

1.2. Optical Label-free Biosensor

From the classification chart of biosensors (figure 1.2) it is clear that choice of proper detection method and material is quite challenging as there are so many options available. In this section, a focussed discussion on optical label-free biosensors has been presented and current trends on such systems have also been discussed.

1.2.1. Optical Detection: Merit and Demerit

Optical detection is preferred due to their high sensitivity, specificity, accuracy, precision and robustness [12, 13]. Optical biosensors are immune to electric and magnetic interferences thus provide lower noise level [13]. Limit of detection i.e., the minimum amount of analyte that can be measured by the sensor increases immensely due to this noise immunity. The main advantage of such sensors lies in their ability towards high speed, real-time biomolecular reaction kinetic analysis where many other detection methods fail [12]. Optical detections are extremely reliable and provide accurate results in analyte detection and measurement.

The main disadvantages faced by optical methods are, many of the reliable instruments are extremely costly and prone to physical damage. Due to this drawback electrochemical sensors are preferred often, despite their high background noise and inaccuracy at lower detection range.

1.2.2. Label based Vs. Label-free Technology

Optical biosensors are classified in two main categories i.e., label based and label-free detection. In label-based detection scheme; a chemical compound called ‘tag’ is attached to the biorecognition element or the analyte molecule. Optical tags may be fluorophores or chemiluminescent compounds, which produce change in optical signals in the presence of analyte molecules. Label based sensing techniques are very sensitive as they can even sense the presence of a single analyte in a whole solution; but as its measurement is dependent on the mass of the analyte, proper amplification and processing is required for small output signals [31]. Also, the major drawback of labelling is, the process is pretty laborious and it sometimes changes the bioactivity of the analyte biomolecules. For

example, it causes reduced mobility or steric hindrance due to misfolding [31]. The tags are not always biocompatible and also the number of fluorophore attachment is not controllable which leads to fluorescence signal bias, resulting difficulty in quantitative measurement [32]. On the contrary, change in optical signal in label-free process is produced directly from the analyte molecules. Label-free detection methods measures biomolecules in their natural form which saves both expensive, time consuming tagging process and prevents biomolecular fouling [32]. Another most incredible advantage of label-free detection is reaction kinetics monitoring where one can record actual binding events of even the weakest biological interactions and difficult target molecules [32]. So, label-free detection method has become a promising field in modern biosensor research.

Table I: Comparison of labelled and label-free detection method

Detection Scheme	Advantage	Disadvantage
Label based detection	➢ Detection is extremely sensitive with detection limit down to a single molecule.	➢ Labelling process is time consuming and laborious. ➢ The labels often interfere with the function of a biomolecule. ➢ Number of fluorophores on each molecule cannot be precisely controlled. ➢ Quantitative analysis is challenging due to the fluorescence signal bias.
Label-free detection	➢ Relatively cheap and easy as no labelling is required. ➢ Quantitative and kinetic measurement of molecular interaction is possible. ➢ Does not interfere with the function of biomolecules. ➢ Detection signal does not scale down with the volume of the sample. Femtoliter to nanoliter detection is possible.	➢ Detection is less sensitive compared to label based detection. ➢ In the refractive index based sensors, the signal intensity often dies out due to larger molecule attachments or complex functionalization process.

1.2.3. Label-free Detection Methods

A lot of label-free optical detection methods are currently available for reliable and precision biomolecule measurement. In this section, only the prominent ones that have proved their worth over the last few years have been discussed.

1.2.3.1. Interferometry: When more than one light wave superimposes on each other, interference patterns occur. Interferometry is a study of these interference patterns, which consists critical information like frequency, phase, path difference, intensity etc. Interferometers are widely used in measuring small distance, refractive index changes and surface irregularities. Some of the interferometer based techniques with significant biosensing application are listed below.

- ***Mach-Zehnder Interferometer (MZI):*** Basic structure of MZI consists of a rib waveguide with two Y junctions as shown in figure 1.3. There are two arms between the Y junctions, sensing arm and reference arm. In the sensing arm, a portion of the cladding is removed, so in this area the evanescent field can interact with the outer surrounding. This is the active sensing area of the structure and the larger this area is, the better the sensitivity of the device. Bio-receptor molecules are implanted on the sensing area like all other optical label-free sensors. Coherent, single frequency, single polarized light is coupled through one end of the guide which should preferably be a single polarization and single mode structure to eliminate multimodal and cross polarization interference at output end [31]. When binding of target molecule occurs, change of refractive index in the sensing arm generates a phase difference from the reference arm, resulting in an interference pattern in the output terminal, where it is detected by a photodetector and thoroughly analyzed.

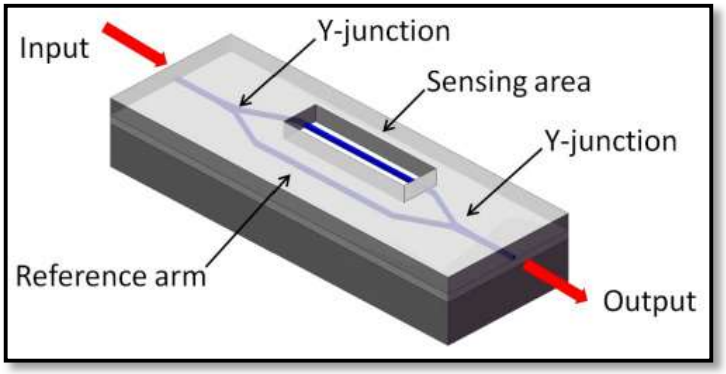

Figure 1.3. Schematic diagram of MZI structure [33]

Heideman et al. first demonstrated the scope of MZI biosensor by detecting human chorionic gonadotropin (hCG) antibody achieving LOD around 5×10^{-6} RIU and experimental DL 50pM hCG [34]. After that, further development has been achieved and biotinylated immunoglobulin immobilized IO-MZ chips [35], sensitive detection of IgG molecular monolayer [36], detection of 1% streptavidin monolayer [37] have been reported. Implementation of high performance antiresonant reflective optical waveguide (ARROW), a five layer guiding structure, for biosensing application has also made a huge improvement in this field [38]. The combination of slot and strip waveguide in the two arms of MZI structure provided detection limit as low as 1pg/ml of streptavidin solution [39].

- ***Young's Interferometer (YI):*** Like MZI, in Young's interferometer coherent, single frequency and single polarized laser light is coupled in the waveguide, which splits in the Y junction as shown in figure 1.4. The only difference with MZI structure is that the reference arm and the sensing arm do not combine. At the end of the sensor chip a CCD is placed, which captures the interference pattern caused by two effective light sources. Change in the phase difference between the two arms due to change in RI in the sensing arm, causes a change in spatial distribution of the interference fringes which is analyzed by fast Fourier transform of spatial intensity [40].

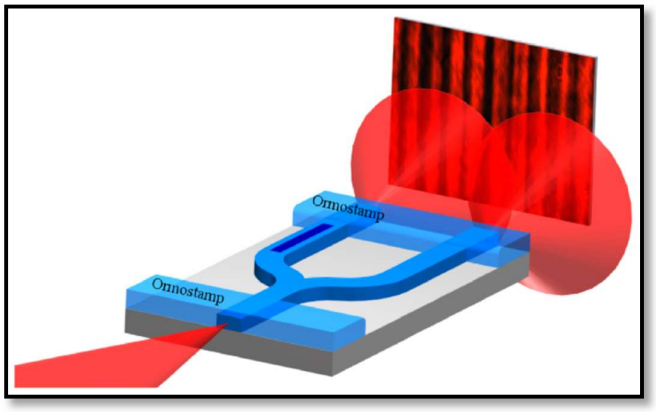

Figure 1.4. Schematic diagram of Young's Interferometer [41]

According to Brandenburg and Henninger, the basic YI scheme yielded system resolution of 10^{-7} RIU [42]. Further development for multiplexed sensing was demonstrated by Ymeti et al [43] in his ultrasensitive, fast virus detection YI model. Later Wang et al.

demonstrated a polymer base rib waveguide YI structure which provided detection limit of 2.4 pg/mm^2 for surface sensing of C-reactive protein solution [44].

➢ ***Fabry-Perot Interferometer (FPI):*** In general, FPI configuration, two partially reflective mirrors separated by some distance form a cavity, where a single incident beam of light breaks down into multiple beams of some phase difference by repeated reflection from the mirror surfaces. The transmitted parts of the beams form interference pattern and by focusing them with a lens, concentric circles of bright and dark fringes can be observed. In 1997, porous silicon based FRI biosensor was reported by Victor et al. [45]. The micro-structured porous silicon layer (figure 1.5) produced Fabry-perot fringes and upon attachment with antibody molecules a shift of the fringes was observed. Afterwards fiber-optic FRI [46, 47], polymer based micromachined FRI [48] were developed for better sensing performance of biomolecules.

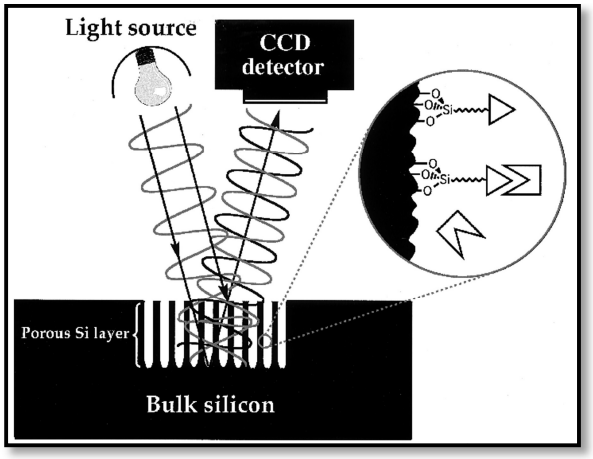

Figure 1.5. Schematic diagram of Porous silicon FPI [45]

There is also Hartman interferometer which proved to be a good sensing technique as detection limit as low as 2µg/L was achieved [49]; but in the last decade report on this interferometric biosensor has been quite low. In the following table some important works on interferometric detection in the last decade has been presented.

Table II: Some significant works in the last decade

Type of Sensor	Analyte	Biorecognition Element	LOD	Year & Reference
Polymer rib waveguide YI	C-reactive protein	Human CRP specific Antiboby	2.4 pg/mm^2	2012 [44]
Silicon nitride slot waveguide MZI	Streptavidin	Biotin	1pg/ml	2013 [39]

Nanostructured FPI	Protein A	Human IgG	<10pg/ml	2013 [50]
Cascaded MZI and ring resonator	Goat IgG	Antigoat IgG	1ng/ml	2014 [51]
Optofluidic FPI	Glucose	-	15ng/ml	2014 [52]
Optical Fiber FPI	Yeast growth	-	-	2016 [53]
Multiplexed YI	Anti-rabbit IgG, streptavidin, atrazine	BSA, atrazine-BSA conjugate	1 ng/ml	2016 [54]
Asymmetric MZI	Aflatoxin M1	Antibodies fragment (Fab')	$< 5x10^{-7}$ RIU	2016 [55]
In-fiber MZI	BSA	-	$2.57x10^{-4}$ mg/ml	2017 [56]
Microfluidic FPI	Biotin	Streptavidin	10^{-12} M	2019 [57]
Surface plasmonic coupled FPI	BSA, HEK-293 cell	-	$9x10^{-4}$ RIU (for BSA)	2020 [58]
Optofluidic YI	BSA	-	0.48 M	2020 [59]

1.2.3.2. Surface Plasmon Resonance (SPR): When an active surface (electron rich metal) at the interface of media with different refractive index, is impacted by polarized light, the free electrons of the metal surface start to oscillate generating surface plasmon waves (SPW). For a particular angle of incidence, resonance occurs and the polarized light is absorbed producing a dip in output reflected intensity pattern, which is monitored in SPR spectroscopy. In Kretchmann's configuration as shown in figure 1.6, Prisms are used to couple light. The top surface of the prism is coated with a thin metal film. Polarized light from an external source is incident on the metal prism interface which results a total internal reflection for a critical angle and the generated evanescent field penetrates through the metal surface. For a particular angle of incidence greater than this critical angle, the propagation constant of the evanescent field exactly matches with the SPW and resonance occurs, resulting photons to be coupled in the SPW. This resonance angle is highly dependent on the properties of the metallic film, wavelength of the incident light and refractive index of the medium on both side of the metallic film [60]. Now if biomolecules get attached to the receptor molecules immobilized on active metal surface, the effective refractive index of the medium changes, thus changing the resonance angle. This change in RI is linearly proportional to the number of analytes attached to the metal surface [61]. So, analyte concentration can be measured by monitoring resonance angle. Also, reaction kinetics in the flow cell can be observed real-time.

GE Healthcare's Biacore systems are the first commercially available prism coupled SPR system. These systems have typical DL 10^{-6} to 10^{-7} RIU [31]. Some instrumental improvement achieved maximum 10^{-8} RIU [62]. The main disadvantage of prism coupling is that it is bulky and cannot be used in 'lab on chip' models. In contrary, fiber optic coupling can be done by removing a small portion of cladding and coating it with thin metal film. In order to achieve better performance another new structure has been developed, where a thin metal layer is sandwiched in between two dielectric layers of same RI [63-67]. This new structure gives better performance in sensing large molecules and complex solutions like whole blood. Due to the presence of two metal dielectric interfaces, Long Range Surface Plasmon (LRSP) and Short Range surface Plasmon (SRSP) are generated. LRSP evanescent field penetrates deeper onto the solution, so it is used to monitor bulk RI change; where SRSP evanescent field penetration is weak and it only monitors surface RI change.

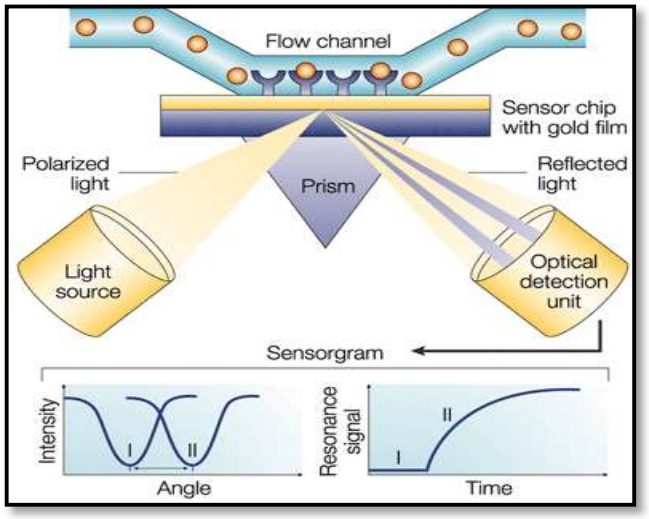

Figure 1.6. SPR biosensor Schematic Diagram [68]

TABLE III: Some significant works in the last decade

Type of Sensor	Analyte	Biorecognition Element	LOD	Year & Reference
SPRCD (Surface Plasmon coupler and disperser)	Micro-ribonucleic acid	Thiolated DNA oligonucleotides	2pM	2010 [69]
LRSP	E. coli O157:H7	cAb, no. ab75244	50 cfu mL^{-1}	2012 [70]
SPR	IgM	Dengu Antigen	-	2014 [71]
Smart phone SPR	Bovine IgG	Staphilococcal protein A	47.4nM	2015 [72]

SPR	Glucose oxidase/ Uricase	Glucose/Uric acid	3.4/0.27 µmol/l^{-1}	2017 [73]
SPR	HER2(+) Exosome	Anti HER2 Antibody	8280 exosomes/µL	2019 [74]
Optical fiber SPR	Infliximab	Anti infliximab	23.5ng/ml	2020 [75]
Magnetic SPR	A H1N1	Corresponding monoclonal Antibody	-	2020 [76]
SPR	Valspodar and cyclosporine	Lentiviral particle	_	2020 [77]

1.2.3.3. Optical Fibers and Waveguides: Optical fibers and waveguides are popular in biosensing field as they are simple, compact and highly sensitive. Due to simplicity of fabrication, they are highly cost effective and there is also a huge scope of material modification for better performance achievements.

- ***Optical Fibers:*** Optical fibers are made up of core and cladding which surrounds the core. Refractive index of cladding material is slightly less than core, so that total internal reflection (TIR) can take place at an incident angle greater than critical value. When TIR occurs some portion of the EM energy leaks out from the core cladding interface which is called evanescent field (EF). The intensity of this Evanescent waves (EW) dies down exponentially with increasing distance from core. This EF intensity is highly sensitive to the surrounding medium. If biomolecules are introduced in fiber optic surrounding medium EF gets affected by the change of effective refractive index in cladding-surrounding medium interface. When cladding is sufficiently thick, EWs are unable to reach sensing interface due to their low penetration depth. Approaches such as, stripping of a small portion of cladding, tapering, bending has been incorporated to increase penetration depth so that interaction between surroundings and EF can be sufficiently strong for reliable sensing application [78]. For different analytes the absorption spectra are different and thus qualitative and quantitative measurement of verities of analytes is possible.

Absorption of EW at 280 nm was demonstrated using Goat Anti-Human IgG as model analyte, and minimum detection limit was found to be 0.1µg/ml [78]. Tapered U bend plastic optical fiber biosensors were also reported for cell detection [79, 80]. Mixed scheme of detection like SPR based optical fiber where a part of the fiber is coated with thin gold or

silver layer to induce plasmonic effects, or Interferometric biosensors with optical fiber, have enhanced overall performance as reported by Cao et. al. and Li et. al. [81, 82].

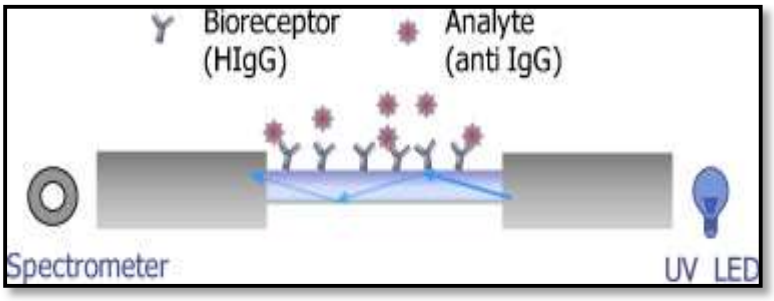

Figure 1.7. Schematic on sensing principle of basic fiber optic biosensor [78]

➢ ***Optical Waveguide Lightmode Spectroscopy (OWLS):*** The basic principle of OWLS (or grating coupler sensor) depends on the grating coupling phenomenon, where light can be coupled into a waveguide structure using optical grating pattern implanted on the surface of the waveguide. The grating acts as a guided-mode resonance filter which gives very narrow bandwidth [83-85]. In OWLS a polarized monochromatic laser beam falls on the grating surface as shown in figure 1.8 and for a particular angle of incidence this light will be guided through the waveguide, which can be detected by two photodetectors connected to the assembly. The angle of incidence, for which guided-mode resonance will take place, is highly dependent on the refractive index of the cover medium, wavelength of incident light and grating pitch. So, if the refractive index of the cover medium changes due to introduction of biomolecules, this coupling angle also changes. Precise measurement and real time monitoring of incident angle vs. guided intensity is possible in OWLS instruments and the adsorbed mass density can be calculated by well defined de Feijter's formula [84].

Microvacuum organization has developed a highly sensitive grating coupler biosensor system OWLS 210 [86], which contains surface functionalized grating coupler waveguide chip OW2400. There is a flow cell in this arrangement which allows analysis of binding kinetics also. J Vörös et al. and J.J Ramsden et al. discussed different biological applications of OWLS like Protein-DNA interaction, Lipid bylayers, Biomembrane etc. in their work [87]. Adányi et al. developed an immunosensor for the detection of Aflatoxin and Ochratoxin in both competitive and in direct immunoassays, which yielded the limit of detection between 0.5 and 10 ng ml^{-1} in both cases [88]. Namsoo Kim et al. performed

Salmonella detection with a direct binding optical grating coupler immunosensor and reached detection limit of 1.3×10^3 CFU/ml [89].

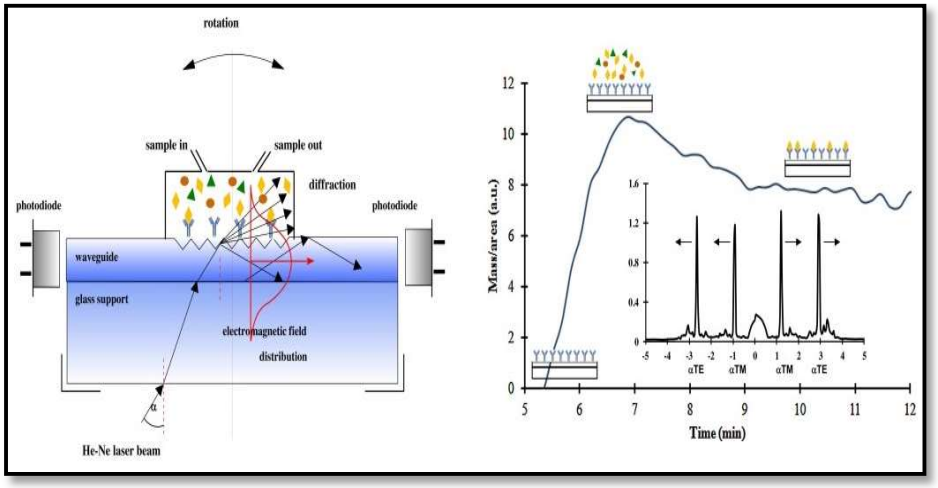

Figure 1.8. Schematic diagram of OWLS [85]

➢ ***Resonant Mirror:*** This type of configuration combines high sensitivity of waveguide device and simple construction of SPR sensors [90]. It is typically a three layer waveguide structure as shown in figure 1.9. The high index waveguide layer and the high index substrate layer which may be a prism, is separated by a low index metal or dielectric layer. At the spacer-substrate layer interface, the waveguide model is leaky; so instead of total internal reflection inside the waveguide structure, light is strongly reflected back from the substrate. The model supports TE and TM both modes [91] unlike SPR structure, which only allows TM mode. When light is incident on the substrate layer at resonance angel, it is strongly coupled in the high index waveguide layer and at each reflection point in this layer, light is leaked out and gives strong reflection at output end. As light propagates along the waveguide layer, the evanescent field interacts with the functionalized sensing layer and with attachment of analyte, RI of the cover changes, changing the detector output.

NeoSensor is a commercially available biosensor using RM structure [92]. Zourob M. et al demonstrated an improved structure of the RM based biosensor, which may be a promising model for further reliable biosensing application and reaction kinetics study [93]. In the last decade reports on resonant mirror biosensor has dropped significantly; but still it is a very successful model worth to be discussed.

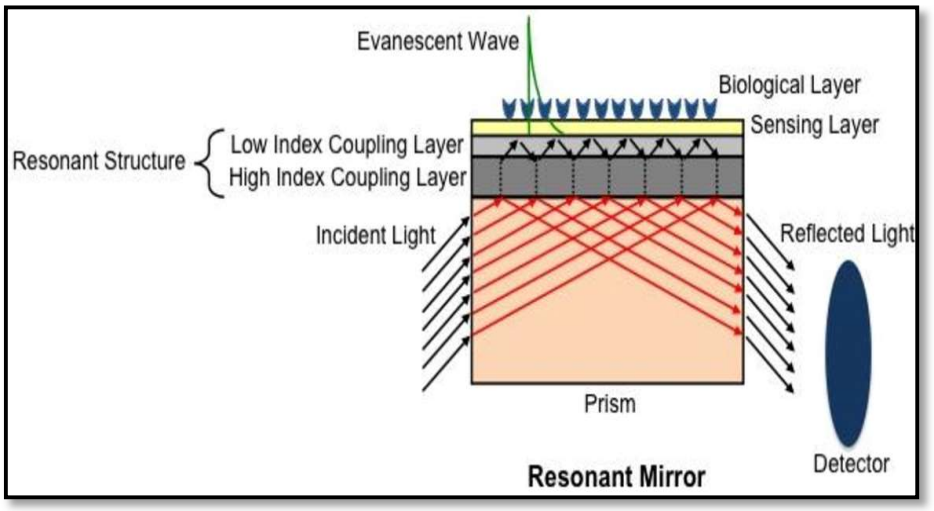

Figure 1.9. Resonant Mirror sensor [90]

- ***Metal Clad Waveguide (MCWG):*** This is also a leaky model, so it is called Metal Clad Leaky Waveguide (MCLW). The structure is not much different from the RM structure, only here the waveguide layer is low index and the spacer layer is a metal layer.

Light is guided along the low index waveguide layer and the presence of the metal layer enhances evanescent field penetration depth in the bulk solution which enhances the sensitivity of the device compared to RM structure [94]. According to Skivesen et al., there are two types of MCWG operational modes, peak type and dip type [95]. When the metal layer, separating low index waveguide layer and high index substrate layer, is about tens of nanometers thick and imaginary part of its dielectric constant is small, a dip in the output response will be observed. And when the opposite happens i.e., the metal thickness is only a few nanometres and dielectric constant imaginary part is large, a peak in the output response is observed. These peaks and dips are very sharp, making the sensor structure extremely sensitive [95]. Skivesen et al. in her later studies demonstrated a refractometric setup of MCWG sensor chips which detected sedimentation of mammalian skin cell with minimum DL 8-9 cells/mm^2 [96]. A DL of 8×10^4 spores/ml for Bacillus subtilis var. niger bacterial spores was observed in peak type waveguide sensor [97]. Won Joo Im et al. recently used MCLW as an immunosensing tool and showed a DL approximately 3.8×10^{-6} RIU for human interleukin 5 [98].

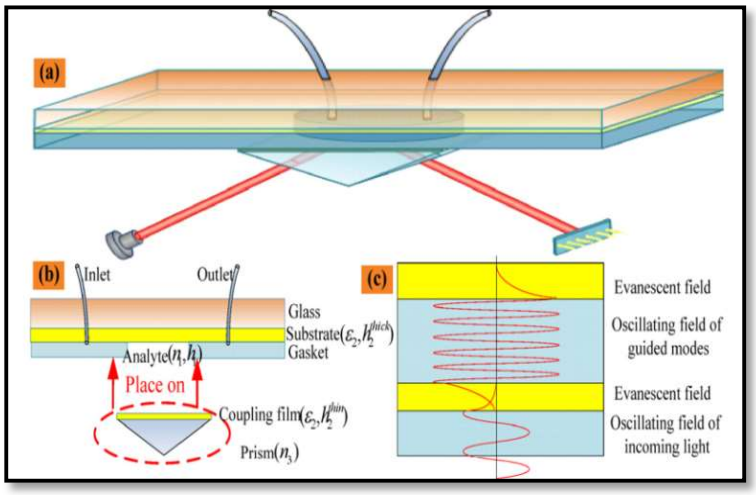

Figure 1.10. MCWG sensor schematic structure [99]

TABLE IV: Some significant works in the last decade

Type of Sensor	Analyte	Biorecognition element	LOD	Year & Reference
OWLS	Deoxynivalenol (DON)	DON specific polyclonal Antibody	0.005ng ml^{-1}	2011 [100]
LSPR optical fiber	Glucose	Glucose oxidase	-	2012 [101]
MCWG	Human interleukin5(hIL5)	hIL5 Antibody	10ng/ml	2012 [98]
OWLS	Carp Vitellogenin	Lipovitellin	0.07ng ml^{-1}	2013 [102]
MCWG	C reactive protein	CRP polyclonal Antibody	1.22x 10^{-4} RIU	2014 [103]
Plastic optical fiber	E. Coli O55	Staphylococcal protein A	-	2014 [80]
OWLS	Polyphenol oxidase (PPO)	polyclonal anti-PPO Antibody	0.005607 U/ml	2015 [104]
Interferometric optical fiber	Human IgG	Anti human IgG	2.3 ng/ml	2018 [105]
OWLS	Sulfamethazine (SMZ)	Anti SMZ Antibody	1pM	2018 [106]
SPR optical fiber	Thrombin	DNA Apt29	1nM	2019 [107]
U bend Plastic optical fiber	CHIKV-nsP3 protein	anti-polyhistidine monoclonal Antibody	0.52 g ml^{-1}	2021 [108]

1.2.3.4. Ring Resonator: The basic principle behind optical ring resonator is Whispering Gallery Modes (WGMs) [109-111], though here the wave that makes the revolution is not sound wave but light wave. The structure (figure 1.11) consists of one or more waveguide

loops with straight waveguides (bus waveguide, coupling waveguides) to couple light in and out of the loop. When light is incoupled at resonance wavelength [109] in the ring waveguide structure, it is guided through the ring with repeated total internal reflections and produces constructive interference by overlapping revolution cycles, allowed by the structure. The detector waveguide outcouples the light from the ring after certain revolution cycles. The WGM and circulating waveguide mode is analyzed by Mei theory [109-111]. The evanescent field of the whispering gallery wave, on the ring resonator surface, responds to the change of effective refractive index on the cover medium due to binding of target molecules. Now this light-analyte interaction length is important, as large interaction length implies higher sensitivity. In ring resonator structure the interaction length does not depend on the physical structure of the sensor chip like all other methods, but the number of revolutions which is determined by the Q factor [112] of the ring resonator. So, the higher the Q factor, the better the sensing performance. The binding of target molecule changes the WGM spectral shift, which is directly or indirectly monitored and this gives the required information about the amount of target molecule and also provides reaction kinetics information. Based on this theory, three major structures have been implemented up until now.

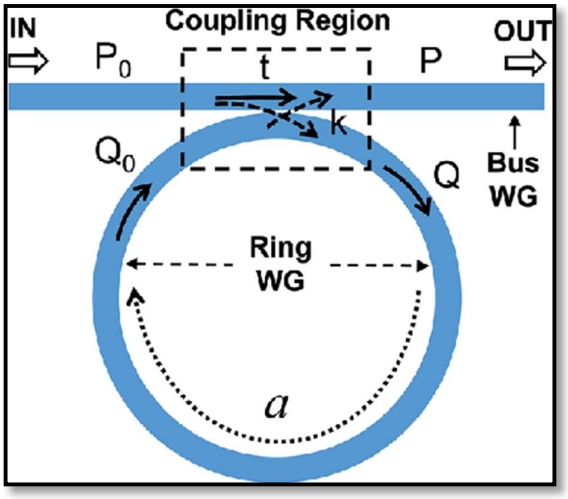

Figure 1.11. Schematic diagram of Ring Resonator [113]

➢ ***Chip-based Ring Resonator:*** In this type, microring, microdisk, microtoroid-shaped resonator structures are fabricated on a chip [114-116]. The advantage of them is, they have mass production and optoelectronic integration capabilities, but their severe disadvantage

is that, except toroidal structure they have poor Q factor, and the structure design procedure it quite laborious and challenging. Though theoretical DL of these models is found to be 10^{-9} RIU [117], practically such precision has not been achieved yet. Ian M. White et al. demonstrated a ring resonator DL of roughly 10^{-7} [118]. Erol Ozgur et al. recently demonstrated a limit of detection 0.11nM for human Interleukin 2 in complex solution, using highly sensitive Microtoroidal structure [116].

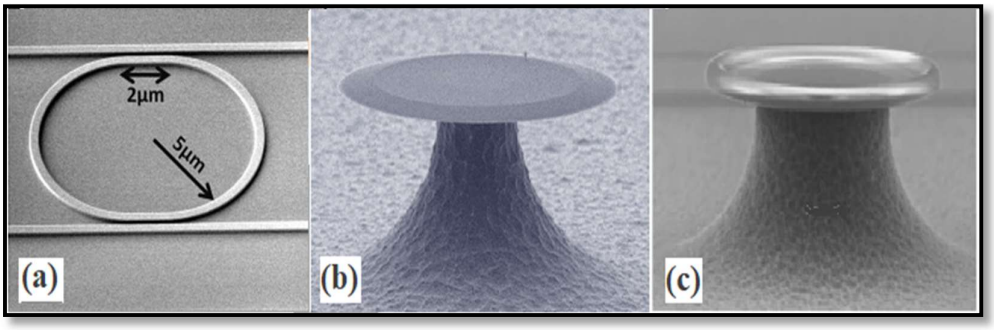

Figure 1.12. FESEM of (a) Microring [119], (b) Microdisk [120], (c) Toroidal-shaped resonator [121]

➢ ***Stand alone Dielectric Microsphere:*** Microsphere resonators have higher Q factor compared to the previous one, so they have better sensitivity and by directly monitoring WGM spectral shift, 10^{-7} DL order can be achieved [122]. Ian M. White showed that small molecules can be detected in trace quantities at the microsphere resonator surface [123]. DNA detection using microsphere was demonstrated by Vollmer et al [124] with 1pg/mm^2 detection limit. Further work on viral detection [125], large molecules like bacteria detection (E. coli) [126] was also performed. In his further studies Ian M. White et al. demonstrated a porous-wall hollow glass microsphere structure (PW-HGM) [127], which gave improved sensitivity due to nanopores introduced in the microsphere structure. Though it was tested for vapour detection at first, it has immense capability in biosensing applications.

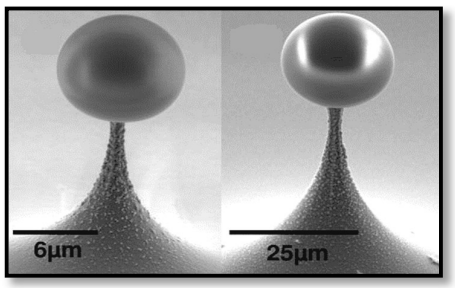

Figure 1.13. SEM image of Microsphere resonator structure [128]

➢ ***Liquid core (LCORR) / Optofluidic Ring Resonator:*** In capillary based optofluidic structure, the capillary wall thickness is made very thin (less than 5µm) and the outer radius of the capillary is made around 100µm [129]. The evanescent field of WGM, due to this thin wall, penetrates the hollow core and interacts with the RI change of the solution inside the core (figure 1.14). This structure is being widely used in biosensing applications recently. For example, H. Zhu et al. demonstrated DNA detection limit 10pM [130], virus particles have been detected with LOD 1000 particles/ml [131], protein (BSA) detection limit was found to be 1pg/mm^2 [132] and so on.

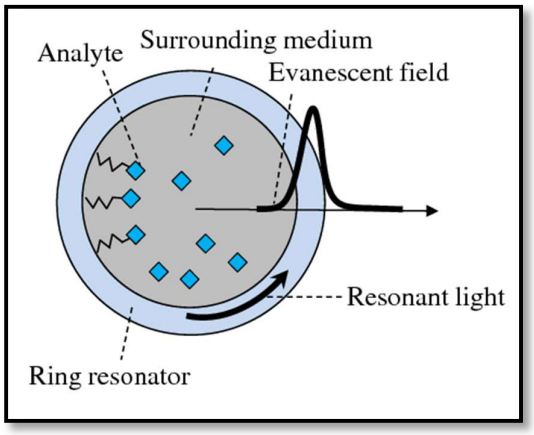

Figure 1.14: Schematic diagram of Capillary based optofluidic ring resonator [133]

TABLE V: Some significant works in the last decade

Type of Sensor	Analyte	Biorecognition element	LOD	Year & Reference
Optofluidic Ring Resonator	T Lymphosite cell	CD4+ and CD8+ Antibody	-	2010 [134]
Silicon Microring	Human IgE and Thrombin	Anti IgE and anti thrombin aptamer	33pM and 1.4nM	2013 [135]
Glass microsphere	Oligonucleotide	Receptor Oligonucleotide	-	2014 [136]
Double-side Ring Add-drop Filter microring	Salmonella bacteria	Salmonalla total Antibody	10^{-8} RIU	2014[137]
Microtoroid resonator	Human interlukin 2	Anti IL-2 Antibody	0.1 nM	2015 [116]
Silicon on insulator microring	Testosterone	Molecularly imprinted polymer	48.7 pg/ml	2015 [138]
SWG microring	Biotinylated BSA / microRNA	Streptavidin / capture DNA	$3.9x10^{-4}$ RIU	2016 [139]

Optofluidic Microbubble resonator	Biotin	Streptavidin	0.41 pM	2018 [140]
Porous silicon microring	BSA	-	0.5 pg mm^{-2}	2018[141]
Microdisk laser	Streptavidin	Biotin	104 ng/ml	2018 [142]
Silicon Microring	Coxiella burnetii	DNA probe	-	2019 [143]
Au-Np coated Silica Microsphere	Glucose	Glucose oxidase	-	2020 [144]
HD microdisk	Human IgG	Goat anti-human IgG	0.060 a_M	2020[145]
Silicon Nitride microring	Neuropeptide Y	-	0.25 g/ml	2020 6]

1.2.4. Label-free Optical Biosensor Materials

Just like different sensing principles, choice of sensor materials is a very important aspect in biosensor fabrication. Biocompatibility, non-toxicity, large surface to volume ratio, good absorption property etc. are the few things need to be taken in consideration while choosing biosensor materials. Here, some of the important materials that are being used extensively in label-free optical biosensing have been presented**.**

1.2.4.1. Nanomaterials: Nanostructured materials have unique physiological and chemical properties that differ from bulk materials. Due to the recent advancement of chemical synthesis process in nanotechnology there is huge scope of preparing different types of nanostructures like nanospheres, nanorods, nanotubes, nanowires, nanofibers, nanoflowers, quantum dots etc. Nanoparticles are typically of the dimension range 1-100nm which is quite comparable to biomolecules thus there is significant interaction between nanostructured layer and analytes which ensures enhanced signals for biosensors. The benefit of using nanomaterials as sensing platform lies in their easily tunable size and shape dependent properties, large surface to volume ratio and capability of fabricating miniaturized biosensors.

Metal Nanoparticles like gold and silver nanospheres are used extensively for signal enhancement of nanoparticle enhanced SPR sensors, fiber optic sensor coating, grating couplers etc. In SPR, signal is generated due to interaction between incident photons and

conduction electrons of the metallic nanoparticles. Peak extinction wavelength of SPR signals was found to be sensitive on the size and shape of the nanoparticles [147]. Triangular silver nanoparticles were found to have remarkable optical properties and combining it in LSPR configuration produced LOD as low as picomole to femtomole [147].

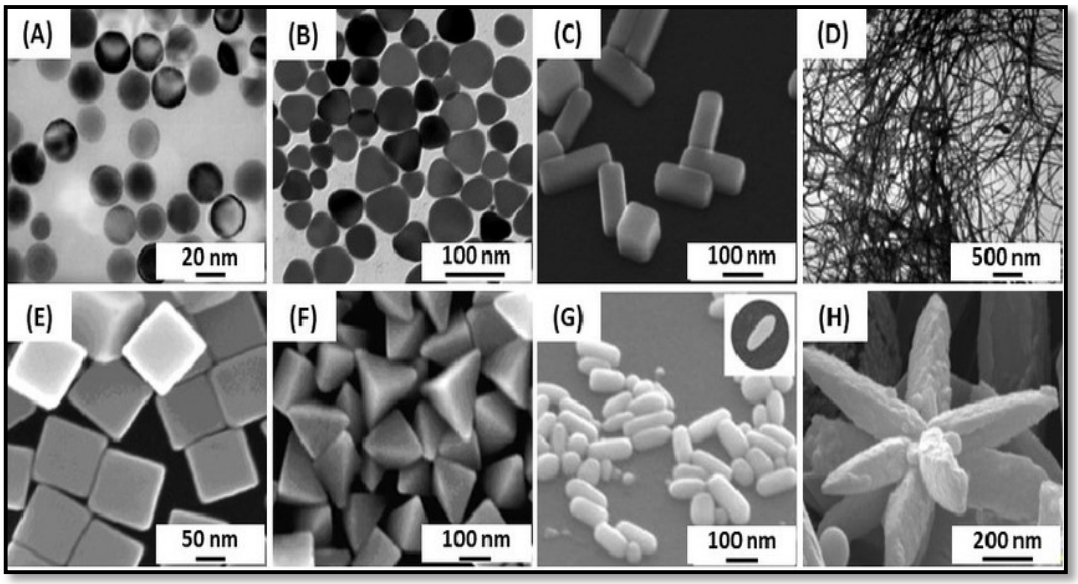

Figure 1.15. TEM image of silver (A) Nanosphere, (B) Nanoprism, (C) Nanobar, (D) Nanowire and SEM image of silver (E) Nanocube, (F) Nanopyramid, (G) Nanorice, (H) Nanoflower [156]

Metal Oxide nanostructures are also of great interest recently due to their biocompatibility, enhanced absorption property and non-toxic nature. Zinc oxide (ZnO) is being investigated for optical biosensors due its room temperature photoluminescence and unique structural properties. ZnO film was reported to have surface structural property favourable for direct immobilization of antibody [148]. Hydrothermally synthesized ZnO nanorod based non-enzymatic optical sensors have been demonstrated for selective, interference free detection of human serum glucose [149]. Titanium Oxide (TiO_2) is also an interesting metal oxide platform due to its stability in aggressive chemical environment, non-toxic nature and room temperature photoluminescence. Viter R. et al. demonstrated Salmonella detection using TiO_2 nanoparticle coated glass sensors [150]. Green synthesis i.e., synthesis of TiO_2 nanoparticles from plant extract was has been reported for antibacterial sensors [151]. Nanoporous structures like porous aluminium and porous silicon are very popular for their large surface to volume ratio which provides increased interaction space with analytes leading to better sensor response. Thin film transducers made of

nanoporous alumina proved to be a reliable diagnostic tool for point of care application in chronic wound healing [152]. Nanoporous anodic alumina barcodes were reported to have biomedical sensing application in UV-visible region [153]. Sha Li et al demonstrated porous silicon microcavity as highly sensitive platform for bacteria detection with LOD as low as 20 bacteria ml^{-1} [154]. Grating coupled porous silicon waveguide was reported by Xing Wei et al., which showed better molecular detection capability than standard grating couplers [155].

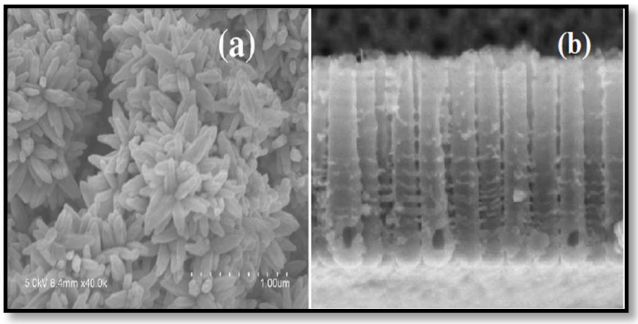

Figure 1.16. SEM image of (a) ZnO Nanoflower [157], (b) TiO_2 Nanotube [158]

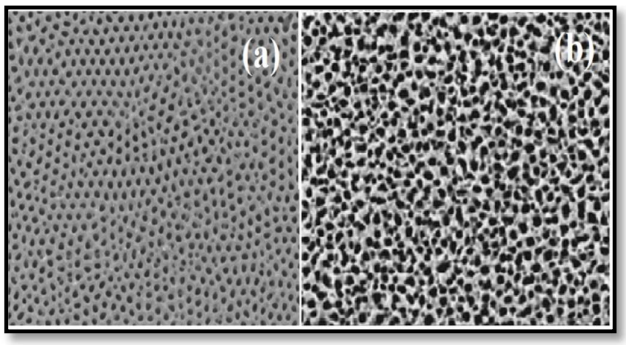

Figure 1.17. SEM image of (a) Porous Alumina [159], (b) Porous Silicon [160]

TABLE VI: Some significant works in the last decade

Sensor Material	Analyte	Biorecognition element	LOD	Year & Reference
TiO_2 Nanotube	Human IgG	Protein A	-	2010 [161]
Porous silicon	Protease	Gelatin	-	2010 [162]
Porous anodic aluminium oxide	Pancreatic cancer cells (PANC-1)	Biotinylated anti-EpCAM Antibody	<1000 cells/ml	2012 [163]
Gold nanorods	Aflatoxin B1	-	0.16 ng ml^{-1}	2013 [164]
TiO_2 coated PSi	Sheep IgG	Rabbit anti-sheep IgG	0.6 µg/ml	2014 [165]

ZnO Nanowire	Uric acid	-	5.74%	2015[166]
Gold nanostar	DNA target	DNA probe	6.1 nM	2015 [167]
TiO_2 Nanoparticle	Salmonella typhimurium	Anti-Salmonella serum	-	2017[150]
Porous silicon	Protein A	Protein A binding aptamer	3.17 µM	2017 [168]
Porous anodic alumina	Tumour necrosis factor-alpha (TNF-α)	Anti TNF-α Antibody	0.13 µg/ml	2018 [152]
Core shell gold/silver nanoparticle	Staphylococcal enterotoxin A (SEA)	Anti SEA Antibody	0.2/0.4 nM	2019 [169]
Porous anodic alumina	Cathepsin B	-	0.08 nM	2020 [170]
Au and ZnO nanoparticle	Cholesterol	Cholesterol-oxidase	0.6161	2020 [171]

1.2.4.2. Composite Materials: Isotropic and inhomogeneous materials which are composed of two or more different materials and possess unique physical and chemical properties are known as composite materials. Composites are classified mainly by matrix or binder material and filler or reinforcement phase [172]. Matrix can be of vast range from polymer, carbon, metal, ceramic etc. Fillers can be different type of nanoparticles, fibers etc. which is supported by the matrix. The mixture of these two or more phases creates properties which are not observed in the constituent individual materials and these properties can be optimized by varying filler or matrix type and concentration. Thus, composites can be created and optimized according to the need of application and thus have become an interesting field of research nowadays.

Polymer Matrix Composites (PMC) is used due to low cost, biocompatibility and diversity in physiochemical properties. PMC physical and chemical properties can be modified easily which enables selective active biomolecule attachment. Biopolymer chitosan and silver nanocube composite was reported by Di Zhang et al. for mouse IgG detection in lower concentration range. It was observed that in presence of the composite film, limit of quantification was four times less than traditional SPR sensors [173]. Gold-Polymethylmethacrylate (PMMA) nanocomposite showed significant improvement in LSPR sensing after surface treatment like annealing which helped the gold nanoparticles to move towards the surface, increasing biomolecular interaction [174]. Gold/Cadmium sulphide

quantum dot in polyamaidoamine (PAMAM) matrix has also been demonstrated for highly sensitive and selective detection of dengue virus [175].

Magnetic nanocomposite Fe_3O_2 and Au nanorod (AuNR) was demonstrated to have both magnetic and optical properties which contribute to enhanced antibody immobilization and sensitive detection [176]. Ceramic composite Au/TiO2 thin films have been used in LSPR sensing and it was observed that plasma treatment increased surface sensitivity of the nanocomposites significantly [177]. Porous silicon-ZnO nanocomposite has also been investigated in biophotonic application for Aflatoxin B1 detection [178]. Two layers of Graphine oxide-Au nanoparticle composite was reported to have amplifying effect in SPR response and detection limit as low as 0.1 fM was achieved for microRNA sensing [179].

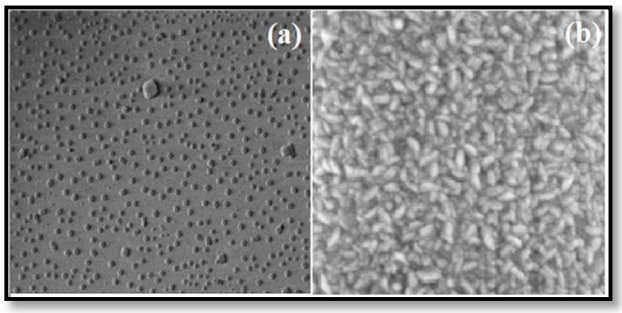

Figure 1.18. SEM image of (a) Au-PMMA nanocomposite [180], (b) PSi-ZnO nanocomposite [181]

TABLE VII: Some significant works in the last decade

Sensor Material	Analyte	Biorecognition element	LOD	Year & Reference
ZnO-Au nanocomposite	Rabbit IgG	Goat anti-rabbit IgG	-	2010 [182]
Fe_3O_2/AuNR magnetic nanocomposite	Goat IgM	Anti- goat IgM	-	2012 [176]
Graphine oxide-Au nanoparticle composite	microRNA-141 and small molecule adenosine	Capture DNA molecule	0.1 fM	2017 [179]
Hybrid Au nanoparticle/graphine oxide composite	Anti BSA	BSA	145 fM	2018 [183]
Zinc oxide and Molybdenum sulphide nanocomposite	Urinary p-cresol	Molecularly imprinted polymer	28 nM	2018 [184]
Porous silicon ZnO nanocomposite	Aflatoxin B1 (AFB1)	Anti-AFB1 Antibody	-	2020 [178]

Au/CdS quantum dot-PAMAM nanocomposite	Dengu Virus E protein	IgM	0.1 pM	2020 [175]
Graphine oxide/ Polyamidoamine nanocomposite	Dengu Virus (DENV) E protein	Anti DENV Antibody	0.08 M	2020 [185]

1.2.4.3. Molecularly Imprinted Polymers (MIP): MIP is comparatively new in the field of biosensor but proved to be huge breakthrough in replacing standard biorecognition elements or capture probes. Their main advantages over biological counterparts are chemical and thermal stability, longer storage life, durability and multi-time usage capability. These artificial bioreceptors are very much cost effective and can be easily fabricated. MIP consists of binding sites which have physical structure and chemical properties complementary to the target molecules or templates. They act similarly to the biological antigen-antibody system. MIP synthesis requires a pre-polymerization mixture which contains template molecule, functional monomer, cross-linking monomer and a radical initiator in a suitable solvent. Polymerization is initiated by exposing the mixture in UV radiation or heat. Higher degree of cross-linking provides mechanically stable micro-structures inside the polymer matrix after extraction of template molecules. There are two methods of MIP synthesis with respect to template and functional monomer interaction, which are non-covalent or self assembly and covalent imprinting. In covalent imprinting process template molecules are covalently attached with functional monomer before preparing pre-polymerization mixture. Though covalent imprinting protocol produces high yield of homogeneous binding sites; self assembly is way more popular due to its simplicity and capability to produce higher affinity binding sites [186].

2D self assembled thiol monolayer with recognition properties towards dansylated amino acids has been prepared on SPR chip and selectivity for the template over didansyl-L-lysine has been observed [187]. Compact, low cost and highly sensitive detection of anesthetic propofol was reported using microfluid optical biochip with on-chip imprinted polymer [188]. Smartphone based aflatoxin B1 detection has been demonstrated with imprinted polymer membranes synthesized with acrylamide functional monomer and LOD was found to be as low as 20ng/ml [189]. MIP based photonic material as integrated optical

antibiotic enrofloxacin sensor has been proposed by C.A Barrios et al. [190]. Multifunctional MIP composites with both magnetic and optical properties have been reported for rapid and cost effective detection of doxycycline in pig plasma and LOD of 117nM was achieved [191].

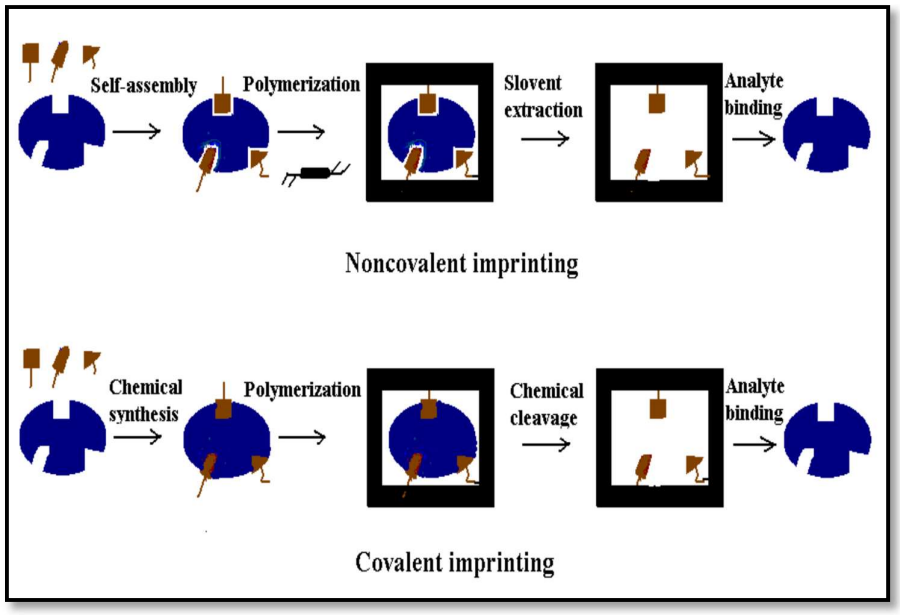

Figure 1.19. Schematic diagram of MIP synthesis [186]

TABLE VIII: Some significant works in the last decade

Sensor Type	Analyte/ Template	Biorecognition element	LOD	Year & Reference
SPR	F_{ab} fragments	Molecularly imprinted polymer	56 ng/ml	2011 [192]
SPR	Procalcitonin	Molecularly imprinted polymer	9.9 ng/ml	2013 [193]
SPR	Citrinin	Molecularly imprinted polymer	1.7 pg/ml	2015 [194]
Microring resonator	Progesterone	Molecularly imprinted polymer	83.5 fg/ml	2017 [195]
Optical Fiber	Urinary p-cresol	Molecularly imprinted polymer	28 nM	2018 [184]
SPR	Troponin T	Molecularly imprinted polymer	14.8 nM	2018 [196]

Interferometry	Parathion methyl	Molecularly imprinted polymer	79.43 fM	2019 [197]
SPR	Aflatoxin B1	Molecularly imprinted polymer	1.04 g/ml	2020 [198]

1.2.4.4. Photonic Crystals: Photonic crystals (PC) are periodically modulated dielectric structures which control the motion of photons. Such materials exhibit distinct optical band gap much like electronic band gaps present in ionic lattice which is responsible for electron motion control. At the boundary of high and low refractive index medium in periodic structure, interference of reflected and refracted photons occurs generating constructive and destructive patterns which produces the effect of photonic bands allowing a range of electromagnetic frequencies to pass through it. On the other hand, the frequencies that lie within the photonic band gap are reflected back and only their evanescent fields penetrate in the crystal. Lord Rayleigh first experimented with stacked periodic dielectric layer and found that they exhibit one dimensional photonic band gap. In recent time, due to immense advancement in nanostructure development processes, two and three dimensional PC structures can be fabricated easily by photolithography, drilling, direct laser writing, self assembly and many more [199].

In 1D PC periodic modulation of refractive index is either in horizontal or in vertical direction. Bragg Mirrors and fiber Bragg gratings (FBG) are some common examples of 1D PC. Mirrors made from dielectric stacks are extremely efficient as absorption of light in dielectric material is minimal. Their only drawback is that they operate in a very narrow range of incident angle close to normal incidence. In FBG refractive index of the core axis is modulated in a periodic sinusoidal pattern. FBG has very narrow bandwidth and they have been used extensively in dispersion compensations, filters etc [200]. In 2D PC periodicity in refractive index is in two directions and propagation of light is restricted in the plane of periodicity. Generally, two types of structures are considered for 2D PC i.e., array of dielectric pillars or rods in homogeneous dielectric medium and array of holes in homogeneous dielectric medium. When refractive index difference between dielectric pillars or hole with background dielectric is significantly high then 2D photonic band gap is

generated for propagation in the plane of periodicity. 3D PC has periodic modulation of refractive index in all three dimensions thus allowing photon confinement in all directions. Initially 3D structure fabrication was a challenge due to their complex geometry. Self assembly produces 3D PC naturally but, in this process, choice of lattice symmetry is limited. On the other hand, lithographic approaches can obtain almost any type of lattice symmetry and large photonic band gap [201]. Woodpile structure fabricated by 3D lithography has the potential to produce full photonic band gap provided the refractive index contrast is sufficiently high.

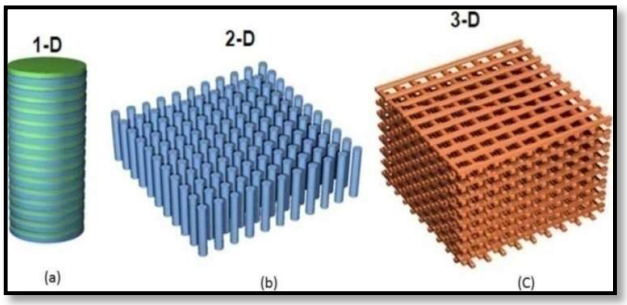

Figure 1.20. Photonic crystal structures [202]

Defect modes are generated intentionally in PC structure to introduce sharp peaks in the band gap region and this sharp peaks changes position with biomolecule introduction into PC environment, which have great importance in biosensing application. PC structures incorporating porous materials, nano and microcavities, waveguides, multilayered thin films etc. have been reported extensively for the detection of protein, nucleic acid, cancer biomarkers and different types of pathogens [203-207]. PC structures incorporating TiO_2 nanorods have been reported for enhancement of detected absorbed mass density of analyte [208]. PC biosensor for rapid screening of cancer cytotoxicity and proliferation has also been reported [209]. PC waveguide structure and PC surface wave biosensor were demonstrated for highly sensitive protein detection platform [210,211]. Long period grating inscribed in PC fiber has been used to monitor in situ antigen antibody binding [212].

TABLE IX: Some significant works in the last decade

Sensor Material	Analyte	Biorecognition element	LOD	Year & Reference
2D PC	Influenza virus	H1N1 haemagglutinin	1 ng/ml	2010 [213]

Open cavity based PC	Myoglobin	Myglobin Antibody	70 ng/ml	2013 [214]
PC optical fiber	Anti IgG	IgG	0.267mg/L	2013 [215]
Open microcavity PC	Cardiac Troponin I (cTnI)	Anti cTnI Antibody	0.1 ng/ml	2014 [216]
PC colloidal crystal hydrogel	Penicillin G	Penicillinase	1 µM	2016 [217]
PC microcavity	Gentamicin	Anti-gentamicin Antibodies	-	2017 [218]
1D PC grating	Parasite Extracellular Vesicles (EV)	EV specific Antibody	2.18×10^9 EVs/ml	2018 [219]
1D PC slabs	IgG & C-reactive protein	-	0.1 & 87 nM	2019 [220]
PC microcavity	Hepatocyte Growth Factor (HGF) & MacrophageInflammatory Proteins (MIP1) Antigen	(HGF) & (MIP1) Antibody	9.813 pg/ml & 15.437 pg/ml	2020 [221]

1.3. Glucose Sensors

Diabetes mellitus is a metabolic disease which can cause serious health issues if left untreated. Normal level of glucose in human serum is in the range of 4-5.8mM (72-105mg/dl). In hyperglycemia, serum glucose level becomes greater than 5.8mM for fasting (10-12 hours) and 9.2mM for postprandial measurements [222]. On the other hand, hypoglycemia causes serum glucose level to drop below 3.6mM [222]. While hypoglycemia can cause emergency conditions immediately, hyperglycemia is a slow killer and severely affects heart, kidney, eyes and nervous system unless diagnosed early. So, role of glucose sensor is tremendous in maintaining healthy population. Also, pressure on the food companies to minimise glucose levels in foods and beverages, has increased the demand of glucose sensors in industrial application.

There are basically three standard techniques for clinical measurement of blood glucose i.e., reducing method, condensation method and enzymatic method. Enzymatic methods are preferred over the other because of their high accuracy, specificity and reliability [223]. Glucose specific enzymes like glucose oxidase, hexokinase and glucose dehydrogenase are generally used in enzymatic method [224]. Glucose Oxidase (GOX) is being widely used in electrochemical, mechanical and optical sensing of blood glucose in the

last few years due to their fast response and low cost. In the following section, significant works on GOX based glucose sensors have been presented.

1.3.1. Electrochemical: Merit and Demerit

Electrochemical sensors are the most common type of glucose sensor due to their high sensitivity, rapid response and ease of miniaturization. Enzyme electrodes and different types of amperometric, voltametric, potentiometric and impedimetric glucose sensors fall under this category. Amperometric glucose sensors are widely used in continuous monitoring systems and wearable sensors.

GOX assembled on graphene platform has been reported by Ping Wu et al. for direct measurement of decrease in reduction current upon glucose introduction [225]. Gold electrode was modified with electrodeposition of chitosan gold nanocomposite and nickel hydroxide for enhanced electron transport for increased sensitivity of the glucose electrodes [226]. Au nanoparticle assembly on PVA/PEI nanofiber mat were reported by E. Sapountzi for ultrasensitive electrochemical glucose monitoring [227]. Amperometric glucose sensors were reported by L. Wang et al. based on Ag nanowire and chitosan-glucose oxidase film [228]. Fine pointed GOX immobilised electrodes were presented by J. Li et al. for low-invasive amperometric glucose monitoring [229]. GOX immobilised graphitic carbon nitride nanosheets were also reported by K. Tian et al. for reliable amperometric glucose sensing [230]. Screen printed carbon electrodes were demonstrated by D. Maity et al. for amperometric detection of blood glucose [231]. Encapsulated GOX in liposome microreactor amperometric glucose sensor were presented by G. Huanan et al. [232]. Paper-based enzymatic electrodes were reported by M. Parilla et al. for enhanced potentiometric response in glucose sensing in biological fluids [233]. A Nafion-GOX/GO/AZO membrane based potentiometric arrayed glucose sensor has been demonstrated by J. C. Chou et al. [234]. GOX immobilised PVDF thin films were utilised by A. Hartono et al. for capacitive glucose sensing [235]. GOX modified Si-Al electrodes were demonstrated by L. Chen et al. for capacitive non-Faradic glucose sensor [236].

Electrochemical glucose sensors have some limitations also. Fabrication process of these sensors is challenging as micro cracks or tears can cause significant drop in output

response. These sensors lack robustness and get affected by external electromagnetic interferences easily [237]. Also, slow biocatalysis due to the interface of enzyme and electrical contacts often reduces response of the electrochemical sensors [238].

1.3.2. Mechanical: Merit and Demerit

Piezoelectric and microcantilevel sensors are comparatively less popular in the field of glucose sensing; but their ability to measure mechanical properties like induced mass, surface stress, viscosity etc. even in sub atomic range makes them an ideal choice for highly sensitive glucose sensor.

Solid mounted thin film piezoelectric resonator was reported by H. Zhao et al. for continuous glucose monitoring through viscometry [239]. GOX/ZnO nanowire array based piezoelectric self powered electronic skin was reported by X. Xue for glucose detection in body fluid [240]. GOX functionalized gold coated glass slides were used as glucose reaction sites to study induced force on microcantilever sensor due to induced mass change [241]. Surface stress induced by the reaction between glucose and GOX is measured using GOX functionalized microcantilever sensor for highly selective glucose detection [242]. Gold coated silicon cantilevers were also reported by S. Subramanian et al. for glucose sensing [243]. Layer-by-layer nanoassembly modification of microcantilever sensors was reported by X. Yan et al. for increased glucose sensitivity [244].

The main disadvantage of microcantilevel sensors is their incredibly small and fragile structure. Also, dynamic mode of operation is strongly affected by unwanted viscous damping [245].

1.3.3. Optical: Merit and Demerit

Optical glucose sensors have high sensitivity, precision, accuracy and robustness. They have lower noise level than standard amperometric sensors and are immune to external electromagnetic interferences. Different types of spectroscopy and interferometry enables high sensitivity even in non-invasive measurements. Enzymatic optical glucose

sensors are generally invasive i.e., they require blood, serum, saliva, tear or urine samples and they can produce limit of detection even as low as femtomole [246, 247].

Glucose sensitive membranes coated on gold-glass sheets were reported by Y. Yuan et al. for broad range SPR based glucose sensing [248]. Silica mesocellular foams with trapped GOX were also used by the same group for SPR based glucose sensing [249]. Spectral interrogation based SPR sensors along with self assembled monolayer based preparation showed higher sensitivity and stability [250]. Fiber optic SPR glucose sensors were also reported largely by different groups [251-256]. Optical fiber based Mach-Zehnder, plasmonic and heterodyne interferometers were reported extensively for glucose detection [257-261]. GOX immobilised PDMS waveguides were reported by D. A. chang-yen and B. K. Gale for fabricating integrated optical glucose sensor [262]. Also, whispering gallery based GOX functionalised glucose sensors were demonstrated by I. Brice et al. for significantly high sensitivity in glucose sensing [263, 264].

Despite of the remarkable sensitivity and accuracy provided by optical detection methods, temperature dependent instabilities are common in these sensors [265]. Also, many of them uses costly components compared to electrochemical sensors.

1.4. Scope of Work

Optical label-free detection techniques discussed in section 1.2.3, relies on either costly instruments or complex and time consuming fabrication methods. Also, most of them measure a single optical parameter for precision analysis. The drawback of single parametric optical system is that, they are unable to detect changes in different optical properties simultaneously and thus fails to explain the overall change in the sensor material properties due to analyte introduction. Also, for different analyte concentration range some parameters may show maximum sensitivity and linearity while the others show poor calibration curve. Thus, it is a well known fact in any measurement system that utilization of more than one parameter enhances reliability and overall performance of the system. So, multi-parametric measurement systems have great advantage over single parametric ones.

Image processing based optical label-free detection system is a comparatively new field and such systems have not been extensively reported yet. Images of reflected or transmitted spot contain intensity and spectral information which can be utilised to acquire several interlinked or non interlinked optical parameters simultaneously for reliable measurements. Also, use of simple components and software based image processing make the system extremely cost efficient. Design and development of such sensitive, reliable and cost efficient system have the potential for significant contribution in the field of optical biosensing.

Among all the types of biosensor material discussed in section 1.2.4, nanostructured and composite thin films have the simplest and cost efficient production process. They are highly sensitive materials with small response time compared to many bulk sensors. Also, porous thin films provide unique properties and large surface area for biomolecule interaction which makes them a suitable choice for precision detection of analyte. Such porous thin film structures combined with multiparametric optical detection system can prove to be an extremely sensitive and cost efficient platform for glucose detection in pathological range.

1.5. Objective of Thesis

From the discussions in section 1.4, objectives of the thesis have been formulated and listed below.

- Design and development of an automated image acquisition system using MATLAB GUI environment.
- Image analysis and processing to acquire five interlinked optical parameters (transmittance, reflectance, internal scattering, surface scattering and output power) simultaneously as sensor system output.
- Fabrication, characterization and optimization of non transparent and semi transparent (in visible spectra) porous thin film sensors for multiparametric optical sensing.
- Performance study and comparison of both sensors in terms of different sensor characteristics for glucose detection in pathological range.

1.6. Thesis Outline

The thesis contains a step by step progression from sensor material fabrication to finally glucose sensing application in multiparametric optical detection system. Initially an extensive review on existing label-free optical biosensor methods and materials has been presented and from the next chapters, objectives undertaken in section 1.5 have been established systematically.

In **Chapter 2**, Porous Silicon (PS) thin film sensors have been fabricated as non transparent sensor material. PS thin films fabricated under different preparation conditions have been characterized and optimized for label-free optical biosensing application.

In **Chapter 3**, Chitosan-Silica nanocomposite (CSNC) thin films have been prepared as semi-transparent sensor material. Silica nanoparticles of different size have been prepared and characterized. CSNC thin films and membranes have been fabricated, characterized and optimized for label-free optical biosensing application.

In **Chapter 4**, MATLAB GUI based automated image acquisition and analysis system has been designed and developed for multiparametric optical detection of bio-analytes. Detailed analysis of system noise originated from different optical components has been carried out and a simple noise reduction method has been proposed for reliable measurements.

In **Chapter 5**, finally glucose sensing performance of surface functionalized PS and CSNC thin films have been studied in the multiparametric optical sensor system and comparison between the two sensors has been presented in terms of different biosensor characteristics (i.e. sensitivity, selectivity, response time, stability etc.).

In **Chapter 6**, final conclusions of the thesis have been drawn and a further outlook on future scope of work has been presented.

References

[1] I Palchetti, and M Mascini. “Biosensor technology: a brief history”. Sensors and Microsystems, 2010

[2] Olivier Lazcka, F. Javier Del Campo, and F. Xavier Munoz. "Pathogen detection: A perspective of traditional methods and biosensors." Biosensors and bioelectronics 22, no. 7 (2007): 1205-1217.

[3] *IUPAC. Compendium of Chemical Terminology, 2nd ed. (the "Gold Book"). Compiled by A. D. McNaught and A. Wilkinson. Blackwell Scientific Publications, Oxford (1997). Online version (2019-) created by S. J. Chalk. ISBN 0-9678550-9-8.* https://doi.org/10.1351/goldbook.

[4] L. C. Clark, and C. Lyons. "Biosensors-A Practical Approach." Jnr. Ann. NY Acad. Sci 102 (1962): 29-45.

[5] George G. Guilbault, and Joseph G. Montalvo Jr. "Enzyme electrode for the substrate urea." Journal of the American Chemical Society 92, no. 8 (1970): 2533-2538.

[6] Leslie Alexander Geddes, and Lee Edward Baker. Principles of applied biomedical instrumentation. John Wiley & Sons, 1975.

[7] John I. Peterson, and Seth R. Goldstein. "A miniature fiberoptic pH sensor potentially suitable for glucose measurements." Diabetes Care 5, no. 3 (1982): 272-274.

[8] Jerome S. Schultz, Sohrab Mansouri, and Irwin J. Goldstein. "Affinity sensor: a new technique for developing implantable sensors for glucose and other metabolites." Diabetes Care 5, no. 3 (1982): 245-253.

[9] Chen Jianrong, Miao Yuqing, He Nongyue, Wu Xiaohua, and Li Sijiao. "Nanotechnology and biosensors." Biotechnology advances 22, no. 7 (2004): 505-518.

[10] C. J. Van Oss, R. J. Good, and M. K. Chaudhury. "Nature of the antigen-antibody interaction: Primary and secondary bonds: optimal conditions for association and dissociation." Journal of Chromatography B: Biomedical Sciences and Applications 376 (1986): 111-119. https://doi.org/10.1016/S0378-4347(00)80828-2

[11] Liviu Nicu, and Thierry Leïchlé. "Bioreceptors and Grafting Methods." Micro-and Nanoelectromechanical Biosensors (2013): 35-63. https://doi.org/10.1002/9781118760857.ch2

[12] Pavel Damborský, Juraj Švitel, and Jaroslav Katrlík. "Optical biosensors." Essays in biochemistry 60, no. 1 (2016): 91-100. https://doi.org/10.1042/EBC20150010

[13] Chen Chen, and Junsheng Wang. "Optical biosensors: An exhaustive and comprehensive review." Analyst 145, no. 5 (2020): 1605-1628. https://doi.org/10.1039/C9AN01998G

[14] M. N. Velasco-Garcia. "Optical biosensors for probing at the cellular level: A review of recent progress and future prospects." In Seminars in cell & developmental biology, vol. 20, no. 1, pp. 27-33. Academic Press, 2009. https://doi.org/10.1016/j.semcdb.2009.01.013

[15] Joseph Wang. "Amperometric biosensors for clinical and therapeutic drug monitoring: a review." Journal of pharmaceutical and biomedical analysis 19, no. 1-2 (1999): 47-53. https://doi.org/10.1016/S0731-7085(98)00056-9

[16] E. Lojou, and P. Bianco. "Application of the electrochemical concepts and techniques to amperometric biosensor devices." Journal of Electroceramics 16, no. 1 (2006): 79-91. https://doi.org/10.1007/s10832-006-2365-9

[17] Jiawang Ding, and Wei Qin. "Recent advances in potentiometric biosensors." TrAC Trends in Analytical Chemistry 124 (2020): 115803. https://doi.org/10.1016/j.trac.2019.115803

[18] Hassan Karimi-Maleh, Yasin Orooji, Fatemeh Karimi, Marzieh Alizadeh, Mehdi Baghayeri, Jalal Rouhi, Somayeh Tajik et al. "A critical review on the use of potentiometric based biosensors for biomarkers detection." Biosensors and Bioelectronics 184 (2021): 113252. https://doi.org/10.1016/j.bios.2021.113252

[19] J. L. Arlett, E. B. Myers, and M. L. Roukes. "Comparative advantages of mechanical biosensors." Nature nanotechnology 6, no. 4 (2011): 203-215. https://doi.org/10.1016/S0378-4347(00)80828-2

[20] Javier Tamayo, Priscila M. Kosaka, José J. Ruz, Álvaro San Paulo, and Montserrat Calleja. "Biosensors based on nanomechanical systems." Chemical Society Reviews 42, no. 3 (2013): 1287-1311. https://doi.org/10.1039/C2CS35293A

[21] Brian T. Cunningham, Meng Zhang, Yue Zhuo, Lydia Kwon, and Caitlin Race. "Recent advances in biosensing with photonic crystal surfaces: a review." IEEE Sensors Journal 16, no. 10 (2015): 3349-3366. 10.1109/JSEN.2015.2429738

[22] Fariborz Parandin, Farsad Heidari, Zahra Rahimi, and Saeed Olyaee. "Two-Dimensional photonic crystal Biosensors: A review." Optics & Laser Technology 144 (2021): 107397. https://doi.org/10.1016/j.optlastec.2021.107397

[23] Jinan Deng, Dandan Han, and Jun Yang. "Applications of Microfluidics in Liquid Crystal-Based Biosensors." Biosensors 11, no. 10 (2021): 385. https://doi.org/10.3390/bios11100385

[24] Lisa M. Kindschy, and Evangelyn C. Alocilja. "A review of molecularly imprinted polymers for biosensor development for food and agricultural applications." Transactions of the ASAE 47, no. 4 (2004): 1375. doi: 10.13031/2013.16542

[25] Robert D. Crapnell, Alexander Hudson, Christopher W. Foster, Kasper Eersels, Bart van Grinsven, Thomas J. Cleij, Craig E. Banks, and Marloes Peeters. "Recent advances in electrosynthesized molecularly imprinted polymer sensing platforms for bioanalyte detection." Sensors 19, no. 5 (2019): 1204. https://doi.org/10.3390/s19051204

[26] Abid Haleem, Mohd Javaid, Ravi Pratap Singh, Rajiv Suman, and Shanay Rab. "Biosensors applications in medical field: a brief review." Sensors International 2 (2021): 100100. https://doi.org/10.1016/j.sintl.2021.100100

[27] Leon A. Terry, Stephen F. White, and Linda J. Tigwell. "The application of biosensors to fresh produce and the wider food industry." Journal of agricultural and food chemistry 53, no. 5 (2005): 1309-1316. https://doi.org/10.1021/jf040319t

[28] Sara Rodriguez-Mozaz, Maria J. Lopez de Alda, and Damià Barceló. "Biosensors as useful tools for environmental analysis and monitoring." Analytical and bioanalytical chemistry 386, no. 4 (2006): 1025-1041. https://doi.org/10.1007/s00216-006-0574-3

[29] Ibtisam E. Tothill. "Biosensors developments and potential applications in the agricultural diagnosis sector." Computers and Electronics in Agriculture 30, no. 1-3 (2001): 205-218. https://doi.org/10.1016/S0168-1699(00)00165-4

[30] Leif K. McGoldrick, and Jan Halámek. "Recent Advances in Noninvasive Biosensors for Forensics, Biometrics, and Cybersecurity." Sensors 20, no. 21 (2020): 5974. https://doi.org/10.3390/s20215974

[31] Xudong Fan, Ian M. White, Siyka I. Shopova, Hongying Zhu, Jonathan D. Suter, and Yuze Sun. "Sensitive optical biosensors for unlabeled targets: A review." analytica chimica acta 620, no. 1-2 (2008): 8-26. https://doi.org/10.1016/j.aca.2008.05.022

[32] W. Gregory Cox, and Victoria L. Singer. "Fluorescent DNA hybridization probe preparation using amine modification and reactive dye coupling." Biotechniques 36, no. 1 (2004): 114-122. https://doi.org/10.2144/04361RR02

[33] Stefania Dante, Daphné Duval, Borja Sepúlveda, Ana Belen González-Guerrero, José Ramón Sendra, and Laura M. Lechuga. "All-optical phase modulation for integrated interferometric biosensors." Optics express 20, no. 7 (2012): 7195-7205. https://doi.org/10.1364/OE.20.007195

[34] R. G. Heideman, R. P. H. Kooyman, and Jan Greve. "Performance of a highly sensitive optical waveguide Mach-Zehnder interferometer immunosensor." Sensors and Actuators B: Chemical 10, no. 3 (1993): 209-217. https://doi.org/10.1016/0925-4005(93)87008-D

[35] J. Ingenhoff, B. Drapp, and G. Gauglitz. "Biosensors using integrated optical devices." Fresenius' journal of analytical chemistry 346, no. 6 (1993): 580-583. https://doi.org/10.1007/BF00321249

[36] Franz Brosinger, Herbert Freimuth, Manfred Lacher, Wolfgang Ehrfeld, Erk Gedig, Andreas Katerkamp, Friedrich Spener, and Karl Cammann. "A label-free affinity sensor with compensation of unspecific protein interaction by a highly sensitive integrated optical Mach–Zehnder interferometer on silicon." Sensors and Actuators B: Chemical 44, no. 1-3 (1997): 350-355. https://doi.org/10.1016/S0925-4005(97)00226-8

[37] M. Weisser, G. Tovar, Silvia Mittler-Neher, Wolfgang Knoll, F. Brosinger, H. Freimuth, M. Lacher, and W. Ehrfeld. "Specific bio-recognition reactions observed with an integrated Mach–Zehnder interferometer." Biosensors and Bioelectronics 14, no. 4 (1999): 405-411. https://doi.org/10.1016/S0956-5663(98)00124-9

[38] Francisco Prieto, Borja Sepúlveda, A. Calle, Andreu Llobera, C. Domınguez, and Laura M. Lechuga. "Integrated Mach–Zehnder interferometer based on ARROW structures for biosensor applications." Sensors and actuators B: Chemical 92, no. 1-2 (2003): 151-158. https://doi.org/10.1016/S0925-4005(03)00257-0

[39] Qing Liu, Xiaoguang Tu, Kyung Woo Kim, Jack Sheng Kee, Yong Shin, Kyungsup Han, Yong-Jin Yoon, Guo-Qiang Lo, and Mi Kyoung Park. "Highly sensitive Mach–Zehnder interferometer biosensor based on silicon nitride slot waveguide." Sensors and Actuators B: Chemical 188 (2013): 681-688. https://doi.org/10.1016/j.snb.2013.07.053

[40] Albrecht Brandenburg, and R. Henninger. "Integrated optical Young interferometer." Applied optics 33, no. 25 (1994): 5941-5947. https://doi.org/10.1364/AO.33.005941

[41] Marianne Hiltunen, Jussi Hiltunen, Petri Stenberg, Sanna Aikio, Lauri Kurki, Pasi Vahimaa, and Pentti Karioja, "Polymeric slot waveguide interferometer for sensor applications," Opt. Express 22, 7229-7237 (2014), https://doi.org/10.1364/OE.22.007229

[42] Albrecht Brandenburg. "Differential refractometry by an integrated-optical Young interferometer." Sensors and Actuators B: Chemical 39, no. 1-3 (1997): 266-271. https://doi.org/10.1016/S0925-4005(97)80216-X

[43] Aurel Ymeti, Jan Greve, Paul V. Lambeck, Thijs Wink, Stephan WFM van Hövell, Tom AM Beumer, Robert R. Wijn, Rene G. Heideman, Vinod Subramaniam, and Johannes S. Kanger. "Fast, ultrasensitive virus detection using a young interferometer sensor." Nano letters 7, no. 2 (2007): 394-397. https://doi.org/10.1021/nl062595n

[44] M. Wang, Jussi Hiltunen, Christina Liedert, Leena Hakalahti, and R. Myllylä. "An integrated Young interferometer based on UV-imprinted polymer waveguides for label-free biosensing applications." Journal of the European Optical Society-Rapid publications 7 (2012). DOI: 10.2971/jeos.2012.12019

[45] Victor S.-Y. Lin, Kianoush Motesharei, Keiki-Pua S. Dancil, Michael J. Sailor, M. Reza Ghadiri, “A Porous Silicon-Based Optical Interferometric Biosensor”, Science 31 Oct 1997:Vol. 278, Issue 5339, pp. 840-843, DOI: 10.1126/science.278.5339.840

[46] Jennifer L. Elster, Mark E. Jones, Mishell K. Evans, Shannon M. Lenahan, Christopher A. Boyce, William H. Velander, Roger VanTassell, "Optical fiber extrinsic Fabry-Perot interferometric (EFPI)-based biosensors," Proc. SPIE 3911, Biomedical Diagnostic, Guidance, and Surgical-Assist Systems II, (3 May 2000); https://doi.org/10.1117/12.384892

[47] Yan Zhang, Helen Shibru, Kristie L. Cooper, and Anbo Wang. "Miniature fiber-optic multicavity Fabry–Perot interferometric biosensor." Optics letters 30, no. 9 (2005): 1021-1023. https://doi.org/10.1364/OL.30.001021

[48] Tianhua Zhang, Zhongcheng Gong and Long Que, "A white-light source operated polymer-based micromachined Fabry-Perot chemo/biosensor," *2009 4th IEEE International Conference on Nano/Micro Engineered and Molecular Systems*, Shenzhen, China, 2009, pp. 181-184, doi: 10.1109/NEMS.2009.5068554.

[49] B. H. Schneider, E. L. Dickinson, M. D. Vach, J. V. Hoijer, and L. V. Howard. "Highly sensitive optical chip immunoassays in human serum." Biosensors and Bioelectronics 15, no. 1-2 (2000): 13-22. https://doi.org/10.1016/S0956-5663(00)00056-7

[40] T. Zhang, P. Pathak, S. Karandikar, R. Giorn, & L. Que. "A polymer nanostructured Fabry–Perot interferometer based biosensor". Biosensors and Bioelectronics 30, no. 1 (2011): 128–132. doi:10.1016/j.bios.2011.08.042

[51] Xianxin Jiang, Yangqing Chen, Fang Yu, Longhua Tang, Mingyu Li, and Jian-Jun He, "High-sensitivity optical biosensor based on cascaded Mach–Zehnder interferometer and ring resonator using Vernier effect," Opt. Lett. 39, 6363-6366 (2014). https://doi.org/10.1364/OL.39.006363

[52] Haibo Wu, Hui Huang, Min Bai, Pengbo Liu, Ming Chao, Jie Hu, Jian Hao, and Tun Cao, "An ultra-low detection-limit optofluidic biosensor based on all glass Fabry-Perot cavity," Opt. Express 22, 31977-31983 (2014). https://doi.org/10.1364/OE.22.031977

[53] Xiaohui Liu, Mingshun Jiang, Qingmei Sui, Shuyang Luo, Xiangyi Geng, "Optical fiber Fabry–Perot interferometer for microorganism growth detection", Optical Fiber Technology, Volume 30, 2016, Pages 32-37, https://doi.org/10.1016/j.yofte.2016.01.014

[54] Eleftheria Savra, Antonia Malainou, Alexandros Salapatas, Athanasios Botsialas, Panagiota Petrou, Ioannis Raptis, Eleni Makarona, Sotirios E. Kakabakos, and Konstantinos Misiakos. "Monolithically-integrated Young interferometers for label-free and multiplexed detection of biomolecules." In Silicon Photonics XI, vol. 9752, p. 97520N. International Society for Optics and Photonics, 2016. doi:10.1117/12.2209011

[55] Tatevik Chalyan, Romain Guider, Laura Pasquardini, Manuela Zanetti, Floris Falke, Erik Schreuder, Rene G. Heideman, Cecilia Pederzolli, and Lorenzo Pavesi. "Asymmetric Mach–Zehnder interferometer based biosensors for aflatoxin M1 detection." Biosensors 6, no. 1 (2016): 1. https://doi.org/10.3390/bios6010001

[56] Zhengyong Li, Changrui Liao, Danni Chen, Jun Song, Wei Jin, Gang-Ding Peng, Feng Zhu, Ying Wang, Jun He, and Yiping Wang, "Label-free detection of bovine serum albumin based on an in-fiber Mach-Zehnder interferometric biosensor," Opt. Express 25, 17105-17113 (2017). https://doi.org/10.1364/OE.25.017105

[57] Kandammathe Valiyaveedu Sreekanth, Sivaramapanicker Sreejith, Yunus Alapan, Metin Sitti, Chwee Teck Lim, and Ranjan Singh. "Microfluidics Integrated Lithography-Free Nanophotonic Biosensor for the Detection of Small Molecules." Advanced Optical Materials 7, no. 7 (2019): 1801313. doi:10.1002/adom.201801313

[58] Seunguk Kim, Jae Yeon Kim, Su Jin Heo, Jae Hoon Yang, Gowoon Son, Hyun Woo Jang, Jihwan P. Choi, Jae Youn Hwang, Cheil Moon, and Jae Eun Jang. "Enhanced color sensitivity by coupling of surface plasmon and fabry-perot resonances for spectrometer-free and label-free biosensing." Sensors and Actuators B: Chemical 319 (2020): 128301. doi:10.1016/j.snb.2020.128301

[59] Ruchi Gupta, Elisabetta Labella, and Nicholas J. Goddard. "An optofluidic Young interferometer sensor for real-time imaging of refractive index in μTAS applications." Sensors and Actuators B: Chemical 321 (2020): 128491. doi:10.1016/j.snb.2020.128491

[60] Biacore AB Biacore technology Handbook (1994)

[61] Esa Stenberg, Björn Persson, Håkan Roos, and Csaba Urbaniczky. "Quantitative determination of surface concentration of protein with surface plasmon resonance using radiolabeled proteins." Journal of colloid and interface science 143, no. 2 (1991): 513-526. https://doi.org/10.1016/0021-9797(91)90284-F

[62] N. J. Tao, S. Boussaad, W. L. Huang, R. A. Arechabaleta, and J. D'Agnese. "High resolution surface plasmon resonance spectroscopy." Review of Scientific Instruments 70, no. 12 (1999): 4656-4660. https://doi.org/10.1063/1.1150128

[63] G. G. Nenninger, P. Tobiška, J. Homola, and S. S. Yee. "Long-range surface plasmons for high-resolution surface plasmon resonance sensors." Sensors and Actuators B: Chemical 74, no. 1-3 (2001): 145-151. https://doi.org/10.1016/S0925-4005(00)00724-3

[64] J. T. Hastings, J. Guo, P. D. Keathley, P. B. Kumaresh, Y. Wei, S. Law, and L. G. Bachas. "Optimal self-referenced sensing using long-and short-range surface plasmons." Optics express 15, no. 26 (2007): 17661-17672. https://doi.org/10.1364/OE.15.017661

[65] Radan Slavík, and Jiří Homola. "Ultrahigh resolution long range surface plasmon-based sensor." Sensors and Actuators B: Chemical 123, no. 1 (2007): 10-12. https://doi.org/10.1016/j.snb.2006.08.020

[66] Jing Guo, P. Donald Keathley, and J. T. Hastings. "Dual-mode surface-plasmon-resonance sensors using angular interrogation." Optics letters 33, no. 5 (2008): 512-514. https://doi.org/10.1364/OL.33.000512

[67] J. T. Hastings. "Optimizing surface-plasmon resonance sensors for limit of detection based on a Cramer–Rao bound." IEEE Sensors Journal 8, no. 2 (2008): 170-175. **DOI:** 10.1109/JSEN.2007.912782

[68] Matthew A. Cooper. "Optical biosensors in drug discovery." Nature reviews Drug discovery 1, no. 7 (2002): 515-528. https://doi.org/10.1038/nrd838

[69] Hana Šípová, Shile Zhang, Aimée M. Dudley, David Galas, Kai Wang, and Jiří Homola. "Surface plasmon resonance biosensor for rapid label-free detection of microribonucleic acid at subfemtomole level." Analytical chemistry 82, no. 24 (2010): 10110-10115.https://doi.org/10.1021/ac102131s

[70] Yi Wang, Wolfgang Knoll, and Jakub Dostalek. "Bacterial pathogen surface plasmon resonance biosensor advanced by long range surface plasmons and magnetic nanoparticle assays." Analytical chemistry 84, no. 19 (2012): 8345-8350. DOI: 10.1021/ac301904x

[71] Peyman Jahanshahi, Erfan Zalnezhad, Shamala Devi Sekaran, and Faisal Rafiq Mahamd Adikan. "Rapid immunoglobulin M-based dengue diagnostic test using surface plasmon resonance biosensor." Scientific reports 4, no. 1 (2014): 1-7. https://doi.org/10.1038/srep03851

[72] Yun Liu, Qiang Liu, Shimeng Chen, Fang Cheng, Hanqi Wang, and Wei Peng. "Surface plasmon resonance biosensor based on smart phone platforms." Scientific reports 5, no. 1 (2015): 1-9. https://doi.org/10.1038/srep12864

[73] Celina Massumi Miyazaki, Flávio Makoto Shimizu, J. R. Mejía-Salazar, Osvaldo N. Oliveira Jr, and Marystela Ferreira. "Surface plasmon resonance biosensor for enzymatic detection of small analytes." Nanotechnology 28, no. 14 (2017): 145501. https://doi.org/10.1088/1361-6528/aa6284

[74] Abu Ali Ibn Sina, Ramanathan Vaidyanathan, Alain Wuethrich, Laura G. Carrascosa, and Matt Trau. "Label-free detection of exosomes using a surface plasmon resonance biosensor." Analytical and bioanalytical chemistry 411, no. 7 (2019): 1311-1318. https://doi.org/10.1007/s00216-019-01608-5

[75] Luigi Zeni, Chiara Perri, Nunzio Cennamo, Francesco Arcadio, Girolamo D'Agostino, Mario Salmona, Marten Beeg, and Marco Gobbi. "A portable optical-fibre-based surface plasmon resonance biosensor for the detection of therapeutic antibodies in human serum." Scientific reports 10, no. 1 (2020): 1-9. https://doi.org/10.1038/s41598-020-68050-x

[76] Haneul Yoo, Junghyun Shin, Jieun Sim, Hyunmin Cho, and Seunghun Hong. "Reusable surface plasmon resonance biosensor chip for the detection of H1N1 influenza virus." Biosensors and Bioelectronics 168 (2020): 112561. doi:10.1016/j.bios.2020.112561

[77] Yuhong Cao, Yan Cao, Yiwei Shi, Ying Cai, Langdong Chen, Dongyao Wang, Yue Liu et al. "Surface plasmon resonance biosensor combined with lentiviral particle stabilization strategy for rapid and specific screening of P-Glycoprotein ligands." Analytical and Bioanalytical Chemistry 413, no. 7 (2021). https://doi.org/10.1007/s00216-021-03170-5

[78] T. Kundu, V. V. R. Sai, R. Dutta, S. Titas, P. Kumar, and S. Mukherjee. "Development of evanescent wave absorbance-based fibre-optic biosensor." Pramana 75, no. 6 (2010): 1099-1113. https://doi.org/10.1007/s12043-010-0193-6

[79] Carolina Beres, Fábio Vieira Batista de Nazaré, Nathália Correa Chagas de Souza, Marco Antônio Lemos Miguel, and Marcelo Martins Werneck. "Tapered plastic optical fiber-based biosensor–tests and application." Biosensors and Bioelectronics 30, no. 1 (2011): 328-332. https://doi.org/10.1016/j.bios.2011.09.024.

[80] Gisele Wandermur, Domingos Rodrigues, Regina Allil, Vanessa Queiroz, Raquel Peixoto, Marcelo Werneck, and Marco Miguel. "Plastic optical fiber-based biosensor platform for rapid cell detection." Biosensors and Bioelectronics 54 (2014): 661-666. https://doi.org/10.1016/j.bios.2013.11.030.

[81] Jie Cao, Minh Hieu Tu, Tong Sun, and Kenneth TV Grattan. "Wavelength-based localized surface plasmon resonance optical fiber biosensor." Sensors and Actuators B: Chemical 181 (2013): 611-619. https://doi.org/10.1016/j.snb.2013.02.052.

[82] Xuegang Li, Linh V. Nguyen, Yong Zhao, Heike Ebendorff-Heidepriem, and Stephen C. Warren-Smith. "High-sensitivity Sagnac-interferometer biosensor based on exposed core microstructured optical fiber." Sensors and Actuators B: Chemical 269 (2018): 103-109. https://doi.org/10.1016/j.snb.2018.04.165.

[83] S. S. Wang, and R. J. A. O. Magnusson. "Theory and applications of guided-mode resonance filters." Applied optics 32, no. 14 (1993): 2606-2613. https://doi.org/10.1364/AO.32.002606

[84] De Feijter, D. J. Benjamins, and F. A. Veer. "Ellipsometry as a tool to study the adsorption behavior of synthetic and biopolymers at the air–water interface." Biopolymers: Original Research on Biomolecules 17, no. 7 (1978): 1759-1772. https://doi.org/10.1002/bip.1978.360170711

[85] Nóra Adányi, Krisztina Majer-Baranyi, Mária Berki, Béla Darvas, Baomin Wang, István Szendrő, and András Székács. "Development of immunosensors based on optical waveguide lightmode spectroscopy (OWLS) technique for determining active substance in herbs." Sensors and actuators B: Chemical 239 (2017): 413-420. https://doi.org/10.1016/j.snb.2016.08.011.

[86] Website, http://www.owls-sensors.com/

[87] J. Vörös, J. J. Ramsden, G. Csúcs, I. Szendrő, S. M. De Paul, M. Textor, and N. D. Spencer. "Optical grating coupler biosensors." Biomaterials 23, no. 17 (2002): 3699-3710. https://doi.org/10.1016/S0142-9612(02)00103-5

[88] N. Adányi, I. A. Levkovets, S. Rodriguez-Gil, A. Ronald, M. Váradi, and I. Szendrő. "Development of immunosensor based on OWLS technique for determining Aflatoxin B1 and Ochratoxin A." Biosensors and Bioelectronics 22, no. 6 (2007): 797-802. https://doi.org/10.1016/j.bios.2006.02.015

[89] Namsoo Kim, In-Seon Park, and Woo-Yeon Kim. "Salmonella detection with a direct-binding optical grating coupler immunosensor." Sensors and Actuators B: Chemical 121, no. 2 (2007): 606-615. https://doi.org/10.1016/j.snb.2006.04.094

[90] Hikmat N. Daghestani, and Billy W. Day. "Theory and Applications of Surface Plasmon Resonance, Resonant Mirror, Resonant Waveguide Grating, and Dual Polarization Interferometry Biosensors" *Sensors* 10, no. 11 (2010): 9630-9646. https://doi.org/10.3390/s101109630

[91] Nicholas J. Goddard, Denise Pollard-Knight, and Colin H. Maule. "Real-time biomolecular interaction analysis using the resonant mirror sensor." Analyst 119, no. 4 (1994): 583-588. https://doi.org/10.1039/AN9941900583

[92] Website, http://www.neosensors.com.

[93] Mohammed Zourob, Stephan Mohr, Bernard J. Treves Brown, Peter R. Fielden, Martin McDonnell, and Nicholas J. Goddard. "The development of a metal clad leaky waveguide sensor for the detection of particles." Sensors and Actuators B: Chemical 90, no. 1-3 (2003): 296-307. https://doi.org/10.1016/S0925-4005(03)00052-2

[94] Mohammed Zourob, Souna Elwary, Xudong Fan, Stephan Mohr, and Nicholas J. Goddard. "Label-free detection with the resonant mirror biosensor." Biosensors and Biodetection (2009): 89-138. https://doi.org/10.1007/978-1-60327-567-5_6

[95] N. Skivesen, R. Horvath, and H. C. Pedersen. "Peak-type and dip-type metal-clad waveguide sensing." Optics letters 30, no. 13 (2005): 1659-1661. https://doi.org/10.1364/OL.30.001659

[96] Nina Skivesen, Robert Horvath, S. Thinggaard, Niels Bent Larsen, and Henrik Chresten Pedersen. "Deep-probe metal-clad waveguide biosensors." Biosensors and Bioelectronics 22, no. 7 (2007): 1282-1288. https://doi.org/10.1016/j.bios.2006.05.025

[97] Mohammed Zourob, Stephan Mohr, Bernard J. Treves Brown, Peter R. Fielden, Martin B. McDonnell, and Nicholas J. Goddard. "An integrated metal clad leaky waveguide sensor for detection of bacteria." Analytical Chemistry 77, no. 1 (2005): 232-242. https://doi.org/10.1021/ac049627g

[98] Won Joo Im, Bo Bae Kim, Ju Young Byun, Hyoung Min Kim, Min-Gon Kim, and Yong-Beom Shin. "Immunosensing using a metal clad leaky waveguide biosensor for clinical diagnosis." Sensors and Actuators B: Chemical 173 (2012): 288-294. https://doi.org/10.1016/j.snb.2012.06.085

[99] Pingping Xiao, X. Wang, Jingjing Sun, Honggen Li, M. Huang, X. Chen and Z. Cao. “Biosensor based on hollow-core metal-cladding waveguide.” Sensors and Actuators A-physical 183 (2012): 22-27. https://doi.org/10.1016/j.sna.2012.05.047

[100] Krisztina Majer-Baranyi, András Székács, István Szendrő, Attila Kiss, and Nóra Adányi. "Optical waveguide lightmode spectroscopy technique–based immunosensor development for deoxynivalenol determination in wheat samples." European Food Research and Technology 233, no. 6 (2011): 1041-1047. https://doi.org/10.1007/s00217-011-1598-2

[101] Sachin K. Srivastava, Vikas Arora, Sameer Sapra, and Banshi D. Gupta. "Localized surface plasmon resonance-based fiber optic U-shaped biosensor for the detection of blood glucose." Plasmonics 7, no. 2 (2012): 261-268. doi:10.1007/s11468-011-9302-8

[102] Nóra Adányi, Krisztina Majer-Baranyi, András Nagy, Gyöngyi Németh, István Szendrő, and András Székács. "Optical waveguide lightmode spectroscopy immunosensor for detection of carp vitellogenin." Sensors and Actuators B: Chemical 176 (2013): 932-939. doi:10.1016/j.snb.2012.10.079

[103] Bo Bae Kim, Won Joo Im, Ju Young Byun, Hyung Min Kim, Min-Gon Kim, and Yong-Beom Shin. "Label-free CRP detection using optical biosensor with one-step immobilization of antibody on nitrocellulose membrane." Sensors and Actuators B: Chemical 190 (2014): 243-248. doi:10.1016/j.snb.2013.08.078

[104] Namsoo Kim, and Woo-Yeon Kim. "Measurement of polyphenol oxidase activity using optical waveguide lightmode spectroscopy-based immunosensor." Food chemistry 169 (2015): 211-217. https://doi.org/10.1016/j.foodchem.2014.07.130

[105] Bo-Tao Wang, and Qi Wang. "An interferometric optical fiber biosensor with high sensitivity for IgG/anti-IgG immunosensing." Optics Communications 426 (2018): 388-394. https://doi.org/10.1016/j.optcom.2018.05.058

[106] Namsoo Kim. "Development of Indirect-Competitive Optical Waveguide Lightmode Spectroscopy-based Immunosensor for Measuring Sulfamethazine." BioChip Journal 12, no. 2 (2018): 128-136. https://doi.org/10.1007/s13206-017-2205-9

[107] Jiajie Lao, Linzi Han, Ze Wu, Xuejun Zhang, Yunyun Huang, Yong Tang, and Tuan Guo. "Gold nanoparticle-functionalized surface plasmon resonance optical fiber biosensor: In situ detection of thrombin with 1 n· M detection limit." Journal of Lightwave Technology 37, no. 11 (2019): 2748-2755.

[108] Ankitha George, M. S. Amrutha, Priyanshu Srivastava, Sujatha Sunil, V. V. R. Sai, and Ramanathan Srinivasan. "Development of a U-bent plastic optical fiber biosensor with plasmonic labels for the detection of chikungunya non-structural protein 3." Analyst 146, no. 1 (2021): 244-252. DOI: 10.1039/D0AN01603A

[109] Richard Kounai Chang, and Anthony J. Campillo. Optical processes in microcavities. Vol. 3. World scientific, 1996.

[110] Craig F. Bohren, and Donald R. Huffman. Absorption and scattering of light by small particles. John Wiley & Sons, 2008.

[111] Chung-Yen Chao, and L. Jay Guo. "Biochemical sensors based on polymer microrings with sharp asymmetrical resonance." Applied Physics Letters 83, no. 8 (2003): 1527-1529. https://doi.org/10.1063/1.1605261

[112] Mikhail L. Gorodetsky, Anatoly A. Savchenkov, and Vladimir S. Ilchenko. "Ultimate Q of optical microsphere resonators." Optics letters 21, no. 7 (1996): 453-455. https://doi.org/10.1364/OL.21.000453

[113] Rajib Ahmed, Ahmmed A. Rifat, Ali K. Yetisen, Michel Saab Salem, Seok-Hyun Yun, and Haider Butt. "Optical microring resonator based corrosion sensing." Rsc Advances 6, no. 61 (2016): 56127-56133. https://doi.org/10.1039/C6RA11538A

[114] Junpeng Guo, Michael J. Shaw, G. Allen Vawter, G. Ronald Hadley, Peter Esherick, and Charles T. Sullivan. "High-Q microring resonator for biochemical sensors." In Integrated Optics: Devices, Materials, and Technologies IX, vol. 5728, pp. 83-92. International Society for Optics and Photonics, 2005. https://doi.org/10.1117/12.589467

[115] Robert W. Boyd, and John E. Heebner. "Sensitive disk resonator photonic biosensor." Applied optics 40, no. 31 (2001): 5742-5747. https://doi.org/10.1364/AO.40.005742

[116] Erol Ozgur, Pelin Toren, Ozan Aktas, Ersin Huseyinoglu, and Mehmet Bayindir. "Label-free biosensing with high selectivity in complex media using microtoroidal optical resonators." Scientific reports 5, no. 1 (2015): 1-9. https://doi.org/10.1038/srep13173

[117] E. Krioukov, Jan Greve, and Cornelis Otto. "Performance of integrated optical microcavities for refractive index and fluorescence sensing." Sensors and Actuators B: Chemical 90, no. 1-3 (2003): 58-67. https://doi.org/10.1016/S0925-4005(03)00022-4

[118] Ian M. White, Hongying Zhu, Jonathan D. Suter, Niranjan M. Hanumegowda, Hesam Oveys, Mohammed Zourob, and Xudong Fan. "Refractometric sensors for lab-on-a-chip based on optical ring resonators." IEEE Sensors Journal 7, no. 1 (2006): 28-35. 10.1109/JSEN.2006.887927

[119] Dongliang Fu, Jaehoon Chung, Qing Liu, Riazul Raziq, Jack Sheng Kee, Mi Kyoung Park, Suresh Valiyaveettil, and Pyng Lee. "Polymer coated silicon microring device for the detection of sub-ppm volatile organic compounds." Sensors and Actuators B: Chemical 257 (2018): 136-142. https://doi.org/10.1016/j.snb.2017.10.166

[120] T. J. Kippenberg, J. Kalkman, A. Polman, & K. J. Vahala. “Demonstration of an erbium doped microdisk laser on a silicon chip”. 2006 Conference on Lasers and Electro-Optics and 2006 Quantum Electronics and Laser Science Conference. doi:10.1109/cleo.2006.4627615

[121] C. Schäfermeier, H. Kerdoncuff, U. Hoff et al. “Quantum enhanced feedback cooling of a mechanical oscillator using nonclassical light”. Nat Commun 7, 13628 (2016). https://doi.org/10.1038/ncomms13628

[122] Niranjan M. Hanumegowda, Caleb J. Stica, Bijal C. Patel, Ian White, and Xudong Fan. "Refractometric sensors based on microsphere resonators." Applied Physics Letters 87, no. 20 (2005): 201107. https://doi.org/10.1063/1.2132076

[123] Ian M. White, Niranjan M. Hanumegowda, and Xudong Fan. "Subfemtomole detection of small molecules with microsphere sensors." Optics letters 30, no. 23 (2005): 3189-3191. https://doi.org/10.1364/OL.30.003189

[124] Frank Vollmer, Stephen Arnold, Dieter Braun, Iwao Teraoka, and Albert Libchaber. "Multiplexed DNA quantification by spectroscopic shift of two microsphere cavities." Biophysical journal 85, no. 3 (2003): 1974-1979. https://doi.org/10.1016/S0006-3495(03)74625-6

[125] S. Arnold, R. Ramjit, D. Keng, V. Kolchenko, and I. Teraoka. "MicroParticle photophysics illuminates viral bio-sensing." Faraday discussions 137 (2008): 65-83. https://doi.org/10.1039/B702920A

[126] D. Keng, S. R. McAnanama, I. Teraoka, and S. Arnold. "Resonance fluctuations of a whispering gallery mode biosensor by particles undergoing Brownian motion." Applied Physics Letters 91, no. 10 (2007): 103902. https://doi.org/10.1063/1.2778351

[127] Hanzheng Wang, Lei Yuan, Cheol-Woon Kim, Qun Han, Tao Wei, Xinwei Lan, and Hai Xiao. "Optical microresonator based on hollow sphere with porous wall for chemical sensing." Optics letters 37, no. 1 (2012): 94-96. https://doi.org/10.1364/OL.37.000094

[128] J-B. Jager, Vincent Calvo, Eric Delamadeleine, Emmanuel Hadji, Pierre Noé, Thibault Ricart, Davide Bucci, and Alain Morand. "High-Q silica microcavities on a chip: From microtoroid to microsphere." Applied Physics Letters 99, no. 18 (2011): 181123. https://doi.org/10.1063/1.3658389

[129] Jonathan D. Suter, and Xudong Fan. "Overview of the optofluidic ring resonator: a versatile platform for label-free biological and chemical sensing." In 2009 Annual International Conference of the IEEE Engineering in Medicine and Biology Society, pp. 1042-1044. IEEE, 2009. 10.1109/IEMBS.2009.5335153

[130] Hongying Zhu, Ian M. White, Jonathan D. Suter, Mohammed Zourob, and Xudong Fan. "Opto-fluidic micro-ring resonator for sensitive label-free viral detection." Analyst 133, no. 3 (2008): 356-360. https://doi.org/10.1039/B716834A

[131] Hongying Zhu, Ian M. White, Jonathan D. Suter, and Xudong Fan. "Phage-based label-free biomolecule detection in an opto-fluidic ring resonator." Biosensors and Bioelectronics 24, no. 3 (2008): 461-466. https://doi.org/10.1016/j.bios.2008.04.028

[132] Hongying Zhu, Ian M. White, Jonathan D. Suter, Paul S. Dale, and Xudong Fan. "Analysis of biomolecule detection with optofluidic ring resonator sensors." Optics Express 15, no. 15 (2007): 9139-9146. https://doi.org/10.1364/OE.15.009139

[133] Y. Sun, and X. Fan. “Optical ring resonators for biochemical and chemical sensing”. Anal Bioanal Chem 399, 205–211 (2011). https://doi.org/10.1007/s00216-010-4237-z

[134] John T. Gohring, and Xudong Fan. "Label free detection of CD4+ and CD8+ T cells using the optofluidic ring resonator." Sensors 10, no. 6 (2010): 5798-5808. https://doi.org/10.3390/s100605798

[135] Mi Kyoung Park, Jack Sheng Kee, Jessie Yiying Quah, Vivian Netto, Junfeng Song, Qing Fang, Eric Mouchel La Fosse, and Guo-Qiang Lo. "Label-free aptamer sensor based on silicon microring resonators." Sensors and Actuators B: Chemical 176 (2013): 552-559. https://doi.org/10.1016/j.snb.2012.08.078.

[136] Martin D. Baaske, Matthew R. Foreman, and Frank Vollmer. "Single-molecule nucleic acid interactions monitored on a label-free microcavity biosensor platform." Nature nanotechnology 9, no. 11 (2014): 933-939. doi:10.1038/nnano.2014.180

[137] Mahdi Bahadoran, Ahmad Fakhrurrazi Ahmad Noorden, Kashif Chaudhary, Faeze Sadat Mohajer, Muhammad Safwan Aziz, Shahrin Hashim, Jalil Ali, and Preecha Yupapin. "Modeling and analysis of a microresonating biosensor for detection of Salmonella bacteria in human blood." Sensors 14, no. 7 (2014): 12885-12899. https://doi.org/10.3390/s140712885

[138] Yangqing Chen, Yong Liu, Xiaodan Shen, Zhimin Chang, Longhua Tang, Wen-Fei Dong, Mingyu Li, and Jian-Jun He. "Ultrasensitive detection of testosterone using microring resonator with molecularly imprinted polymers." Sensors 15, no. 12 (2015): 31558-31565. https://doi.org/10.3390/s151229877

[139] Hai Yan, Lijun Huang, Xiaochuan Xu, Swapnajit Chakravarty, Naimei Tang, Huiping Tian, and Ray T. Chen. "Unique surface sensing property and enhanced sensitivity in microring resonator biosensors based on subwavelength grating waveguides." Optics express 24, no. 26 (2016): 29724-29733. https://doi.org/10.1364/OE.24.029724

[140] Zihao Li, Chenggang Zhu, Zhihe Guo, Bowen Wang, Xiang Wu, and Yiyan Fei. "Highly sensitive label-free detection of small molecules with an optofluidic microbubble resonator." Micromachines 9, no. 6 (2018): 274. https://doi.org/10.3390/mi9060274

[141] Paul Azuelos, Pauline Girault, Nathalie Lorrain, Yannick Dumeige, Loïc Bodiou, Luiz Poffo, Mohammed Guendouz, Monique Thual, and Joel Charrier. "Optimization of porous silicon waveguide design for micro-ring resonator sensing applications." Journal of Optics 20, no. 8 (2018): 085301. doi:10.1088/2040-8986/aad01b

[142] S. F. Wondimu, M. Hippler, C. Hussal, A. Hofmann, S. Krämmer, J. Lahann, H. Kalt, W. Freude, and C. Koos. "Robust label-free biosensing using microdisk laser arrays with on-chip references." Optics express 26, no. 3 (2018): 3161-3173. https://doi.org/10.1364/OE.26.003161

[143] Bonhan Koo, Choong Eun Jin, Moonsuk Bae, Yoon Ok Jang, Ji Yeun Kim, Sung-Han Kim, and Yong Shin. "Detection of Coxiella burnetii using silicon microring resonator in patient blood plasma." Micromachines 10, no. 7 (2019): 427. https://doi.org/10.3390/mi10070427

[144] Inga Brice, Karlis Grundsteins, Aigars Atvars, Janis Alnis, Roman Viter, and Arunas Ramanavicius. "Whispering gallery mode resonator and glucose oxidase based glucose biosensor." Sensors and Actuators B: Chemical 318 (2020): 128004. doi:10.1016/j.snb.2020.128004

[145] Zhihe Guo, Yingchun Qin, Peizong Chen, Jinliang Hu, Yi Zhou, Xuyang Zhao, Zhiran Liu, Yiyan Fei, Xiaoshun Jiang, and Xiang Wu. "Hyperboloid-Drum Microdisk Laser Biosensors for Ultrasensitive Detection of Human IgG." Small 16, no. 26 (2020): 2000239. https://doi.org/10.1002/smll.202000239

[146] Subrata Das, Sarath C. Samudrala, Kyu J. Lee, Mohammad G. Abdallah, Brett R. Wenner, Jeffery W. Allen, Monica S. Allena, Robert Magnusson, and Michael Vasilyev. "SiN-microring-resonator-based optical biosensor for neuropeptide Y detection." IEEE Photonics Technology Letters (2021). doi: 10.1109/LPT.2021.3069765.

[147] Amanda J. Haes, and Richard P. Van Duyne. "A nanoscale optical biosensor: sensitivity and selectivity of an approach based on the localized surface plasmon resonance spectroscopy of triangular silver nanoparticles." Journal of the American Chemical Society 124, no. 35 (2002): 10596-10604. DOI: 10.1021/ja020393x

[148] Alla Tereshchenko, Viktoriia Fedorenko, Valentyn Smyntyna, Igor Konup, Anastasiya Konup, Martin Eriksson, Rositsa Yakimova, Arunas Ramanavicius, Sebastien Balme, and Mikhael Bechelany. "ZnO films formed by atomic layer deposition as an optical biosensor platform for the detection of Grapevine virus A-type proteins." Biosensors and Bioelectronics 92 (2017): 763-769. doi:10.1016/j.bios.2016.09.071

[149] Sachindra Nath Sarangi, Shinji Nozaki, and Surendra Nath Sahu. "ZnO nanorod-based non-enzymatic optical glucose biosensor." Journal of biomedical nanotechnology 11, no. 6 (2015): 988-996. doi:10.1166/jbn.2015.2048

[150] Roman Viter, Alla Tereshchenko, Valentyn Smyntyna, Julia Ogorodniichuk, Nickolay Starodub, Rositsa Yakimova, Volodymyr Khranovskyy, and Arunas Ramanavicius. "Toward development of optical biosensors

based on photoluminescence of TiO2 nanoparticles for the detection of Salmonella." Sensors and Actuators B: Chemical 252 (2017): 95-102. doi:10.1016/j.snb.2017.05.139

[151] A. Mobeen Amanulla, and R. J. M. T. P. Sundaram. "Green synthesis of TiO2 nanoparticles using orange peel extract for antibacterial, cytotoxicity and humidity sensor applications." Materials Today: Proceedings 8 (2019): 323-331. https://doi.org/10.1016/j.matpr.2019.02.118.

[152] Gayathri Rajeev, Elisabet Xifre-Perez, Beatriz Prieto Simon, Allison J. Cowin, Lluis F. Marsal, and Nicolas H. Voelcker. "A label-free optical biosensor based on nanoporous anodic alumina for tumour necrosis factor-alpha detection in chronic wounds." Sensors and Actuators B: Chemical 257 (2018): 116-123. https://doi.org/10.1016/j.snb.2017.10.156.

[153] Abel Santos, Victor S. Balderrama, María Alba, Pilar Formentín, Josep Ferré-Borrull, Josep Pallarès, and Lluís F. Marsal. "Nanoporous anodic alumina barcodes: toward smart optical biosensors." Advanced Materials 24, no. 8 (2012): 1050-1054. https://doi.org/10.1002/adma.201104490

[154] Sha Li, Jianfeng Huang, and Lintao Cai. "A porous silicon optical microcavity for sensitive bacteria detection." Nanotechnology 22, no. 42 (2011): 425502. doi:10.1088/0957-4484/22/42/425502

[155] Xing Wei, and Sharon M. Weiss. "Guided mode biosensor based on grating coupled porous silicon waveguide." Optics express 19, no. 12 (2011): 11330-11339. https://doi.org/10.1364/OE.19.011330

[156] Alexis Loiseau, Victoire Asila, Gabriel Boitel-Aullen, Mylan Lam, Michèle Salmain, and Souhir Boujday. "Silver-based plasmonic nanoparticles for and their use in biosensing." Biosensors 9, no. 2 (2019): 78. https://doi.org/10.3390/bios9020078

[157] R. Vinod, P. Sajan, Sreekumar Rajappan Achary, Carmen Martinez Tomas, Vicente Munoz-Sanjosé, and M. Junaid Bushiri. "Enhanced UV emission from ZnO nanoflowers synthesized by the hydrothermal process." Journal of Physics D: Applied Physics 45, no. 42 (2012): 425103. DOI:10.1088/0022-3727/45/42/425103.

[158] Tae-Hyung Koo, Jyoti S. Borah, Zhi-Cai Xing, Sung-Mo Moon, Yongsoo Jeong, and Inn-Kyu Kang. "Immobilization of pamidronic acids on the nanotube surface of titanium discs and their interaction with bone cells." Nanoscale research letters 8, no. 1 (2013): 1-9. Doi:10.1186/1556-276X-8-124.

[159] Chin-Guo Kuo, Chi-Wu Huang, Jung-Hsuan Chen, and Yueh-Han Liu. "Fabrication of a miniature zinc aluminum oxide nanowire array gas sensor and application for environmental monitoring." International Journal of Photoenergy 2014 (2014). Doi:10.1155/2014/515268.

[160] Hae Yong Kim, Ricardo Hitoshi Maruta, Danilo Roque Huanca, and Walter Jaimes Salcedo. "Correlation-based multi-shape granulometry with application in porous silicon nanomaterial characterization." Journal of Porous Materials 20, no. 2 (2013): 375-385. Doi:10.1007/s10934-012-9607-9.

[161] Kyu-Shik Mun, Sara D. Alvarez, Won-Youl Choi, and Michael J. Sailor. "A stable, label-free optical interferometric biosensor based on TiO2 nanotube arrays." Acs Nano 4, no. 4 (2010): 2070-2076. doi:10.1021/nn901312f

[162] Hong Qiao, Bin Guan, J. Justin Gooding, and Peter J. Reece. "Protease detection using a porous silicon based Bloch surface wave optical biosensor." Optics express 18, no. 14 (2010): 15174-15182. https://doi.org/10.1364/OE.18.015174

[163] Tushar Kumeria, Mahaveer D. Kurkuri, Kerrilyn R. Diener, Luke Parkinson, and Dusan Losic. "Label-free reflectometric interference microchip biosensor based on nanoporous alumina for detection of circulating tumour cells." Biosensors and Bioelectronics 35, no. 1 (2012): 167-173. https://doi.org/10.1016/j.bios.2012.02.038.

[164] Xia Xu, Xiangjiang Liu, Yanbin Li, and Yibin Ying. "A simple and rapid optical biosensor for detection of aflatoxin B1 based on competitive dispersion of gold nanorods." Biosensors and Bioelectronics 47 (2013): 361-367. doi:10.1016/j.bios.2013.03.048

[165] Jianlin Li, and Michael J. Sailor. "Synthesis and characterization of a stable, label-free optical biosensor from TiO2-coated porous silicon." Biosensors and Bioelectronics 55 (2014): 372-378. doi:10.1016/j.bios.2013.12.016

[166] A. Lokman, S. W. Harun, Z. Harith, H. A. Rafaie, R. M. Nor, and H. Arof. "Inline Mach–Zehnder interferometer with ZnO nanowires coating for the measurement of uric acid concentrations." Sensors and Actuators A: Physical 234 (2015): 206-211. doi:10.1016/j.sna.2015.09.013

[167] Stefano Mariani, Simona Scarano, Jolanda Spadavecchia, and Maria Minunni. "A reusable optical biosensor for the ultrasensitive and selective detection of unamplified human genomic DNA with gold nanostars." Biosensors and Bioelectronics 74 (2015): 981-988. https://doi.org/10.1016/j.bios.2015.07.071.

[168] Katharina Urmann, Peggy Reich, Johanna-Gabriela Walter, Dieter Beckmann, Ester Segal, and Thomas Scheper. "Rapid and label-free detection of protein a by aptamer-tethered porous silicon nanostructures." Journal of biotechnology 257 (2017): 171-177. https://doi.org/10.1016/j.jbiotec.2017.01.005.

[169] Alexis Loiseau, Lu Zhang, David Hu, Michèle Salmain, Yacine Mazouzi, Raphaël Flack, Bo Liedberg, and Souhir Boujday. "Core–shell gold/silver nanoparticles for localized surface Plasmon resonance-based naked-eye toxin biosensing." ACS applied materials & interfaces 11, no. 50 (2019): 46462-46471. DOI: 10.1021/acsami.9b14980

[170] Mahmoud Amouzadeh Tabrizi, Josep Ferré-Borrull, and Lluis F. Marsal. "An optical biosensor for the determination of cathepsin B as a cancer-associated enzyme using nanoporous anodic alumina modified with human serum albumin-thionine." Microchimica Acta 187, no. 4 (2020): 1-9. https://doi.org/10.1007/s00604-020-4188-9

[171] Niteshkumar Agrawal, Bingyuan Zhang, Chinmoy Saha, Chandrakanta Kumar, Xipeng Pu, and Santosh Kumar. "Ultra-Sensitive Cholesterol Sensor Using Gold and Zinc-Oxide Nanoparticles Immobilized Core Mismatch MPM/SPS Probe." Journal of Lightwave Technology 38, no. 8 (2020): 2523-2529.

[172] Mohamed M. Dawoud, and Hosam M. Saleh. "Introductory chapter: Background on composite materials." In Characterizations of Some Composite Materials. IntechOpen, 2018. DOI: 10.5772/intechopen.80960

[173] Di Zhang, Ying Sun, Qiong Wu, Pinyi Ma, Hua Zhang, Yuanpeng Wang, and Daqian Song. "Enhancing sensitivity of surface plasmon resonance biosensor by Ag nanocubes/chitosan composite for the detection of mouse IgG." Talanta 146 (2016): 364-368. https://doi.org/10.1016/j.talanta.2015.08.050.

[174] Mohammed Alsawafta, Simona Badilescu, Abhilash Paneri, Vo-Van Truong, and Muthukumaram Packirisamy. "Gold-poly (methyl methacrylate) nanocomposite films for plasmonic biosensing applications." Polymers 3, no. 4 (2011): 1833-1848. doi:10.3390/polym3041833

[175] Nur Alia Sheh Omar et al. "Experimental evaluation on surface plasmon resonance sensor performance based on sensitive hyperbranched polymer nanocomposite thin films." Sensors and Actuators A: Physical 303 (2020): 111830. https://doi.org/10.1016/j.sna.2020.111830

[176] Hua Zhang, Ying Sun, Jing Wang, Jia Zhang, Hanqi Zhang, Hao Zhou, and Daqian Song. "Preparation and application of novel nanocomposites of magnetic-Au nanorod in SPR biosensor." Biosensors and Bioelectronics 34, no. 1 (2012): 137-143. doi:10.1016/j.bios.2012.01.032

[177] Marco Sampaio Rodrigues, D. Costa, R. P. Domingues, Mihai Apreutesei, Paulo Pedrosa, Nicolas Martin, V. M. Correlo et al. "Optimization of nanocomposite Au/TiO2 thin films towards LSPR optical-sensing." Applied Surface Science 438 (2018): 74-83. https://doi.org/10.1016/j.apsusc.2017.09.162

[178] Mykola Pavlenko, Valerii Myndrul, Gloria Gottardi, Emerson Coy, Mariusz Jancelewicz, and Igor Iatsunskyi. "Porous silicon-zinc oxide nanocomposites prepared by atomic layer deposition for biophotonic applications." Materials 13, no. 8 (2020): 1987. doi:10.3390/ma13081987

[179] Qing Li, Qing Wang, Xiaohai Yang, Kemin Wang, Hua Zhang, and Wenyan Nie. "High sensitivity surface plasmon resonance biosensor for detection of microRNA and small molecule based on graphene oxide-gold nanoparticles composites." Talanta 174 (2017): 521-526. https://doi.org/10.1016/j.talanta.2017.06.048

[180] Mohammed Alsawafta, Simona Badilescu, Abhilash Paneri, Vo-Van Truong, and Muthukumaram Packirisamy. "Gold-poly (methyl methacrylate) nanocomposite films for plasmonic biosensing applications." Polymers 3, no. 4 (2011): 1833-1848. https://doi.org/10.3390/polym3041833

[181] Dong Wang, Yong Yan, Peter Schaaf, Thomas Sharp, Sven Schönherr, Carsten Ronning, and Ran Ji. "ZnO/porous-Si and TiO2/porous-Si nanocomposite nanopillars." Journal of Vacuum Science & Technology A: Vacuum, Surfaces, and Films 33, no. 1 (2015): 01A102. Doi:10.1116/1.4891104.

[182] Liying Wang, Ying Sun, Jian Wang, Jing Wang, Aimin Yu, Hanqi Zhang, and Daqian Song. "Water-soluble ZnO–Au nanocomposite-based probe for enhanced protein detection in a SPR biosensor system." Journal of colloid and interface science 351, no. 2 (2010): 392-397. doi:10.1016/j.jcis.2010.07.050

[183] Nan-Fu Chiu, Chi-Chu Chen, Cheng-Du Yang, Yu-Sheng Kao, and Wei-Ren Wu. "Enhanced plasmonic biosensors of hybrid gold nanoparticle-graphene oxide-based label-free immunoassay." Nanoscale research letters 13, no. 1 (2018): 1-11. https://doi.org/10.1186/s11671-018-2565-7

[184] Sruthi P. Usha, and Banshi D. Gupta. "Urinary p-cresol diagnosis using nanocomposite of ZnO/MoS2 and molecular imprinted polymer on optical fiber based lossy mode resonance sensor." Biosensors and Bioelectronics 101 (2018): 135-145. https://doi.org/10.1016/j.bios.2017.10.029

[185] Nur Alia Sheh Omar, Yap Wing Fen, Jaafar Abdullah, Amir Reza Sadrolhosseini, Yasmin Mustapha Kamil, Nurul'Illya Muhamad Fauzi, Hazwani Suhaila Hashim, and Mohd Adzir Mahdi. "Quantitative and selective surface plasmon resonance response based on a reduced graphene oxide–polyamidoamine nanocomposite for detection of dengue virus e-proteins." Nanomaterials 10, no. 3 (2020): 569. https://doi.org/10.3390/nano10030569

[186] H. Yan, and K. H. Row. "Characteristic and Synthetic Approach of Molecularly Imprinted Polymer". *International Journal of Molecular Sciences* 7, no. 5 (2006) :155-178. https://doi.org/10.3390/i7050155

[187] Xiao Li, and Scott M. Husson. "Two-dimensional molecular imprinting approach to produce optical biosensor recognition elements." Langmuir 22, no. 23 (2006): 9658-9663. doi:10.1021/la0612163

[188] Chien-Chong Hong, Po-Hsiang Chang, Chih-Chung Lin, and Chian-Lang Hong. "A disposable microfluidic biochip with on-chip molecularly imprinted biosensors for optical detection of anesthetic propofol." Biosensors and Bioelectronics 25, no. 9 (2010): 2058-2064. doi:10.1016/j.bios.2010.01.037

[189] Tetyana Sergeyeva, Daria Yarynka, Elena Piletska, Rostyslav Linnik, Olga Zaporozhets, Oleksandr Brovko, Sergey Piletsky, and Anna El'skaya. "Development of a smartphone-based biomimetic sensor for aflatoxin B1 detection using molecularly imprinted polymer membranes." Talanta 201 (2019): 204-210. https://doi.org/10.1016/j.talanta.2019.04.016

[190] C. Angulo Barrios, S. Carrasco, M. Francesca, P. Yurrita, F. Navarro-Villoslada, and M. C. Moreno-Bondi. "Molecularly imprinted polymer for label-free integrated optical waveguide bio (mimetic) sensors." Sensors and Actuators B: Chemical 161, no. 1 (2012): 607-614. https://doi.org/10.1016/j.snb.2011.11.008

[191] Jon Ashley, XiaoTong Feng, and Yi Sun. "A multifunctional molecularly imprinted polymer-based biosensor for direct detection of doxycycline in food samples." Talanta 182 (2018): 49-54. https://doi.org/10.1016/j.talanta.2018.01.056.

[192] Gizem Ertürk, Lokman Uzun, M. Aşkın Tümer, Rıdvan Say, and Adil Denizli. "Fab fragments imprinted SPR biosensor for real-time human immunoglobulin G detection." Biosensors and Bioelectronics 28, no. 1 (2011): 97-104. https://doi.org/10.1016/j.bios.2011.07.004.

[193] Gulsu Sener, Erdogan Ozgur, Abbas Yousefi Rad, Lokman Uzun, Ridvan Say, and Adil Denizli. "Rapid real-time detection of procalcitonin using a microcontact imprinted surface plasmon resonance biosensor." Analyst 138, no. 21 (2013): 6422-6428. https://doi.org/10.1039/C3AN00958K

[194] Necip Atar, Tanju Eren, and Mehmet Lütfi Yola. "A molecular imprinted SPR biosensor for sensitive determination of citrinin in red yeast rice." Food chemistry 184 (2015): 7-11. https://doi.org/10.1016/j.foodchem.2015.03.065.

[195] Zhenyi Xie, Ziwei Cao, Yong Liu, Qingwen Zhang, Jun Zou, Liyang Shao, Yi Wang, Jianjun He, and Mingyu Li. "Highly-sensitive optical biosensor based on equal FSR cascaded microring resonator with intensity interrogation for detection of progesterone molecules." Optics Express 25, no. 26 (2017): 33193-33201. https://doi.org/10.1364/OE.25.033193

[196] P. Palladino, M. Minunni, and S. Scarano. "Cardiac Troponin T capture and detection in real-time via epitope-imprinted polymer and optical biosensing." Biosensors and Bioelectronics 106 (2018): 93-98. https://doi.org/10.1016/j.bios.2018.01.068.

[197] Anand M. Shrivastav, Gaurav Sharma, and Rajan Jha. "Hypersensitive and selective biosensing based on microfiber interferometry and molecular imprinted nanoparticles." Biosensors and Bioelectronics 141 (2019): 111347. https://doi.org/10.1016/j.bios.2019.111347.

[198] Semra Akgönüllü, Handan Yavuz, and Adil Denizli. "SPR nanosensor based on molecularly imprinted polymer film with gold nanoparticles for sensitive detection of aflatoxin B1." Talanta 219 (2020): 121219. https://doi.org/10.1016/j.talanta.2020.121219.

[199] Costas M. Soukoulis. "The history and a review of the modelling and fabrication of photonic crystals." Nanotechnology 13, no. 3 (2002): 420. https://doi.org/10.1088/0957-4484/13/3/335

[200] Xiangfei Chen, Jianping Yao, and Zhichao Deng. "Ultranarrow dual-transmission-band fiber Bragg grating filter and its application in a dual-wavelength single-longitudinal-mode fiber ring laser." Optics letters 30, no. 16 (2005): 2068-2070. https://doi.org/10.1364/OL.30.002068

[201] Mei-Li Hsieh, Shu-Yu Chen, Alex Kaiser, Yang-Jhe Yan, B. Frey, Ishwara Bhat, Rajendra Dahal, Sayak Bhattacharya, Sajeev John, and Shawn-Yu Lin. "A low cost and large-scale synthesis of 3D photonic crystal with SP2 lattice symmetry." AIP Advances 9, no. 8 (2019): 085206. https://doi.org/10.1063/1.5113549

[202] S. Robinson, and R. Nakkeeran. "Photonic crystal ring resonator based optical filters." Advances in Photonic Crystals 1 (2013): 1-26. DOI: 10.5772/54533

[203] Yunbo Guo, Jing Yong Ye, Charles Divin, Baohua Huang, Thommey P. Thomas, James R. Baker, Jr, and Theodore B. Norris. "Real-time biomolecular binding detection using a sensitive photonic crystal biosensor." Analytical chemistry 82, no. 12 (2010): 5211-5218. DOI: 10.1021/ac100576y

[204] Yousef Nazirizadeh, Uwe Bog, Sylwia Sekula, Timo Mappes, Uli Lemmer, and Martina Gerken. "Low-cost label-free biosensors using photonic crystals embedded between crossed polarizers." Optics express 18, no. 18 (2010): 19120-19128. doi:10.1364/OE.18.019120.

[205] Philip St J. Russell. "Photonic-crystal fibers." Journal of lightwave technology 24, no. 12 (2006): 4729-4749. doi: 10.1126/science.1079280.

[206] Joshua N. Winn, Yoel Fink, Shanhui Fan, and John D. Joannopoulos. "Omnidirectional reflection from a one-dimensional photonic crystal." Optics letters 23, no. 20 (1998): 1573-1575. doi: 10.1364/ol.23.001573.

[207] Friederike Fleischhaker, André C. Arsenault, Frank C. Peiris, Vladimir Kitaev, Ian Manners, Rudolf Zentel, and Geoffrey A. Ozin. "DNA designer defects in photonic crystals: optically monitored biochemistry." Advanced Materials 18, no. 18 (2006): 2387-2391. https://doi.org/10.1002/adma.200600579

[208] Wei Zhang, Nikhil Ganesh, Ian D. Block, and Brian T. Cunningham. "High sensitivity photonic crystal biosensor incorporating nanorod structures for enhanced surface area." Sensors and Actuators B: Chemical 131, no. 1 (2008): 279-284. https://doi.org/10.1016/j.snb.2007.11.017.

[209] Leo L. Chan, Saujanya L. Gosangari, Kenneth L. Watkin, and Brian T. Cunningham. "A label-free photonic crystal biosensor imaging method for detection of cancer cell cytotoxicity and proliferation." Apoptosis 12, no. 6 (2007): 1061-1068. https://doi.org/10.1007/s10495-006-0031-y

[210] Nina Skivesen, Amølie Têtu, Martin Kristensen, Jørgen Kjems, Lars H. Frandsen, and Peter I. Borel. "Photonic-crystal waveguide biosensor." Optics Express 15, no. 6 (2007): 3169-3176. https://doi.org/10.1364/OE.15.003169

[211] Valery N. Konopsky, Tanya Karakouz, Elena V. Alieva, Chiara Vicario, Sergey K. Sekatskii, and Giovanni Dietler. "Photonic crystal biosensor based on optical surface waves." Sensors 13, no. 2 (2013): 2566-2578. https://doi.org/10.3390/s130202566

[212] Zonghu He, Fei Tian, Yinian Zhu, Nina Lavlinskaia, and Henry Du. "Long-period gratings in photonic crystal fiber as an optofluidic label-free biosensor." Biosensors and Bioelectronics 26, no. 12 (2011): 4774-4778. https://doi.org/10.1016/j.bios.2011.05.048.

[213] Tatsuro Endo, Satoshi Ozawa, Norimichi Okuda, Yasuko Yanagida, Satoru Tanaka, and Takeshi Hatsuzawa. "Reflectometric detection of influenza virus in human saliva using nanoimprint lithography-based flexible two-dimensional photonic crystal biosensor." Sensors and Actuators B: Chemical 148, no. 1 (2010): 269-276. doi:10.1016/j.snb.2010.05.036

[214] Bailin Zhang, Juan Manuel Tamez-Vela, Steven Solis, Gilbert Bustamante, Ralph Peterson, Shafiqur Rahman, Andres Morales, Liang Tang, and Jing Yong Ye. "Detection of myoglobin with an open-cavity-based label-free photonic crystal biosensor." Journal of Medical Engineering 2013 (2013). http://dx.doi.org/10.1155/2013/808056

[215] Wei Chang Wong, Chi Chiu Chan, Jia Liang Boo, Zi Yong Teo, Zhi Qiang Tou, Hong Bin Yang, Chang Ming Li, and Kam Chew Leong. "Photonic crystal fiber surface plasmon resonance biosensor based on protein G immobilization." IEEE Journal of Selected Topics in Quantum Electronics 19, no. 3 (2013): 4602107-4602107. doi: 10.1109/JSTQE.2013.2244560.

[216] Bailin Zhang, Andres W. Morales, Ralph Peterson, Liang Tang, and Jing Yong Ye. "Label-free detection of cardiac troponin I with a photonic crystal biosensor." Biosensors and Bioelectronics 58 (2014): 107-113. https://doi.org/10.1016/j.bios.2014.02.057.

[217] Fubing Xiao, Guoguo Li, Yan Wu, Qianshan Chen, Zhaoyang Wu, and Ruqin Yu. "Label-free photonic crystal-based β-lactamase biosensor for β-lactam antibiotic and β-lactamase inhibitor." Analytical chemistry 88, no. 18 (2016): 9207-9212. doi:10.1021/acs.analchem.6b02457

[218] Hai Yan, Chun-Ju Yang, Naimei Tang, Yi Zou, Swapnajit Chakravarty, Amanda Roth, and Ray T. Chen. "Specific detection of antibiotics by silicon-on-chip photonic crystal biosensor arrays." IEEE Sensors Journal 17, no. 18 (2017): 5915-5919. doi:10.1109/jsen.2017.2734885

[219] Yifei Wang, Wang Yuan, Michael Kimber, Meng Lu, and Liang Dong. "Rapid differentiation of host and parasitic exosome vesicles using microfluidic photonic crystal biosensor." ACS sensors 3, no. 9 (2018): 1616-1621. doi:10.1021/acssensors.8b00360

[220] Gabriel Sancho-Fornes, Miquel Avella-Oliver, Javier Carrascosa, Estrella Fernandez, Eva M. Brun, and Ángel Maquieira. "Disk-based one-dimensional photonic crystal slabs for label-free immunosensing." Biosensors and Bioelectronics 126 (2019): 315-323. https://doi.org/10.1016/j.bios.2018.11.005.

[221] Chun-Ju Yang, Hai Yan, Naimei Tang, Yi Zou, Yas Al-Hadeethi, Xiaochuan Xu, Hamed Dalir, and Ray T. Chen. "Ultra sensitivity silicon-based photonic crystal microcavity biosensors for plasma protein detection in patients with pancreatic cancer." Micromachines 11, no. 3 (2020): 282. https://doi.org/10.3390/mi11030282

[222] American Diabetes Association, “Diagnosis and classification of diabetes mellitus,” Diabetes Care, vol. 37, no. 1 , pp. S81-S90, Jan. 2014

[223] J. Michael McMillin. “Clinical Methods: The History, Physical, and Laboratory Examinations.” Chapter 141. 3rd edition. Boston: Butterworths; 1990. Available from: https://www.ncbi.nlm.nih.gov/books/NBK248/

[224] Nguyen Thi Bao Ngoc, “ ANALYSIS METHODS OF BLOOD GLUCOSE: Case in Vietnam.” Thesis: Chapter 4, November 2018

[225] Ping Wu, Qian Shao, Yaojuan Hu, Juan Jin, Yajing Yin, Hui Zhang, and Chenxin Cai. "Direct electrochemistry of glucose oxidase assembled on graphene and application to glucose detection." Electrochimica Acta 55, no. 28 (2010): 8606-8614. https://doi.org/10.1016/j.electacta.2010.07.079

[226] Manjusha Mathew, and N. Sandhyarani. "A highly sensitive electrochemical glucose sensor structuring with nickel hydroxide and enzyme glucose oxidase." Electrochimica Acta 108 (2013): 274-280. https://doi.org/10.1016/j.electacta.2013.07.010

[227] Eleni Sapountzi, Mohamed Braiek, Francis Vocanson, Jean-François Chateaux, Nicole Jaffrezic-Renault, and Florence Lagarde. "Gold nanoparticles assembly on electrospun poly (vinyl alcohol)/poly (ethyleneimine)/glucose oxidase nanofibers for ultrasensitive electrochemical glucose biosensing." Sensors and Actuators B: Chemical 238 (2017): 392-401. https://doi.org/10.1016/j.snb.2016.07.062

[228] Lisha Wang, Xia Gao, Lingyan Jin, Qi Wu, Zhichun Chen, and Xianfu Lin. "Amperometric glucose biosensor based on silver nanowires and glucose oxidase." Sensors and Actuators B: Chemical 176 (2013): 9-14. https://doi.org/10.1016/j.snb.2012.08.077

[229] Jiang Li, Pankaj Koinkar, Yusuke Fuchiwaki, and Mikito Yasuzawa. "A fine pointed glucose oxidase immobilized electrode for low-invasive amperometric glucose monitoring." Biosensors and Bioelectronics 86 (2016): 90-94. https://doi.org/10.1016/j.bios.2016.06.037

[230] KaiJin Tian, Hui Liu, YongPing Dong, XiangFeng Chu, and ShangBing Wang. "Amperometric detection of glucose based on immobilizing glucose oxidase on g-C3N4 nanosheets." Colloids and Surfaces A: Physicochemical and Engineering Aspects 581 (2019): 123808. https://doi.org/10.1016/j.colsurfa.2019.123808

[231] Debasis Maity, C. R. Minitha, and Rajendra Kumar RT. "Glucose oxidase immobilized amine terminated multiwall carbon nanotubes/reduced graphene oxide/polyaniline/gold nanoparticles modified screen-printed carbon electrode for highly sensitive amperometric glucose detection." Materials Science and Engineering: C 105 (2019): 110075. https://doi.org/10.1016/j.msec.2019.110075

[232] Huanan Guan, Dezhuang Gong, Yan Song, Bolin Han, and Na Zhang. "Biosensor composed of integrated glucose oxidase with liposome microreactors/chitosan nanocomposite for amperometric glucose sensing." Colloids and Surfaces A: Physicochemical and Engineering Aspects 574 (2019): 260-267. https://doi.org/10.1016/j.colsurfa.2019.04.076

[233] Marc Parrilla, Rocío Cánovas, and Francisco J. Andrade. "based enzymatic electrode with enhanced potentiometric response for monitoring glucose in biological fluids." Biosensors and Bioelectronics 90 (2017): 110-116. https://doi.org/10.1016/j.bios.2016.11.034

[234] Jung-Chuan Chou, Si-Hong Lin, Tsu-Yang Lai, Po-Yu Kuo, Chih-Hsien Lai, Yu-Hsun Nien, and Tzu-Yu Su. "A facile fabrication of a potentiometric arrayed glucose biosensor based on nafion-GOx/GO/AZO." Sensors 20, no. 4 (2020): 964. https://doi.org/10.3390/s20040964

[235] Ambran Hartono, Edi Sanjaya, and Ramli Ramli. "Glucose sensing using capacitive biosensor based on polyvinylidene fluoride thin film." Biosensors 8, no. 1 (2018): 12. https://doi.org/10.3390/bios8010012

[236] Lizhen Chen, Wenyang Xie, Yao Luo, Xiaolan Ding, Bing Fu, Subash CB Gopinath, and Yuanhuan Xiong. "Sensitive silica-alumina modified capacitive non-Faradaic glucose sensor for gestational diabetes." Biotechnology and applied biochemistry (2021). https://doi.org/10.1002/bab.2155

[237] Angela Mihaela Baracu, and Livia Alexandra Dinu Gugoasa. "recent advances in microfabrication, design and applications of amperometric sensors and biosensors." Journal of The Electrochemical Society 168, no. 3 (2021): 037503. https://doi.org/10.1149/1945-7111/abe8b6

[238] G. Alarcon-Angeles, G.A. Álvarez-Romero, A. Merkoçi, "Electrochemical Biosensors: Enzyme Kinetics and Role of Nanomaterials," Encyclopedia of Interfacial Chemistry (2018): 140-155. https://doi.org/10.1016/B978-0-12-409547-2.13477-8

[239] Hongyuan Zhao, Xinyi Guo, Yanyan Wang, Xuexin Duan, Hemi Qu, Hao Zhang, Daihua Zhang, and Wei Pang. "Microchip based electrochemical-piezoelectric integrated multi-mode sensing system for continuous glucose monitoring." Sensors and Actuators B: Chemical 223 (2016): 83-88. https://doi.org/10.1016/j.snb.2015.09.022

[240] Xinyu Xue, Zhi Qu, Yongming Fu, Binwei Yu, Lili Xing, and Yan Zhang. "Self-powered electronic-skin for detecting glucose level in body fluid basing on piezo-enzymatic-reaction coupling process." Nano Energy 26 (2016): 148-156. https://doi.org/10.1016/j.nanoen.2016.05.021

[241] Mardhiah Mohd Nor, Badariah Bais, Norazreen Abd Aziz, Rosminazuin Ab Rahim, and Burhanuddin Yeop Majlis. "Induced mass change technique for glucose detection in microcantilever-based sensors." In 2012 10th IEEE International Conference on Semiconductor Electronics (ICSE), pp. 340-343. IEEE, 2012. 10.1109/SMElec.2012.6417155

[242] Jianhong Pei, Fang Tian, and Thomas Thundat. "Novel glucose biosensor based on the microcantilever." MRS Online Proceedings Library (OPL) 776 (2003). https://doi.org/10.1557/PROC-776-Q11.21

[243] A. Subramanian, P. I. Oden, S. J. Kennel, K. B. Jacobson, R. J. Warmack, T. Thundat, and M. J. Doktycz. "Glucose biosensing using an enzyme-coated microcantilever." Applied Physics Letters 81, no. 2 (2002): 385-387. https://doi.org/10.1063/1.1492308

[244] Xiaodong Yan, Xiaohe Karen Xu, and Hai-Feng Ji. "Glucose oxidase multilayer modified microcantilevers for glucose measurement." Analytical chemistry 77, no. 19 (2005): 6197-6204. https://doi.org/10.1021/ac050801q

[245] Blake N. Johnson, and Raj Mutharasan. "Biosensing using dynamic-mode cantilever sensors: A review." Biosensors and bioelectronics 32, no. 1 (2012): 1-18.

[246] Helen J. Watts, Debra Yeung, and Helen Parkes. "Real-time detection and quantification of DNA hybridization by an optical biosensor." Analytical chemistry 67, no. 23 (1995): 4283-4289. https://doi.org/10.1021/ac00119a013

[247] Matthew A. Cooper. "Optical biosensors in drug discovery." Nature reviews Drug discovery 1, no. 7 (2002): 515-528.

[248] Yinquan Yuan, Na Yuan, Dejing Gong, and Minghong Yang. "A high-sensitivity and broad-range SPR glucose sensor based on improved glucose sensitive membranes." Photonic Sensors 9, no. 4 (2019): 309-316. https://doi.org/10.1007/s13320-019-0538-9

[249] Yayun Li, Yinquan Yuan, Dejing Gong, Wenbin Hu, and Minghong Yang. "A SPR glucose sensor based on immobilized glucose oxidases and silica mesocellular foams." IEEE Sensors Journal 18, no. 6 (2018): 2229-2235. 10.1109/JSEN.2018.2794510

[250] S. K. Srivastava, and I. Abdulhalim. "Spectral interrogation based SPR sensor for blood glucose detection with improved sensitivity and stability." J. Biosens. Bioelectron 6 (2015): 10-12.

[251] Wanlu Zheng, Bo Han, E. Siyu, Yang Sun, Xuegang Li, Yi Cai, and Ya-nan Zhang. "Highly-sensitive and reflective glucose sensor based on optical fiber surface plasmon resonance." Microchemical Journal 157 (2020): 105010. https://doi.org/10.1016/j.microc.2020.105010

[252] Yinquan Yuan, Xi Yang, Dejing Gong, Fang Liu, Wenbin Hu, Weiquan Cai, Jun Huang, and Minghong Yang. "Investigation for terminal reflection optical fiber SPR glucose sensor and glucose sensitive membrane with immobilized GODs." Optics express 25, no. 4 (2017): 3884-3898. https://doi.org/10.1364/OE.25.003884

[253] Roli Verma, and Banshi D. Gupta. "A novel approach for simultaneous sensing of urea and glucose by SPR based optical fiber multianalyte sensor." Analyst 139, no. 6 (2014): 1449-1455. https://doi.org/10.1039/C3AN01983G

[254] Yun Cai, Wei Li, Ye Feng, Jian-Sheng Zhao, Gang Bai, Jie Xu, and Jin-Ze Li. "Sensitivity enhancement of WS2-coated SPR-based optical fiber biosensor for detecting glucose concentration." Chinese Physics B 29, no. 11 (2020): 110701. https://doi.org/10.1088/1674-1056/aba601

[255] Qingshan Yang, Guo Zhu, Lokendra Singh, Yu Wang, Ragini Singh, Bingyuan Zhang, Xia Zhang, and Santosh Kumar. "Highly sensitive and selective sensor probe using glucose oxidase/gold nanoparticles/graphene oxide functionalized tapered optical fiber structure for detection of glucose." Optik 208 (2020): 164536. https://doi.org/10.1016/j.ijleo.2020.164536

[256] Sruthi P. Usha, Anand M. Shrivastav, and Banshi D. Gupta. "FO-SPR based dextrose sensor using Ag/ZnO nanorods/GOx for insulinoma detection." Biosensors and Bioelectronics 85 (2016): 986-995. https://doi.org/10.1016/j.bios.2016.05.082

[257] Jia-xin Li, Wei-hua Zhang, Zheng-rong Tong, and Jing-wei Liu. "Fiber optic sensor modified by graphene oxide–glucose oxidase for glucose detection." Optics Communications 492 (2021): 126983. https://doi.org/10.1016/j.optcom.2021.126983

[258] Yanpeng Li, Qizhen Sun, Haipeng Luo, Zhilin Xu, Xiaohui Sun, Deming Liu, and Lin Zhang. "A high sensitive glucose sensor based on GOD-immobilized fiber microprobe." In 2015 Optoelectronics Global Conference (OGC), pp. 1-3. IEEE, 2015. 10.1109/OGC.2015.7336862

[259] Vince S. Siu, Jing Feng, Patrick W. Flanigan, G. Tayhas R. Palmore, and Domenico Pacifici. "A “plasmonic cuvette”: dye chemistry coupled to plasmonic interferometry for glucose sensing." Nanophotonics 3, no. 3 (2014): 125-140. https://doi.org/10.1515/nanoph-2013-0057

[260] Chao-Wei Wu. "S-shaped long period fiber grating glucose concentration biosensor based on immobilized glucose oxidase." Optik 203 (2020): 163960. https://doi.org/10.1016/j.ijleo.2019.163960

[261] V. G. Pahurkar, Y. S. Tamgadge, A. B. Gambhire, and G. G. Muley. "Glucose oxidase immobilized PANI cladding modified fiber optic intrinsic biosensor for detection of glucose." Sensors and Actuators B: Chemical 210 (2015): 362-368. https://doi.org/10.1016/j.snb.2014.12.125

[262] David A. Chang-Yen, and Bruce K. Gale. "Integrated optical glucose sensor fabricated using PDMS waveguides on a PDMS substrate." In Microfluidics, BioMEMS, and Medical Microsystems II, vol. 5345, pp. 98-107. SPIE, 2003. https://doi.org/10.1117/12.530062

[263] Inga Brice, Karlis Grundsteins, Aigars Atvars, Janis Alnis, and Roman Viter. "Whispering gallery mode resonators coated with Au nanoparticles." In Nanoengineering: Fabrication, Properties, Optics, Thin Films, and Devices XVI, vol. 11089, p. 110891T. International Society for Optics and Photonics, 2019. https://doi.org/10.1117/12.2528677

[264] Inga Brice, Karlis Grundsteins, Aigars Atvars, Janis Alnis, Roman Viter, and Arunas Ramanavicius. "Whispering gallery mode resonator and glucose oxidase based glucose biosensor." Sensors and Actuators B: Chemical 318 (2020): 128004. https://doi.org/10.1016/j.snb.2020.128004

[265] Michael Mcgrath, and Cliodhna Ni Scanaill. “Sensing and Sensor Fundamentals”. Sensor Technologies, Apress, Berkeley,CA (2013): 15-50. https://doi.org/10.1007/978-1-4302-6014-1_2.

Chapter 2

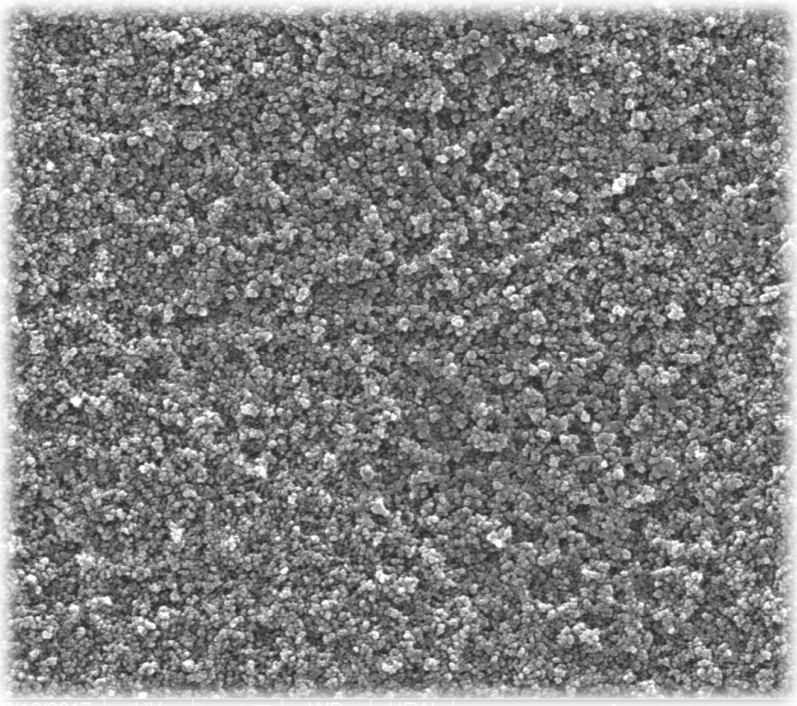

Chapter 2

Porous Silicon as Biosensing Material

2.1. Introduction

Porous Silicon (PS) was first discovered by Uhlir in 1956 [1] while working on electrochemical polishing of silicon surface at Bell's Laboratories (USA). The discovery did not receive much attention from the scientific society at that time. In 1990, Canham reported photoluminescence of PS in visible range upon UV excitation [2] which caught a significant amount of interest in the material because silicon devices were unable to produce efficient luminescence due to their indirect band gap. Electrochemical etching

procedure for PS preparation was also simple and cost efficient compared to conventional lithography or epitaxial techniques for nanostructure preparation. So, further research on the properties and application of PS has been carried out from then onwards. PS is a nanostructured thin film electrochemically etched on Silicon wafer surface with thickness ranging within few micrometers. Also, its pore diameter or particle size, thickness and porosity can be varied easily by controlling the etching parameters [3]. PS is classified in three categories based on their pore size i.e. microporous (pore size ≤ 2nm), mesoporous (pore size ~ 2-50nm) and macroporous (pore size > 50nm) [4]. Nanoporous silicon is comparatively a new term and the range of its pore size is not well defined. In general, any structure that is in < 100nm range can be safely defined as nanostructures. So, pore size of nano PS is considered in between 1-100nm. Electrochemically prepared PS has found a wide range of applications due to its easily controllable morphological and physical properties. Also due to their large surface to volume ratio and biocompatibility [5], they have found significant application in biological fields like biosensor [6,7], tissue engineering [8,9], drug delivery [10] etc. Numerous biosensors have been reported based on optical and electrical properties of PS. Initially optical biosensors were reported utilising only photoluminescence emission as transduction method [11-13]. Later on, study of other aspects of nanocrystalline structure introduced different types of unique optical transduction methods. For example, interferometric PS thin film for IgG detection [14], DNA modified PS double Bragg mirror structure for AOB detection [15], nanostructured PS supporting Bloch surface modes for protease detection [16], PS resonant microcavity based matrix metalloproteinase detection [17] and many more [18-22] have been reported in the last few years.

In this chapter, physiochemical properties and preparation method of PS films have been discussed first. Then, PS thin films formed with different preparation conditions were characterized and finally, optimization of the thin films has been carried out for successful biosensing application. This work has been published in [23].

2.2. Properties

Nanostructured materials in general, show significant change in physical and chemical properties compared to their bulk counterparts. As the size of bulk material

reduces and reaches to nanometer range, quantum effects become dominant and the material no longer behaves the same way. PS has unique structural, mechanical, electrical, optical, thermal, physiochemical and biochemical properties which enable its use in versatile fields like optoelectronics, biotechnology, sensing, microelectronics and micromachining, energy conversion, environmental monitoring etc. Tunable properties of mesoporous silicon are compared with bulk silicon in Table I. Main emphasis in this section is given on structural and optical properties of PS as transduction method opted in this work is purely optical.

Table I: Comparison of tunable properties of meso PS with bulk Si

(Table adapted from [24])

	Property	Bulk Si	Meso PS
Structural	Porosity	—	20–95%
	Density	2.33 g/cm^3	0.12–1.9 g/cm^3
	Pore size (diameter)	—	2–50 nm
	Surface to volume ratio	1 m^2/ cm^3	500 m^2/ cm^3
	Lattice structure	Diamond	Diamond
Mechanical	Young's modulus	160 GPa	1–100 GPa
	Hardness	11.5 GPa	0.2–10 GPa (layer)
			0.05–1 GPa (composite)
	Yield strength	7 GPa	—
	Fracture toughness	0.6 MPam^{½}	—
Optical	Bandgap	1.1 eV	1.1–3.2 eV
	Infrared refractive index	3.5	1.1–3.0
	Color	Gray	All colors (layer)
			Brown-yellow (particle)
	Reflectivity (500–1000 nm)	10–35%	0.1–10%
Electrical	Resistivity	10^{-2}–10^3 Ωcm	10^3–10^{12} Ωcm
	Free electron mobility	1350 cm^2/Vs	0.1–30 cm^2/Vs
	Hole mobility	480 cm^2/Vs	2–6 cm^2/Vs
	Dielectric constant	11.5	2–8
Thermal	Conductivity	150 W/mK	0.03–20 W/mK
	Melting point	1414°C	800–1414°C
	Specific heat	0.7 J/gK	—
	Diffusivity	0.8 cm^2/s	—
Emissive	PL wavelength	1000–1200 nm	400–1300 nm
	PL efficiency	10^{-6}	0.01–0.23 (films)
			0.01–0.6 (suspensions)
	EL efficiency	10^{-8}	0.01–0.1
Physiochemical	Isoelectric point	pH 1.6–2.5	pH 1.6–7.7
	Zeta potential (pH 7)	–(45–70) mV	—
	Surface wettability	5–96°	<0.5–167°

	Property	Bulk Si	Meso PS
Biochemical	Medical biodegradability	—	Months (implants)
			Days (microparticles)
			Hours (nanoparticles)

2.2.1. Structural Property

PS is like a quantum sponge which contains nanocrystallites and pores forming a complex web like structure [25]. As the nanocrystalline skeleton is immersed in a network of pores, the structure shows very high surface to volume ratio ($\sim 500\ m^2/cm^3$). Depending upon preparation conditions, PS films can have a wide range of structural variation in terms of pore shape, size, orientation, interconnection, branching and distribution. It was found that, PS formed from p type Si and n type Si show significant change in pore size, shape and branching degree. Also doping concentration of Si wafer, presence of illumination etc. plays major role in the diverse morphology. Generally, size of pores depends greatly on doping type and concentration. In p type Si, pore size increases with increase in doping concentration, while for n type Si the phenomenon is reversed [3]. The most interesting application of variable pore morphology is that they can act as binding sites for different size and shape of bio-analyte in biosensor application. The analytes are absorbed in the sponge like matrix and due to the presence of large interaction space because of the large surface to volume ratio of PS, sensitivity increases significantly [26]. Also, PS is a biocompatible material [27] and its surface can be chemically modified easily which also increases its application in biosensor field.

2.2.2. Optical Properties

Visible photoluminescence (PL) of freshly etched PS made it a prospective material for optoelectronic device fabrication. Bulk Si has indirect bandgap and carrier recombination process mainly emits a weak infrared radiation. But PS contains silicon column structure of nanometer range leading to quantum confinement (QC) effect which generates direct bandgaps [28]. At first, QC was considered to be the only reason for visible PL peak [29], but in later studies, hydrogenated silicon compounds were investigated as silicon hydride

complexes have room temperature PL [30]. Detailed study on Siloxene derivatives present in oxidised PS provided further explanation on PL peak shift and large distribution of radiative lifetime in PS materials [31]. Also, generation of other optical properties like cathodoluminescence (CL) and electroluminescence (EL) could be described completely by the new models.

PS based structures have the ability to generate PL in a wide range of spectra due to their tunable S-band which can produce emission in visible range from deep red to blue upon excitation with near UV source [32]. Also, rapid thermal oxidation of PS produces quite strong blue-green PL emission from F-band [33]. Soft x-ray excitation of oxidised PS reported to have UV emission [34]. Also, IR emission at room temperature was observed for PS annealed under ultrahigh vacuum [35].

CL in PS samples was observed in three broad bands (~ 290nm, 440nm and 620nm) which were generated mainly due to impurities or defects within oxide phases of the material and can be completely quenched by post oxidation hydrogen plasma treatment [36]. But CL signal strength was found much lower than PL and extremely unstable for freshly etched PS samples.

EL spectra of PS based diode was first observed using Koshida LED and it was found that external quantum efficiency (EQE) of EL was five orders of magnitude lower than PL efficiency [37]. Later, LED fabricated with only microporous Si layer [38] was reported to attain efficiency close to practically useful level; still device lifetime needed to be improved further for practical application.

2.3. Fabrication

PS can be prepared on bulk Si substrate by different methods like anodic etching, stain etching, photoetching, spark erosion, ion implantation, laser ablation and many more [39]. Among them anodic etching which is also called electrochemical etching, is the most common fabrication method. Initially, electrochemical etching was used for electropolishing Si wafers. Then in 1956, accidental fall of etching current in electropolishing procedure produced PS for the first time [1]. Later it was found that, above a critical current density (J_C)

electropolishing takes place and for $J < J_C$, porosification of Si wafer is possible [3]. In this section electrochemical etching procedure and formation mechanism is discussed in details.

2.3.1. Electrochemical Etching Procedure

Generally, three types of cell configuration (lateral cell, single pond cell and double pond cell) are used in this method of PS fabrication [39]. Single cell is suitable for uniform thickness and porosity of prepared PS and also for the simplicity of fabrication process [40]. Figure 2.1 shows a schematic diagram of single cell structure where the etching chamber body is made of an acid resistant polymer like Teflon. Si wafer is used as anode and for uniform porosity a copper plate contact is used under the wafer. An 'O' ring seals the electrolyte solution allowing only one side of Si wafer to take part in etching procedure. A Graphite cathode which is of same diameter as of the 'O' ring, is used to introduce uniform current density over Si surface. A thin aluminium film is deposited on the back of Si wafer and annealed at ~ 600^{o}C for the formation of uniform contact for high resistivity wafers.

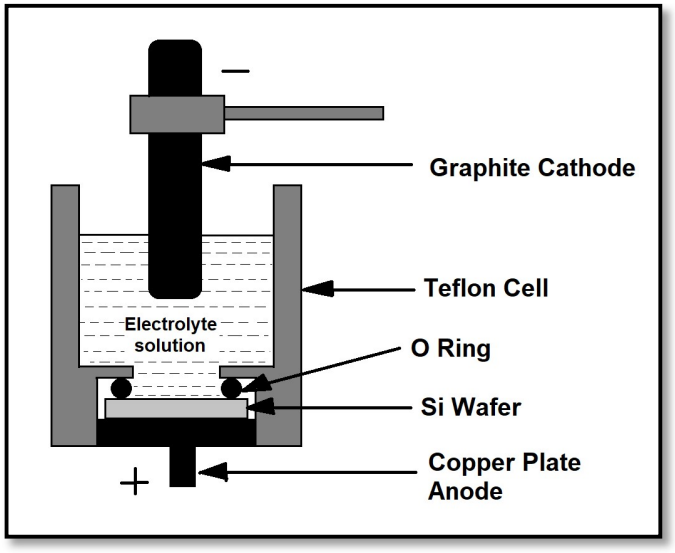

Figure 2.1. Schematic diagram of single cell setup

Two types of PS i.e. nano and macro PS were fabricated in the single cell configuration from p-type <100> single crystalline silicon wafer with resistivity of 1-10Ωcm and 10-20Ωcm respectively. First the single side polished silicon wafers were ultrasonicated in acetone solution for 20 minutes. Then they were cleaned in piranha solution and finally

dipped in 2% hydrofluoric acid (HF) solution to make the polished surface hydrophobic. Back contact has been made by coating thin film of Al paste and firing afterwards at 600^{o}C for 45 seconds. For nano PS preparation, 48% HF and absolute ethanol in 1:1 volume ratio was used as electrolyte solution. 10mA/cm^2 current density was maintained from a constant current source for different etching time to prepare nano PS samples of different thickness. For macro PS, 48% HF and > 99% N, N Dimethyl Formamide (DMF) in 1:3 volume ratio was used as electrolyte solution and 10mA/cm^2 current density was maintained for 30 minutes. After etching the samples were washed vigorously with DI water and left overnight for room temperature drying. Finally, the samples were annealed at 450^{o}C for 40 minutes for thermal stabilization.

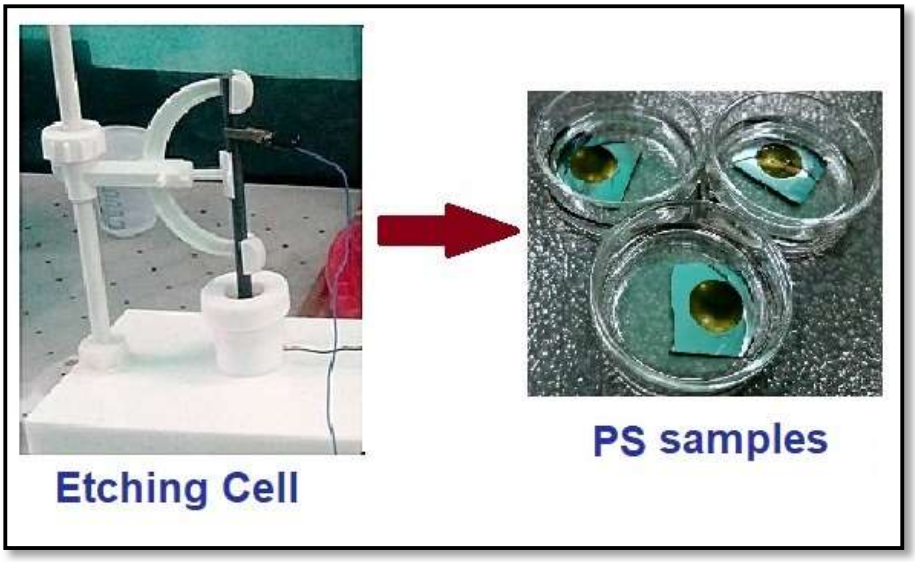

Figure 2.2. Photograph of single cell Teflon etching chamber and PS samples

Table II: Etching parameters for different types of PS samples

Sample Type	Wafer Resistivity	Electrolyte	Etching Time	Etching Current
Nano_5min.	1-10Ωcm	HF:ethanol (1:1)	5(minute)	10 mA/cm^2
Nano_10min.	1-10 Ωcm	HF:ethanol (1:1)	10 (minute)	10 mA/cm^2
Nano_20min.	1-10 Ωcm	HF:ethanol (1:1)	20 (minute)	10 mA/cm^2
Macro	10-20 Ωcm	HF:DMF (1:1)	30 (minute)	10 mA/cm^2

2.3.2. Formation Mechanism

Dissolution of tetravalent Si atoms in electrolyte solution takes place in multiple steps [3]. In each step, H_2 is generated which can be visually seen as bubbles coming out of the electrolyte surface. Initially, in HF solution Si wafer surface is terminated by hydrogen i.e. Si-H bonds. When a hole travels up to the surface in anodic dissolution process, F^- ions attack these surface Si-H bonds due to hole induced charge instability. Replacement of Si-H with Si-F bond weakens the Si-Si back bond structure and becomes vulnerable to further attack from HF or H_2O present in electrolyte solution. The dissolution process can occur in two competing reaction paths shown in figure 2.3. In direct dissolution (path I), Si-Si back bond is attacked with HF directly and in indirect dissolution (path II), H_2O attacks Si-SiF bond producing oxide layer (Si-O-Si) [41]. Reaction path I dominate in lower potential and with increasing potential domination of path II produces large number of Si-O-Si bonds which almost passivates the surface making it less active for direct dissolution. PS formation is possible when oxide layer does not fully cover the surface which leaves scope for direct dissolution to take place.

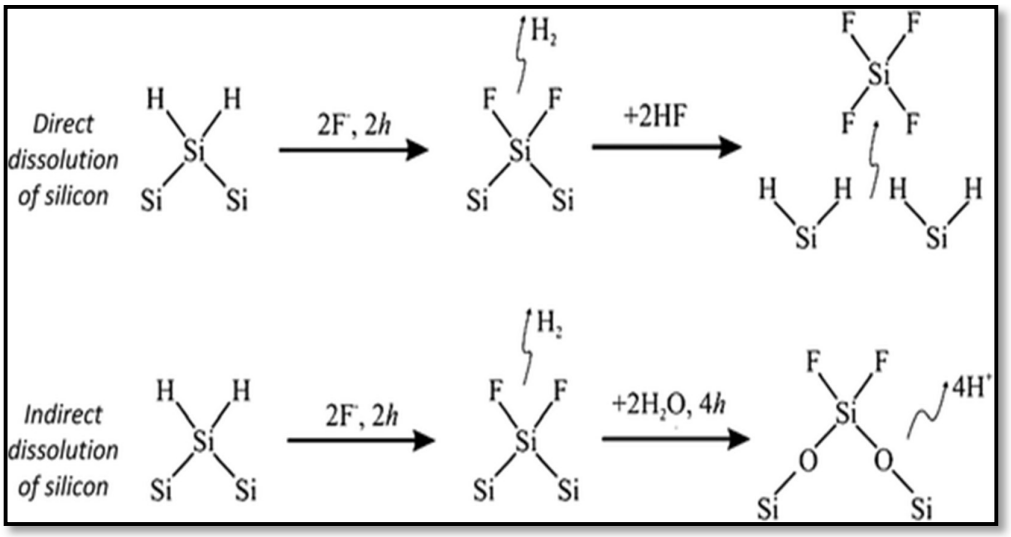

Figure 2.3. PS formation reaction paths (Image taken from [41])

Step by step reaction chemistry is depicted in figure 2.5. In PS formation process, reaction (1) and (2) are found to be favoured while reaction (3) was found less favoured [42]. All the three reactions in figure 2.4 occur simultaneously and the final product of electrochemical etching process is Hexafluorosilicic acid (H_2SiF_6).

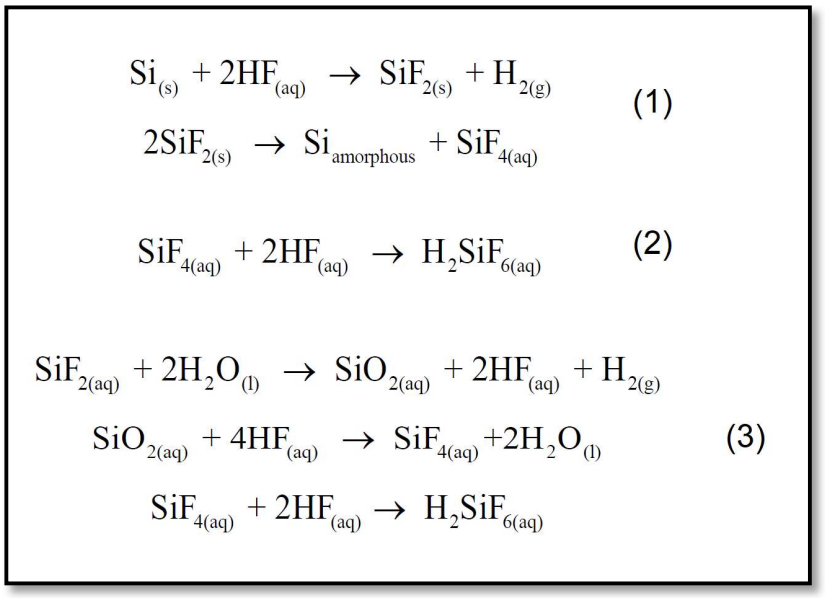

Figure 2.4. Reaction steps for PS formation (Image adapted from [42])

2.4. Characterization

Morphological and structural characterizations of the PS films were carried out using FESEM (FEI, INSPECT F50), AFM (Bruker, Multimode 8) and XRD (Bruker, D8 Advance) analysis. As discussed before, two types of PS films i.e. nano and macro PS were prepared and etching time of nano PS was varied to obtain different thickness. In this section, difference in morphology of thick and thin nano PS layers is discussed first and then comparison between nano and macro PS morphology is performed.

2.4.1. Thin vs. Thick Nano PS

Figure 2.5 shows FESEM images of nano PS prepared for 5, 10 and 20 minute etching time. 5 minute samples are called thin nano PS while 10 or 20 minute samples are called thick ones. Kumar and Huber reported that with increase in etching time with constant etching current density, both porosity and film thickness increases [43]. From the FESEM images, it was observed that with increase in etching time, agglomeration of nanoparticles on PS surface increases and distinct increase in nanoparticle clusters (as large as ~400nm) can be observed for 20 minute sample (figure 2.5.c). Particle size and film thickness was

found to be 18-25nm and 1.1µm respectively for 5 minute sample. Below 5 minute, non uniform coverage of PS layer was observed on Si surface thus it was avoided.

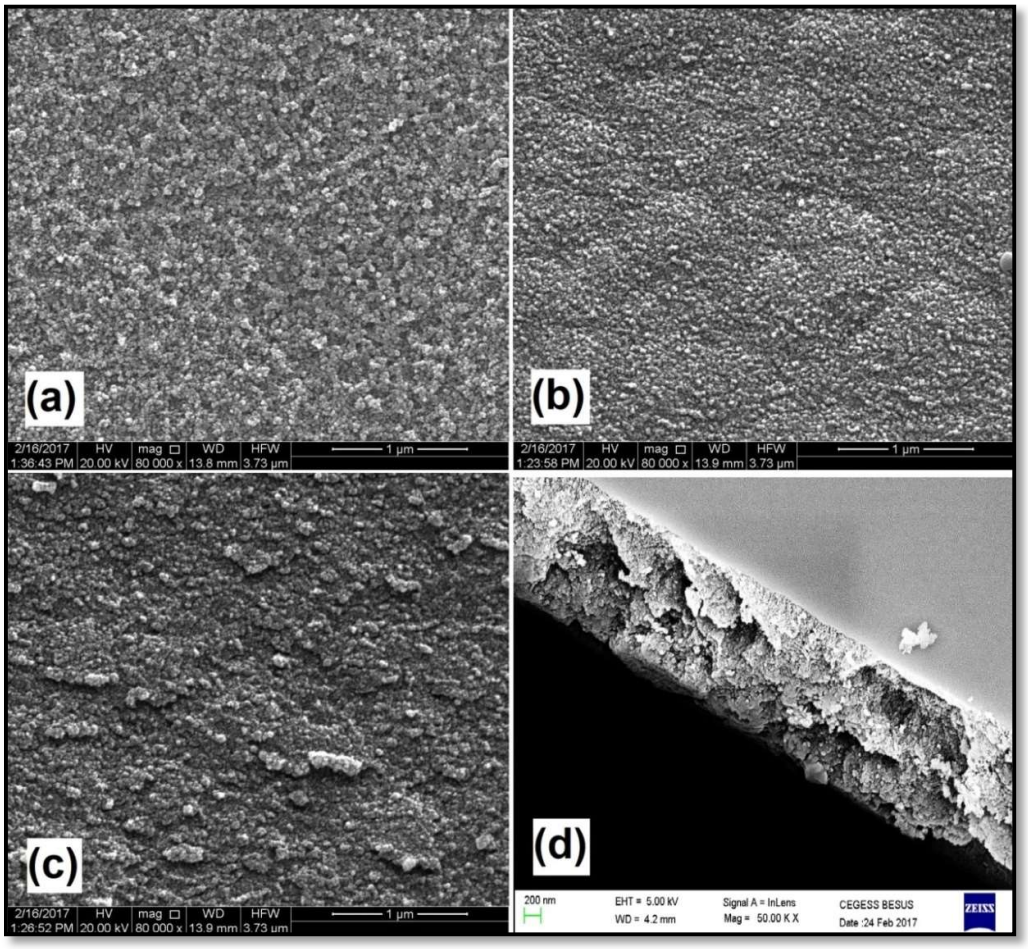

Figure 2.5. FESEM micrograph of nano PS top surface for (a) 5 minute, (b) 10 minute, (c) 20 minute etching time and (d) cross sectional view of 5 minute sample

Higher magnification of 20 minute sample (figure 2.6) further shows a fish scale like structure which indicates the loosening of PS nanoparticle clusters from base. This type of unstable structure is not suitable for biosensor application as they need to go through incubation and several washing procedures which may remove the loosely bound clustered structure from the sensor surface reducing sensitivity significantly. In section 4.7 also, we observed poor glucose sensing performance of thick nano PS which verifies their incompetence in biosensing application.

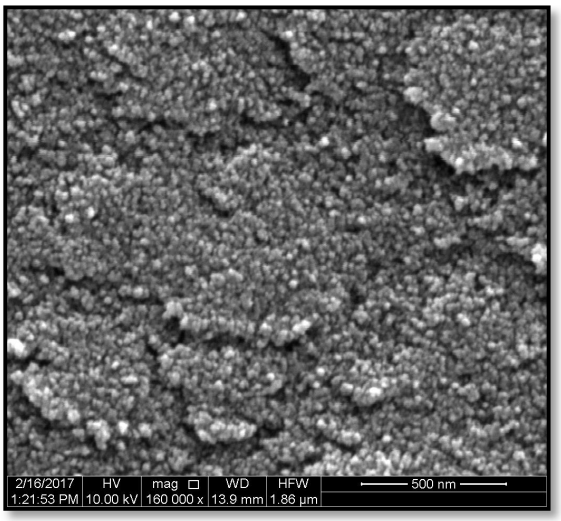

Figure 2.6. FESEM micrograph of 20 minute sample

AFM images in figure 2.7 also demonstrate increase in surface roughness due to increase in etching time, as expected from FESEM micrographs. For 5 minute and 20 minute samples, r.m.s. value of surface roughness was found to be 75.8nm and 104nm respectively.

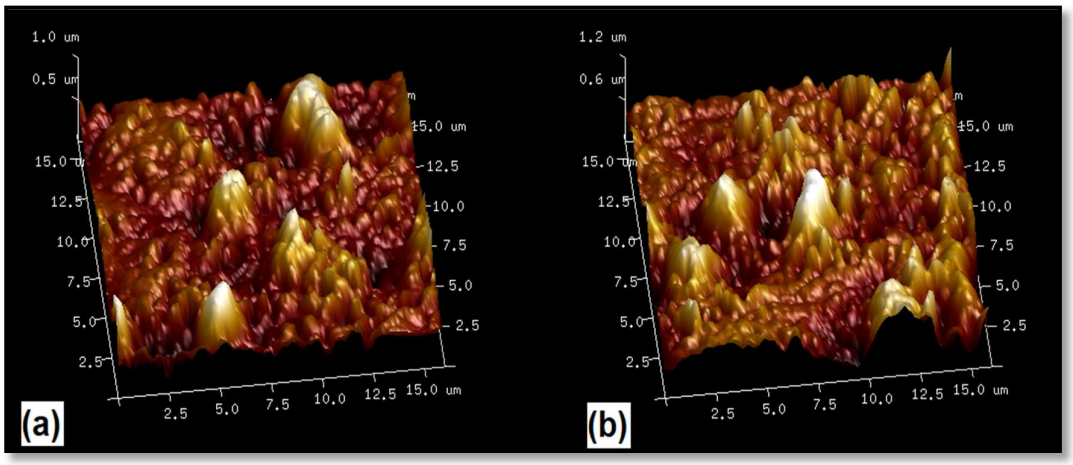

Figure 2.7. 3D AFM image of (a) 5 minute and (b) 20 minute sample

X-ray diffraction pattern for Cu Kα (λ ≈ 1.54 Å) radiation source has been recorded for 2θ range of 20-80^{o} with 30kV and 30mA generator setting. All the nano PS samples show double peak at 2θ ~ 69^{o} (figure 2.8) which is standard for p type silicon wafer with <100> orientation [44]. D-spacing was calculated from the obtained peak position and found to be 0.14nm for the nano PS samples.

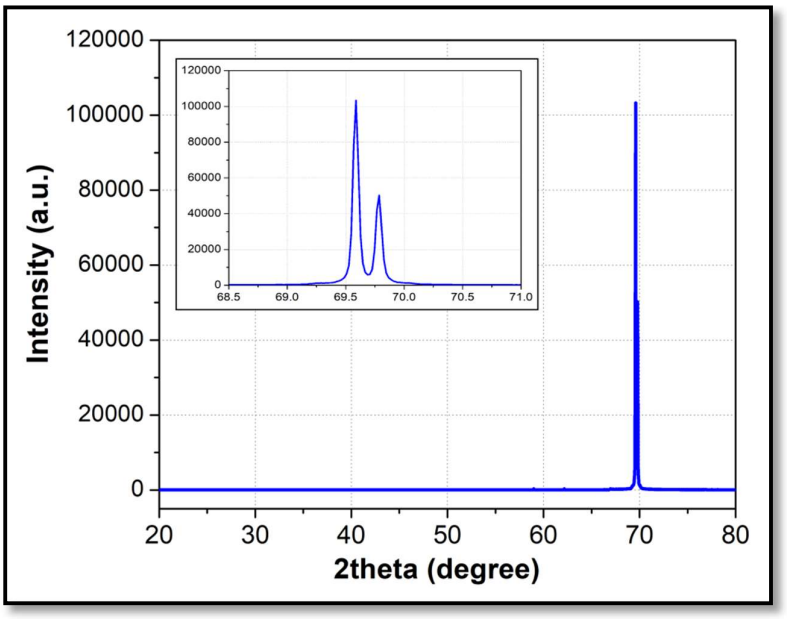

Figure 2.8. Baseline corrected XRD plot of nano PS sample

2.4.2. Nano vs. Macro PS

The main difference of nano and macro PS is that nano PS produces visible PL at room temperature upon excitation with UV source while macro PS does not produce such PL. Image of nano and macro PS after preparation is shown in figure 2.9 where bright red PL is observed for nano PS samples.

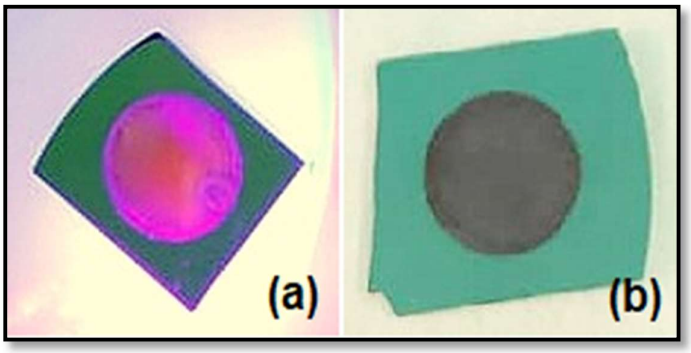

Figure 2.9. Image of prepared (a) Nano PS and (b) Macro PS

FESEM image of macro PS shows well defined pores (figure 2.10(b)), which is not visible in nano PS samples (figure 2.10(a)). Pore diameter range of macro PS was observed to be 0.8-2.3µm and such huge deviation in pore/particle dimension was not observed in nano PS samples.

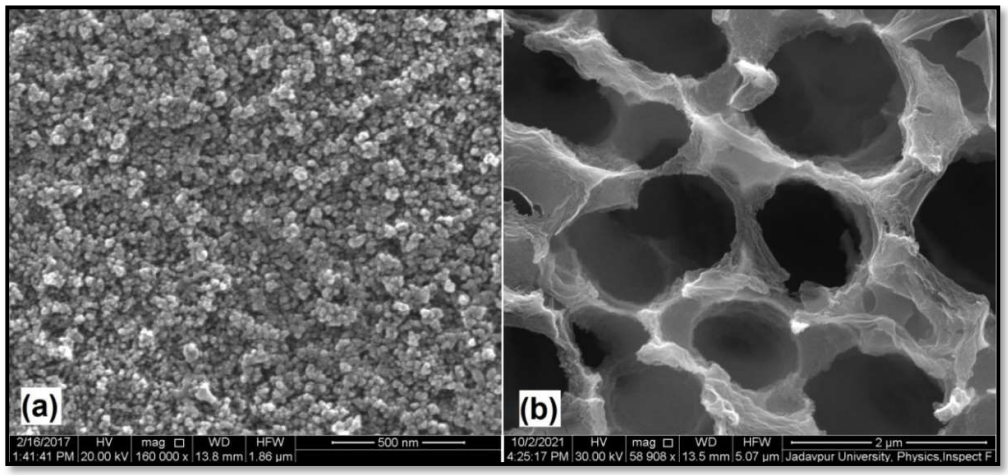

Figure 2.10. FESEM micrograph (a) Nano PS and (b) Macro PS

2.5. Surface Functionalization

Physisorption technique was used to modify PS surface for selective attachment of glucose molecules. 50mM sodium acetate buffer was prepared from 3mM stock solution at pH 5.1. Then 2mg glucose oxidase (GOX) powder obtained from Sigma-Aldrich was mixed in 10ml of sodium acetate buffer with light stirring. The mixture turns pale yellow after 10 minutes and the PS samples were incubated in GOX solution for 48 hours at 4^{o}C. Afterwards the sensors were washed in 9% Polysorbate-20 or Tween20 solution under mild vibration to remove loosely attached GOX molecules. Finally, the sensors were washed in DI water and stored at 4^{o}C.

2.6. Glucose Sensing

Glucose sensing performance of the 4 PS samples (Nano_5min, Nano_10min, Nano_20min and Macro) was observed in reflection mode with LED-LDR arrangement which measured change in reflectance of the PS sensors with glucose introduction [23].

White LED has been used as an optical source and a collimator arrangement produces a spot of ~15mm diameter on PS surface. The reflected spot is again passed through a collimator and photoresistor or LDR produces voltage level corresponding to reflection intensity. Schematic diagram of the system is depicted in figure 2.11. Glucose

solution of different concentration is sprayed on the surface functionalized PS samples and corresponding percentage response was calculated with the following formula.

$$\% \text{ Response} = \left| {}^{(R_f - R_0)}\!/_{R_0} \right| \times 100\ \%$$

Where, R_0 = Baseline reflectance

R_f = Reflectance after analyte introduction

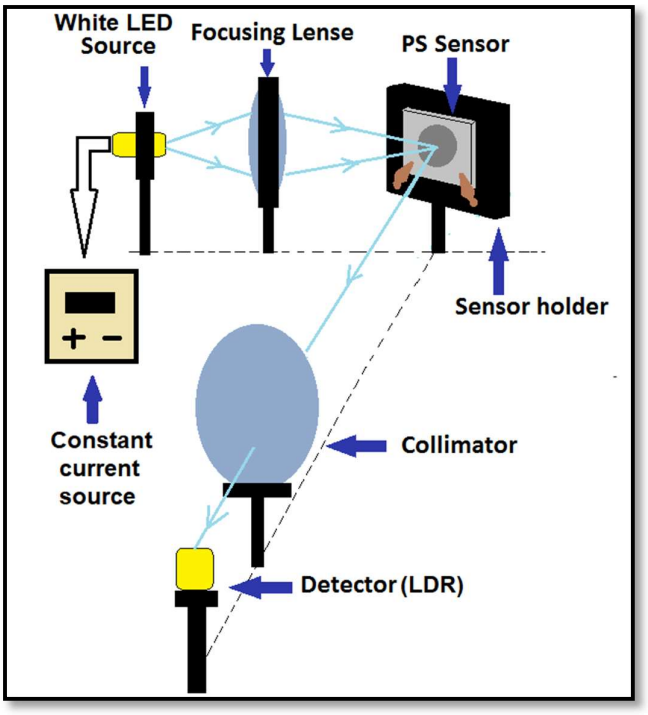

Figure 2.11. Schematic diagram of single parametric measurement setup

The response plot in figure 2.12 shows comparison of %Response among 4 types of PS sensors for 5mM and 15mM glucose concentrations. It is clearly visible that with increasing thickness of nano PS samples, % Response falls significantly. This may be due to the morphological change of PS surface with increase in etching time discussed in section 2.4.1. Macro PS sensors show significant change in reflectance which is almost in comparable range with Nano_5min samples and for higher glucose concentration (15mM), it exceeds nano PS response value. To estimate the reliability of the obtained output, repeated measurements on identical samples prepared under same conditions were performed for both Nano_5min and Macro PS sensors.

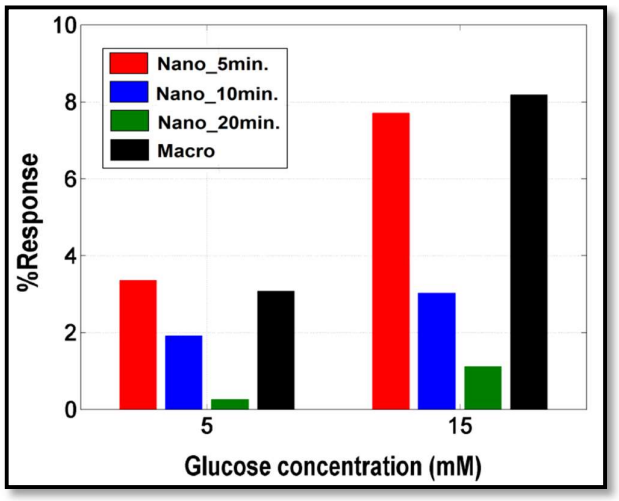

Figure 2.12. Comparison of %Response for different PS sensors

Deviation in response for each measurement was also observed from mean value of response for each sample (figure 2.13). While Nano_5min samples show only ~5.3% deviation from mean value (SD = 0.1422), Macro samples produce as large as 1.7740 SD corresponding to ~72% deviation in mean value of response.

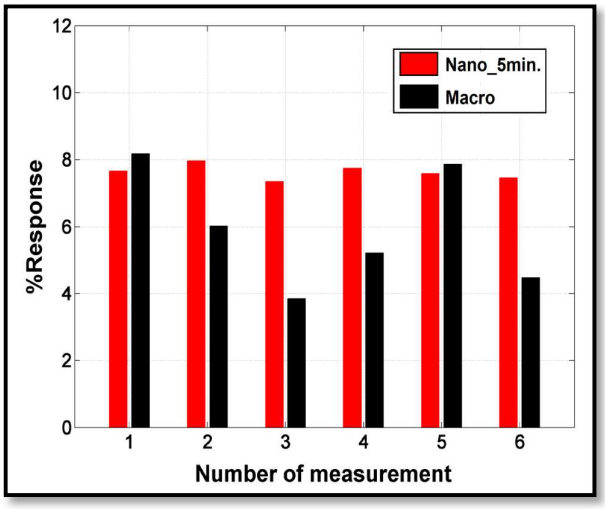

Figure 2.13. Response Reliability test for 15mM Glucose concentration

Physisorption process of GOX attachment on PS surface may be responsible for such huge response fluctuation in Macro PS samples. Nano PS pore size is comparable with GOX molecule size thus restricting unwanted GOX removal in intermediate Tween20 wash or DI water wash process. Macro samples have huge pores in them (in micrometer range) which are not suitable for trapping GOX molecules inside the structure thus response deviates significantly for repeated measurements.

To estimate the settling time of sensor output, time response of both nano_5min and macro samples was compared for 15mM glucose solution. Baseline reading was recorded and after glucose solution spray, data is monitored after every 30 second interval for the next 20 minutes. Initial spike in output voltage after glucose solution spray (figure 2.14) is due to the sharp rise in reflectance intensity as a result of the lensing effect of water present on sensor surface. Settling time of nano_5min sample was found to be ~90 seconds while for macro PS, it was almost 210 seconds. Even after settling time, the output voltage for macro PS was found very much fluctuating in nature. A large amount of error ($\pm$ 4.6% deviation from mean value) was observed for macro PS sensors which can severely affect reliability of the calibration curve. Thus, macro PS samples were found to be nonsuitable for fast response.

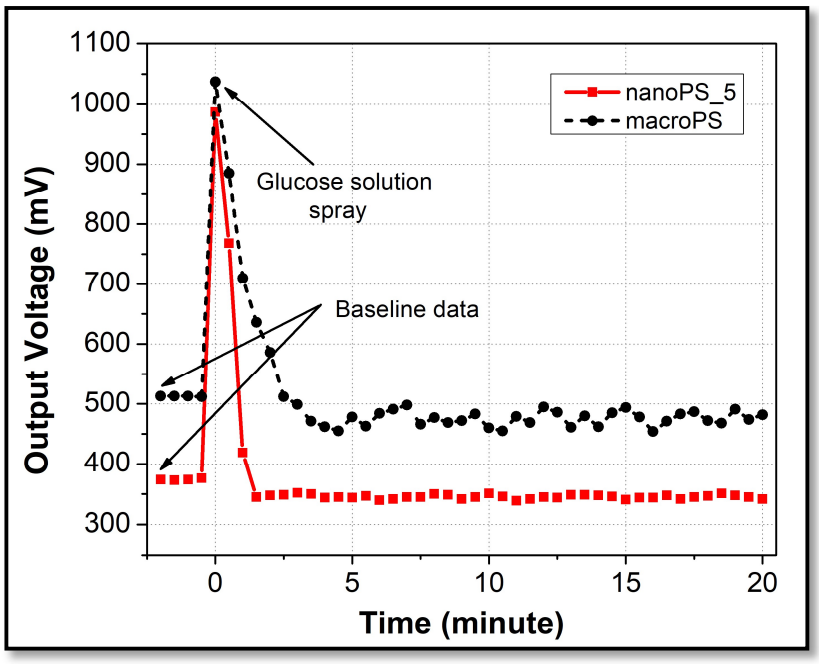

Figure 2.14. Settling time comparison of PS sensors

2.7. Conclusion

In this chapter, PS properties and formation mechanism were discussed first. Then two types of PS i.e. nano and macro PS was prepared using electrochemical etching procedure in single pond cell configuration. The PS samples were characterized by FESEM, AFM and XRD.

It was found that for nano PS, less than 5 minute etching time produced non uniform film on Si wafer. It was observed from FESEM micrographs that with increasing etching time, agglomeration or cluster formation of nanoparticles occurs on nano PS surface. For 20 minutes etching time fish scale like structures were observed which gets detached easily from the surface during surface modification steps. AFM study showed that, with increase in etching time r.m.s. value of surface roughness increases for nano PS samples which also proves the presence of nanoparticle clusters. Macro PS samples on the other hand showed well defined pores of the order of ~1.5µm which was not observed in nano PS samples. In XRD analysis, peak at $2\theta \sim 69^{o}$ was observed for the PS samples which is standard for p type silicon wafer with <100> orientation. Also, D-spacing was found to be 0.14nm which was calculated from the peak position.

Nano PS layers prepared for 5 minute etching time were found to have ~1µm film thickness and they produced maximum response among the three nano samples for glucose sensing application. Macro PS samples also produced significantly large response but their reproducibility was found to be very poor. As physisorption process of enzyme attachment favours structure that are comparable to enzyme dimension, nano PS samples with pore size of ~20nm attach enzymes way better than macro samples with pore dimension of a few micron. Also, settling time of macro PS output was found very much large compared to nano PS sample and transient response showed severe fluctuation even at steady state. So nano PS prepared for five minutes etching time was found to be the perfect choice for glucose sensors.

References

[1] Arthur Uhlir Jr and Ingeborg Uhlir. "Historical perspective on the discovery of porous silicon." Physica Status Solidi C Current Topics 2, no. 9 (2005): 3185-3187. DOI: 10.1002/pssc.200461100

[2] Leigh T. Canham. "Silicon quantum wire array fabrication by electrochemical and chemical dissolution of wafers." Applied physics letters 57, no. 10 (1990): 1046-1048. https://doi.org/10.1063/1.103561

[3] X. G. Zhang. "Morphology and formation mechanisms of porous silicon." Journal of the Electrochemical Society 151, no. 1 (2003): C69. https://doi.org/10.1149/1.1632477

[4] Z. Gaburro, N. Daldossoh and L. Pavesi. "Porous Silicon", Encyclopedia of Condensed Matter Physics, Elsevier, 2005, Pages 391-401, https://doi.org/10.1016/B0-12-369401-9/01149-9.

[5] Suet P. Low, Nicolas H. Voelcker, Leigh T. Canham and Keryn A. Williams. "The biocompatibility of porous silicon in tissues of the eye." Biomaterials 30, no. 15 (2009): 2873-2880. https://doi.org/10.1016/j.biomaterials.2009.02.008

[6] Saakshi Dhanekar and Swati Jain. "Porous silicon biosensor: Current status." Biosensors and bioelectronics 41 (2013): 54-64. https://doi.org/10.1016/j.bios.2012.09.045

[7] Farid A. Harraz. "Porous silicon chemical sensors and biosensors: A review." Sensors and Actuators B: Chemical 202 (2014): 897-912. https://doi.org/10.1016/j.snb.2014.06.048

[8] Jeffery L. Coffer, Melanie A. Whitehead, Dattatri K. Nagesha, Priyabrata Mukherjee, Giridhar Akkaraju, Mihaela Totolici, Roghieh S. Saffie, and Leigh T. Canham. "Porous silicon-based scaffolds for tissue engineering and other biomedical applications." physica status solidi (a) 202, no. 8 (2005): 1451-1455. https://doi.org/10.1002/pssa.200461134

[9] Wei Sun, J. Edward Puzas, Tzong-Jen Sheu, and Philippe M. Fauchet. "Porous silicon as a cell interface for bone tissue engineering." physica status solidi (a) 204, no. 5 (2007): 1429-1433. https://doi.org/10.1002/pssa.200674377

[10] Tushar Kumeria, Steven JP McInnes, Shaheer Maher, and Abel Santos. "Porous silicon for drug delivery applications and theranostics: recent advances, critical review and perspectives." Expert Opinion on Drug Delivery 14, no. 12 (2017): 1407-1422. https://doi.org/10.1080/17425247.2017.1317245

[11] Valentyna M. Starodub, Leonid L. Fedorenko, Andriy P. Sisetskiy, and Nickolaj F. Starodub. "Control of myoglobin level in a solution by an immune sensor based on the photoluminescence of porous silicon." Sensors and Actuators B: Chemical 58, no. 1-3 (1999): 409-414. https://doi.org/10.1016/S0925-4005(99)00104-5

[12] Michael T. Kelly, and Andrew B. Bocarsly. "Mechanisms of photoluminescent quenching of oxidized porous silicon applications to chemical sensing." Coordination chemistry reviews 171 (1998): 251-259. https://doi.org/10.1016/S0010-8545(98)90039-X

[13] Stéphane Content, William C. Trogler, and Michael J. Sailor. "Detection of nitrobenzene, DNT, and TNT vapors by quenching of porous silicon photoluminescence." Chemistry–A European Journal 6, no. 12 (2000): 2205-2213. https://doi.org/10.1002/1521-3765(20000616)6:12<2205::AID-CHEM2205>3.0.CO;2-A

[14] Keiki-Pua S. Dancil, Douglas P. Greiner, and Michael J. Sailor. "A porous silicon optical biosensor: detection of reversible binding of IgG to a protein A-modified surface." Journal of the American Chemical Society 121, no. 34 (1999): 7925-7930. https://doi.org/10.1021/ja991421n

[15] Hongyan Zhang, Jie Lv, and Zhenhong Jia. "Detection of ammonia-oxidizing bacteria (AOB) using a porous silicon optical biosensor based on a multilayered double Bragg mirror structure." Sensors 18, no. 1 (2018): 105. https://doi.org/10.3390/s18010105

[16] Hong Qiao, Bin Guan, J. Justin Gooding, and Peter J. Reece. "Protease detection using a porous silicon based Bloch surface wave optical biosensor." Optics express 18, no. 14 (2010): 15174-15182. https://doi.org/10.1364/OE.18.015174

[17] Fransiska SH Krismastuti, Stephanie Pace, and Nicolas H. Voelcker. "Porous silicon resonant microcavity biosensor for matrix metalloproteinase detection." Advanced functional materials 24, no. 23 (2014): 3639-3650. https://doi.org/10.1002/adfm.201304053

[18] Lisa M. Bonanno, and Lisa A. DeLouise. "Whole blood optical biosensor." Biosensors and Bioelectronics 23, no. 3 (2007): 444-448. https://doi.org/10.1016/j.bios.2007.05.008

[19] Hongyan Zhang, Zhenhong Jia, Xiaoyi Lv, Jun Zhou, Liangliang Chen, Rongxia Liu, and Ji Ma. "Porous silicon optical microcavity biosensor on silicon-on-insulator wafer for sensitive DNA detection." Biosensors and Bioelectronics 44 (2013): 89-94. https://doi.org/10.1016/j.bios.2013.01.012

[20] Luca De Stefano, Mauro Rossi, Maria Staiano, Gianfranco Mamone, Antonoietta Parracino, Lucia Rotiroti, Ivo Rendina, Mosè Rossi, and Sabato D'Auria. "Glutamine-Binding Protein from Escherichia c oli Specifically Binds a Wheat Gliadin Peptide Allowing the Design of a New Porous Silicon-Based Optical Biosensor." Journal of proteome research 5, no. 5 (2006): 1241-1245. https://doi.org/10.1021/pr0600226

[21] Nalin H. Maniya, and Divesh N. Srivastava. "Fabrication of porous silicon based label-free optical biosensor for heat shock protein 70 detection." Materials Science in Semiconductor Processing 115 (2020): 105126. https://doi.org/10.1016/j.mssp.2020.105126

[22] Yanyu Li, Zhenhong Jia, Guodong Lv, Hao Wen, Peng Li, Hongyan Zhang, and Jiajia Wang. "Detection of Echinococcus granulosus antigen by a quantum dot/porous silicon optical biosensor." Biomedical optics express 8, no. 7 (2017): 3458-3469. https://doi.org/10.1364/BOE.8.003458

[23] Deeparati Basu, Tanusree Sarkar, Kaustav Sen, Syed Minhaz Hossain, and Jayoti Das. "Multi-Parametric optical glucose sensor based on surface functionalized nano-porous silicon." IEEE Sensors Journal 18, no. 24 (2018): 9940-9947. DOI: 10.1109/JSEN.2018.2872846

[24] L. T. Canham "Tunable Properties of Porous Silicon. In: Canham L. (eds) Handbook of Porous Silicon. Springer. (2014) https://doi.org/10.1007/978-3-319-04508-5_19-1

[25] Olmes Bisi, Stefano Ossicini, and Lorenzo Pavesi. "Porous silicon: a quantum sponge structure for silicon based optoelectronics." Surface science reports 38, no. 1-3 (2000): 1-126. https://doi.org/10.1016/S0167-5729(99)00012-6Get rights and content

[26] Michael Tiemann. "Porous metal oxides as gas sensors." Chemistry–A European Journal 13, no. 30 (2007): 8376-8388. https://doi.org/10.1002/chem.200700927

[27] Suet P. Low, and Nicolas H. Voelcker. "Biocompatibility of porous silicon." In Handbook of porous silicon, pp. 381-393. Springer, 2014.

[28] A. G. Cullis, and L. T. Canham. "Visible light emission due to quantum size effects in highly porous crystalline silicon." Nature 353, no. 6342 (1991): 335-338. https://doi.org/10.1038/353335a0

[29] V. Lehmann, and Ulrich Gösele. "Porous silicon formation: A quantum wire effect." Applied Physics Letters 58, no. 8 (1991): 856-858. https://doi.org/10.1063/1.104512

[30] S. M. Prokes, O. J. Glembocki, V. M. Bermudez, R. Kaplan, L. E. Friedersdorf, and P. C. Searson. "SiH x excitation: An alternate mechanism for porous Si photoluminescence." Physical Review B 45, no. 23 (1992): 13788. https://doi.org/10.1103/PhysRevB.45.13788

[31] M. S. Brandt, H. D. Fuchs, M. Stutzmann, J. Weber, and M. Cardona. "The origin of visible luminescencefrom "porous silicon": A new interpretation." Solid State Communications 81, no. 4 (1992): 307-312. https://doi.org/10.1016/0038-1098(92)90815-Q

[32] Hiroyuki Mizuno, Hideki Koyama, and Nobuyoshi Koshida. "Oxide-free blue photoluminescence from photochemically etched porous silicon." Applied physics letters 69, no. 25 (1996): 3779-3781. https://doi.org/10.1063/1.116996

[33] L. Tsybeskov, Ju V. Vandyshev, and P. M. Fauchet. "Blue emission in porous silicon: Oxygen-related photoluminescence." Physical Review B 49, no. 11 (1994): 7821. https://doi.org/10.1103/PhysRevB.49.7821

[34] D. T. Jiang, I. Coulthard, T. K. Sham, J. W. Lorimer, S. P. Frigo, X. H. Feng, and R. A. Rosenberg. "Observations on the surface and bulk luminescence of porous silicon." Journal of applied physics 74, no. 10 (1993): 6335-6340. https://doi.org/10.1063/1.355156

[35] P. M. Fauchet, E. Ettedgui, A. Raisanen, L. J. Brillson, F. Seiferth, S. K. Kurinec, Y. Gao, C. Peng, and L. Tsybeskov. "Can Oxidation and Other Treatments Help Us Understand the Nature of Light-Emitting Porous Silicon?." MRS Online Proceedings Library (OPL) 298 (1993). https://doi.org/10.1557/PROC-298-271

[36] Toshimichi OHTA, Osamu ARAKAKI, Toshimichi ITO, and Akio HIRAKI. "Microcrystalline Silicon in Oxide Matrix Prepared from Partial Oxidation of Anodized Porous Silicon." IEICE TRANSACTIONS on Electronics 75, no. 9 (1992): 1025-1030.

[37] Nobuyoshi Koshida, and Hideki Koyama. "Visible electroluminescence from porous silicon." Applied physics letters 60, no. 3 (1992): 347-349. https://doi.org/10.1063/1.106652

[38] A. Loni, A. J. Simons, T. I. Cox, P. D. J. Calcott, and I. T. Canham. "Electroluminescent porous silicon device with an external quantum efficiency greater than 0.1% under CW operation." Electronics Letters 31, no. 15 (1995): 1288-1289.

[39] Farshid Karbassian. "Porous Silicon" In Porosity: Process, Technologies and Applications, edited by Taher Ghrib. London: IntechOpen, 2018. 10.5772/intechopen.72910

[40] W. Lang, P. Steiner, and H. Sandmaier. "Porous silicon: a novel material for microsystems." Sensors and Actuators A: Physical 51, no. 1 (1995): 31-36. https://doi.org/10.1016/0924-4247(95)01066-1

[41] E. Xifré-Pérez, J. Ferré-Borrull, J. Pallarés, L.F. Marsal. “Methods, Properties and Applications of Porous Silicon”. In: Losic, D., Santos, A. (eds) Electrochemically Engineered Nanoporous Materials. Springer Series in Materials Science, vol 220. Springer, Cham. (2015). https://doi.org/10.1007/978-3-319-20346-1_2

[42] E. C. Muñoz, C. A. Heyser, R. S. Schrebler, R. G. Henriquez, and R. E. Marotti. "Photoelectrochemical reduction of nitrate ions on porous silicon and different silicon modified electrodes." Journal of the Chilean Chemical Society 56, no. 3 (2011): 781-785. http://dx.doi.org/10.4067/S0717-97072011000300014

[43] Pushpendra Kumar, and Patrick Huber. "Effect of etching parameter on pore size and porosity of electrochemically formed nanoporous silicon." Journal of Nanomaterials 2007 (2007). https://doi.org/10.1155/2007/89718

[44] W. S. Yan, D. Y. Wei, S. Xu, and H. P. Zhou. "Highly doped p-type nanocrystalline silicon thin films fabricated by low-frequency inductively coupled plasma without H 2 dilution." Journal of Applied Physics 110, no. 6 (2011): 063302. https://doi.org/10.1063/1.3642983

Chapter 3

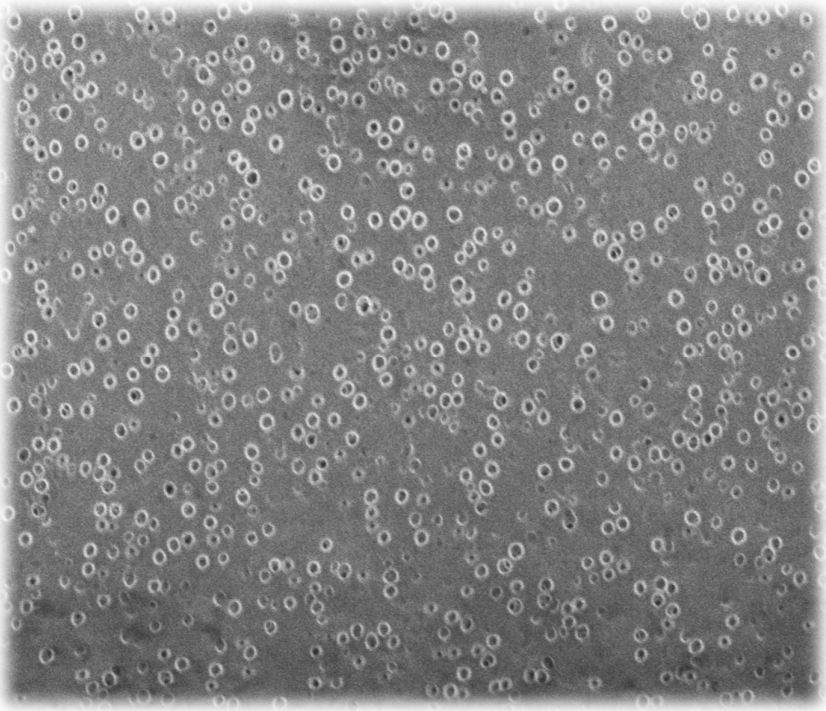

Chapter 3

Chitosan Silica Nanocomposite as Biosensing Material

3.1. Introduction

Nanocomposite materials are made of two or more constituent phases among which at least one has one, two or three dimensions in nanometer range. As they are heterogeneous materials, their properties are governed by the structure, composition and properties of the constituent materials and interfacial interactions between them [1]. There are several types of nanocomposites like metal matrix [2], polymer matrix [3], ceramic matrix [4] etc. Among them polymer matrix nanocomposites (PMNC) are used extensively in

biomedical applications like drug delivery, tissue engineering and biosensor [5-9]. PMNC structures have different types of nanoparticle fillers dispersed in natural or synthetic polymer matrix. PMNC are used due to low cost, biocompatibility and diversity in physiochemical properties. Moreover, the physical and chemical properties of PMNC can be modified easily which enables selective attachment of active biomolecules for biosensing application.

In this chapter, first two sections contain physiochemical properties and preparation procedures of Silica nanoparticle fillers and Chitosan polymer matrix. Next, Chitosan-Silica Nanocomposite (CSNC) porous membrane and thin film preparation, characterization and optimization for biosensing application have been studied. The work done in this chapter has been published in [10].

3.2. Silica Nanoparticle

Silica or silicon dioxide is the most abundant material found in earth's crust and they are found both in amorphous and crystalline form. Silica nanoparticles (SiNp) are nanospheres of silica ranging from 10-1000nm in diameter. In this section, structure, properties and preparation of SiNp are described.

3.2.1. Chemical Structure

Silicon dioxide atoms form a network like structure through covalent bonding. SiNp contains a large number of Si-O-Si bridges or siloxane groups inside the spherical structure and the outer surface is mostly terminated by silanol groups (Si-OH). Si-O-Si bond angle can vary from 136^{o}-180^{o} whereas bond lengths can vary from 1.55-1.65Å [11]. A typical schematic structure of SiNp is demonstrated in figure 3.1.

3.2.2. Physiochemical Properties

SiNps are amorphous materials and appear in the form of white powder after drying. They can be both nonporous (S-type) and mesoporous (P-type) depending on the preparation procedure [12]. S-type SiNps have high water absorption capability and they are abrasive [13]. Due to their enhanced mechanical stability, they are used as fillers in polymer

or ceramic matrix composite for strengthening [14, 15]. On the other hand, P-type SiNps are mainly used for drug delivery system and nanomedicine due to their biocompatibility, biodegradable and low-toxic nature [16, 17]. In general, SiNps can have a wide range of size and their surface can be modified easily for a variety of applications. SiNps are thermal and electrical insulators and their physical properties are listed in table I.

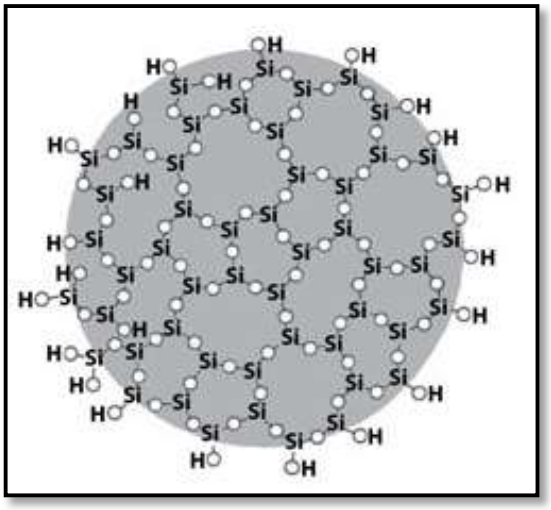

Figure 3.1. Schematic internal and surface structure of SiNp (Image taken from [18])

Table I: Physical properties of SiNp

Density	2.4 gm/cm^3
Molar mass	59.96 gm/mol
Melting Point	1600 ^oC
Boiling point	2230 ^oC
Refractive index	1.43

3.2.3. Stober's Method of Preparation

Stober's method [19] is a standard process for colloidal solution of monodispersed SiNp preparation. This bottom up sol-gel technique consists of first hydrolysis followed by condensation reaction. Chemicals required for the process are (i) Tetraethyl Orthosilicate (TEOS), (ii) Ethanol, (iii) Ammonium Hydroxide (NH_4OH) and (iv) DI water. First desired amount of Ethanol and DI water is mixed and stirred under room temperature for 5-10 minutes. Then TEOS and NH_4OH are added drop wise to the solution and stirred for further

2 hours. In hydrolysis reaction between TEOS and water molecules, NH_4OH acts as catalyst and immediately after hydrolysis, condensation reaction takes place forming a large number of Si-O-Si bridge structures. As SiNp starts to form, the clear suspension slowly turns opaque and after some time a milky white colloidal solution of SiNp is formed. The colloidal solution was centrifuged at 6000 r.p.m. and the precipitate was redispersed in ethanol solution. The procedure was repeated for 3 times to remove unreacted TEOS. Finally, the precipitate was dried at 50^oC overnight and grinded in mortar pestle to obtain fine SiNp dust.

Three different sizes of SiNp were prepared named as NP1, NP2 and NP3. Also, Optimization of chemical concentrations for different SiNp size is listed in table II.

TABLE II: Optimized values of SiNp preparation parameters

SiNp size	Ethanol	Water	TEOS	NH_4OH	Centrifugation time
NP1∼ (100nm)	75ml	10ml	1ml	3ml	1 hrs 30 min.
NP2∼ (300nm)	30ml	4ml	2.4ml	1.2ml	50 min.
NP3∼ (500nm)	30ml	4ml	4ml	2ml	20 min.

Formation mechanism of SiNp is depicted in figure 3.2. First the ethoxy groups of TEOS are partially or fully replaced by hydroxyl groups and in this hydrolysis reaction NH_4OH acts as catalyst to produce hydrolysed precursors. Next condensation takes place and water molecules are removed from the precursors producing Si-O-Si bridge structures. In supersaturated solution nuclei or primary particles are formed during initial induction period and after this period further generation of precursors contribute to the growth of primary particles which leads to stable nanoparticle formation. Higher concentration of TEOS and NH_4OH leads to larger particle size because such condition shortens initial induction period. So, less number of primary particles or seeds is formed and further generation of precursor increases particle size [20].

Diameter of NP1 was maintained $\geq$ 100nm because it was observed that < 100nm SiNp requires almost 3 hours of centrifugation time and the final product becomes a soft gel like structure instead of fine nanoparticle dust. This is due to the high level of coagulation in smaller nanoparticles and in such condition SiNp powder preparation becomes impossible. Also, it is seen in table II that (ethanol+water): TEOS ratio for NP1 is almost six times larger

compared to NP2. This is because, in the induction phase when primary seeds are formed inter seed distance needs to be sufficiently large to prevent coagulation at the time of particle growth. Also, high concentration of NH_4OH makes induction period short which ensures less number of primary seeds [20] and consequently less number of nanoparticles are formed in final colloidal solution. So, effect of coagulation or agglomeration remains insignificant.

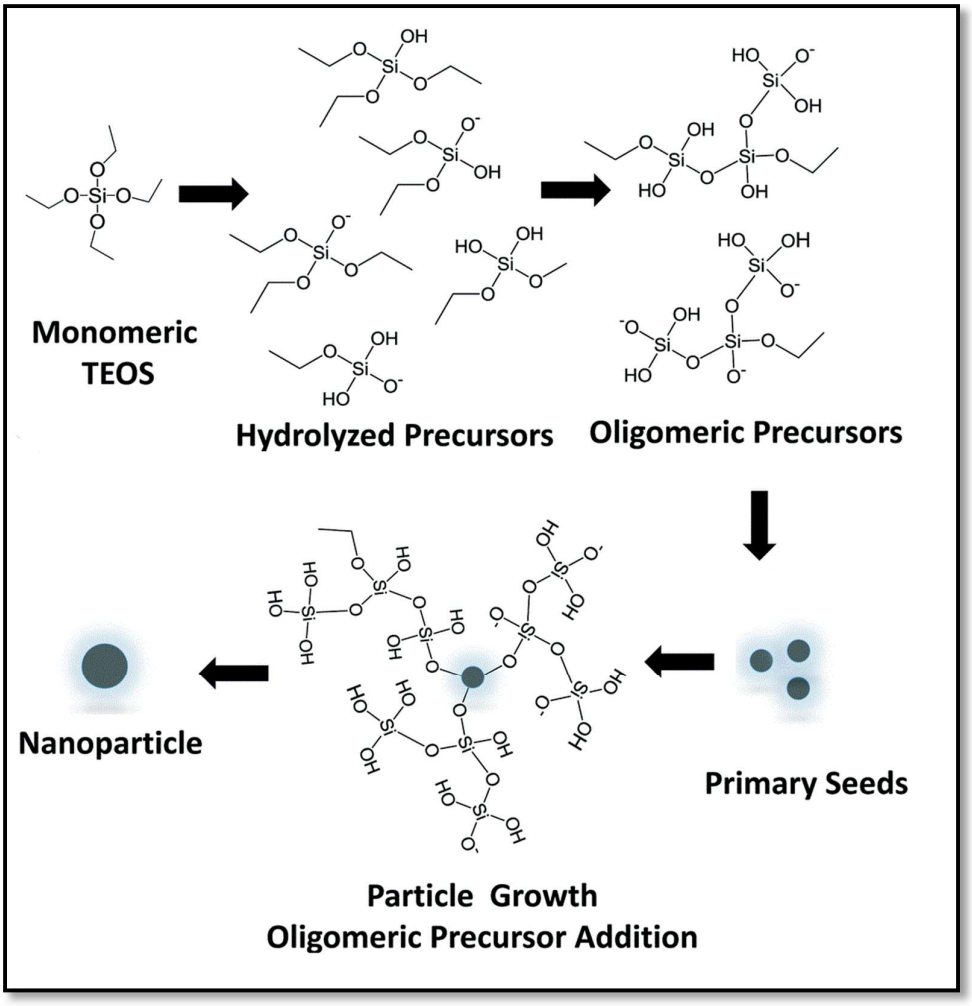

Figure 3.2. Schematic diagram depicting SiNp formation mechanism (Image taken from [21])

The colloidal solution was drop casted on clear cover slips immediately after preparation and left overnight for room temperature drying. The samples were gold coated prior to FESEM analysis. FESEM images in figure 3.3 show that particle diameter of NP1, NP2 and NP3 are in the range of 125-132nm, 263-288nm and 511-529nm respectively. As TEOS concentration in the solution was kept very low for NP1, density of nanoparticles is also low

as shown in figure 3.3(b), compared to NP2 and NP3. It was also observed that for much higher TEOS and NH_4OH concentration aggregates form, instead of monodispersed colloidal solution as reported by Bogush et al. [22], which is clearly visible in figure 3.3(a).

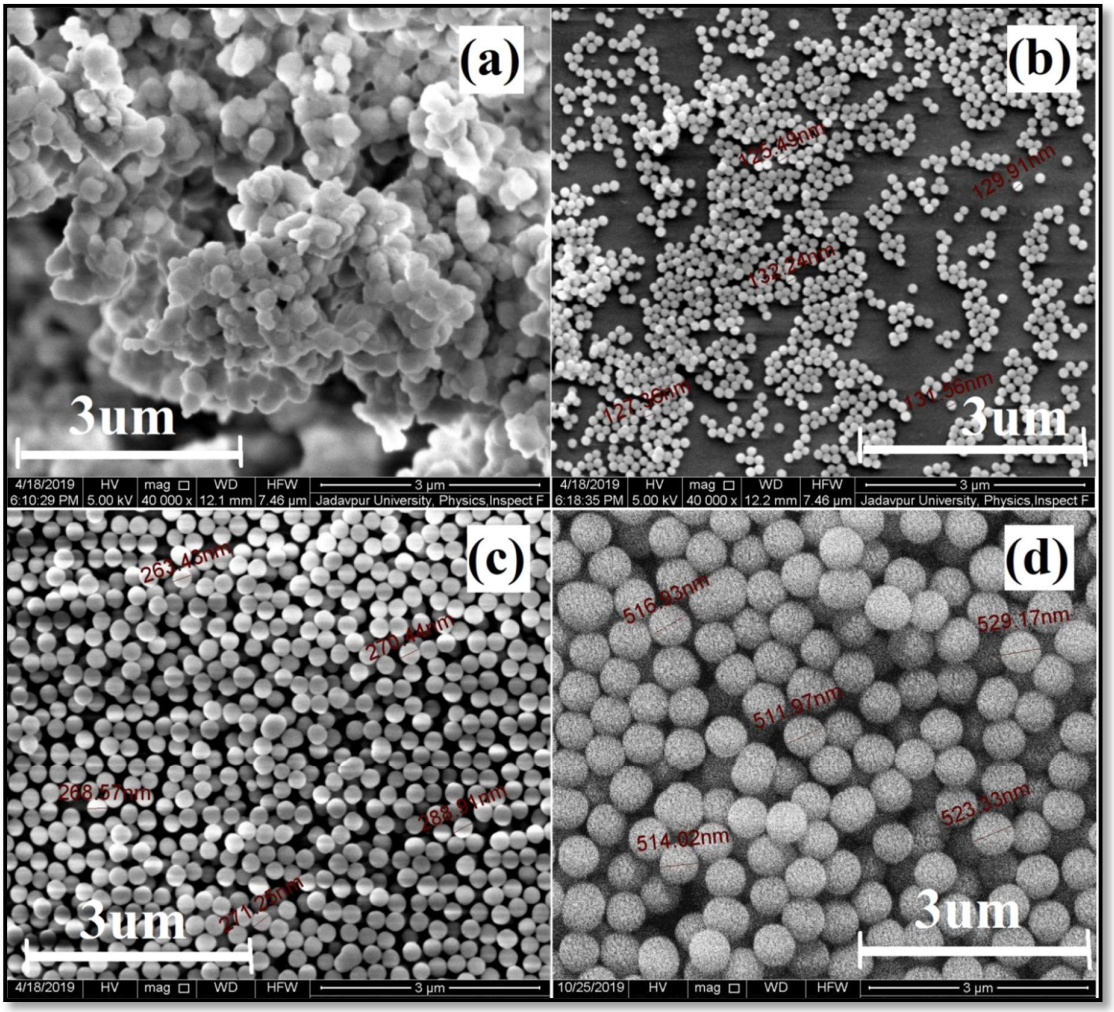

Figure 3.3. FESEM micrographs of (a) aggregate formation for higher concentration of TEOS [Ethanol: 30ml, water: 4ml, TEOS: >7ml], (b) NP1, (c) NP2 and (d) NP3

3.3. Chitosan

Chitosan is a semi-synthetic polymer obtained from deacetylation of chitin which is found abundantly in the exoskeletons of crabs, shrimps, lobsters etc. and cell walls of fungi. Due to its unique properties chitosan is vastly used in agricultural [23], biomedical [24] and commercial fields [25]. In this section, chitosan structure, properties and preparation are described.

3.3.1. Chemical Structure

Chitosan is linear polysaccharide containing randomly distributed deacetylated monomer D-glucosamine and acetylated monomer N-acetyl-D-glucosamine connected via β-1→4 glycosidic bonds [26]. Presence of acetyl groups (CH3-CO-) in the structure is due to partial deacetylation process of chitin and depends on the degree of deacetylation. A typical chitosan polymeric chain is shown is figure 3.4 [26].

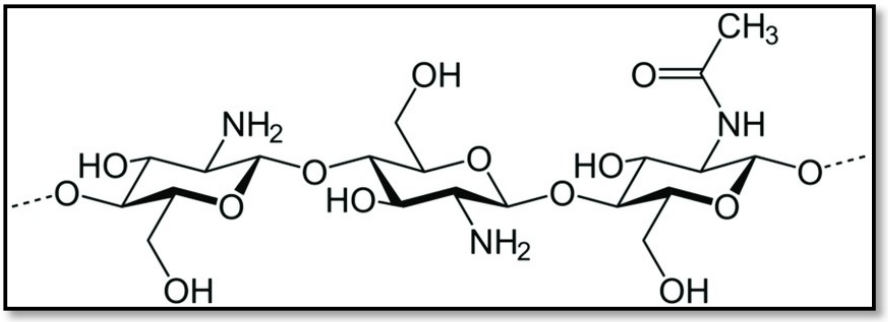

Figure 3.4. Structure of chitosan polymer (Image taken from [26])

3.3.2. Physiochemical Properties

Chitosan is off white powder which upon dissolution in acidic solution produces clear suspension. Physiochemical properties of chitosan depend greatly on degree of deacetylation and molecular weight. Protonation of the amino groups in chitosan makes it cationic in nature and it is the only positively charged natural polysaccharide [27]. Due to the unique biological properties of chitosan, they are used extensively in biomedical applications. They are biocompatible, biodegradable and non-toxic material with antibacterial, antifungal and wound healing properties [28-32]. Chitosan has good film forming capability which makes it suitable for thin film biosensor application. Some basic properties of chitosan are listed in Table III.

Table III: Properties of Chitosan (high to medium molecular weight)

Density (bulk)	0.2-0.38 gm/mL
Molecular weight	310000-375000 Da
Melting Point	~290^{o}C
Solubility	H_2O/organic solvents: Insoluble
PKa	~ 6.5

3.3.3. Preparation

In deacetylation process acetyl groups of the chitins are removed by hydrolysis reaction in 40-50% NaOH or KOH solution above 100^{o}C. The reaction process is depicted in figure 3.5 [33]. In this work, chitosan powder was directly purchased from Acros Organics.

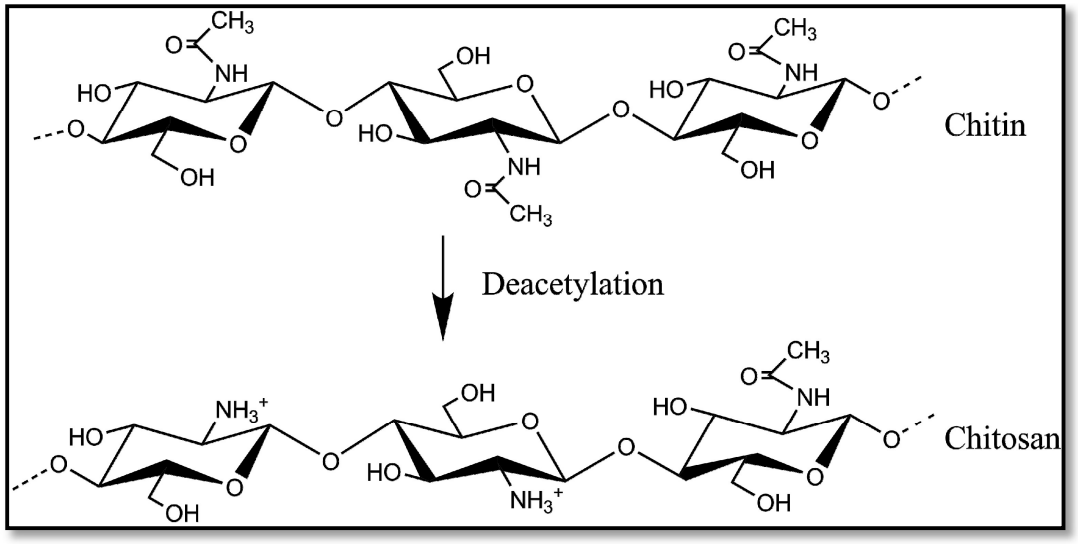

Figure 3.5. Deacetylation reaction of Chitin (Image taken from [33])

3.4. Chitosan-Silica Nanocomposite

Like any other nanocomposites [34], Chitosan-Silica nanocomposites (CSNC) have properties that are different from their constituent materials. In this section preparation and characterization of CSNC membranes and thin films have been discussed. Selective study of some important properties and optimization of preparation parameters have been performed for suitable application in biosensor.

3.4.1. Preparation

Chitosan solution was prepared by adding chitosan powder in 2% acetic acid solution. The solution was stirred until clear suspension obtained. Then previously prepared SiNp dust was added to this solution and stirred for further 30 minutes. The solution was ultrasonicated for 30 minutes to obtain monodispersed composite mixture. Just before drop casting, magnetic stirring was done for another 5 minutes. 40µl of solution was drop casted immediately on cleaned cover slips and left for drying for 24 hrs at room temperature. Next

5% NaOH solution was prepared and the cover slips containing composite thin films were dipped in the solution at 90°C. Composite films get detached from glass surface at temperature > 60°C and float in the NaOH solution as free standing membranes. After 40 minutes of heat treatment the membranes were carefully collected and washed in methanol 2 times, then dried at room temperature. For thin films on glass substrate, the membranes were washed in DI water instead of methanol and collected on the cleaned cover slips. The thin films were left for slow drying at room temperature for 48 hours which aids the attachment of the films on glass cover slips. Preparation steps of CSNC samples are depicted in figure 3.6.

Different amount of chitosan and SiNp (~300nm) dust were mixed to obtain composite membranes (M1-M5) listed in Table IV. Between these 5 types of composition variations, only M3 was found to have good freestanding membrane forming capability. So composition of M3 is used to produce freestanding membranes and thin films on glass substrate with different size of SiNps (NP1, NP2 & NP3) and named as CSN1, CSN2 and CSN3 respectively.

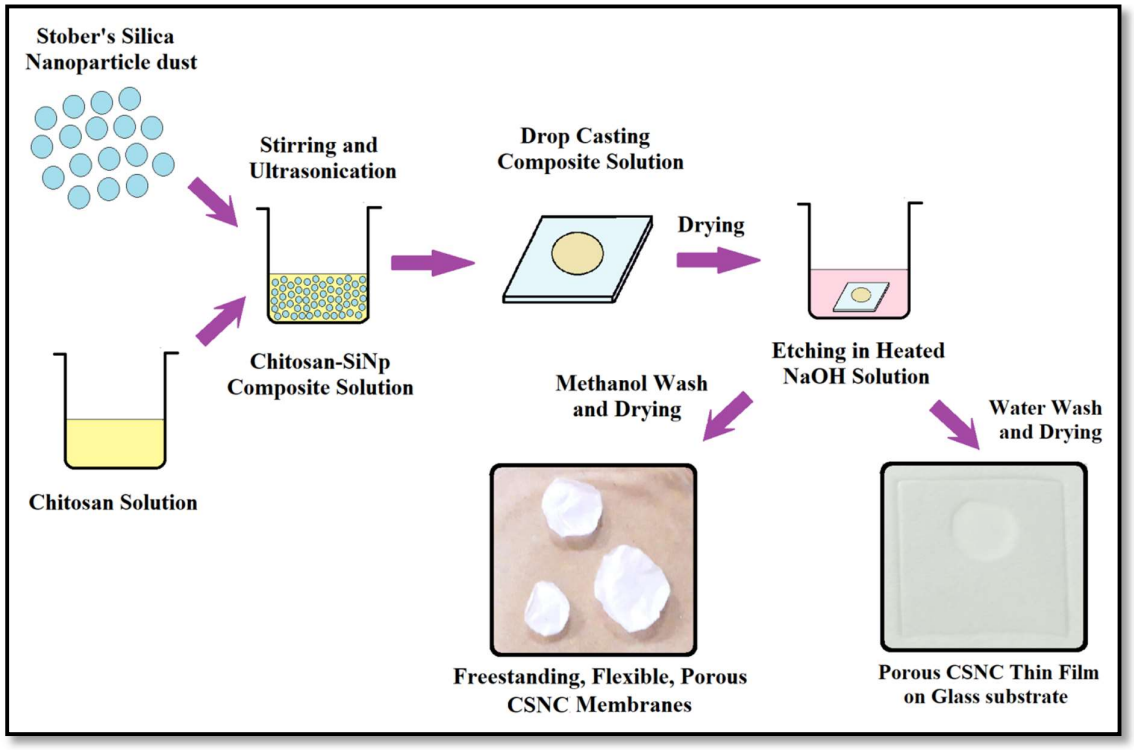

Figure 3.6. Preparation steps of CSNC

As stated earlier, it was found that membrane M3 was the best choice in respect of dimensional stability and handling convenience. M1 membranes were very fragile and most of them could not be collected after methanol drying. As chitosan and SiNp concentration ratio in M2 is 2:1, they show a tendency of curling and side bending at the time of drying as seen in most pure chitosan membranes. On the other hand, M4 membranes have chitosan and SiNp concentration ratio 1:2 and they show brittle nature after drying. In M5 membranes, maximum deformity and crack lines have been noticed after drying. M3, with chitosan and SiNp ratio 1:1, was found to have deformationless, free-standing capability and all of them could be collected easily after drying. 20µL, 40µL and 60µL of composite solution were used to produce M3 membranes shown in figure 3.7(c). Larger membranes may be produced for M3 samples according to the need for specific uses, but 40µL drops were used for this work as it is just adequate for all the experiments. The thickness of the drop casted thin films was measured to be around 4-5µm, varying a little with different pore size [10].

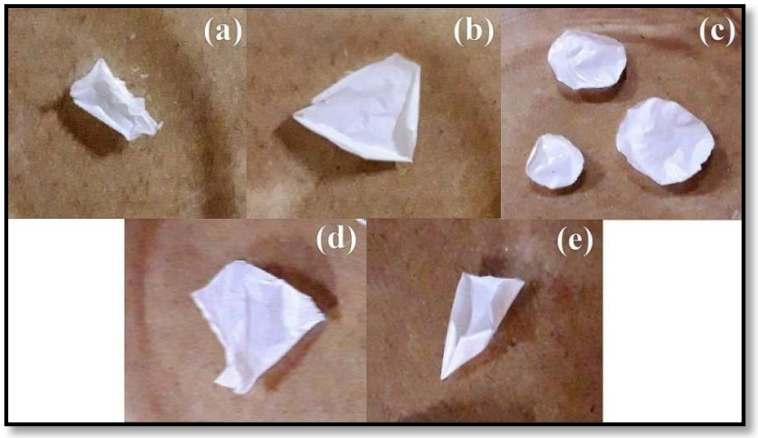

Figure 3.7. Images of (a) M1, (b) M2, (c)M3, (d) M4 and (e) M5

TABLE IV: CSNC membrane preparation compositions

Membrane no.	Solvent	Chitosan powder in mg	SiNp dust in mg (~300nm)
M1	10ml of 2% acetic acid solution	100	100
M2		200	100
M3		200	200
M4		100	200
M5		300	300

3.4.2. FESEM Analysis

FESEM images of the CSNC samples show that the pore sizes are a little smaller than the original nanoparticle size. These may be due to shrinkage of pores at the time of drying after SiNp removal [35]. Figure 3.8 show that CSN1 has pores in the range of 83-115nm where NP1 size was found to be 116-134nm. Similarly, CSN2 and CSN3 have pore size in the range of 139-179nm and 389-405nm respectively. With decreasing particle diameter, surface to volume ratio of the SiNp increases which allows increased interaction with neighbouring particles leading to agglomeration [36]. Thus, NP1 has higher tendency towards agglomeration compared to NP2 and NP3. Agglomeration in SiNps leads to clustered pore formation in CSN1 sample, visible in FESEM image (figure 3.8(a)). Large inter-filler distance is also observed in CSN1 sample as overall density of SiNp decreases due to agglomeration formation. In CSN3 sample, number of pores on top surface was significantly low which has been discussed later in section 3.4.4. This may be due to the fact that heavy NP3 particles settle down under composite solution at the time of drying. Sedimentation rate is proportional to particle diameter [37]. So NP3 particles have more inclination towards sedimentation leading to uneven distribution of nanoparticles, after complete drying. On the other hand, NP2 particles probably have low agglomeration and sedimentation effect, thus having best pore distribution of CSN2 among the three samples.

Etching time is an important parameter for porous CSNC preparation. Etching time was varied in the range of 5 minutes to 1 hour 30 minutes at 90°C in 5% NaOH solution. From FESEM image of 5 minutes etching (figure 3.9(a)), it can be observed that SiNps on the top surface has not dissolved at all and no pores has been formed yet. Images for 40 minute etching time has been shown previously in figure 3.8 and for up to 60 minutes etching, the pore size distribution improves. But after 60 minutes, uncontrolled erosion of the chitosan film starts deforming the evenly porous structure as shown in FESEM image in figure 3.9(b). Comparatively lower magnification has been taken to show the uncontrolled erosion all over the film. Deep craters even as large as 10-15 micron was observed on the top surface of the film. So the optimum time for etching was found to be between 30-50 minutes.

Also, concentration of NaOH solution has been varied from 2% to 10% (w/v) and etching was performed for 40 minutes. It was found that, with NaOH solution weight concentration higher than 7%, vigorous etching deforms the membrane with generation of

uncontrolled large sized pores in the range of micrometers. 2%-5% (w/v) NaOH solution was found to be optimum for etching.

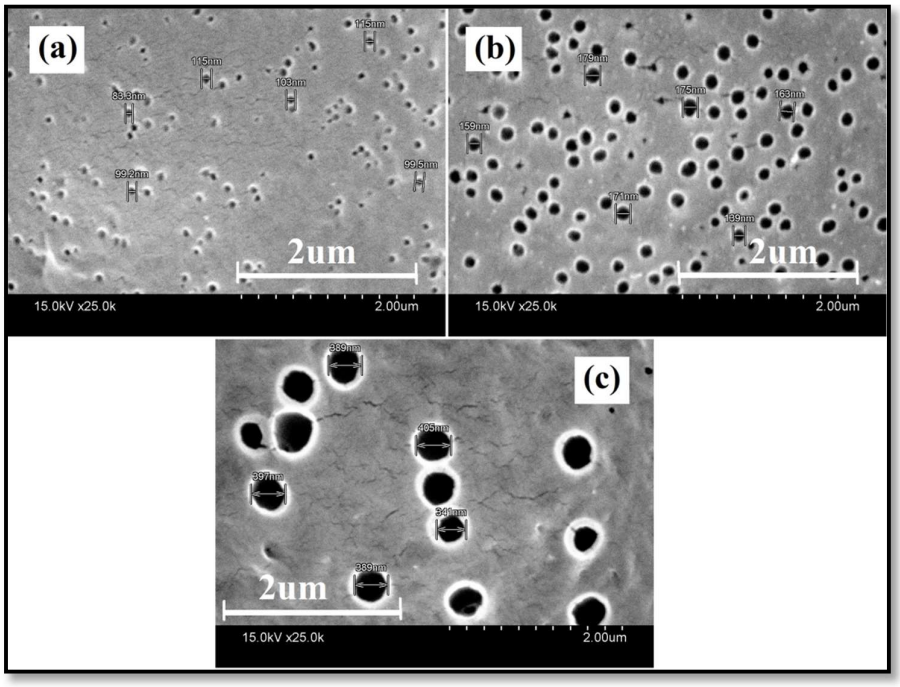

Figure 3.8. FESEM micrograph of (a) CSN1, (b) CSN2 and (c) CSN3 samples

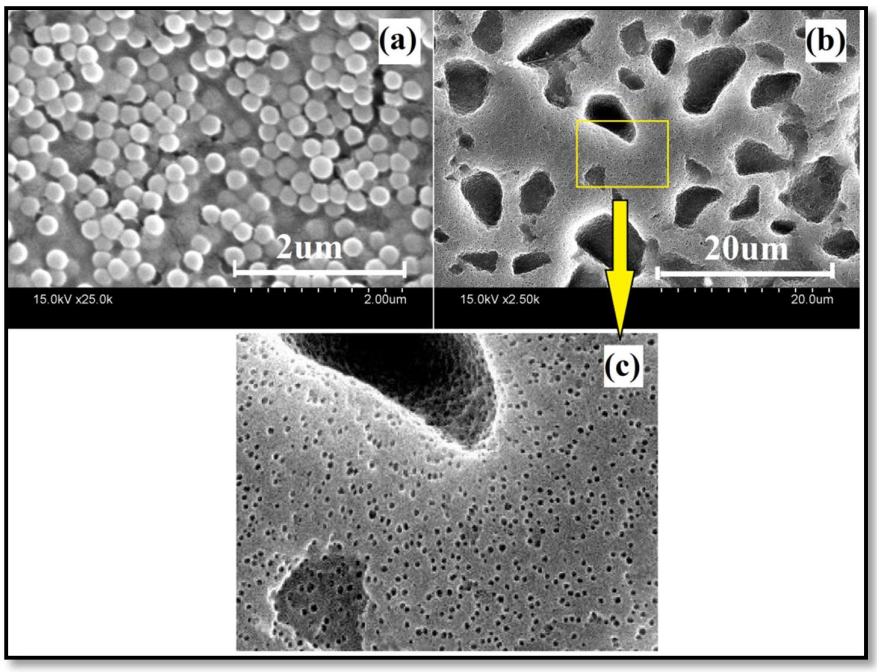

Figure 3.9. FESEM micrograph of CSN2 after (a) 5 minutes, (b) 1hour 30 minutes etching time, (c) magnified image of (b)

3.4.3. AFM Analysis

3D AFM images of CSN1, CSN2, CSN3 samples are shown in figure 3.10 and r.m.s. values of their surface roughness were found to be 76.4nm, 38.1nm and 53.4nm respectively. The scanning area was $8\times8\mu m^2$ for all the samples. In general, with increase in pore size, surface roughness increases [38]. But here it is observed that CSN1 has maximum roughness value. This may be due to the fact that with smaller particle size ≤100nm, agglomeration occurs which was found in FESEM image also. Sudden agglomeration spots may increase surface roughness abruptly.

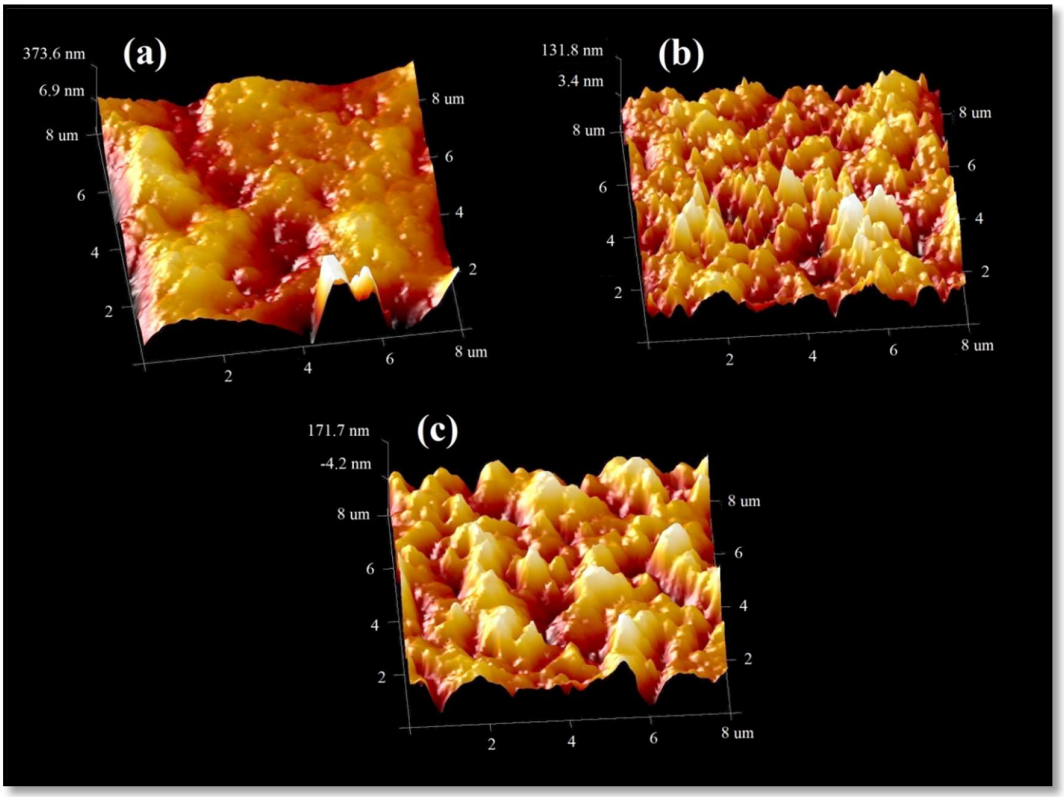

Figure 3.10. AFM image of (a) CSN1, (b) CSN2 and (c) CSN3

3.4.4. Surface Pore Distribution

From FESEM images of CSNC, pore distribution on the top surface was studied through image processing using ImageJ software. Pore area analysis steps have been depicted in figure 3.11. Proper threshold adjustment is crucial for binarization of image which if done properly will produce '0' value for pixels inside pores and '1' otherwise (figure

3.11: column 2). Finally contouring the dark spots (figure 3.11: column 3) will produce total pore area from which pore distribution can be obtained.

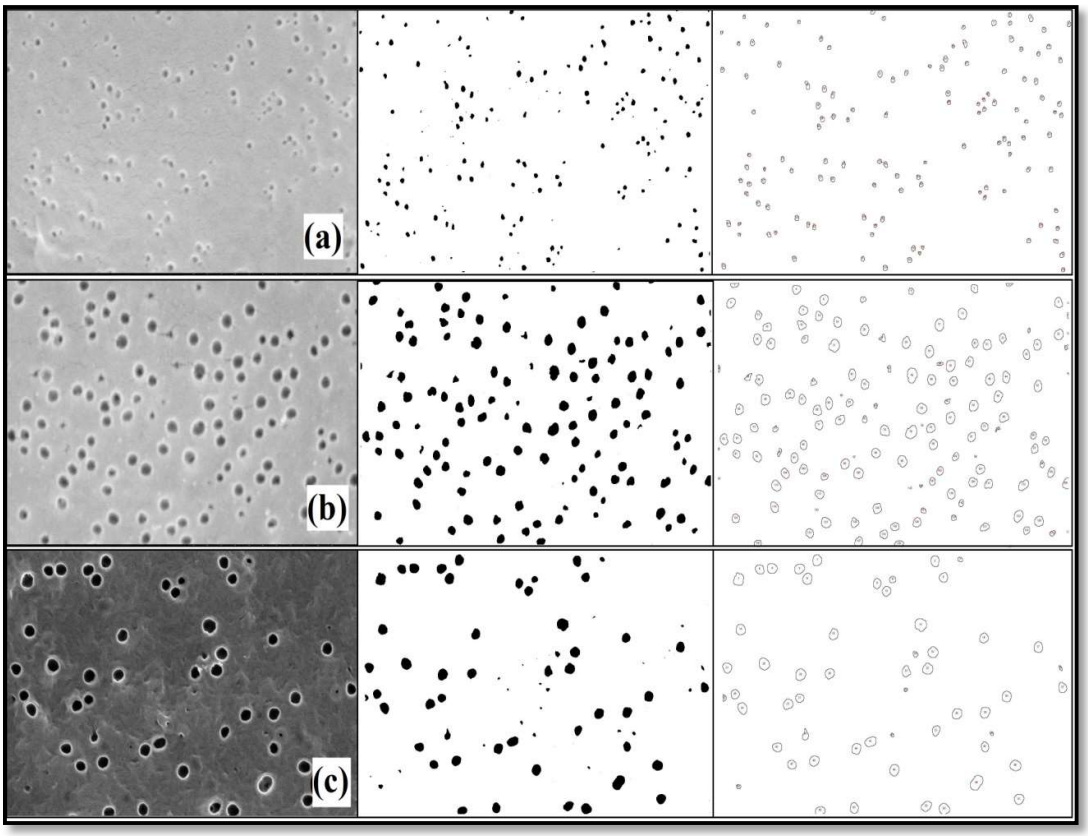

Figure 3.11. Pore area analysis output of (a) CSN1, (b) CSN2 and (c) CSN3 in ImageJ

Number of pores in CSN1 and CSN2 were found as 125 and 140 respectively in 40.1μm^2 surface area. For CSN3 sample 120.9 μm^2 surface area was considered due to large particle size and number of pores was found to be just 55. This may be because of the sedimentation effect discussed in section 3.4.2. Surface pore density of the CSNC samples, were found to be 3/μm^2, 3.5/μm^2 and 0.5/μm^2 respectively. Histograms below in figure 3.12 show that CSN2 has best pore diameter uniformity among the three samples, due to the sharp peak present at pore diameter range 180-200nm. CSN1 has large deviation in pore diameters, indicated by the flattened histogram. CSN3 also shows peak around 500nm; but most of the pores are clustered in the range 450-550nm. So pore diameter deviation of 100nm was observed which is too large for considering uniform pore diameter over the sample surface. Pores in the range of 0-50nm are generated due to the tiny crack lines present in the CSNC sample surface visible in SEM micrographs (figure 3.8).

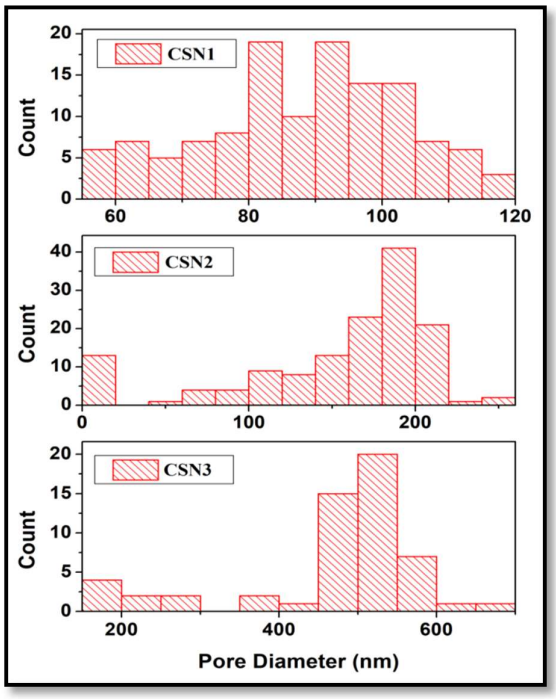

Figure 3.12. Histogram of pore distribution of CSNC samples

3.4.5. XRD Analysis

In general, a hump around 20^{o} is assigned to amorphous solids and all the three samples show such behaviour in XRD images as shown in figure 3.13(a). Pure Silica nanoparticles show amorphous hump at 20^{o} [39] and characteristic peak of chitosan is also located at 20^{o} [40]. A peak location at 23^{o} was found for all the three composite amorphous samples.

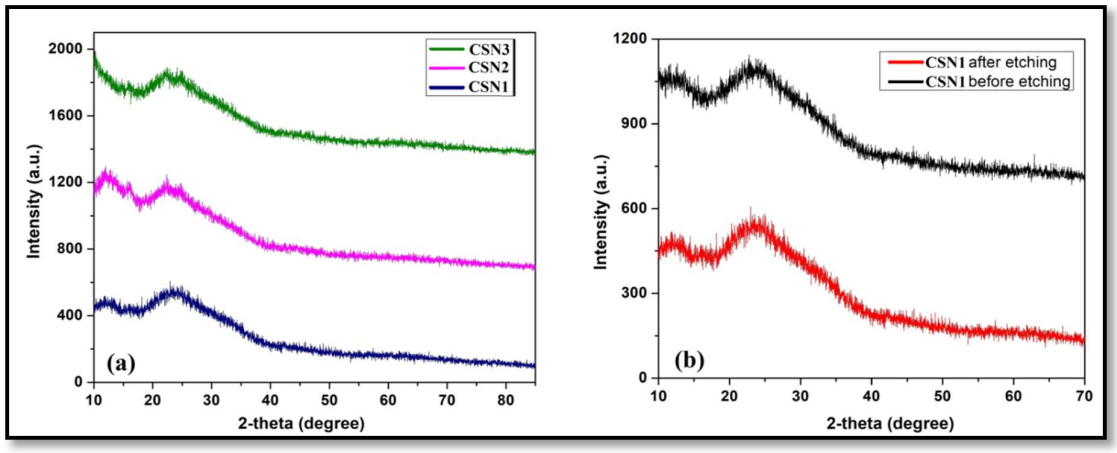

Figure 3.13. (a) XRD of the three CSNC samples, (b) effect of heat treatment

From the peak location, d-spacing was calculated to be 3.86Å, which may be the interlayer spacing in case of the polymer matrix [41]. Also, it was observed that heat treatment at the time of etching in preparation steps does not affect the amorphous characteristics of the samples. In figure 3.13(b), XRD intensity pattern remains same for CSN1 sample before and after heat treatment at 90°C for 40 minutes.

3.4.6. FTIR Analysis

FTIR spectra in figure 3.14 show a broad absorption peak around 3300-3500 cm^{-1} which indicates presence of intermolecular O-H group stretching in chitosan molecules [42]. Strong peaks at 1732cm^{-1} and 1363cm^{-1} indicate C=O stretching and O-H bending in carboxylic acid i.e. acetic acid used to prepare chitosan solution. Absorption peak at 1585cm^{-1} is due to N-H bending of amino group present in chitosan molecule. Inside amorphous SiNp, huge number of Si-O-Si bridge is formed and due to asymmetric stretching of oxygen atoms in the bridge structure, strong peak at 1056cm^{-1} is observed. With increase in Oxygen content, asymmetric stretching vibration peak of Si-O-Si bridge shifts towards higher energy and for three neighbouring oxygen atoms the peak is reported to be near 1060cm^{-1} [43].

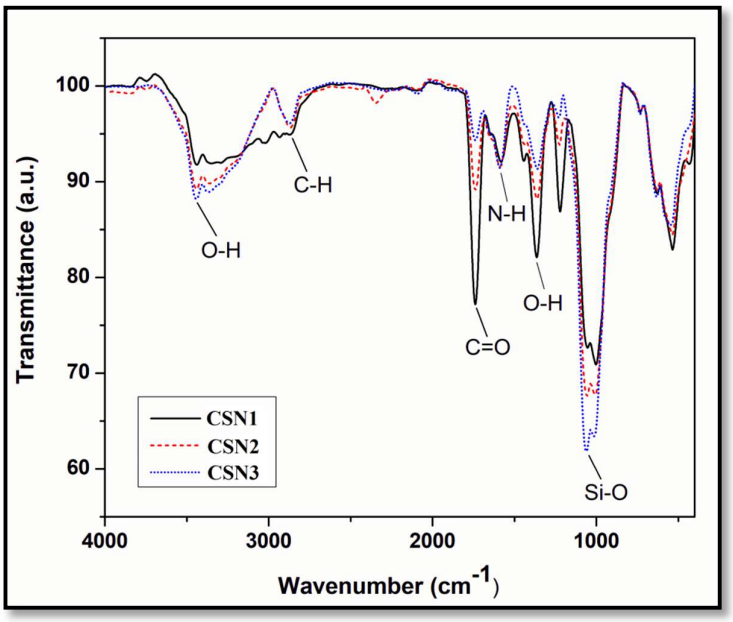

Figure 3.14. FTIR spectra of CSNC samples

Absorption bands in the range of 800 to 1260cm^{-1} is generally described as different SiO_2 peaks and residual organic group peaks [44]. Presence of peak at 2872cm^{-1} may be described as the C-H groups present from unreacted TEOS at the time of SiNp preparation which remained even after centrifugation and washing procedure.

3.4.7. Optical Property

Chitosan films are optically transparent. Adding SiNp at the time of membrane preparation produces visible reduction in transparency. Decrease in visible transparency of the thin films was observed with increasing nanoparticle size. Optical setup used to measure CSNC optical property and sensing performance is discussed thoroughly in chapter 4.

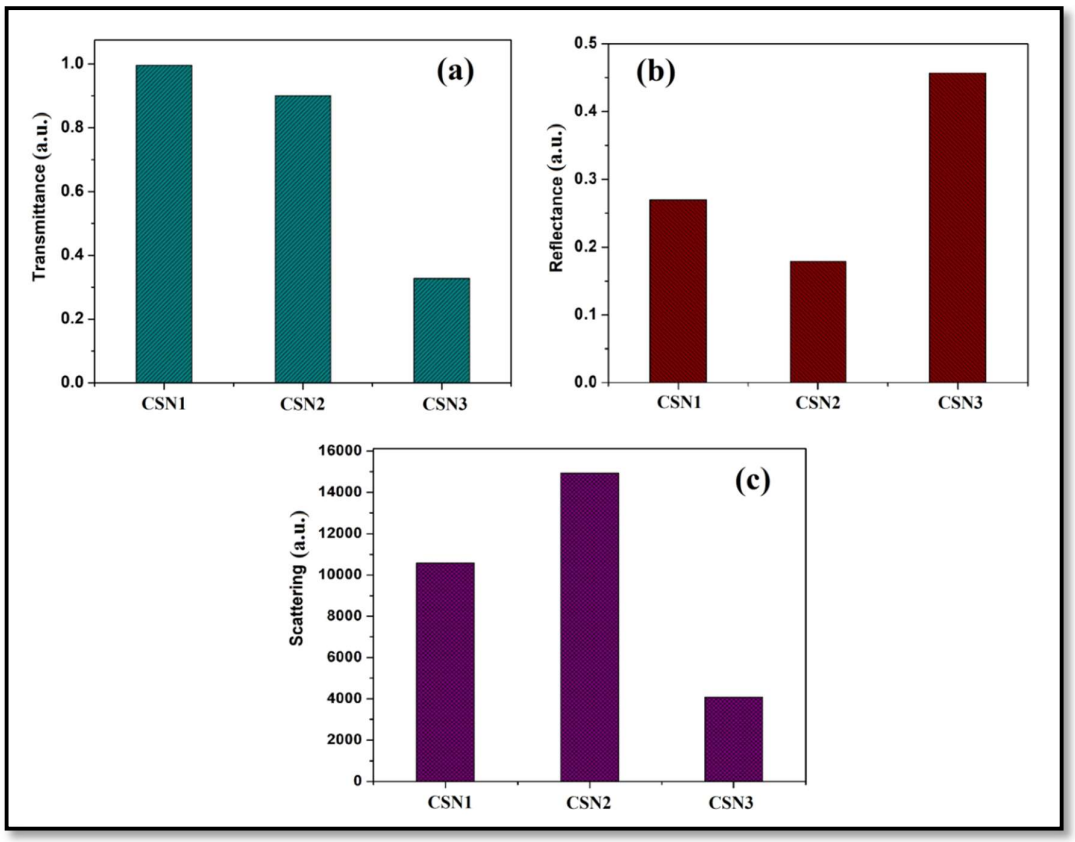

Figure 3.15. Optical properties of CSNC samples

For measurement of transmittance, normal incidence of laser beam (λ=650nm) is used and as expected, it was found that CSN3 has significant reduction in transmittance (figure 3.15(a)). Due to the presence of large nanoparticles of the order of 500nm, CSN3

shows huge amount of absorption in 650nm band. On the other hand, reflection data obtained from 30° oblique incidence shows that CSN3 has minimum scattering thus allowing maximum reflectance. This may be due to the fact that CSN3 has lowest number of scattering centers inside the spot size area of laser beam as particle size is large. Between CSN1 and CSN2 it was noticed that CSN2 has higher scattering and lower reflectance. This is because there is larger number of pores or scattering centers for a particular area (140 in $40\mu m^2$) on the CSN2 sample surface which was observed in pore distribution analysis (figure 3.12). So, transmittance is inversely proportional to the size of the pores/particles, while scattering is directly proportional to the number of pores on the surface.

3.4.8. Dielectric Property

Real part of relative permittivity and dielectric loss has been plotted against frequency, for the three CSNC samples in figure 3.16. As frequency increases, permittivity decreases gradually which is caused due to existence of space charge at low frequency, dipolar contribution and loss induced due to phase lag at higher frequency [45]. There are four types of polarization taking place in a dielectric material i.e. space charge, orientation, ionic and electronic polarization. Lower frequency response of relative permittivity is dominated by interfacial or space charge polarization. Interfacial polarization occurs due to inhomogeneity of the material or presence of some sort of charge distribution in the material. CSNC samples have phase difference between chitosan matrix and SiNp fillers thus showing prominent increase in interfacial polarization [46].

Specific surface is described as the surface of the filler particles per unit volume. The more the specific surface the more interfacial polarization takes place. According to Tanaka et al. [47] specific surface increases significantly with decrease in nanoparticle size of same wt% composition. The behaviour of CSN1 and CSN3 samples may be described this way that CSN1 has SiNp size around 100nm and CSN3 has of 500nm; thus CSN1 has much higher effective surface available for interfacial polarization to take place. But CSN2 sample show minimum relative permittivity value thus indicating minimum interfacial polarization. This may be due to the fact that, CSN2 has best pore distribution among the three and we may conclude that CSN2 has lowest amount of SiNps available after etching, as pore formation

all over the sample volume is homogeneous. Thus, CSN2 has lowest specific surface and as a result lowest amount of interfacial polarization.

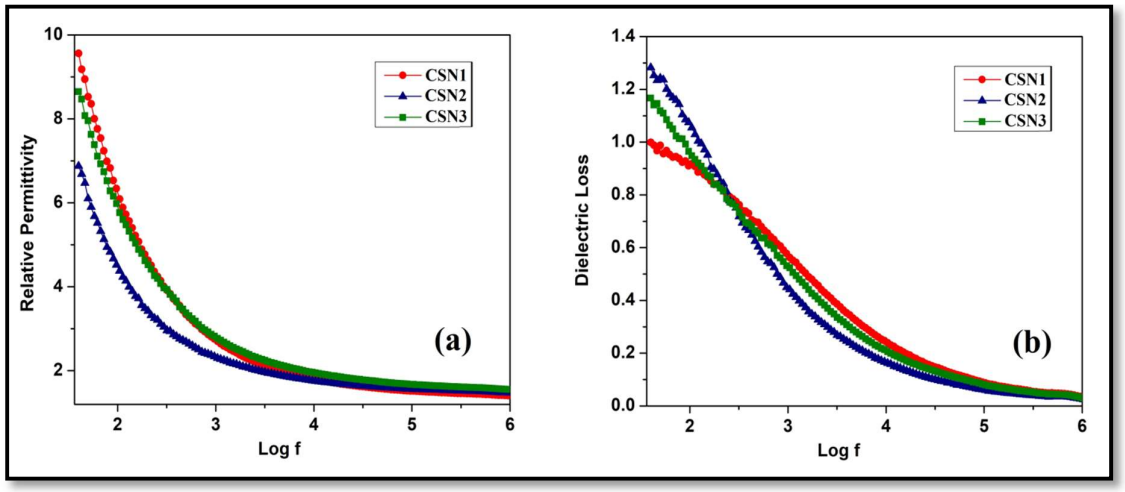

Figure 3.16. Dielectric properties of CSNC samples. (a) Relative permittivity and (b) Dielectric loss plot

3.5. Surface Functionalization

CSNC thin films were surface modified by activation with Glutaraldehyde (GTA) solution and further Glucose Oxidase (GOX) is attached in chemisorptions process for selective absorption of glucose molecules on activated sensor surface. The process and reaction of surface functionalization steps are discussed briefly in this section.

3.5.1. GTA Crosslinking with Chitosan

GTA or $OCH(CH_2)_3CHO$ is a transparent liquid often used as disinfectant, preservative, crosslinking agent etc. [48]. In aqueous solution of different concentration, GTA forms an equilibrium mixture of different structures depicted in figure 3.17. Oligomeric or polymeric structure of GTA shown in figure 3.17(VI) is observed for either higher solution concentration (≥70% solution) [49] or mild to moderate pH value (≥7.3) [50]. At pH ≥ 5.6, proton exchange of $OCHCH_2$ group occurs which enhances formation of anion indicating the first stage of aldol reaction. Up to pH 7.2 oligomers of GTA are not formed as complete aldol reaction does not take place. In mild alkaline medium complete aldol reaction occurs and

aldol condensates (figure 3.18(VIII)) are formed, thus oligomeric structures of GTA are produced above 7.2 pH value [50].

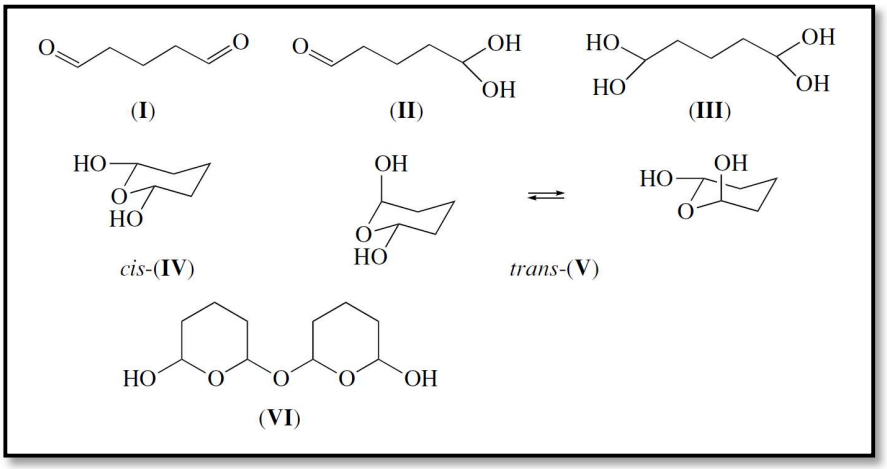

Figure 3.17. GA structures in aqueous solution (Image taken from [50])

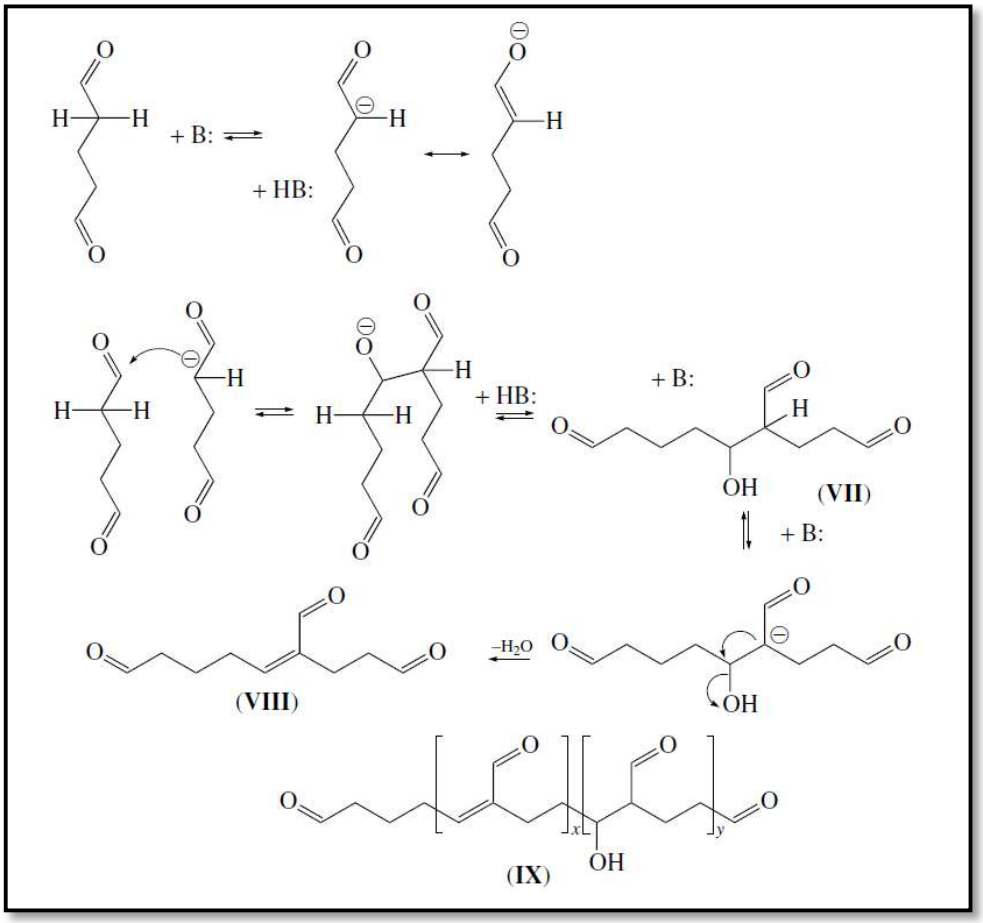

Figure 3.18. Aldol reaction of GA in alkaline medium (Image taken from [50])

Chitosan is an amino polysaccharide containing large number of $–NH_2$ bond. For GTA activated chitosan, strong presence of imine group (C=N) is observed in FTIR spectra (Chapter 5: figure 5.13). This is due to the formation of aldimine bond (R-HC=N-R') which activates the added GTA molecules to enhance the process of oligomeric chain elongation of GTA on chitosan. Then already crosslinked product further transforms through condensation of $–NH_2$ groups of chitosan with modified chitosan's carbonyl (C=O) group or through aldol reaction and condensation of GTA chains in modified chitosan to produce final structure depicted in figure 3.19 [50].

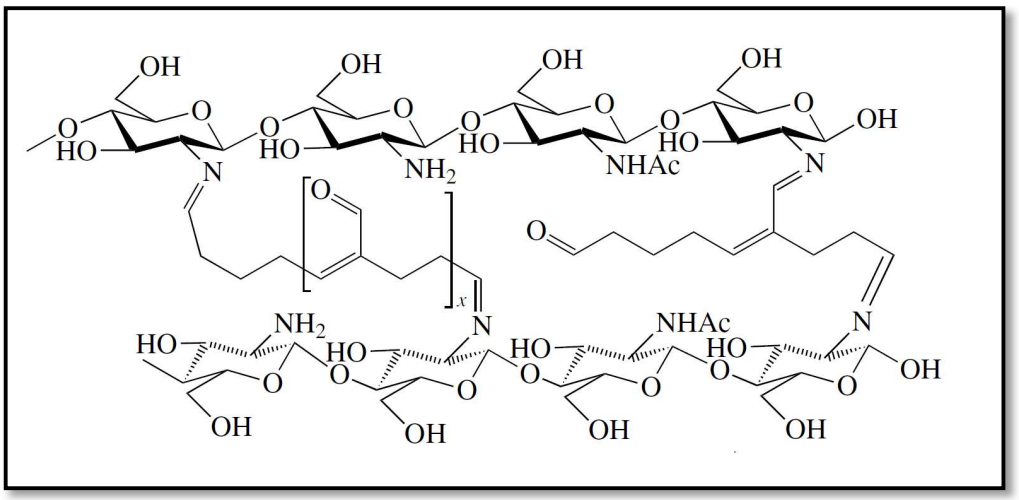

Figure 3.19. Modified or crosslinked chitosan structure (Image taken from [50])

For GTA crosslinking, CSNC thin films were dipped in 0.1% (v/v) GTA solution at pH 7.5 for 2 hours and rinsed in DI water afterwards. Higher concentration of GTA makes the film dark yellow and brittle in nature. Such brittle films are unable to withstand enzyme incubation steps afterwards. For GTA concentration as high as 0.8%, most of the thin films gets detached from glass substrate at the time of drying after enzyme immobilization and cracklines are formed afterwards causing the thin films to break into pieces. Also, enzyme activity is affected for higher GTA concentration which is discussed in chapter 5.

3.5.2. GOX Immobilization

GOX enzyme immobilization is a chemisorption process because unlike physisorption method where enzymes get absorbed physically in thin film surface, here GOX attaches to crosslinked chitosan surface via GTA chains. Enzymes are proteins with abundance of $–NH_2$

groups present in their structure. These $-NH_2$ groups replace C=O groups in GTA oligomeric chains of modified or activated chitosan surface and produce C=N groups in enzyme end, thus attaching the enzyme molecules via strong covalent bond. Such attachment is hard to break and the structure is much more stable than physisorbed samples.

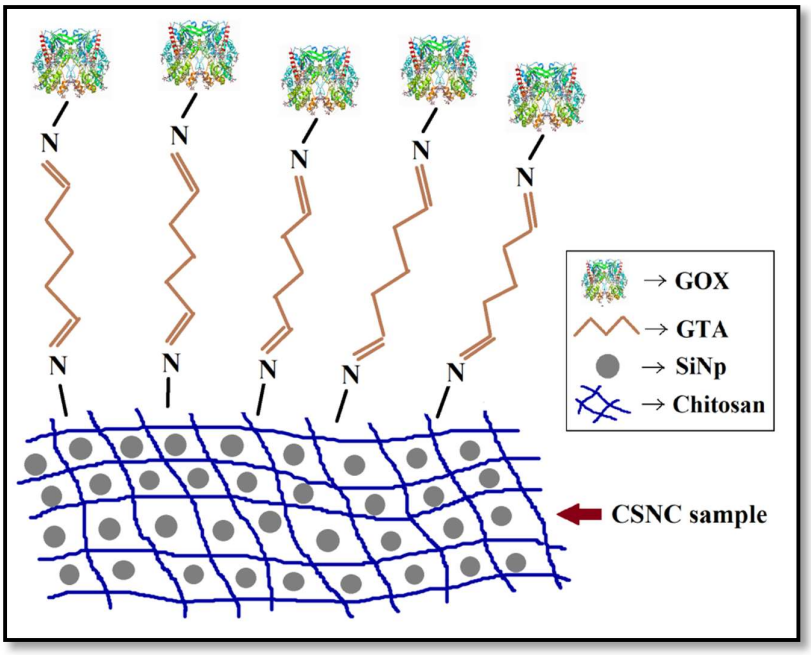

Figure 3.20. GOX functionalised CSNC sample

For GOX functionalization, 4mg GOX powder was mixed in 10ml of 1mM phosphate buffer solution at pH 6.8 under mild stirring. The activated CSNC thin films were dipped in the solution for 24 hours at 4^{o}C. Afterwards the samples were washed in tween20 solution and phosphate buffer and finally stored in 4^{o}C. Effect of higher GTA concentration is shown in figure 3.21.

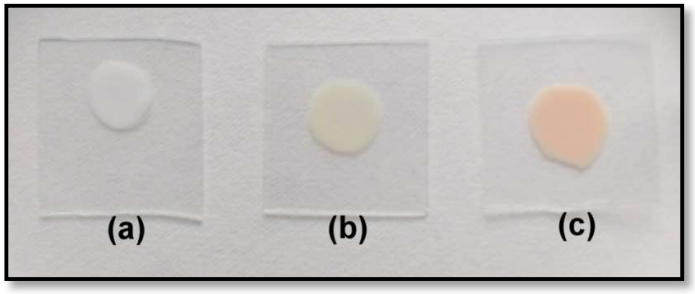

Figure 3.21. CSNC sample (a) without surface functionalization and surface functionalization with (b) 0.1% GTA solution, (c) 0.4% GTA solution

3.6. Glucose Sensing

Percentage response of CSNC thin films for transmission, reflection and scattering is depicted in figure 3.22 for 5mM and 15mM glucose concentration. For initial measurements, physisorption of glucose molecules on CSNC films was considered without surface functionalization. In chapter 5, sensor characteristic analysis has been performed thoroughly for surface functionalised CSNC thin film sensors.

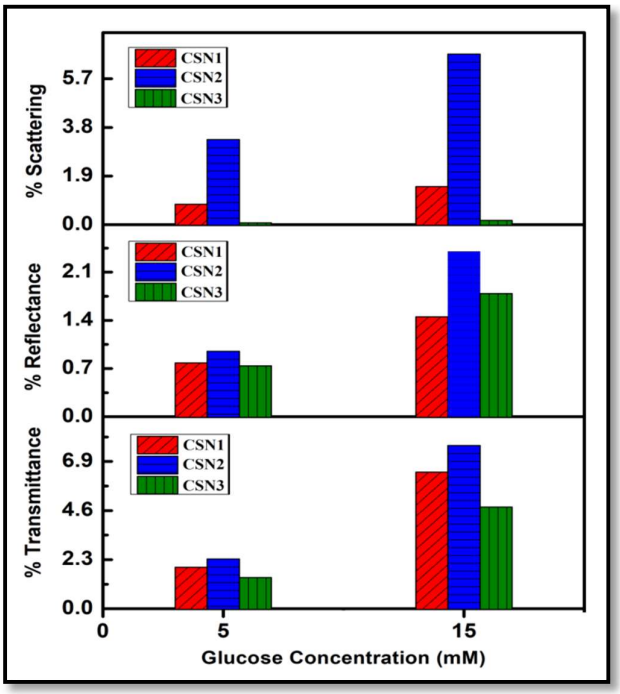

Figure 3.22. CSNC thin film sensor response (without surface functionalization)

Percentage transmittance show high value for all the three membranes, but CSN2 shows maximum response probably because of best pore distribution among the three. Evenly distributed pores enhance homogeneous physisorption of glucose molecules on sensor surface, thus providing better response. On the other hand, overall percentage reflectance of all the thin films is pretty low due to their semi-transparent characteristics, which means all the three samples show less sensitivity for reflection measurements. Still CSN2 shows comparatively better response among the three samples. Next, percentage scattering is almost negligible for CSN3 samples. CSN1 also shows low sensitivity in scattering measurement, while only CSN2 membranes have high value of percentage scattering. So, it can be concluded that, as all the parameters i.e. transmittance, reflectance

and scattering have significantly high value for CSN2 sample; thus they can be used for multi-parametric measurements.

3.7. Conclusion

A simple method of CSNC thin film and membrane preparation is presented in this chapter. Preparation parameters of Stober's method were optimized to produce SiNp of ~100nm, 300nm and 500nm size. For hot NaOH etching process, there is a critical value for etching time and NaOH concentration for successful pore formation on CSNC surface. More than 7% NaOH concentration or 60 minute etching time the samples show uncontrolled erosion. 2-5% (w/v) NaOH concentration and 30-50 minute etching time were found to be ideal for controlled pore formation. As shrinkage of the pores occurs at the time of drying, size of SiNp should be carefully chosen for desired pore size on CSNC samples. Shrinkage of pores was observed to increase with increase in SiNp size. For CSN2 samples maximum pore shrinkage of ~100nm was observed while for CSN1 it is negligible. CSN2 sample with ~300nm SiNp size resulting 149-179nm pore size was found to have best pore distribution due to less possibility of agglomeration and sedimentation.

CSNC samples were found to be amorphous in nature with XRD peak at $2\theta=23^{o}$ and d-spacing or interlayer spacing of polymer matrix was found to be 3.8Å. Also, from XRD data it was confirmed that heating of the CSNC samples at 90^{o}C does not change their amorphous nature or d-spacing. FTIR analysis proves the fact that with increase in SiNp size, number of Si-O-Si bridge structure increases in the composite. Also, lower size of SiNp (~100nm) tends to carry unreacted TEOS in the composite solution due to the agglomeration present in them even after multiple washing and repeated ultrasonication.

Methanol wash after etching can produce flexible, freestanding membrane, while water wash and slow drying produce thin films on glass substrate of thickness 4-5µm. Optimum proportion for deformationless membrane formation was found to be 1:1 (200mg of chitosan powder and 200mg SiNp dust in 10ml of 2% acetic acid solution).

Study of optical properties of the CSNC thin films demonstrate that transmittance is inversely proportional to the size of the pores/particles, while scattering is directly proportional to the number of pores on the surface. As the surface pores are of the order

compared to wavelength of incident light, elastic scattering is dominated by Mie scattering and with decrease in pore size Rayleigh scattering increases.

For selective glucose sensing, chemical modification of the CSNC surface was done for GOX enzyme attachment. GOX molecules get attached to CSNC film via activation with GTA crosslinking. Higher GTA concentration in intermediate surface modification step produces dark yellow, brittle films which often get detached from glass substrate. Standard physisorption process of glucose molecules was used for initial sensing performance study in this chapter and it was found that CSN2 samples show maximum optical response for all three measurement parameters i.e. transmittance, reflectance and scattering. So CSN2 samples with optimised preparation parameters were chosen for further GOX surface functionalization and selective glucose sensing in chapter 5.

References

[1] József Hári, and Béla Pukánszky. "Nanocomposites: preparation, structure, and properties." In Applied plastics engineering handbook, pp. 109-142. William Andrew Publishing, 2011. https://doi.org/10.1016/B978-1-4377-3514-7.10008-X

[2] Krishan K. Chawla. "Metal matrix composites." In Composite materials, pp. 197-248. Springer, New York, NY, 2012. https://doi.org/10.1007/978-0-387-74365-3_6

[3] Ru-Min Wang, Shui-Rong Zheng, and Ya-Ping George Zheng. Polymer matrix composites and technology. Elsevier, 2011.

[4] S. Schmidt, S. Beyer, H. Knabe, H. Immich, R. Meistring, and A. Gessler. "Advanced ceramic matrix composite materials for current and future propulsion technology applications." Acta Astronautica 55, no. 3-9 (2004): 409-420.

[5] Mohammed Haneef, J. Fazlur Rahman, Mohammed Yunus, Syed Zameer, Shanawaz Patil, and Tajuddin Yezdani. "Hybrid polymer matrix composites for biomedical applications." Int. J. Modern. Eng. Res 3, no. 2 (2013): 970-979.

[6] Waleed Asim Hanna, Faiza E. Gharib, and Ismail Ibrahim Marhoon. "Characterization of ceramic filled polymer matrix composite used for biomedical applications." Journal of Minerals and Materials Characterization and Engineering 10, no. 12 (2011): 1167.

[7] Rohan A. Hule, and Darrin J. Pochan. "Polymer nanocomposites for biomedical applications." MRS bulletin 32, no. 4 (2007): 354-358.

[8] Viviana Mouriño, Juan P. Cattalini, Judith A. Roether, Prachi Dubey, Ipsita Roy, and Aldo R. Boccaccini. "Composite polymer-bioceramic scaffolds with drug delivery capability for bone tissue engineering." Expert opinion on drug delivery 10, no. 10 (2013): 1353-1365.

[9] Abhinay Mishra, Abdul Rahim Ferhan, Chee Meng Benjamin Ho, JooHyun Lee, Dong-Hwan Kim, Young-Jin Kim, and Yong-Jin Yoon. "Fabrication of plasmon-active polymer-nanoparticle composites for biosensing applications." International Journal of Precision Engineering and Manufacturing-Green Technology 8, no. 3 (2021): 945-954.

[10] Deeparati Basu, Kaustav Sen, Syed Minhaz Hossain, and Jayoti Das. "Influence of pore diameter on physical and sensing properties of free-standing Chitosan-Silica Nanocomposite membrane." Journal of Porous Materials (2021): 1-13.

[11] Ruchi Nandanwar, Purnima Singh, and Fozia Zia Haque. "Synthesis and properties of silica nanoparticles by sol-gel method for the application in green chemistry." Material Science Research India 10, no. 1 (2013): 85-92.

[12] Vanitha Selvarajan, Sybil Obuobi, and Pui Lai Rachel Ee. "Silica nanoparticles—a versatile tool for the treatment of bacterial infections." Frontiers in chemistry (2020): 602. https://doi.org/10.3389/fchem.2020.00602

[13] Shadi Hassanajili, Mohammadamin Khademi, and Peyman Keshavarz. "Influence of various types of silica nanoparticles on permeation properties of polyurethane/silica mixed matrix membranes." Journal of Membrane Science 453 (2014): 369-383. https://doi.org/10.1016/j.memsci.2013.10.057

[14] Feifei Sun, Meiqin Lin, Zhaoxia Dong, Juan Zhang, Cheng Wang, Shuanglong Wang, and Feifei Song. "Nanosilica-induced high mechanical strength of nanocomposite hydrogel for killing fluids." Journal of colloid and interface science 458 (2015): 45-52.

[15] Yan Lv, Yong Du, Wen-Ze Qiu, and Zhi-Kang Xu. "Nanocomposite membranes via the codeposition of polydopamine/polyethylenimine with silica nanoparticles for enhanced mechanical strength and high water permeability." ACS applied materials & interfaces 9, no. 3 (2017): 2966-2972.

[16] Zongxi Li, Jonathan C. Barnes, Aleksandr Bosoy, J. Fraser Stoddart, and Jeffrey I. Zink. "Mesoporous silica nanoparticles in biomedical applications." Chemical Society Reviews 41, no. 7 (2012): 2590-2605.

[17] Ying Wang, Qinfu Zhao, Ning Han, Ling Bai, Jia Li, Jia Liu, Erxi Che et al. "Mesoporous silica nanoparticles in drug delivery and biomedical applications." Nanomedicine: Nanotechnology, Biology and Medicine 11, no. 2 (2015): 313-327.

[18] M. Myers. "Current and impeding developments in silica nanoparticle use in UV-curable systems." Paints & Coatings Industry (2011).

[19] W. Stober, A. Fink and E. Bohn. “Controlled Growth of Monodisperse Silica Spheres in the Micron Size Range,” Journal of Colloid and Interface Science 26 (1968): 62-69

[20] Ismail AM Ibrahim, A. A. F. Zikry, and Mohamed A. Sharaf. "Preparation of spherical silica nanoparticles: Stober silica." J. Am. Sci 6, no. 11 (2010): 985-989.

[21] Chandra K. Dixit, Snehasis Bhakta, Ajeet Kumar, Steven L. Suib, and James F. Rusling. "Fast nucleation for silica nanoparticle synthesis using a sol–gel method." Nanoscale 8, no. 47 (2016): 19662-19667. https://doi.org/10.1039/C6NR07568A

[22] G. H. Bogush, M. A. Tracy, and C. F. Zukoski. “Preparation of monodisperse silica particles - control of size and mass fraction”, Journal of Non-Crystalline Solids 104 (1988):95-106.

[23] Laura Orzali, Beatrice Corsi, Cinzia Forni, and Luca Riccioni. "Chitosan in agriculture: a new challenge for managing plant disease." Biological activities and application of marine polysaccharides (2017): 87-96.

[24] Shabnam Mohebbi, Mojtaba N. Nezhad, Payam Zarrintaj, Seyed Hassan Jafari, Saman Seyed Gholizadeh, Mohammad Reza Saeb, and Masoud Mozafari. "Chitosan in biomedical engineering: a critical review." Current stem cell research & therapy 14, no. 2 (2019): 93-116. https://doi.org/10.2174/1574888X13666180912142028

[25] Divya Nataraj, Seema Sakkara, Murlidhar Meghwal, and Narendra Reddy. "Crosslinked chitosan films with controllable properties for commercial applications." International journal of biological macromolecules 120 (2018): 1256-1264. https://doi.org/10.1016/j.ijbiomac.2018.08.187

[26] Philippe M. Loiseau, Sébastien Pomel, and Simon L. Croft. "Chitosan contribution to therapeutic and vaccinal approaches for the control of leishmaniasis." Molecules 25, no. 18 (2020): 4123. DOI: 25. 10.3390/molecules25184123.

[27] Masoud Farshbaf, Soodabeh Davaran, Amir Zarebkohan, Nasim Annabi, Abolfazl Akbarzadeh, and Roya Salehi. "Significant role of cationic polymers in drug delivery systems." Artificial cells, nanomedicine, and biotechnology 46, no. 8 (2018): 1872-1891. https://doi.org/10.1080/21691401.2017.1395344

[28] Gheorghe Adrian Martău, Mihaela Mihai, and Dan Cristian Vodnar. "The use of chitosan, alginate, and pectin in the biomedical and food sector—biocompatibility, bioadhesiveness, and biodegradability." Polymers 11, no. 11 (2019): 1837. https://doi.org/10.3390/polym11111837

[29] N. R. Sudarshan, D. G. Hoover, and D. Knorr. "Antibacterial action of chitosan." Food Biotechnology 6, no. 3 (1992): 257-272. https://doi.org/10.1080/08905439209549838

[30] Zhanyong Guo, Ronge Xing, Song Liu, Zhimei Zhong, Xia Ji, Lin Wang, and Pengcheng Li. "Antifungal properties of Schiff bases of chitosan, N-substituted chitosan and quaternized chitosan." Carbohydrate research 342, no. 10 (2007): 1329-1332. https://doi.org/10.1016/j.carres.2007.04.006

[31] Viorica Patrulea, Vasile Ostafe, Gerrit Borchard, and Olivier Jordan. "Chitosan as a starting material for wound healing applications." European Journal of Pharmaceutics and Biopharmaceutics 97 (2015): 417-426. https://doi.org/10.1016/j.ejpb.2015.08.004

[32] Hiroshi Ueno, Takashi Mori, and Toru Fujinaga. "Topical formulations and wound healing applications of chitosan." Advanced drug delivery reviews 52, no. 2 (2001): 105-115. https://doi.org/10.1016/S0169-409X(01)00189-2

[33] Julie Nilsen-Nygaard, Sabina P. Strand, Kjell M. Vårum, Kurt I. Draget, and Catherine T. Nordgård. "Chitosan: gels and interfacial properties." Polymers 7, no. 3 (2015): 552-579. https://doi.org/10.3390/polym7030552

[34] Pedro Henrique Cury Camargo, Kestur Gundappa Satyanarayana, and Fernando Wypych. "Nanocomposites: synthesis, structure, properties and new application opportunities." Materials Research 12, no. 1 (2009): 1-39.

[35] Mats Haggkvist, Tie-Qiang Li, and Lars Odberg. "Effects of drying and pressing on the pore structure in the cellulose fibre wall studied by 1H and 2H NMR relaxation." Cellulose 5, no. 1 (1998): 33-49. https://doi.org/10.1023/A:1009212628778

[36] Muhammad Aqeel Ashraf, Wanxi Peng, Yasser Zare, and Kyong Yop Rhee. "Effects of size and aggregation/agglomeration of nanoparticles on the interfacial/interphase properties and tensile strength of polymer nanocomposites." Nanoscale research letters 13, no. 1 (2018): 1-7. https://doi.org/10.1186/s11671-018-2624-0

[37] Sneha Samal. "Effect of shape and size of filler particle on the aggregation and sedimentation behavior of the polymer composite." Powder Technology 366 (2020): 43-51. https://doi.org/10.1016/j.powtec.2020.02.054

[38] Jia-Ning Sun, Yifan Hu, William E. Frieze, Wei Chen, and David W. Gidley. "How pore size and surface roughness affect diffusion barrier continuity on porous low-k films." Journal of the Electrochemical Society 150, no. 5 (2003): F97.

[39] Kethirabalan Chitra, and Gurusamy Annadurai. "Fluorescent silica nanoparticles in the detection and control of the growth of pathogen." Journal of Nanotechnology 2013 (2013). DOI: 10.1155/2013/509628

[40] De Queiroz Antonino, Rayane Santa Cruz Martins, Bianca Rosa Paschoal Lia Fook, Vitor Alexandre de Oliveira Lima, Raid Icaro de Farias Rached, Eunice Paloma Nascimento Lima, Rodrigo Jose da Silva Lima, Carlos Andres Peniche Covas, and Marcus Vinicius Lia Fook. "Preparation and characterization of chitosan obtained from shells of shrimp (Litopenaeus vannamei Boone)." Marine drugs 15, no. 5 (2017): 141. https://doi.org/10.3390/md15050141

[41] M. G. García, J. Marchese, and N. A. Ochoa. "Effect of the particle size and particle agglomeration on composite membrane performance." Journal of applied polymer science 118, no. 4 (2010): 2417-2424. 118. 2417 - 2424. 10.1002/app.32274.

[42] P. Negrea, A. Caunii, I. Sarac, and M. Butnariu. "The study of infrared spectrum of chitin and chitosan extract as potential sources of biomass." Digest Journal of Nanomaterials & Biostructures (DJNB) 10, no. 4 (2015).

[43] S. M. Iftiquar. "Structural studies on semiconducting hydrogenated amorphous silicon oxide films." High Temperature Material Processes: An International Quarterly of High-Technology Plasma Processes 6, no. 1 (2002). DOI: 10.1615/HighTempMatProc.v6.i1.40

[44] Aldona Beganskienė, Valdas Sirutkaitis, Marytė Kurtinaitienė, Remigijus Juškėnas, and Aivaras Kareiva. "FTIR, TEM and NMR investigations of Stöber silica nanoparticles." Mater Sci (Medžiagotyra) 10 (2004): 287-290.

[45] Santanu Jana, Samiran Garain, Shrabanee Sen, and Dipankar Mandal. "The influence of hydrogen bonding on the di electric constant and the piezoelectric energy harvesting performance of hydrated metal salt mediated PVDF films." Physical Chemistry Chemical Physics 17, no. 26 (2015): 17429-17436. DOI: 10.1039/C5CP01820J

[46] G. C. Psarras. "Fundamentals of dielectric theories." In Dielectric Polymer Materials for High-Density Energy Storage, pp. 11-57. William Andrew Publishing, 2018. doi:10.1016/b978-0-12-813215-9.00002-6

[47] Toshikatsu Tanaka, Masahiro Kozako, Norikazu Fuse, and Yoshimichi Ohki. "Proposal of a multi-core model for polymer nanocomposite dielectrics." IEEE transactions on dielectrics and electrical insulation 12, no. 4 (2005): 669-681.**DOI:** 10.1109/TDEI.2005.1511092

[48] A. D. Russell. "Glutaraldehyde: current status and uses." Infection Control & Hospital Epidemiology 15, no. 11 (1994): 724-733. https://doi.org/10.1086/646845

[49] Jun-ichi Kawahara, Takao Ohmori, Teiji Ohkubo, Shigeru Hattori, and Mitsutaka Kawamura. "The structure of glutaraldehyde in aqueous solution determined by ultraviolet absorption and light scattering." Analytical biochemistry 201, no. 1 (1992): 94-98. https://doi.org/10.1016/0003-2697(92)90178-A

[50] N. R. Kil'deeva, P. A. Perminov, L. V. Vladimirov, V. V. Novikov, and S. N. Mikhailov. "Mechanism of the reaction of glutaraldehyde with chitosan." Russ. J. Bioorg. Chem 35, no. 3 (2009): 360-369. DOI: 10.1134/S106816200903011X

Chapter 4

Chapter 4

Design and Development of Multiparametric Optical Measurement System

4.1. Introduction

Many of the label-free detection methods discussed in chapter 1 require highly expensive instruments for precision measurements and also most of them monitor change of a single parameter due to the presence of target analyte. Multiparametric sensor systems are in general way better than single parametric sensors in terms of reliability. Also, for a particular concentration range of analyte, some parameters might show high sensitivity

while the others may not change significantly. In such cases finding out the most sensitive parameter is crucial for sensitive measurement which can easily be obtained by simultaneous monitoring of all accessible parameters. Though the field of multiparametric optical detection systems is lacking in number of publications; in recent years a few such biosensor systems were reported. R. Moretta et al. demonstrated reflectance spectra and photoluminescence to characterize PSi-GO hybrid samples [1]. S. Rampazzi et al. showed sensitivity of 10^{-4} RIU in refractive index with a portable surface plasmon resonance based multiparametric device [2]. Multiparametric fiber optic sensors were also reported measuring different non-interlinked parameters like reflectance spectra, temperature and pressure [3]. Most of these systems measure non-interlinked parameters like refractive index, temperature, pressure etc. and some of them even require two separate instruments for measurement.

In this chapter, a simple, cost effective and reliable optical multiparametric measurement system has been designed and developed for bio-analyte detection. The instrument measures mainly interlinked parameters i.e. change in any one parameter will affect the others. Such interlinked parameters give a detailed idea of the total optical phenomenon occurring inside the sensor sample upon analyte absorption. Thus, importance of such instrument in biosensor field is quite significant. First, the design principle is discussed, then noise analysis of the system is performed and finally a noise reduction method is proposed. Also, drawbacks and future scope for improvement has been discussed in the last section of this chapter.

4.2. Design Concept

Image files in general contain lots of information which if extracted properly can provide a detailed insight about an object. Image analysis is also a cost effective method as it does not require any precision component.

A single image of transmitted or reflected optical spot obtained from a thin film sample can provide information about different optical properties of the sample. Information stored in an image can be analysed quite easily in MATLAB image processing

environment. Here, five interlinked optical parameters i.e. transmittance (T), reflectance (R), internal and surface scattering (IS and SS respectively) and output power (OP), were chosen for simultaneous measurement. Also in some cases, RGB components of the colour image were measured as non-interlinked parameters. A simple yet robust optical setup with image acquisition and analysis feature was developed for analyte detection.

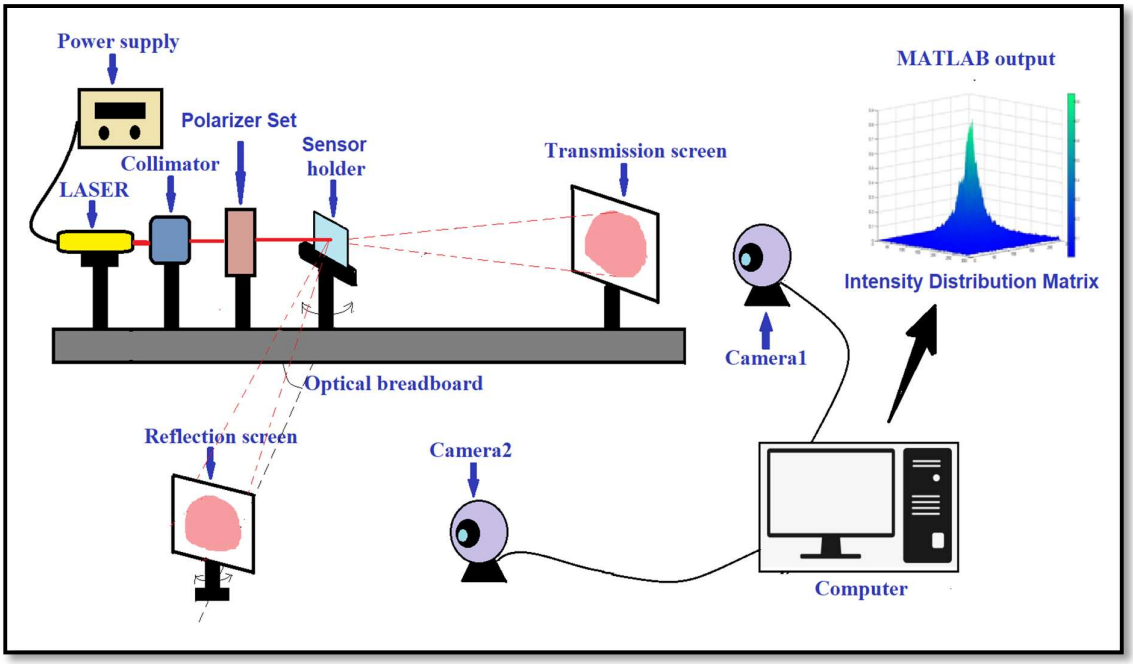

Figure 4.1. Schematic diagram of the optical setup

The system is constructed on an optical breadboard setup (figure 4.1) inside a darkroom environment. LED or Laser Diode (LD) was used as optical source followed by a collimator and an intensity modulator. The thin film samples were placed on a sample holder which can be rotated about its axis for adjusting normal and oblique incidences. Two CMOS cameras were used as detectors which feed image data to the computer (PC). For non-transparent samples, reflected spot image was captured by a single camera and for semi-transparent samples transmitted and reflected spot images were collected by two cameras simultaneously. The spot images form an Intensity Distribution Matrix in MATLAB image processing environment and they are further modified to find out peak intensity value (PIV) and full width half maxima (FWHM) of the spots. The PIV of transmitted and reflected spot provides transmittance (T) and reflectance (R) of the sample respectively. FWHM of transmitted and reflected spot provides an estimation of internal scattering (IS)

and surface scattering (SS) respectively. Absorption is calculated from the IDM information which will be discussed in the next section. A graphical user interface (GUI) has been developed in MATLAB for interfacing and automation of the whole system.

4.3. Image Processing Steps

Initially, the spot images captured by the cameras are in RGB format. First, they are converted into grayscale so that only one colour channel exists describing the intensity levels (0 – 1 a.u. corresponding to 256 steps) of different pixels. Now from this grayscale image, a 3D image matrix is developed having X and Y axis as row and column value of pixels and Z axis as intensity value of the corresponding pixel. This image matrix having the intensity information of all the pixels is called Intensity Distribution Matrix (IDM) shown in figure 4.2. The IDM produced by transmitted and reflected spots were found to be Gaussian in nature. So a Gaussian distribution model is developed from the IDM which gives further information about PIV and FWHM values of the IDM. PIV of transmitted and reflected spot gives specular component of transmittance and reflectance respectively. Due to scattering within the thickness of the sample and also on top of the surface of incidence, diffuse component is also generated. The FWHM value of transmitted spot gives an idea of internal scattering, while FWHM of reflected spot denotes mainly surface scattering.

In any system total incident power $\boldsymbol{P_i}$ is defined as,

$$\boldsymbol{P_i = P_t + P_r + P_a + P_l} \quad \text{..... (4.1)}$$

Where, P_i = *Total incident power on sample surface*
P_t = *Transmitted power*
P_r = *Reflected power*
P_a = *Power absorbed inside the sample*
P_l = *Power loss in environment*

Output Power (OP) is defined as the total power delivered in transmission and reflection i.e. $\sim(\boldsymbol{P_t} + \boldsymbol{P_r})$. OP is calculated from the sum of 3D volume under IDMs generated from transmitted and reflected spots, captured at a particular instant of time. As $\boldsymbol{P_i}$ and $\boldsymbol{P_l}$ is constant for same environmental condition, $\boldsymbol{P_a}$ can be estimated from OP. Increase in the value of OP will denote decrease in optical absorption within the sample. This is particularly effective when relative measurement is performed in sensor application.

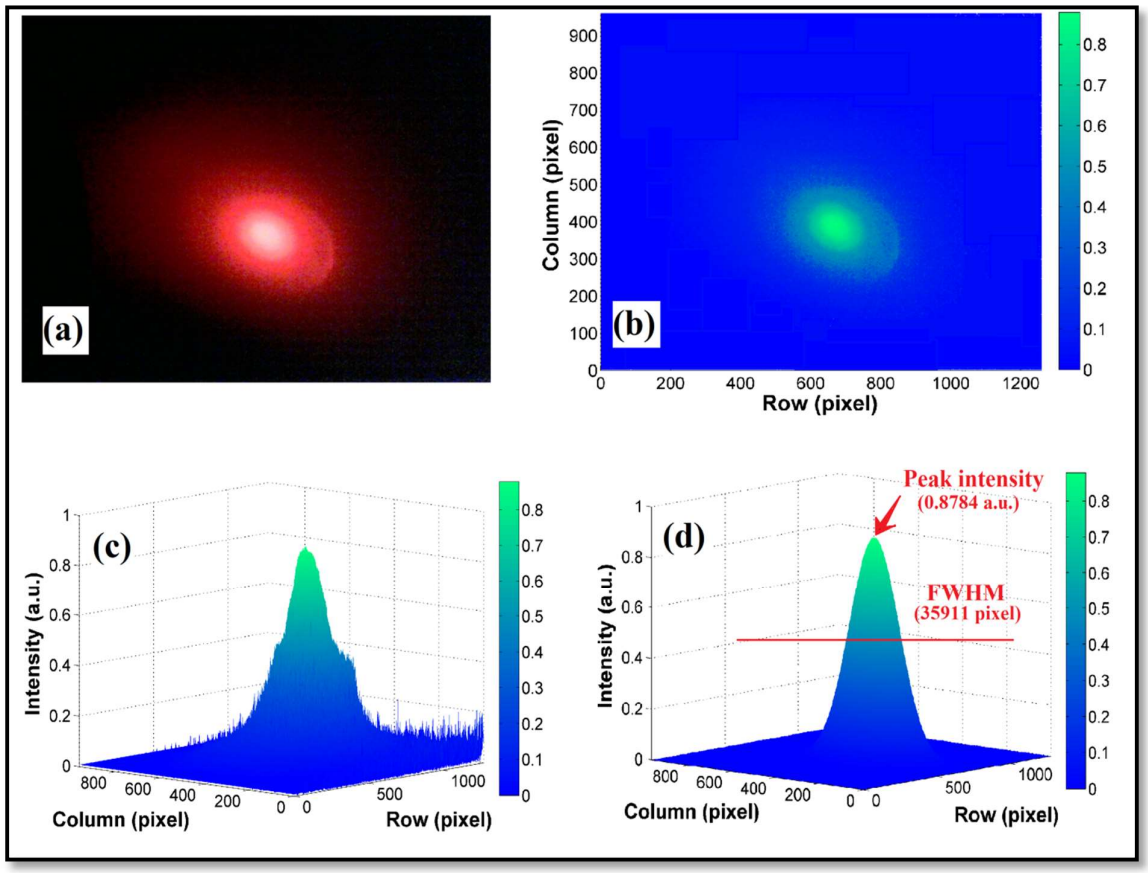

Figure 4.2. (a) Original image captured by the camera, (b) 2D view of IDM, (c) 3D view of IDM and (d) Gaussian model of the IDM

For relative response measurement, baseline data or data without presence of desired analyte is recorded at first. This data is often called ‘blank’ in many literatures [4-6]. Then after introduction of analyte in the sensor sample, data is recorded again.

The relative response is defined as,

$$\text{Relative Response} = \left| {(V_f - V_0)}/{V_0} \right| \times 100\ \% \ \ldots\ldots\ldots\ldots\ldots\ldots\ldots\ldots\ldots\ldots\ (4.2)$$

Where, V_0 = *Baseline reading of individual parameters*

V_f = *Reading after analyte introduction*

In this type of measurement, change in OP before and after analyte introduction gives an idea of whether absorption has increased or decreased. Similarly, comparison of all the parameters gives an idea of the optical mechanism responsible for change in output due

to the presence of analyte. This is the main advantage of the multi-parametric arrangement discussed before.

4.4. MATLAB GUI Design

MATLAB environment is very much effective in producing problem specific Graphical User Interface (GUI) which saves manual data collection and processing labour. The GUI designed for this multiparametric measurement is shown below in figure 4.3. The section for ***'Noise Analysis'*** is used to understand and analyse system noise. With ***'Snapshot Interval'*** and ***'Acquisition Time'*** input edit boxes; time interval between each snapshot and total time for data acquisition can be entered by the operator. When number and interval of snapshot is fed to the corresponding edit boxes, the system monitors PIV and FWHM fluctuation in the output images captured by ***'Trans_Camera'*** (camera dedicated for transmission data) or ***'Ref_Camera'*** (camera dedicated for reflection data). Selection between the two cameras can be done by radio button shown in the GUI window. Excel files are generated automatically upon completion of ***'Start'*** pushbutton cycle containing all the fluctuation states for the selected camera. Dataset in the excel files can further be processed to produce noise plot and noise analysis output like mean value (μ), standard deviation (σ), percent deviation (PD) and deviation range (DR) for PIV and FWHM noise. In general, different time span like 1, 10, 60 minutes etc. with snapshot interval 1, 2, 5 and 10 seconds were analysed. For faster performing PC system, 1 second interval could be achieved, but for slower systems interval below 2 second was not possible.

The radio buttons ***'Tr_Camcheck'*** and ***'Rf_Camcheck'*** produces live preview from the cameras. These are used mainly for initial checking of system functionality. In the ***'Sensor Data Analysis'*** section, snapshot interval can only be changed as time span of data acquisition is fixed to 1 minute here which we found enough for capturing maximum fluctuation states (discussed in section 4.8.2 and 4.9.2). Upon initialising senor data acquisition, the two cameras take snapshots simultaneously i.e. 60 snapshots in 1 minute time span and produces mean value of different parameters in the output edit boxes. For samples with high level of scattering, often 2/3rd value of the Gaussian peak is required which also appears in ***'Tr_FWQM'*** and ***'Rf_FWQM'*** output edit boxes. This is to note here,

that the ***'Absorption'*** editbox actually gives Output Power (OP) data. As OP gives an idea of the optical absorption discussed in section 4.3, it is named so. Detailed programming of GUI and image processing is provided in Annexure I-IV.

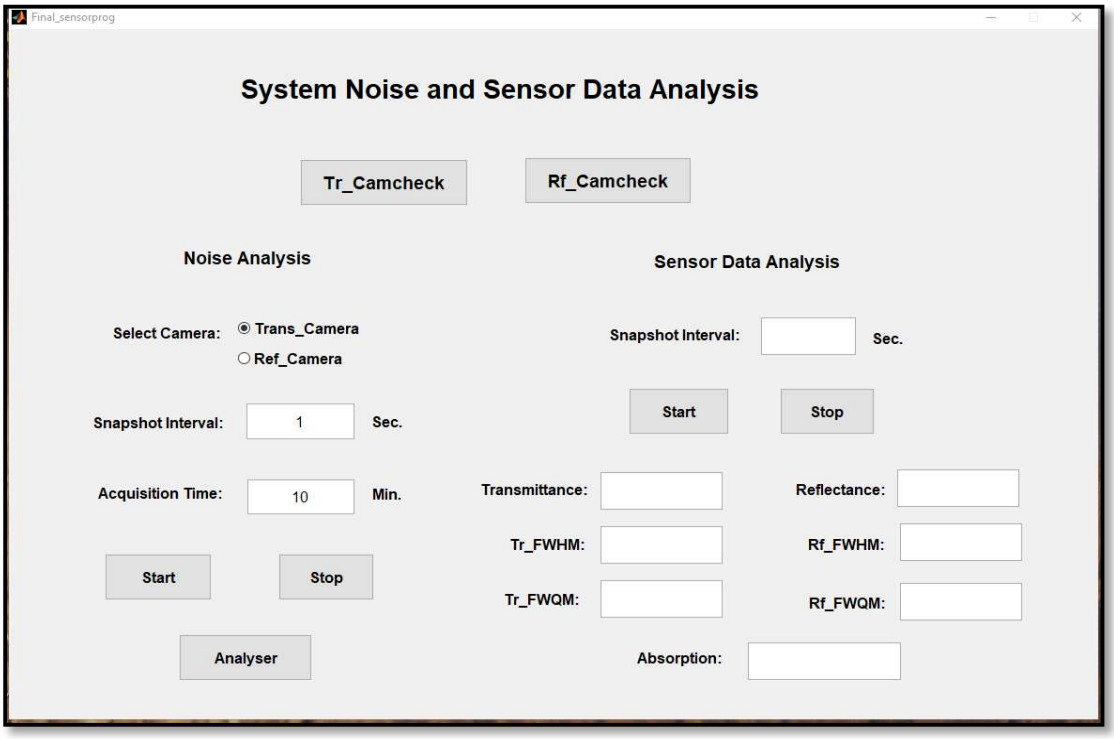

Figure 4.3. MATLAB GUI window

4.5. Sensor Measurement

As mentioned before, sensor output response is not absolute, but relative to the baseline data. As the output is very much dependent on angle and position of light incidence on the sample, it is critical to obtain results without error if samples are removed from holder repeatedly for analyte introduction. That is why the analyte solution is sprayed on the sample which ensures exactly same positional and environmental conditions before and after analyte introduction. Baseline images are first taken and then change in response due to the presence of analyte is observed with respect to baseline response. Often, right after solution spray transmittance or reflectance value becomes excessively high due to lensing effect of water droplets present on the thin film samples. So, a drying time is given after solution spray to get reliable results. Also, before taking sensor data, it is important to

adjust intensity of the source so that peak intensity of transmitted and reflected spot lies in the range of operation. Detailed study on the operating range of the system is discussed in section 4.7.

Relative responses for different parameters are defined as,

$$\% \text{ Transmittance (\%T)} = \left| \left(T_f - T_0\right) / T_0 \right| \times 100\ \% \quad \text{..... (4.3)}$$

Where, T_0 = *Baseline value of transmittance*

T_f = *Transmittance after analyte introduction*

$$\% \text{ Internal Scattering (\%IS)} = \left| \left(IS_f - IS_0\right) / IS_0 \right| \times 100\ \% \quad \text{..... (4.4)}$$

Where, IS_0 = *Baseline value of internal scattering*

IS_f = *Internal scattering after analyte introduction*

$$\% \text{ Reflectance (\%R)} = \left| \left(R_f - R_0\right) / R_0 \right| \times 100\ \% \quad \text{..... (4.5)}$$

Where, R_0 = *Baseline value of reflectance*

R_f = *Reflectance after analyte introduction*

$$\% \text{ Surface Scattering (\%SS)} = \left| \left(SS_f - SS_0\right) / SS_0 \right| \times 100\ \% \quad \text{..... (4.6)}$$

Where, SS_0 = *Baseline value of surface scattering*

SS_f = *Surface scattering after analyte introduction*

$$\% \text{ Output Power (\%OP)} = \left| \left(OP_f - OP_0\right) / OP_0 \right| \times 100\ \% \quad \text{..... (4.7)}$$

Where, OP_0 = *Baseline value of output power*

OP_f = *Output power after analyte introduction*

4.6. Noise Measurement

Development of any instrument requires proper noise level analysis so that reliable range of operation can be determined. Also, for biosensing application limit of detection is an important characteristic which can be determined from the system noise level considering S/N $\geq$ 3.

Here, when the camera captures repeated instantaneous snapshots of same baseline spots with fixed external condition, it was found that PIV and FWHM of the spots fluctuate randomly, thus existence of noise level is evident. In this system, main components are optical source and detector camera. So, any one or both can contribute to this random fluctuation. To understand the contribution of different components on system noise, a detailed component wise noise analysis is performed and then a noise reduction method is applied for minimising output fluctuation.

System noise is evaluated by the following parameters.

1) Percent Deviation (PD) = $\frac{V_{max}-V_{min}}{\mu} \times 100\%$ ..... (4.8)

Where, V_{max}= *maximum value of PIV or FWHM for instantaneous snapshots*

V_{min} = *minimum value of PIV or FWHM for instantaneous snapshots*

μ = *mean value of PIV or FWHM taken for a particular time span*

2) Relative Standard Deviation (RSD) = $\frac{\sigma}{\mu} \times 100\%$ ..... (4.9)

Where, σ = *standard deviation in PIV or FWHM*

For system noise analysis either transmitted or reflected spot is considered and deviation in PIV and FWHM is monitored for different time span and intervals. The more the PD and RSD value the noisier is the system. This method of noise analysis is applied for LED and Laser Diode (LD) sources and CMOS camera detectors. Also, mean value of PIV or FWHM data for different sets are compared considering fixed time span and interval for each set. To measure the fluctuation of mean value in different sets mean value deviation is calculated. The thorough noise analysis of the system provided an insight towards the applicable noise reduction method.

Mean value deviation is defined as,

$$\text{Mean Value Deviation (MVD)} = \frac{\mu_{max} - \mu_{min}}{\mu_{avg}} \times 100\% \quad \text{..... (4.10)}$$

Where, μ_{max} = *maximum value of mean*

μ_{min} = *minimum value of mean*

μ_{avg} = *average mean value of different sets*

4.7. Operating Range

Operating Range generally depends on the sensitivity and range of the detectors. So, specification of the camera is important to have a rough estimate of noise free detection range. In specification of camera (Table I), the most important terms are 'Mega Pixel' and 'Bit Depth'. An image is constructed of a number of micro-segments called pixels. The more the number of these pixels, the better the quality of the image becomes. Bit depth or colour depth is the number of bits used for each colour component in a single pixel. For RGB image of bit depth 8, each pixel will have 3 colour channels (Red, Green & Blue) with 2^8 or 256 levels of intensity value in each channel. When the images are converted to grayscale there will be only one channel of 256 intensity levels with minimum and maximum value at 0a.u. and 1a.u. respectively. Here, 0 corresponds to black and 1 corresponds to white. ***Resolution of pixel intensity value for the camera is 1/256 or 0.0039a.u.*** The camera cannot detect any changes below this 0.0039 a.u. value. For cost efficiency of the system, we have used 2MP CMOS camera with 8bit depth. In general, CMOS cameras are noisier than CCD and with limitation in resolution the system becomes unable to detect lower concentration of bio-analyte. But for glucose sensing in pathological range, it was found to be sufficient.

Table I: Camera Specification (CMOS)

Resolution	Mega Pixel	Focus Type	Bit Depth	Diagonal Field of View
720p/30fps	2 MP	Fixed focus	8 bit	60^o

In a darkroom without any optical source, when snapshot is taken using camera, the images are called **Dark Image**. Ideally, pixels in a dark image should produce 0.0a.u. value, but due to internal noise of camera generated from sensors and circuitry [7], the pixels produce nonzero value which fluctuates with time in a random manner. In applications, where average value of image pixel intensity is considered, such fluctuation is of least importance. As our system measures PIV of transmitted and reflected spot (transmittance and reflectance), the main focus is not on the average value of the pixels but in the peak intensity. So, deviation in the peak intensity is observed in the dark images and this deviation is called **Dark Noise**.

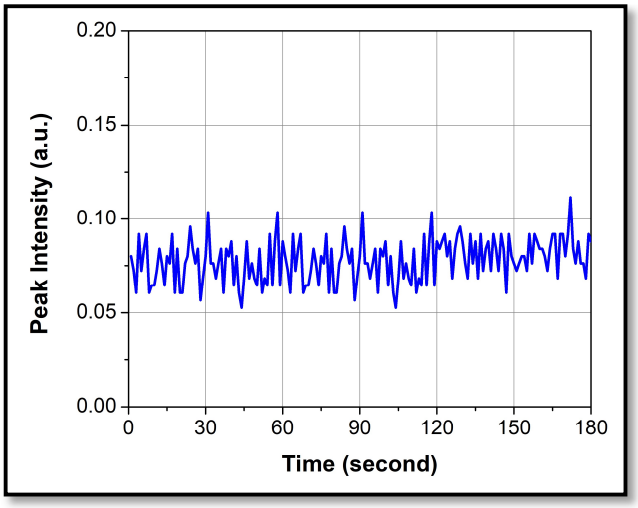

Figure 4.4. Dark noise response (Time span = 3 min., Interval = 1 sec.)

Figure 4.4 shows a typical pattern of dark noise observed for 3 minutes time span with 1 second interval. The mean value of this noise is found around 0.0779 for Trans_Camera and 0.0712 for Ref_Camera. PD was found to be maximum 72% for 1 minute span, which is unexpectedly high. Next, 5 sets of 1 minute time span data was recorded and mean value of the sets were observed. Table II and III lists down the data obtained from the two cameras.

It is observed that for dark noise, deviation range (DR) is fixed (0.051a.u.) for both cameras. This may be due to the same internal properties of the camera. But dark noise mean value was found to be slightly different even for the same type of camera. MVD is remarkably low compared to PD i.e. 0.24% for Trans_Camera and 0.29% for Ref_Camera

respectively. So, by taking mean value of 1 minute set, it is possible to reduce dark noise fluctuation into a level where it can almost be neglected.

Table II: Trans_Camera dark noise data

Set no.	Mean	SD*	DR**
Set I	0.07797	0.01193	***0.051***
Set II	0.07801	0.01028	***0.051***
Set III	0.07801	0.01193	***0.051***
Set IV	0.07816	0.01139	***0.051***
Set V	0.07798	0.00926	***0.051***

Table III: Ref_Camera dark noise data

Set no.	Mean	SD*	DR**
Set I	0.07116	0.01155	***0.051***
Set II	0.07094	0.01121	***0.051***
Set III	0.07094	0.01046	***0.051***
Set IV	0.07094	0.01121	***0.051***
Set V	0.0712	0.01097	***0.051***

*SD = standard deviation in PIV
** DR= Deviation Range i.e. (maximum-minimum) of the PIV

Now for reliable operating range, FWHM level of any image should be well above this mean value of dark noise. So, minimum PIV was set to be ≥ 0.25a.u. i.e. > 2 × (mean dark noise value + DR/2) and this is the lower cutoff of the system. For determining upper cutoff of PIV, it is to be noted that maximum value of any pixel is 1.0a.u. Higher brightness of the spot will produce burnt images as most of the pixel intensity value would lie at 1a.u. due to camera saturation and consequently a flathead distribution of IDM will be generated instead of Gaussian distribution shown in figure 4.5. Actual peak intensity cannot

be retrieved from this unwanted flathead distributions and half maxima level would also be fixed at 0.5a.u. So, both peak intensity and FWHM measurements would be faulty. So, higher range of PIV is set ≤ 0.9a.u. Baseline value of PIV is always maintained within this operating range of ***0.25a.u.≤ PIV ≤ 0.9a.u***., by adjusting optical source intensity.

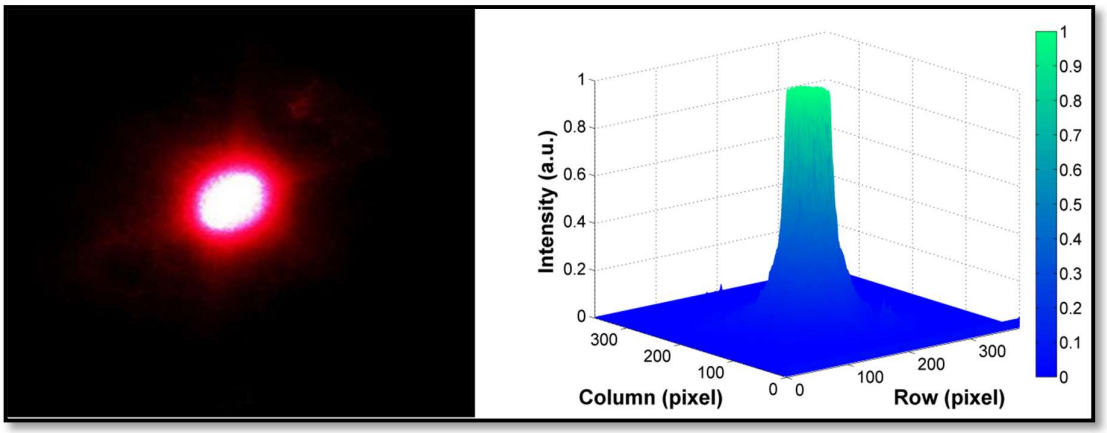

Figure 4.5. Flathead IDM distribution of burnt image

4.8. LED Source

Typical 10mm Red LED (wavelength: 620-635nm, luminous intensity: 2000-3000mcd) and White LED (luminous intensity: 18000-20000mcd) were used as optical source. A collimator arrangement was required to achieve final spot size of 6mm. Further reduction of spot size causes intensity to fall severely which hampers performance of the system. Though LEDs are considered to be much stable optical source than halogen, xenon, tungsten lamps or lasers [8], they still have fluctuation in the output intensity and taking instantaneous snapshots makes the fluctuation more prominent.

4.8.1. Noise Generation

Fluctuation in LED intensity is caused mainly by the combined effect of 1/f noise from active region, generation-recombination noise, thermal and shot noise [9]. Shot noise is high frequency noise and can be eliminated using a constant current source. But current sources also have small amount of fluctuation in output level which induces LED intensity fluctuation. 1/f and generation-recombination noise are low frequency noise generated due

to defect levels and tail states in different regions of the device. When LED current increases, low frequency noise may increase or decrease for different devices, which may be an effect of LEDs superluminescent operation [10].

4.8.2. Noise Analysis

Figure 4.6 shows typical PIV of Red LED after reflection from PS thin film surface. For PS samples, reflected spot PIV produced by maximum intensity of red LED, was so low that it was very close to dark noise level and in this situation; it is extremely hard to extract FWHM value as the Gaussian distribution becomes almost flat. After 5minutes stabilisation time, PIV was found to be only at near 0.1a.u. which is out of the operating range of the system. Thus, Red LED was not found suitable for PS samples due to their very much low intensity level in reflection spot analysis.

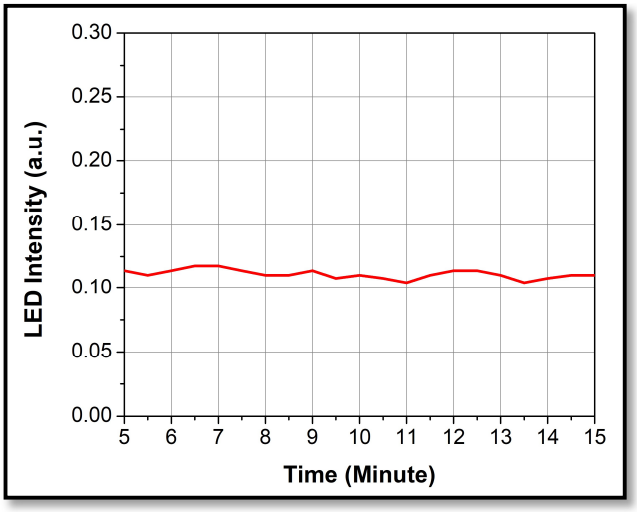

Figure 4.6. Red LED time response after initial stabilization time (Time span: 10 min., Interval: 30sec., Sensor sample: PS)

Next, 10mm white LED source were used as they have sufficiently high intensity level (luminous intensity: 18000-20000mcd). Maximum intensity of white LED was found to be ~ 0.31 a.u. for reflected spot of PS samples and up to ~ 0.92 a.u. for transmission spot of CSNC samples. Intensity of the LED was adjusted by linear polariser sheets when required. Typical time response of this white LED for reflectance is shown in Figure 4.7. In this curve, effect of temperature in LED stability is clearly visible. The junction between LED die and substrate produces maximum heat and an aluminium base is attached to the bottom of the

substrate which acts as an inbuilt heatsink, but for long time use it is still not adequate. For prolonged use, the LED junction heats up gradually over time and efficiency falls [11]. After approximately 110 minutes of continuous use, LED intensity falls slowly in figure 4.7. So, continuous operation time was set under 1hour 40 minutes.

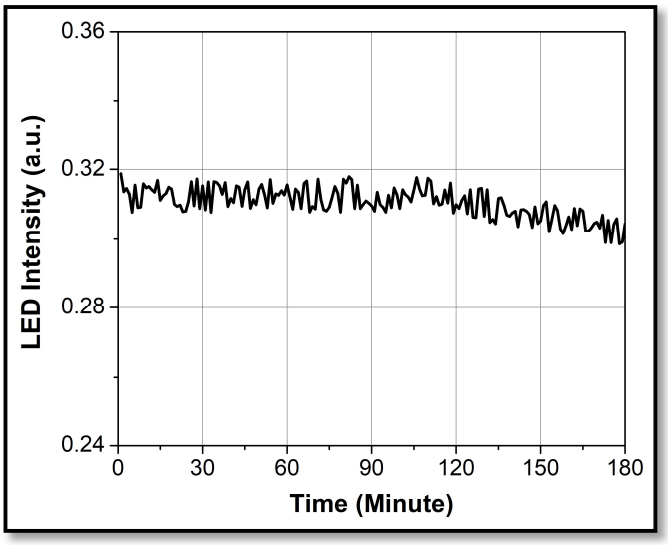

Figure 4.7. White LED response (Time span: 3hrs., Interval: 1min., Sensor Sample: PS)

For white LED, maximum PD was found to be around 3.3% and 4.1% for PIV and FWHM value respectively. Both reflected spot for PS samples and reflected and transmitted spot for CSNC samples were analysed. Almost same level of PD was found in PIV and FWHM value, which proves that the fluctuation in instantaneous snapshots was not dependent on sensor sample type. Fluctuation in FWHM is a combined effect of intensity variation and non homogeneous diffusion of LED source. For CSNC samples transmittance was much higher than reflectance for white LED. Reflectance value was found to be ≤ 0.27a.u. which is almost near the lower cutoff limit of operating range. Also, scattering of CSNC samples were much higher compared to PS samples. The combined effect of scattering and LED divergence produces a flattened intensity distribution pattern (Figure 4.8) of the reflected spot image for CSNC samples. Such patterns are not suitable for sensor analysis as it is very difficult to find out actual FWHM value from the intensity distribution which lies so close to dark noise level. So, LED sources are not suitable for samples that have low reflectance and large scattering. Instead, more directive and high intensity sources are required for this type of application.

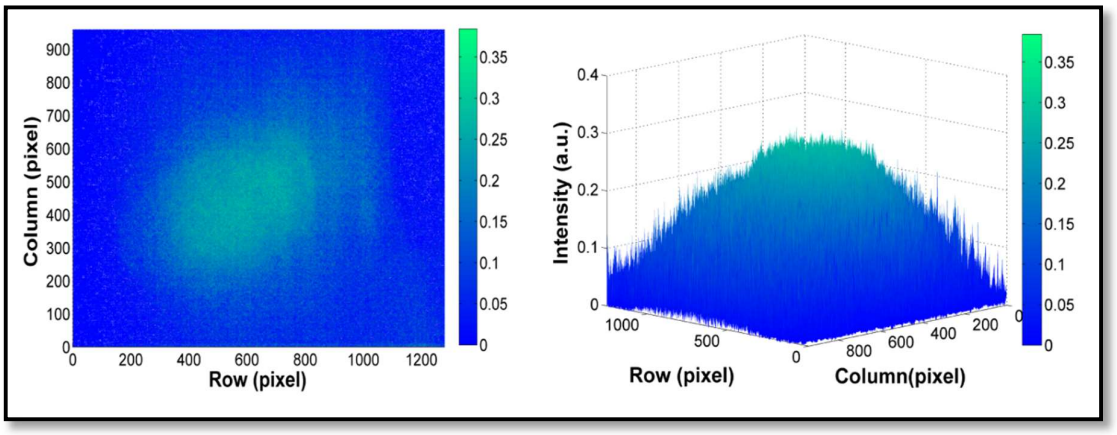

Figure 4.8. Flattened IDM for low reflectance and high scattering samples

PIV and FWHM fluctuation for instantaneous snapshots were monitored for different time spans with 1second time interval. It was found that 1 minute time span reached maximum PD value which indicates that inside this 1 minute almost all the fluctuation levels can be captured. In Table IV, detailed analysis of PIV fluctuation for transmitted spot of CSNC sample has been shown and it is clear that RSD and mean value remains almost fixed for time span above 1 minute. So, data monitoring for 1 minute time span was found to be sufficient for system noise analysis.

Table IV: LED PIV noise analysis data

Time Span	Mean(μ)	SD(σ)	RSD	PD
1 minute	0.8379	0.0055	0.66%	3.3%
10 minutes	0.8385	0.0056	0.67%	2.8%
20 minutes	0.8378	0.0056	0.67%	2.9%

In figure 4.9, PIV and FWHM fluctuation of instantaneous snapshots is depicted for 1 minute and 10 minute time span. In figure 4.9 (c) and (d) sharp spikes of fluctuation was observed which may be due to the combined effect of fluctuations in power supply and LED internal noise. As the LED noise profile seems to have some repetitive spike patterns it cannot be considered as random noise. Five sets of 1 minute noise data were taken for further analysis. It was found that deviation in mean value of different sets is very much low compared to deviation in instantaneous snapshot data. Table V and VI show noise profile data analysis of different sets.

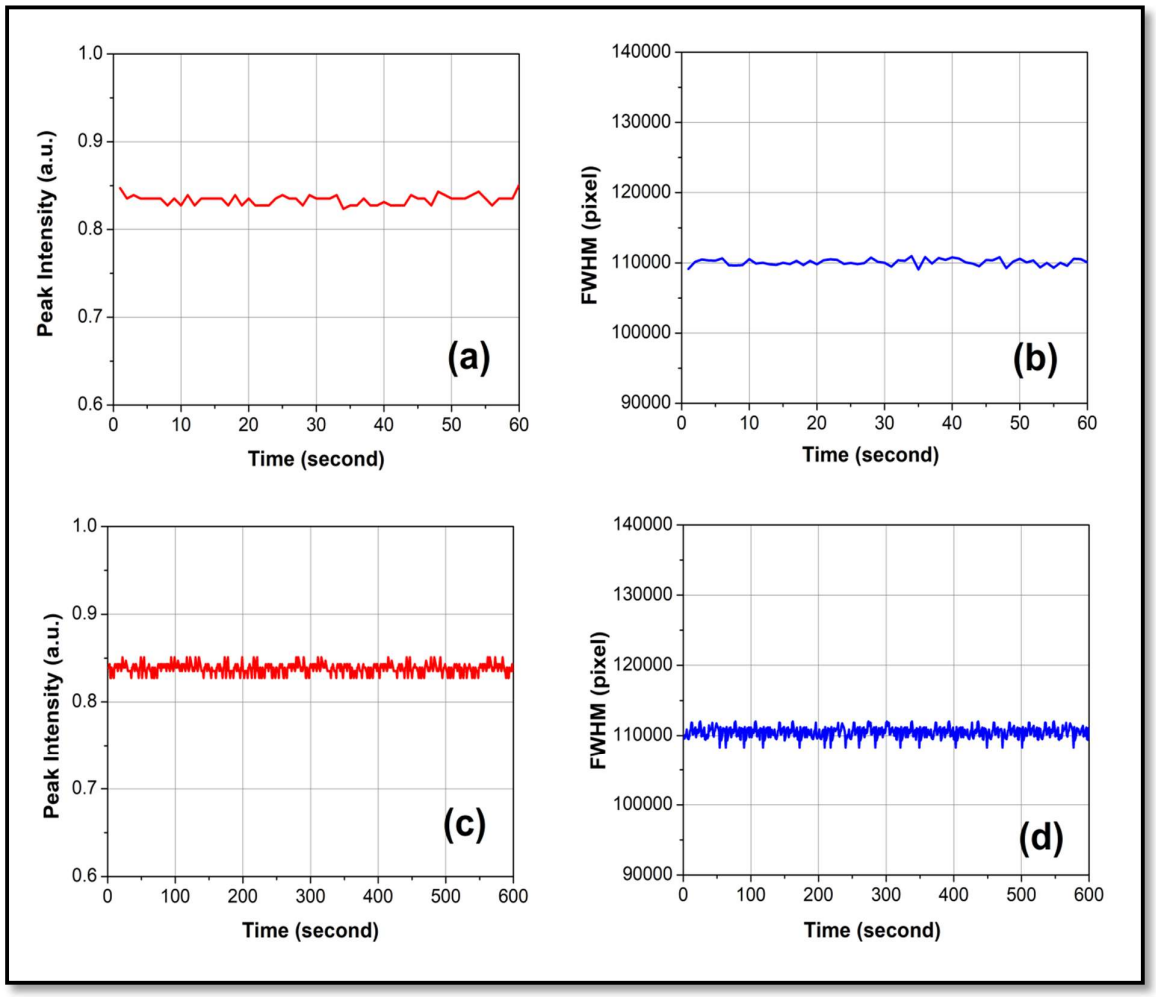

Figure 4.9. LED instantaneous fluctuation in (a) PIV, (b) FWHM for 1 minute time span and (c) PIV, (d) FWHM for 10 minute time span (Interval: 1sec., Sensor sample: CSNC)

Table V: LED PIV MVD analysis table

Set no.	Mean(μ)	SD(σ)	DR	PD
Set I	0.8341	0.0055	*0.0275*	*3.3%*
Set II	0.83856	0.0056	*0.0254*	*3.03%*
Set III	0.83572	0.0056	*0.0254*	*3.04%*
Set IV	0.83856	0.0058	*0.0254*	*3.03%*
Set V	0.83463	0.0055	*0.0208*	*2.5%*

Table VI: LED FWHM MVD analysis table

Set no.	Mean(μ)	SD(σ)	DR	PD
Set I	110053	792	*4512*	*4.09%*
Set II	109172	760	*4186*	*3.83%*
Set III	110003	784	*4373*	*3.97%*
Set IV	109235	766	*4178*	*3.82%*
Set V	109627	787	*44485*	*4.09%*

MVD for five sets of data was found to be 0.5% for PIV and 0.8% for FWHM respectively. So, taking mean value of a particular time span instead of instantaneous snapshot data can reduce LED fluctuations significantly. This simple mean value method sets noise level of the system inside tolerable range for glucose sensing application.

4.9. Laser Diode Source

Laser Diodes (LD) are highly intense and directive, monochromatic optical sources. They are compact in size, consume less power, very much cost effective; but lacks in temperature stability. Red LD (Holmarc DL-R-5, 650nm, 5mW, Intensity fluctuation: ±0.5%) was obtained from Holmarc Opto-mechatronics Pvt. Ltd. for noise analysis of the system and sensor measurements.

4.8.1. Noise Generation

Intensity and phase noise in LD limit their application in precision measurement techniques. The quantum noises are generated due to intrinsic fluctuation in carrier and photon numbers, interaction of lasing field with injected charge carriers etc. Also, re-injection of photon in optical feedback system amplifies this intrinsic fluctuation further [12]. Mode hopping takes place due to increase in case temperature and defects present in

the diode structure. Each LD has unique tuning curve which changes with aging. Also when mode hopping occurs in erratic manner output intensity fluctuates causing undesired noise value [13]. Most LD has much larger noise level than standard gas lasers and for reliable operation, LD requires individually tuned current sources which reduce fluctuation level significantly [14].

4.8.2. Noise Analysis

CSNC samples were used for LD noise analysis. Initially PIV value of transmitted spot was measured for different time span (fixed interval: 1sec.) to ensure whether 1 minute time span was sufficient for LD sources also. It was found that up to approximately 40 minutes, PD was comparatively low for both PIV and FWHM value. But after 40 minutes, fluctuation increases and PD becomes extremely high. To understand the origin of this undesired huge PD value, PIV was monitored for almost an hour and it was found that after approximately 40 minutes, there is a sharp fall on PIV value which is shown in figure 4.10. This could be due to excessive heating effect or some defects in LD. So, the LD was operated for maximum 30 minutes strictly. Within 30 minute continuous operating time, PD was studied for 1, 10 and 20 minute time span and it was found that 1 minute was sufficient here also to capture almost all the fluctuation states.

Table VII: LD PIV noise analysis data

Time Span	Mean(μ)	SD(σ)	RSD	PD
1 minute	0.84879	0.00757	0.89%	3.9%
10 minutes	0.84906	0.00773	0.91%	3.9%
20 minutes	0.84662	0.00743	0.87%	3.6%

After initial stabilization time of 6-7 minutes, the system with LD source becomes ready for operation and after every 30 minutes the system needs to be shut down. After 20-30 minutes of resting time the system is reinitialised again. This is a severe drawback for continuous measurements which come with the choice of using cost efficient LDs. As the use of much stable laser sources can make a significant change in time response, the system with LD source has scope for further improvement.

In figure 4.11, study of instantaneous fluctuation inside and beyond operating time is shown. It was found that inside 30 minute operating time, PD was around 3.9% and 7.8% for PIV and FWHM value respectively. But as 40 minutes crosses, PD increases and becomes as large as 13% and 28% for PIV and FWHM value respectively. Beyond operating time, combined effect of intensity and beam diameter fluctuation of LD produces huge FWHM PD value. In this time range, even mean value method cannot reduce system fluctuation level in tolerable range for biosensing application.

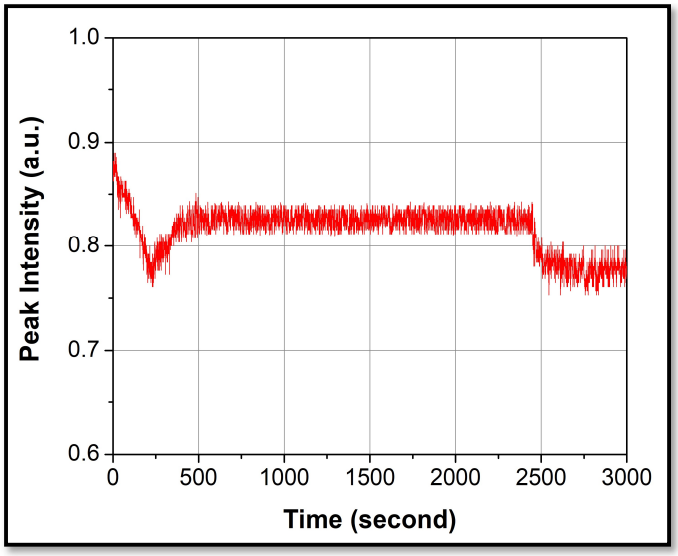

Figure 4.10. PIV study of Holmarc LD (Time span: 50min., Interval: 1sec., Sensor sample: CSNC, Parameter: Transmittance)

Table VIII: LD PIV MVD analysis table

Set no.	Mean(μ)	SD(σ)	DR	PD
Set I	0.84879	0.00757	*0.0329*	*3.9%*
Set II	0.84828	0.00741	*0.0322*	*3.8%*
Set III	0.84662	0.00763	*0.033*	*3.9%*
Set IV	0.84351	0.00739	*0.0315*	*3.7%*
Set V	0.84766	0.00701	*0.0297*	*3.5%*

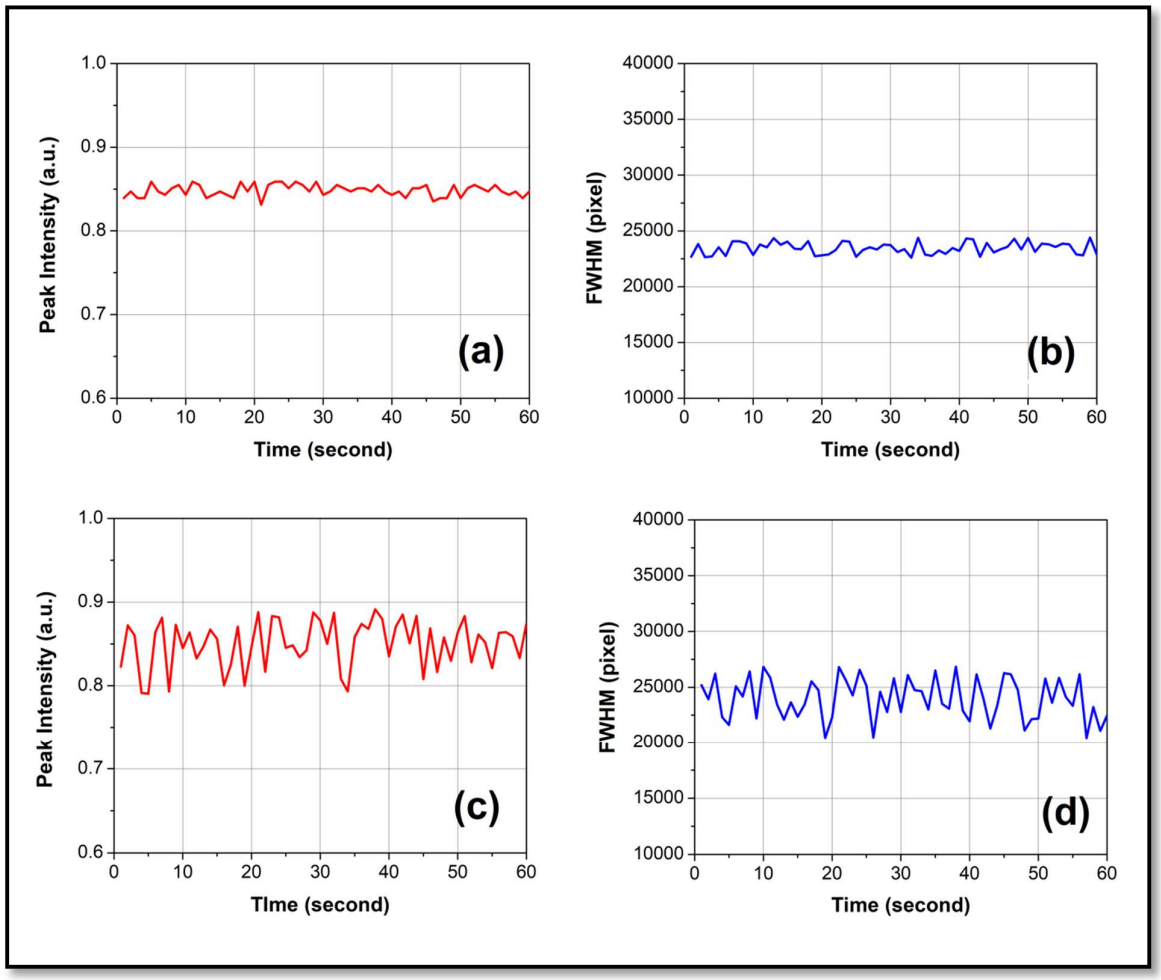

Figure 4.11. LD instantaneous fluctuation in (a) PIV, (b) FWHM inside operating time and (c) PIV, (d) FWHM beyond operating time (Time span: 1min., Interval: 1sec., Sensor sample: CSNC)

Table IX: LD FWHM MVD analysis table

Set no.	Mean(μ)	SD(σ)	DR	PD
Set I	23464	550	*1832*	*7.8%*
Set II	23331	516	*1773*	*7.6%*
Set III	23297	513	*1770*	*7.6%*
Set IV	23423	502	*1733*	*7.4%*
Set V	23258	544	*1814*	*7.8%*

Here also, five sets of 1minute data were taken within operating time to calculate MVD. From Table VIII and IX it is found that, MVD for PIV and FWHM is in the range of 0.6% and 0.9% respectively. Though the MVD is a little large compared to LED MVD, it was still found suitable for glucose sensor application.

4.10. RGB Analysis

The pixels of an image contain intensity information and spectral information in RGB format as discussed in section 4.7. Before converting the image matrix into grayscale, RGB channel information is extracted for RGB analysis. Though actual spectral analysis from RGB channel information is quite a complex procedure; the PIV, FWHM and average value of histograms obtained from individual channels can provide additional non-interlinked parameters to the system. For RGB channel analysis white LED is used as it contains different spectral components in visible range. The white LED that we have used, is actually a phosphorus coated Gallium Nitride (GaN) blue LED. When the phosphorous layer is excited by the blue light emitted from diode, it produces a broad range of emission spectra which in combination with the blue light generates white light [15]. Power spectrum of such LED is shown in figure 4.11. The sharp peak near 440nm is generated from GaN blue LED and the comparatively low intensity broad spectra is produced from phosphorus emission in the range of 500-650nm covering almost all the green, yellow, orange and red shades. So the broad spectrum of the LED is utilised to investigate RGB analysis of the reflected and transmitted spots for PS and CSNC samples.

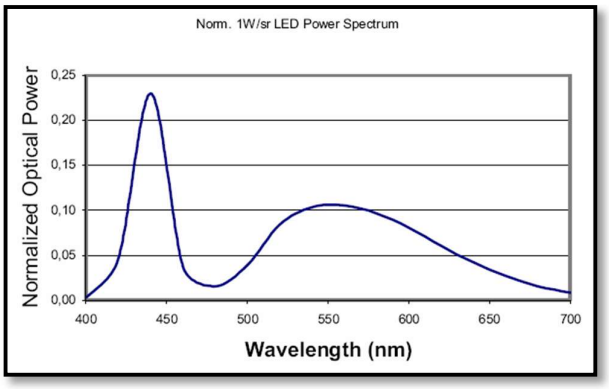

Figure 4.12. White LED power spectrum (Image taken from [16])

The histograms of different channel for PS sample show that blue channel intensity is minimum for reflection from PS surface. This may be due to the fact that shorter wavelengths tend to scatter more because of Rayleigh scattering. Broadening of the blue channel histogram compared to other two channels as shown in figure 4.13 indicates the presence of different intensity levels pixel distribution which proves Rayleigh scattering phenomenon.

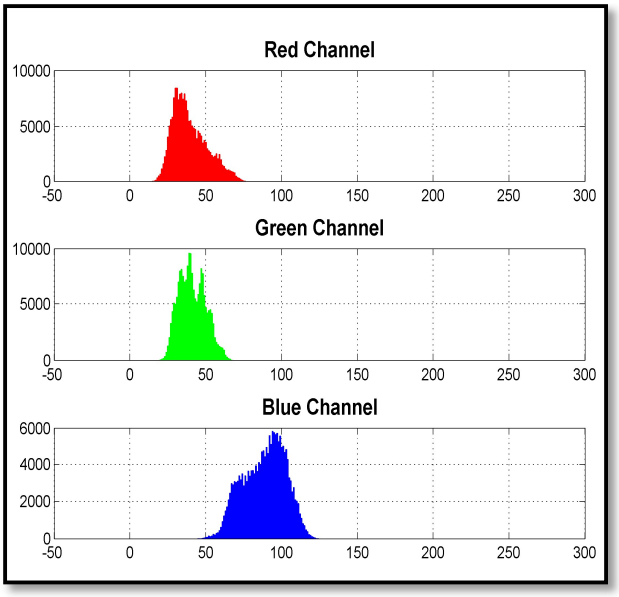

Figure 4.13. RGB histogram of reflected spot from PS sample

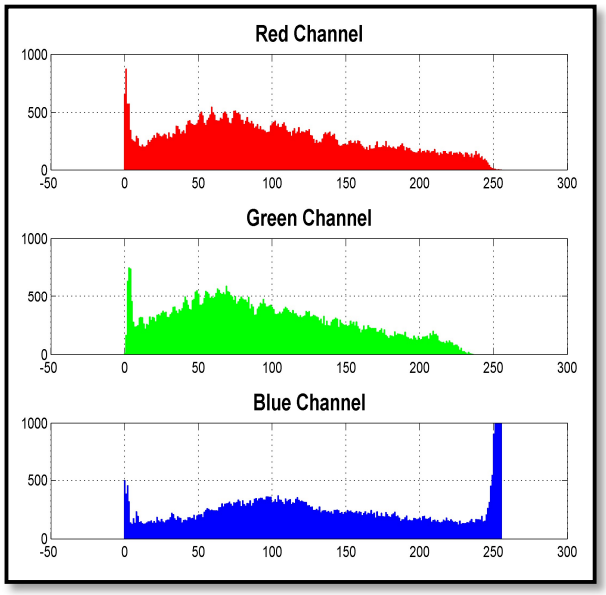

Figure 4.14. RGB histogram of transmitted spot from CSNC sample

For CSNC samples, reflection of White LED was negligible. So transmitted spots were analysed and it was found that most of the pixels are concentrated at blue channel maxima. Red and green channels mostly produce a broad spectrum of low intensity levels for CSNC samples. Such distribution is not suitable for PIV and FWHM analysis of individual histograms. Thus, RGB analysis for CSNC samples needs further investigation for application in biosensor field.

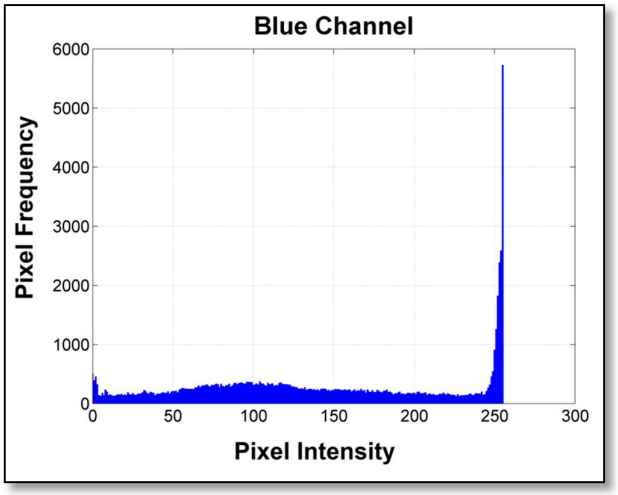

Figure 4.15. Blue channel information of transmitted spot from CSNC sample

4.11. Conclusion and Future Scope

A cost effective, multiparametric optical measurement system has been designed and developed in this chapter. Operating range of the system for reliable sensor measurements has been set to ***0.25a.u.≤ PIV ≤ 0.9a.u***. Detailed noise analysis of individual system component is performed and effect of different component noise on total system noise has been discussed. A simple noise reduction method i.e. Mean Value Method has been proposed for successful application in biosensing field. It was found that rather than extracting parameter information from instantaneous snapshots, if mean value of parameters is taken for 1 minute time span (interval: 1sec., snapshot no.: 60), system noise level can be reduced significantly. A comparison table (Table X) for LED and LD sources has been presented below which shows the gist of all the analysis results found in different section of this chapter. Also, it should be mentioned here that all the noise calculations are

made based on maximum possible fluctuations in the system. In different environmental conditions and times, much lower noise levels have been observed in sensor measurement. For example, the range of MVD in PIV for white LED and LD was found to be 0.08-0.5% and 0.2-0.6% respectively.

Table X: Performance comparison of LED and LD source

Optical Source		PD	PSD	MVD	COT*
White LED	**PIV**	3.3%	0.67%	0.5%	1hr. 40min.
	FWHM	4.1%	0.72%	0.8%	
Laser Diode	**PIV**	3.9%	0.91%	0.6%	30min.
	FWHM	7.8%	2.3%	0.9%	

COT*= Continuous Operating Time

For making the system sufficiently cost effective some sacrifices are made in choosing system components, which led to shorter continuous operating time (COT), lesser system resolution and higher level of noise. With proper choice of component, performance of the system can be improved significantly and the system can also be used in measurement of low concentration of analyte and detection of low dimensional biomolecules. Also detailed investigation of RGB analysis may increase number of parameters of the system further.

References

[1] Rosalba Moretta, Monica Terracciano, Principia Dardano, Maurizio Casalino, Luca De Stefano, Chiara Schiattarella, and Ilaria Rea. "Toward multi-parametric porous silicon transducers based on covalent grafting of Graphene oxide for biosensing applications." Frontiers in chemistry 6 (2018): 583. https://doi.org/10.3389/fchem.2018.00583

[2] Sara Rampazzi, Giovanni Danese, Lucia Fornasari, Francesco Leporati, Franco Marabelli, Nelson Nazzicari, and Armand Valsesia. "Lab on chip: portable optical device for on-site multi-parametric analysis." In 2013 Euromicro Conference on Digital System Design, pp. 807-810. IEEE, 2013.

[3] Simon Pevec, and Denis Donlagić. "Multiparameter fiber-optic sensors: A review." Optical Engineering 58, no. 7 (2019): 072009. https://doi.org/10.1117/1.OE.58.7.072009

[4] David G. Myszka. "Improving biosensor analysis." Journal of molecular recognition 12, no. 5 (1999): 279-284.

[5] Peter Stenlund, Åsa Frostell-Karlsson, and Olof P. Karlsson. "Studies of small molecule interactions with protein phosphatases using biosensor technology." Analytical Biochemistry 353, no. 2 (2006): 217-225.

[6] Anjali Struss, Patrizia Pasini, C. Mark Ensor, Nilesh Raut, and Sylvia Daunert. "Paper strip whole cell biosensors: a portable test for the semiquantitative detection of bacterial quorum signaling molecules." Analytical chemistry 82, no. 11 (2010): 4457-4463.

[7] Rainer Hain, Christian J. Kähler, and Cam Tropea. "Comparison of CCD, CMOS and intensified cameras." Experiments in fluids 42, no. 3 (2007): 403-411. https://doi.org/10.1007/s00348-006-0247-1

[8] S. L. Rumyantsev, S. Sawyer, N. Pala, M. S. Shur, Yu Bilenko, J. P. Zhang, X. Hu, A. Lunev, J. Deng, and R. Gaska. "Low frequency noise of light emitting diodes." In Noise in Devices and Circuits III, vol. 5844, pp. 75-85. International Society for Optics and Photonics, 2005. https://doi.org/10.1117/12.608559

[9] James J. Brophy. "Fluctuations in luminescent junctions." Journal of Applied Physics 38, no. 6 (1967): 2465-2469. https://doi.org/10.1063/1.1709929

[10] S. L. Rumyantsev, M. S. Shur, Yu Bilenko, P. V. Kosterin, and B. M. Salzberg. "Low frequency noise and long-term stability of noncoherent light sources." Journal of applied physics 96, no. 2 (2004): 966-969. DOI:10.1063/1.1763225

[11] Sameer Chhajed, Yangang Xi, Thomas Gessmann, Jing-Qun Xi, Jay M. Shah, Jong Kyu Kim, and E. Fred Schubert. "Junction temperature in light-emitting diodes assessed by different methods." In Light-Emitting Diodes: Research, Manufacturing, and Applications IX, vol. 5739, pp. 16-24. International Society for Optics and Photonics, 2005. DOI:10.1117/12.593696

[12] Moustafa Ahmed, Minoru Yamada, and Masayuki Saito. "Numerical modeling of intensity and phase noise in semiconductor lasers." IEEE journal of quantum electronics 37, no. 12 (2001): 1600-1610. **DOI:** 10.1109/3.970907

[13] T. Acsente. "Laser diode intensity noise induced by mode hopping." Romanian reports in physics 59, no. 1 (2007): 87.

[14] Dirk Semleit, Andreas Trampe, and Heinz Fissan. "Fluctuations and noise of the optical output power of laser diodes and the effect on optical particle size determination." Aerosol science and technology 26, no. 4 (1997): 356-367. https://doi.org/10.1080/02786829708965436

[15] Theerawut Jinayim, Somchai Arunrungrasmi, Tanes Tanitteerapan, and Narong Mungkung. "Highly efficient low power consumption tracking solar cells for white LED-based lighting system." International Journal of Electrical Computer and Systems Engineering 1, no. 2 (2007): 1307-5179.

[16] FJ Lopez Hernandez, E. Poves, R. Perez-Jimenez, and J. Rabadan. "Low-cost diffuse wireless optical communication system based on white LED." In 2006 IEEE International Symposium on Consumer Electronics, pp. 1-4. IEEE, 2006. DOI: 10.1109/ISCE.2006.1689461

Chapter 5

Chapter 5

Thin Film Multiparametric Glucose Sensor

5.1. Introduction

Diabetes mellitus causes high level of blood glucose in human body and if left untreated can lead to heart disease, kidney failure, vision loss, nerve damage, cognitive problems and many more [1]. Normal level of glucose in human blood is found to be 4-5.8mM (72-105mg/dl). In hyperglycemia, serum glucose level becomes greater than 5.8mM for 10-12 hours fasting and 9.2mM for postprandial measurements and in hypoglycemia it becomes less than 3.6mM [1]. Early detection of blood glucose level can prevent severe consequences thus making glucose sensors an important field of research. Also, constant

need of diabetic patients to monitor their glucose level in daily basis has led to investigation and innovation of different types of glucose sensors for cost effective and reliable measurements. A lot of works has been reported for effective electrochemical and optical sensing of blood glucose [2-16] which has already been discussed elaborately in chapter 1. Image processing based optical multiparametric sensing is a new approach where several interlinked or non-interlinked optical parameters are monitored simultaneously. Such multiparametric detection systems combined with thin film sensors have the potential for sensitive, reliable and cost effective glucose measurement.

In this chapter, PS and CSNC thin film glucose sensors have been thoroughly studied with optical multiparametric measurement setup discussed in chapter 4. The sensor performance has been analysed in terms of different biosensor characteristics like sensitivity, selectivity, response time, stability etc. and both sensors have been compared with existing close works by different research groups. Finally, a comparison chart has been presented between the two sensors in the conclusion section.

5.2. Biosensor Characteristics

Every sensor has some characteristics by which their merit is determined. These characteristics can either be obtained from the calibration curve or individual study. For biosensors, the list of these main characteristics is given below [17].

- ***Sensitivity:*** Sensitivity of a biosensor is defined as the response or amount of change in the output per unit concentration of analyte. Sensitivity can be calculated from the slope of linear calibration curve. Calibration curve or response curve is the output signal response of a sensor vs. analyte concentration plot. Thus, the slope gives response per unit analyte concentration for linear systems. For nonlinear curves sensitivity is not a fixed quantity.
- ***Selectivity:*** Selectivity is the ability of a sensor to detect a specific analyte from a complex solution. In general, the testing solutions are complex mixtures and they contain large number of different elements which if attached in sensor may produce unnecessary background noise. If the noise level is high enough it can interrupt with specific analyte detection. Thus, bioreceptors play a crucial role in the selectivity of a

biosensor, as they can selectively capture target analyte from complex solutions. For selectivity study, sensor response is observed for solutions containing different analytes and compared with the response produced by target analyte solution for a particular concentration range. If the sensor produces low response value for other solutions and high response value for target analyte solution, it can be called sensitive towards that specific analyte of interest.

- ***Dynamic Range:*** It is the range of analyte concentration where the biosensor produces reliable output response. Dynamic range can be directly obtained from the x axis range of linear calibration or response curve.

- ***Limit of Detection (LOD):*** The minimum amount of analyte concentration that the sensor can measure is called LOD [18]. It is generally defined as,

$$\boldsymbol{LOD = [Blank + 3 \times \sigma_{blank}]/m}$$

Where, Blank = sensor output in absence of analyte

σ_{blank} *= Standard deviation in blank data*

m = Slope of the calibration curve

When blank is eliminated for final sensor output in relative response measurement, LOD becomes just $\boldsymbol{[3 \times \sigma_{blank}]/m}$ [18].

- ***Response Time:*** When the sensor is exposed to analyte, it takes some time to produce steady state response and this time is called response time (τ). The smaller the value of τ, the better the sensor performance. To measure τ, sensor output is plotted with respect to time. After analyte introduction, time taken for the sensor output to reach 90% of the steady state value, is considered to be the response time.

- ***Repeatability:*** Repeatability is defined as ability of the sensor to produce response close to the initial response upon testing multiple times keeping other parameters fixed. Repeatability provides information about the sensor's multi-time usage capability. If a sensor sample can produce results close to the initial value for different measurement cycles the sensor is called repeatable and suitable for multi-time use.

- ***Reproducibility:*** Sensors fabricated under identical preparation and environmental conditions should ideally produce exactly same calibration curve. In practical cases,

output response deviates even for identical samples. Reproducibility is the ability to produce output response close to mean value for measurements with different identical sensor samples.

- ***Stability:*** It is the measure of drift in output response due to ambient changes. The main cause of instabilities in a biosensor, are due to temperature change, degradation of bio-receptors over time and forming unstable bonding with analytes. Stability of a biosensor is crucial for long term continuous monitoring of analytes.

5.3. Glucose Sensing Mechanism

Both PS and CSNC thin films were functionalized with Glucose Oxidase (GOX) enzyme for selective glucose sensing. In aqueous solution at pH 7, glucose exists in cyclic hemiacetal form. Almost ~ 63% glucose molecules form β-D-glucopyranose while only ~ 37% exists as α-D-glucopyranose [19]. Linear and furanose formation is negligible in aqueous solution. GOX enzyme has the ability to selectively bind to β-D-glucopyranose in glucose solution. To maintain solution equilibrium more α-D-glucopyranose structures convert to β-D-glucopyranose which is further consumed in the reaction process [20].

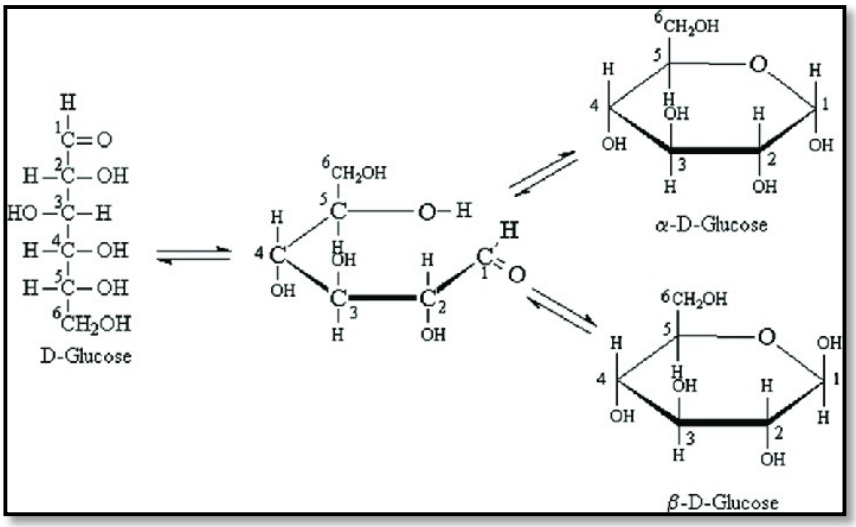

Figure 5.1. Glucopyranose structure formation in aqueous solution (Image taken from [19])

GOX acts as a catalyst in the oxidation reaction of glucose which produces D-glucono-δ-lactone and hydrogen peroxide. The FAD group (flavin adenine dinucleotide) present in GOX takes part in redox reaction and becomes $FADH^-$ upon accepting electron

[20]. $FADH^{-}$ is further oxidised by molecular oxygen which produces H_2O_2 and FAD. So GOX molecules only aid the redox reaction process while remaining intact after reaction. In the next step of reaction, D-glucono-δ-lactone reacts spontaneously with water molecules and produces gluconic acid. These gluconic acid crystals change surface and internal properties of thin film sensors producing significant change in optical response.

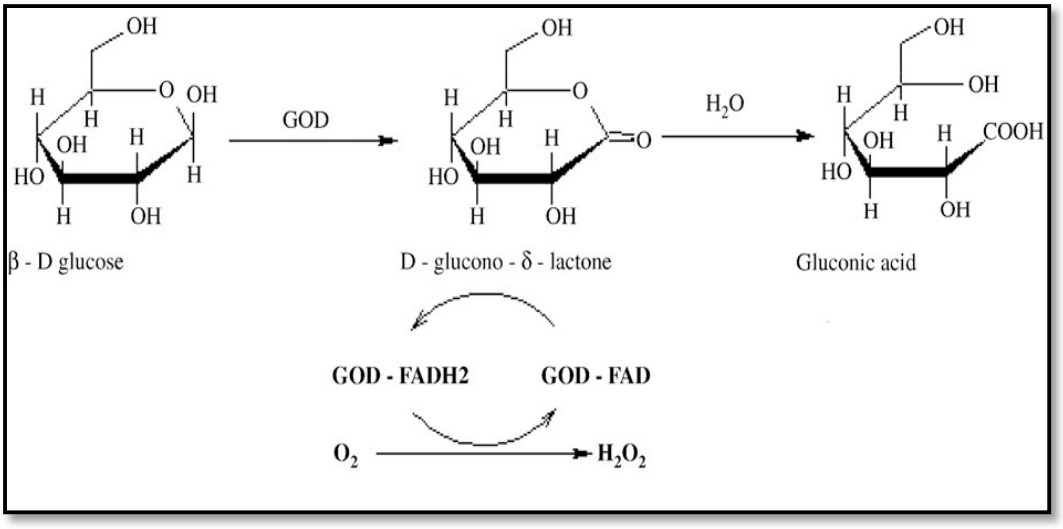

Figure 5.2. Glucose oxidase (GOX or GOD) catalytic reaction (Image taken from [20])

5.4. PS Glucose Sensor

Detailed study of PS thin film glucose sensor is performed in multiparametric optical setup and results are discussed thoroughly in this section based on different biosensor characteristics. As discussed in chapter 2, nano PS samples with 5 minute etching time produced best sensor response. Also, in chapter 4 it was observed that white LED proved to be a suitable source for PS sensor analysis. Thus, all the sensor measurements were performed using white LED on PS samples having 5 minute etching time.

5.4.1. Characterization

Changes in morphology were observed for PS thin films due to surface functionalization and further glucose introduction. FESEM (JOEL, JSM-7610F) image of PS surface (figure 5.3(a)) shows that the particle diameters are in the range of 18-25nm as observed in chapter 2 also. After surface functionalization, change in morphology was

observed in higher magnification range. Clustered attachment of GOX molecules due to physisorption process is clearly visible on PS surface in figure 5.3(b). Binding of glucose molecules on GOX sites for lower glucose concentration (5mM) and overall glucose absorption on PS thin film surface for higher glucose concentration (30mM) can be observed in figure 5.3(c) and (d) respectively. As GOX sites produce gluconic acid after introduction of glucose solution, the uneven region around GOX in figure 5.3(c) might be generated due to loosely attached gluconic acid crystals.

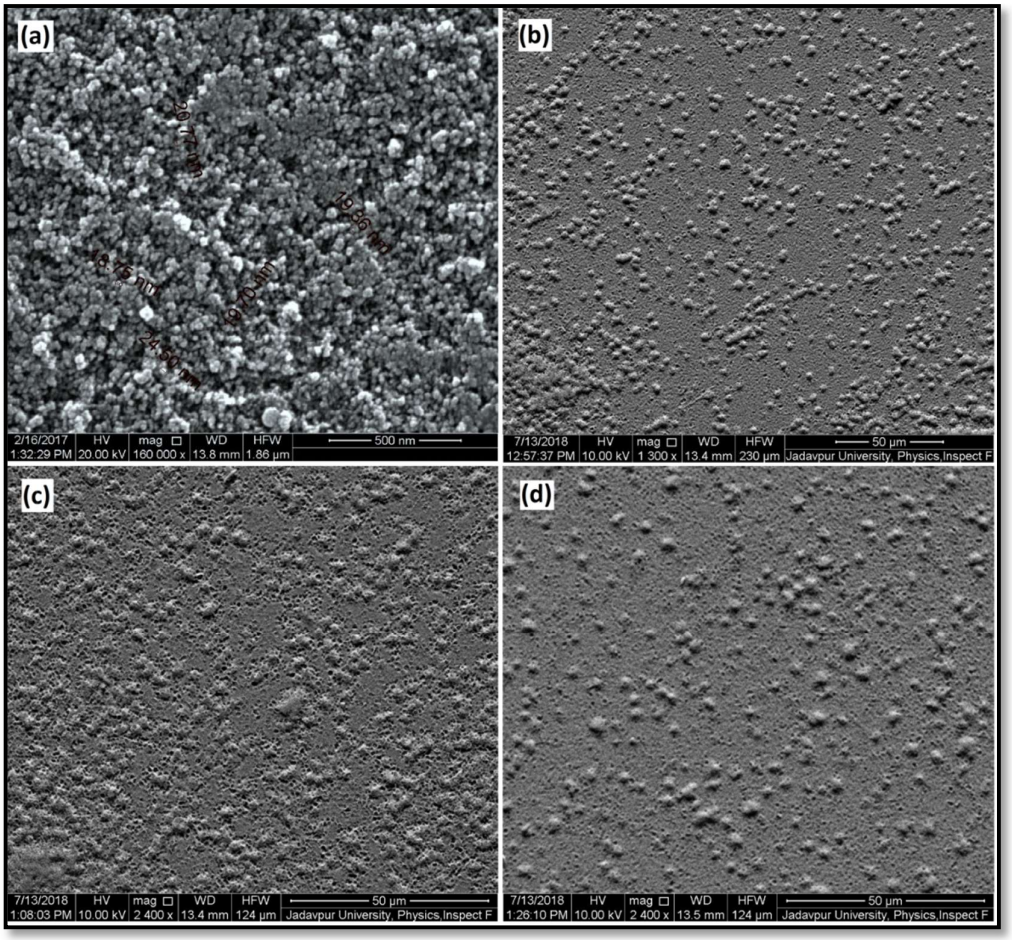

Figure 5.3. FESEM micrographs of PS thin film surface (a) before and (b) after GOX physisorption, after (c) 5mM and (d) 30mM glucose solution absorption respectively.

AFM was performed to study the surface roughness before and after glucose absorption (figure 5.4). 3D sinusoidal surface roughness has been observed with period approximately 1µm for GOX modified PS film. Surface roughness value was found to increase from 75nm to 104nm (r.m.s. value) due to 5mM glucose solution absorption. So,

deposition of gluconic acid crystals around GOX site increases the surface roughness which in turn affects reflectance and scattering parameters.

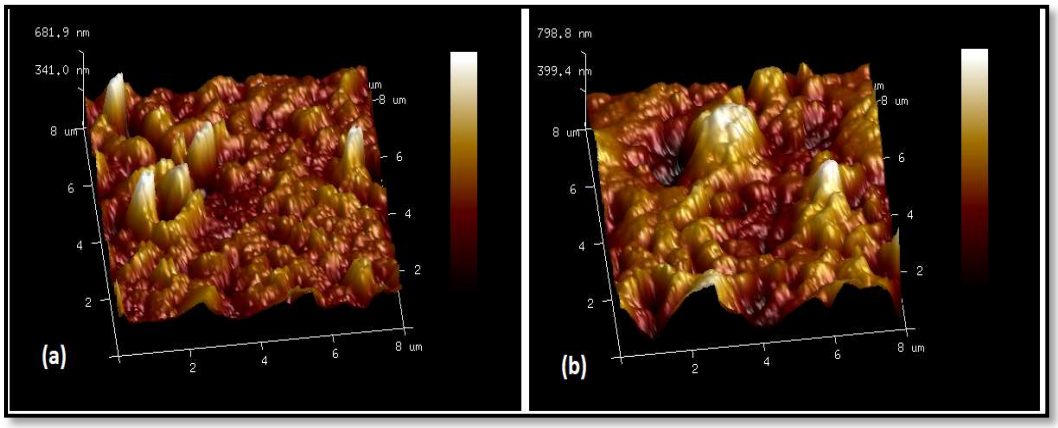

Figure 5.4. AFM images of sensor surface (a) before and (b) after 5mM glucose solution absorption

5.4.2. Image Processing Output

As PS sensors are non-transparent in visible spectra, only three optical parameters i.e. specular reflectance or simply reflectance (R), Surface Scattering (SS) and Output Power which is termed as Absorption (A) here, can be obtained. For absorption calculation, only the 3D volume under Gaussian plot produced by reflected spot IDM is considered.

Effect of 30mM glucose solution introduction is analysed in figure 5.5. Intensity pattern of the two IDMs (figure 5.5 (a) & (b)) are basically contour plots, which show significant fall in image peak intensity and rise in beam divergence or scattering due to glucose absorption. To compare these two IDMs, 3D and 2D Gaussian models are developed as shown in figure 5.5(c), (d) and (e) respectively. In 2D Gaussian model (figure 5.5(e)), only a central row of the IDMs has been considered for plotting intensity distribution before and after 30mM glucose absorption. It is evident that due to glucose absorption, specular intensity falls and scattering increases. FWHM can be calculated from 2D model also, but it decreases system sensitivity as only a single row is considered as FWHM value. In 3D Gaussian model, FWHM is actually an area with large number of pixels having half of the maxima value, thus increasing sensitivity. The 3D Gaussian models of figure 5.5(c) and (d) contain same information from the two IDMs, but for ease of viewing changes in reflectance and scattering, slight modification has been done at the time of plotting. In figure 5.5(c),

0mM reference IDM is plotted as shaded curve and 30mM IDM is plotted as solid curve to observe fall of peak intensity. In figure 5.5(d), shaded and solid curves are interchanged i.e. 0mM reference IDM is plotted as solid curve and 30mM IDM is plotted as shaded curve to observe increase in FWHM value. Volume under the Gaussian plots represent output power which decreases compared to 0mM reference value with increasing glucose concentration. This indicates increase in optical absorption with glucose attachment.

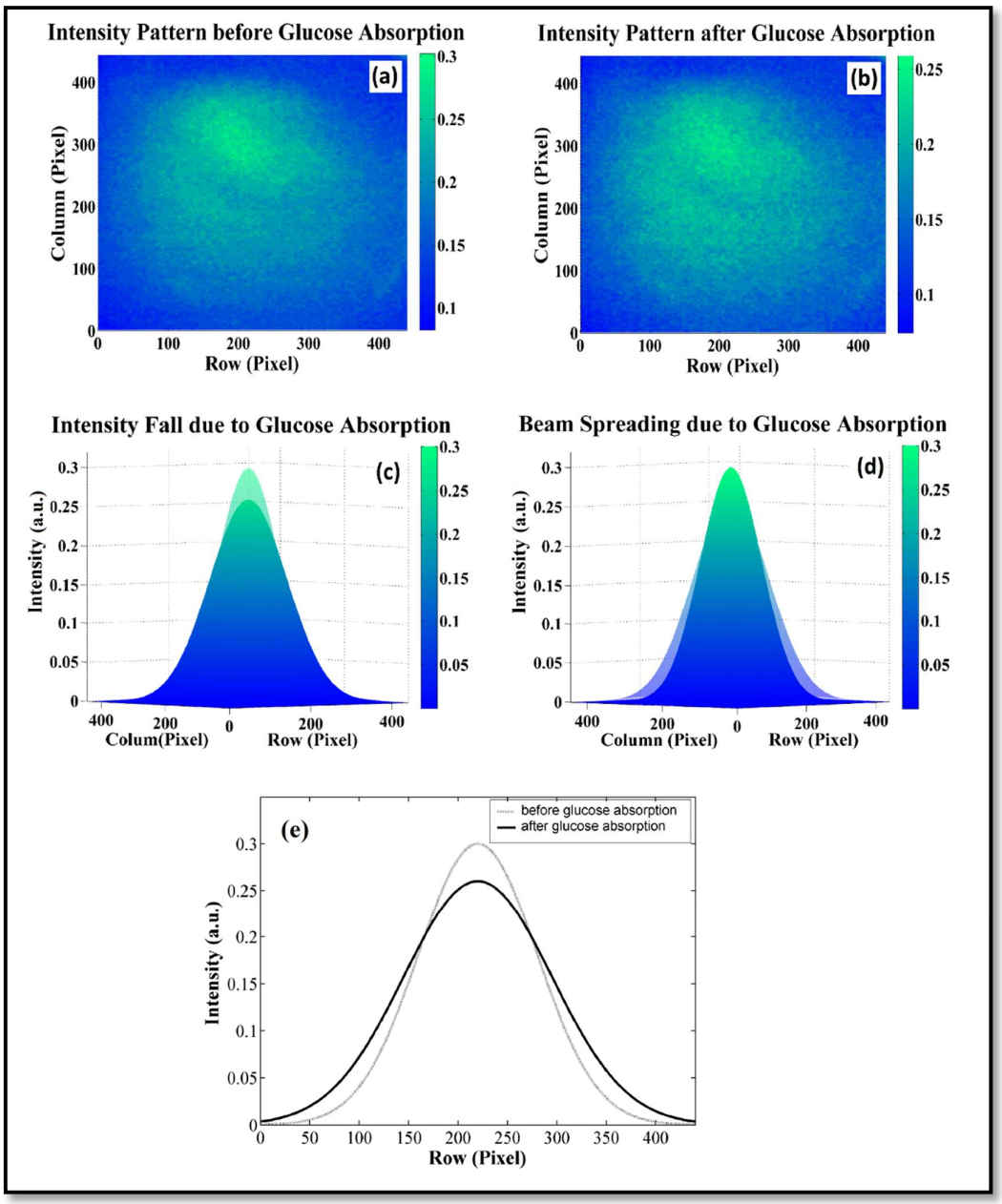

Figure 5.5. Reflected IDMs (a) before and (b) after 30mM glucose solution absorption. (c), (d):3D Gaussian curve corresponding to IDM plot (a), (b) respectively. (e): 2D Gaussian comparison curve for a central row of the two IDMs.

5.4.3. Sensitivity

%Response was measured for 1-30mM glucose concentration range. Baseline data (before glucose introduction) was taken first, and then 0.25ml of glucose solution was sprayed on sensor surface. After 10 minutes drying time, response data was taken again. It was found that while reflectance and scattering parameters show good linear response; absorption parameter shows nonlinear response (figure 5.6). Thus, multiparametric sensing is possible for PS thin film sensors but all the parameters might not show linear response.

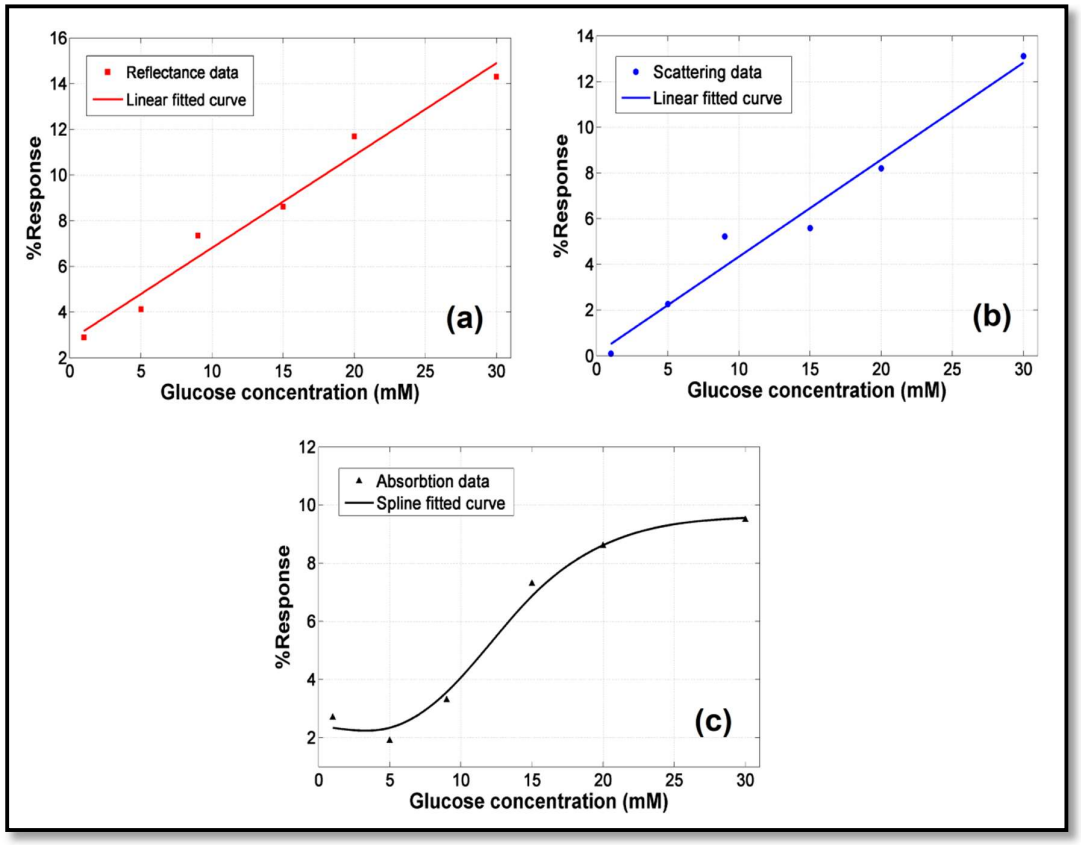

Figure 5.6. Response curve of PS sensor for (a) Reflectance parameter, (b) Scattering parameter and (c) Absorption parameter

Figure 5.7 shows individual parameter sensitivity (%Response/Glucose concentration) in the whole detection range of the sensor. It can be observed from the figure that for lower concentration, specular reflection and absorption sensitivity have higher values compared to higher glucose concentrations. Whereas, scattering sensitivity is initially low, but as surface roughness increases with increasing glucose concentration more and more scattering takes place. From the linear fit of calibration curves in figure 5.6,

maximum sensitivity for reflectance and scattering parameters were found to be 0.40mM^{-1} and 0.42mM^{-1} respectively (Annexure V).

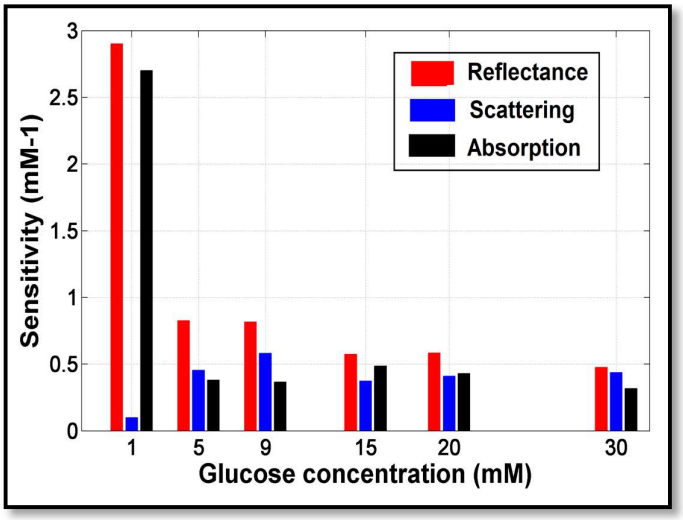

Figure 5.7. Sensitivity of individual parameters

5.4.4. Dynamic Range and LOD

The linear dynamic range for PS sensors was found to be 2-30mM for reliable glucose sensing which covers both hypo and hyper glycemia levels. System resolution was found to be 0.33mM corresponding to 0.0039a.u. step size of detector camera. Due to presence of LED noise, blank data fluctuates and system LOD increases. Using mean value method discussed in chapter 4, LOD can be reduced into tolerable range. Considering S/N ≥ 3, minimum LOD was found 1.23mM for reflectance parameter (calculated in Annexure V).

5.4.5. Selectivity

Selectivity study of PS sensor was performed with 15mM glucose, fructose, galactose, maltose and sucrose solution. Phosphate buffer solution (PBS) was considered as control. In figure 5.8 it is observed that the sensor shows good selectivity towards glucose solution. Response due to PBS lie in the noise range of the system while for fructose, galactose, maltose and sucrose significant amount of %Response was observed, though still they were much lower compared to glucose response. This may be due to small amount of non-selective molecular attachment on sensor surface.

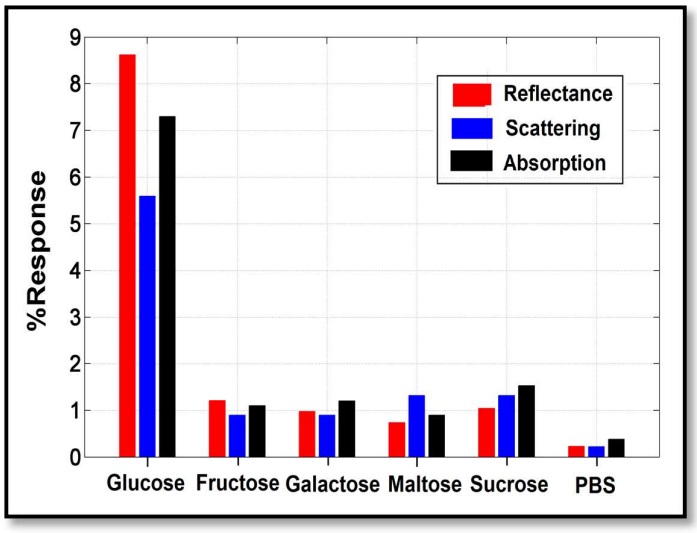

Figure 5.8. Selectivity of PS sensor towards glucose (15mM response)

5.4.6. Response Time

Transient response of PS sensor was observed to measure response time (τ) in figure 5.9. 15mM glucose solution was used for the measurement and change in reflectance was observed with time.

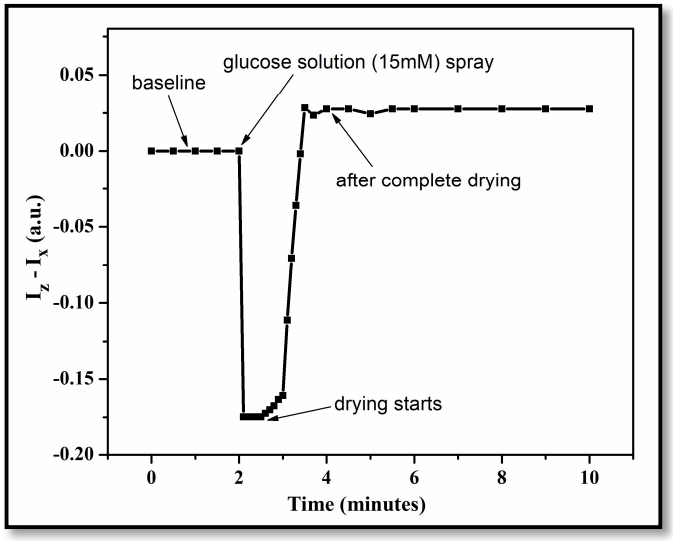

Figure 5.9. Transient response of PS sensor

Specular reflectance value for 0mM glucose solution has been chosen as the baseline (I_z). When different concentrations of glucose solution are sprayed on the sensor surface, a sharp peak of specular reflection intensity (I_x) is observed. This is caused due to the lensing effect of water layer present on top of the sensor surface. So, in (I_z-I_x) vs. time plot (figure

5.9), a sharp dip from zero baseline was observed. As drying starts, (I_z-I_x) value increases and after about 180 seconds saturates at a value higher than the baseline value. The (I_z-I_x) value reaches at 90% of the steady state value in approximately 90 seconds. So, the response time of the sensor is considered to be ~ 90 seconds; but this time may further be reduced by reducing drying time.

5.4.7. Repeatability

PS sensors were found suitable for multi-time usage. In figure 5.10, six cycles of reflectance response for 15mM glucose solution is depicted for same PS sample and it was found that response in 6th cycle drops to only ~ 87% of 1st cycle value which makes the sensor effective for multi-time use. The reason behind almost unchanged response for repeated measurement is that GOX enzyme remains unaffected in the gluconic acid production as they only catalyse the reaction process. Gluconic acids are soluble in water and when PS sensors are washed in Tween20 followed by DI water after every use, Gluconic acid build-ups around GOX site is removed. Thus, PS sensors can be used repeatedly almost up to 12-15 cycles without significant fall in response.

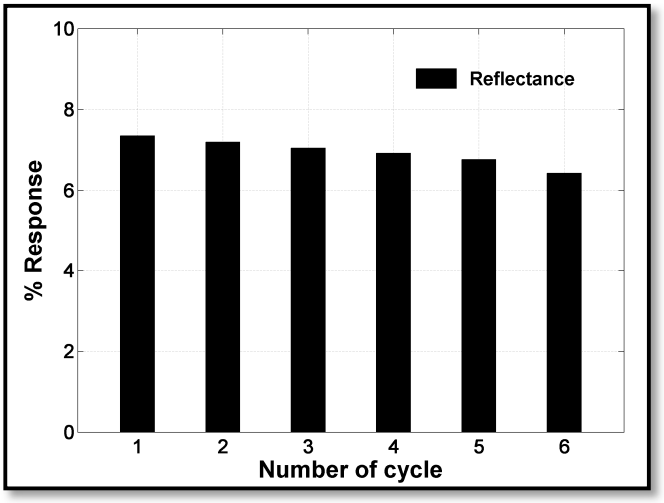

Figure 5.10. Repeatability of PS sensor

5.4.8. Stability

Storage stability of the PS sensors was observed for a span of 28 days for storage temperature of 4^{o}C. 15mM glucose solution was prepared freshly everyday and %response

was measured after every two days. It was found from figure 5.11 that after first 10 days %response slowly decreases and after 25 days falls rapidly due to degradation of GOX enzyme. In 25th day %response of reflectance becomes almost 78% of the first day value, thus it can be concluded that maximum storage time for PS sensors is not more than 20 days for reliable operation.

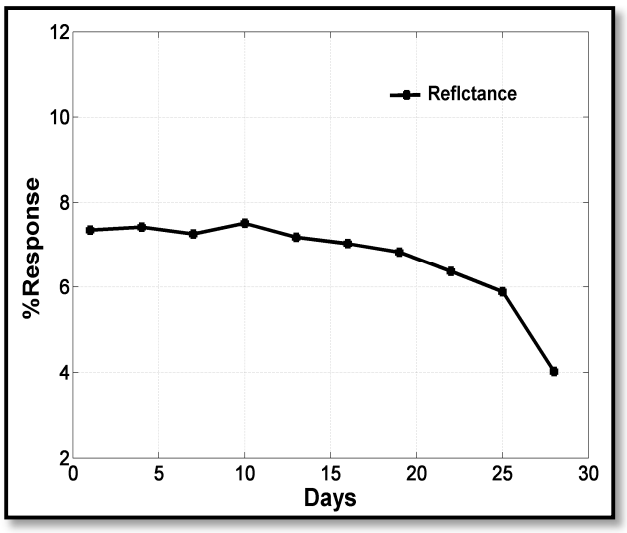

Figure 5.11. Storage stability of PS sensor

5.4.9. RGB Histogram Analysis

RGB analysis of the images was also performed by separating red, green and blue channels. Histograms of the three channels are plotted in figure 5.12 for baseline and 30mM glucose solution data image. As discussed in chapter 4; PS samples show distinct Gaussian pattern of histogram distribution for individual channels. So, PIV and FWHM of individual channel can be observed to understand the effect of glucose absorption. In figure 5.13 %Response of the three channel's PIV with increasing glucose concentration is plotted. Though significant amount of response is observed for red and green channels, they show nonlinearity. While blue channel shows linear increase in %Response and it was found to be much more sensitive than the other two channels. As PS samples have a tendency to pass higher wavelengths, most of the blue channel information is reflected back. So, blue channel PIV becomes a significantly sensitive parameter which can be added as a non-interlinked parameter to the system.

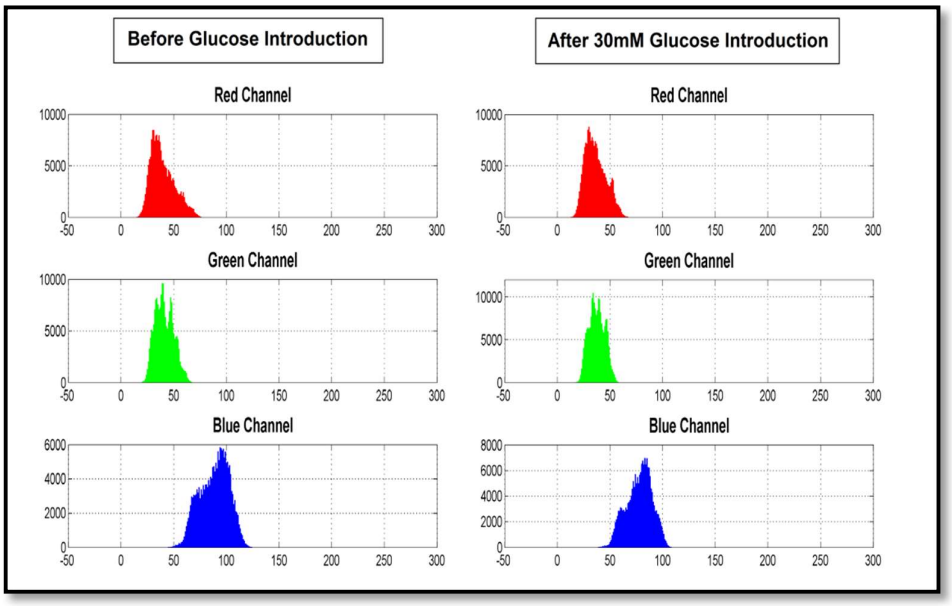

Figure 5.12. Histograms of three RGB channels before and after glucose absorption

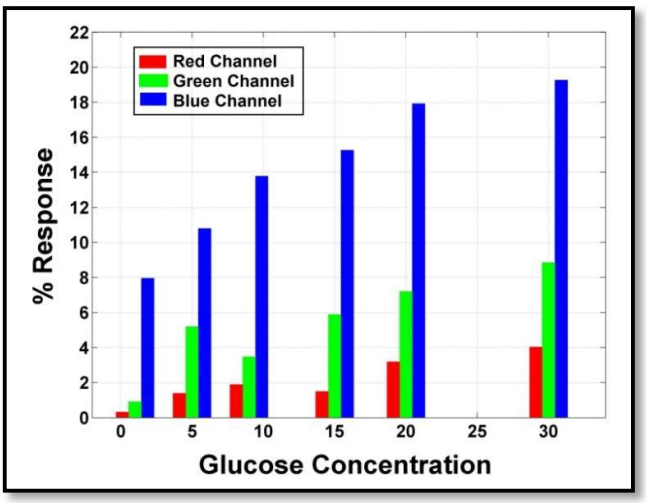

Figure 5.13. Glucose response plot for three RGB channels

5.5. CSNC Glucose Sensor

CSNC thin film glucose sensor performance based on different biosensor characteristics is presented in this section. According to chapter 3, CSNC thin films with SiNp diameter ~ 300nm were most suitable for biosensing application. So such films were fabricated on glass substrate and all the sensor measurements were done with red laser diode source (λ=650nm).

5.5.1. Characterization

FESEM micrographs in figure 5.14 show even pore distribution on CSNC surface after NaOH etching. From the cross sectional view, approximate thickness of the drop casted films were found to be 4.7-5.5µm and a sponge like internal structure was also observed. At the time of etching, first SiNp on the top surface is attacked and external surface pores are generated. Then with time, hot NaOH flows through the pores and dissolves the internal SiNps producing numerous interlinked channels thus finally generating a sponge like net structure. Surface pore diameters were found to be around 194-247nm for CSNC film and shrinkage of pore size was observed after GOX attachment shown in figure 5.14(c).

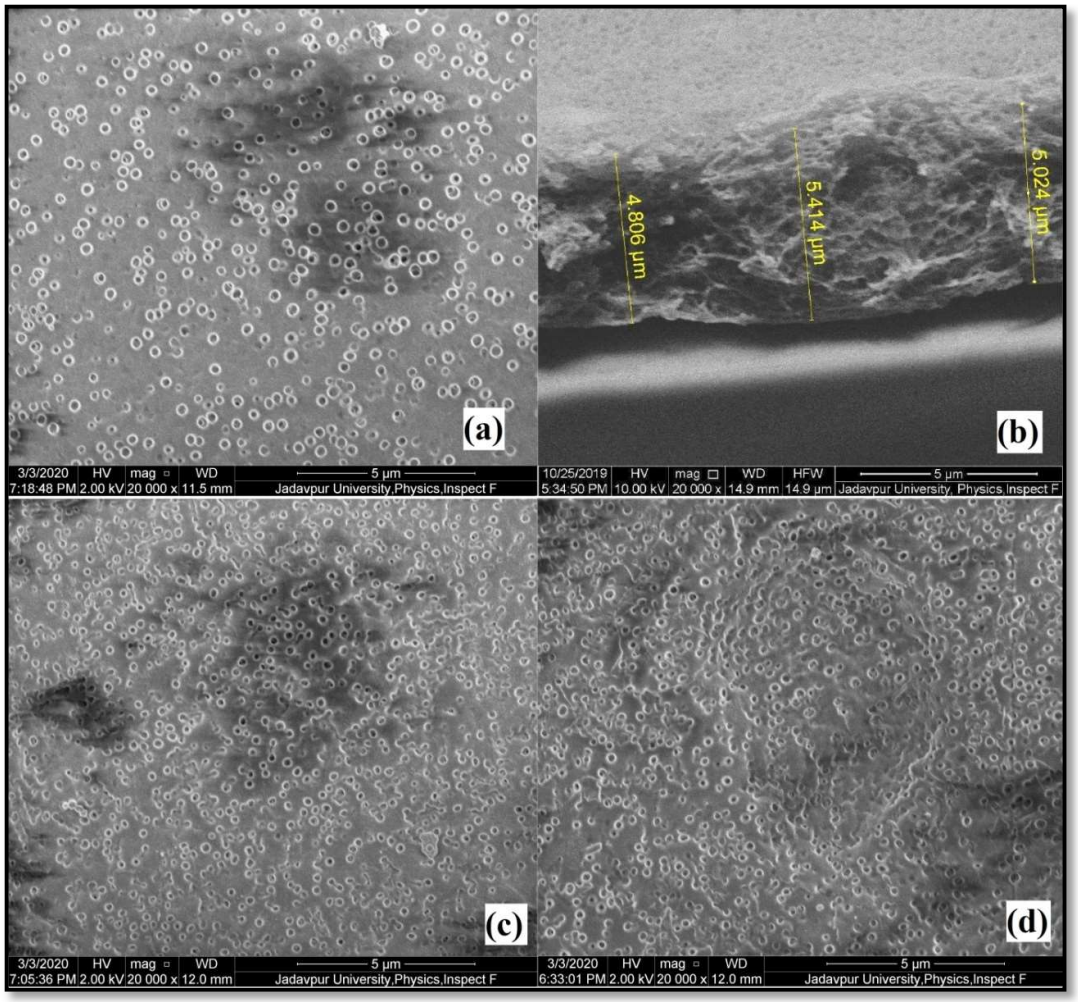

Figure 5.14. FESEM micrograph of (a) CSNC film top view, (b) CSNC film cross section, (c) GOX modified CSNC film and (d) GOX modified film after glucose solution introduction

Absorbance spectra of pure CSNC sample has already been discussed in chapter 3. In figure 5.15(a), broad peak around 3550-3200cm^{-1} is produced due to intermolecular O-H group stretching in chitosan polymer chain. Also peak at ~3454cm^{-1} indicates presence of N-H bond stretching of primary amine. Absorption band in 800-1260cm^{-1} range is described as different SiO_2 peaks of SiNp and residual organic groups [21]. Absorption peak at ~1735cm^{-1} represents C=O stretching of carboxylic acid which in this case is acetic acid present in composite solution mixture discussed in chapter 3. For GOX functionalised surface in figure 5.15(b), absence of 1735cm^{-1} carbonyl group peak and existence of strong imine (C=N) group peak at ~1642cm^{-1} is observed. This indicates successful attachment of GOX molecules into CSNC film because in surface functionalization process all the carbonyl groups are replaced by imine groups. After introduction of glucose solution, again the C=O stretching peak of carboxylic acid appears at ~1711cm^{-1} in figure 5.15(c) which indicates further generation of gluconic acid in GOX sites [22]. 1720-1706cm^{-1} is reported to be the band for carboxylic acid dimers and in anhydrous form, gluconic acid crystals forms dimers which indicates the presence of gluconic acid crystals in the sensor film upon evaporation of liquid analyte solution.

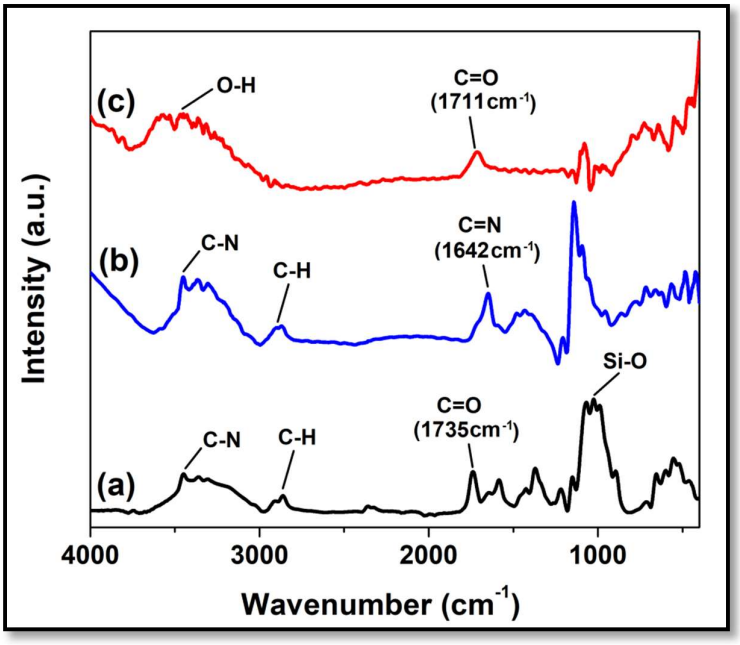

Figure 5.15. FTIR spectra of (a) pure CSNC film, (b) GOX modified CSNC film and (c) GOX modified film after glucose introduction

5.5.2. Image Processing Output

Transmitted and reflected spot IDMs were analysed to find the changes in five interlinked parameters due to glucose absorption on CSNC sensors. Figure 5.16 shows 2D IDM plot of transmitted spot before and after 30mM glucose absorption. From the Gaussian fit plots in figure 5.17, it is clearly visible that transmittance (T) increases and internal scattering (IS) decreases due to glucose absorption. From cross-sectional view of FESEM micrographs, presence of sponge like internal structure can be seen in CSNC films. With glucose introduction interlinked channels become filled with glucose molecules thus reducing inter-channel light propagation or scattering. This may be the effect of reduced IS value and more focussed beam than air filled channels, which in turn increases T value.

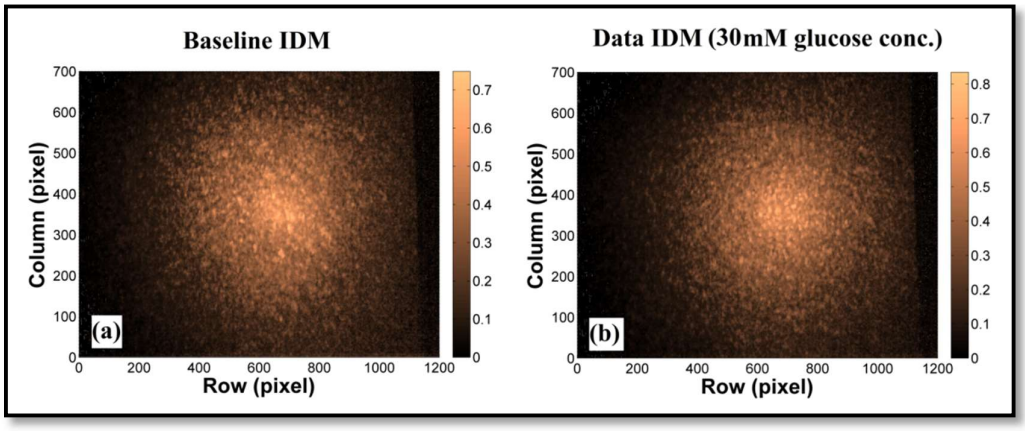

Figure 5.16. 2D IDM plot of (a) baseline snapshot and (b) snapshot after 30mM glucose introduction for transmitted spot

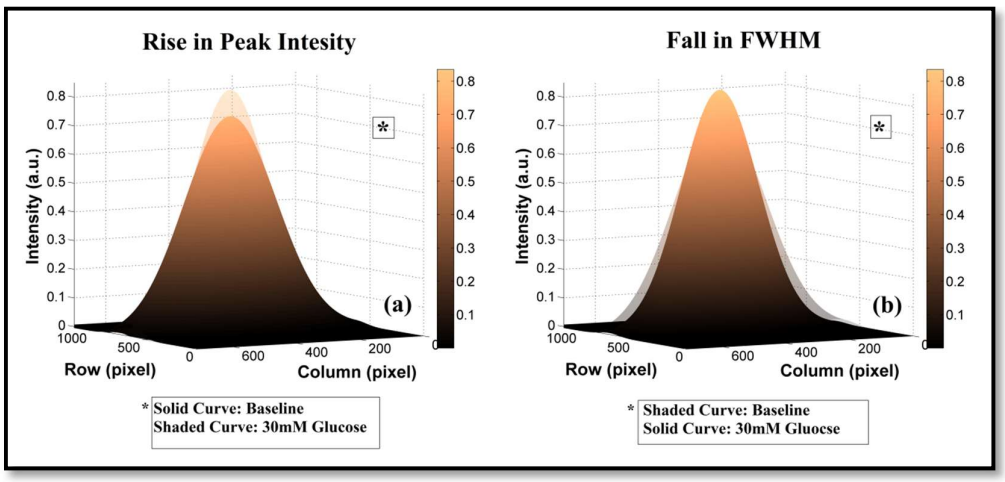

Figure 5.17. 3D Gaussian model for understanding (a) peak intensity rise and (b) FWHM fall of transmitted spot after 30mM glucose introduction.

On the other hand, from reflected spot IDM and Gaussian fit (figure 5.18 and 5.19 respectively), it can be observed that reflectance (R) deceases and surface scattering (SS) increases due to glucose absorption. This is due to the fact that surface scattering increases with clustered attachment of glucose molecules around GOX sites on sensor surface. In section 5.4.1, it was observed that increase in clustered attachment of glucose on GOX molecules, increases surface roughness significantly; thus increasing SS value which in turn reduces R value. From the IDMs obtained from reflected and transmitted spot it was observed that OP increases with glucose introduction, thus it can be concluded that optical absorption falls due to the presence of glucose molecules on CSNC samples.

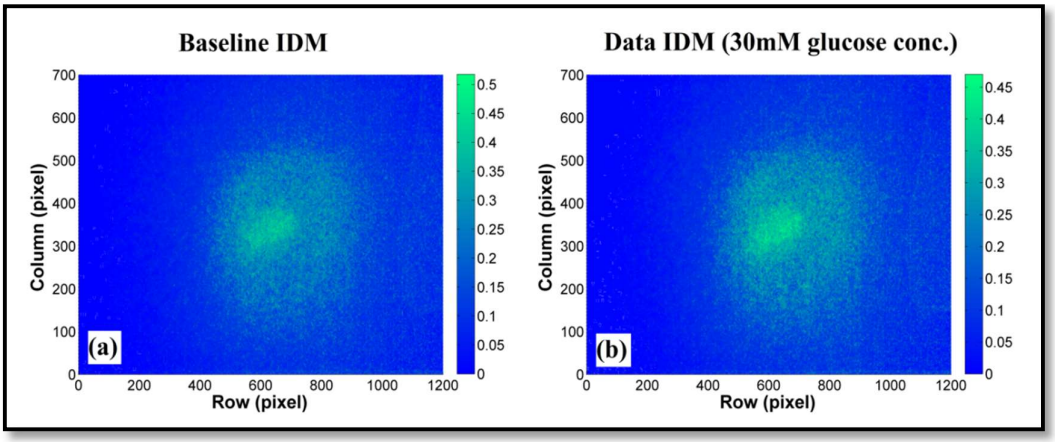

Figure 5.18. 2D IDM plot of (a) baseline snapshot and (b) snapshot after 30mM glucose introduction for reflected spot

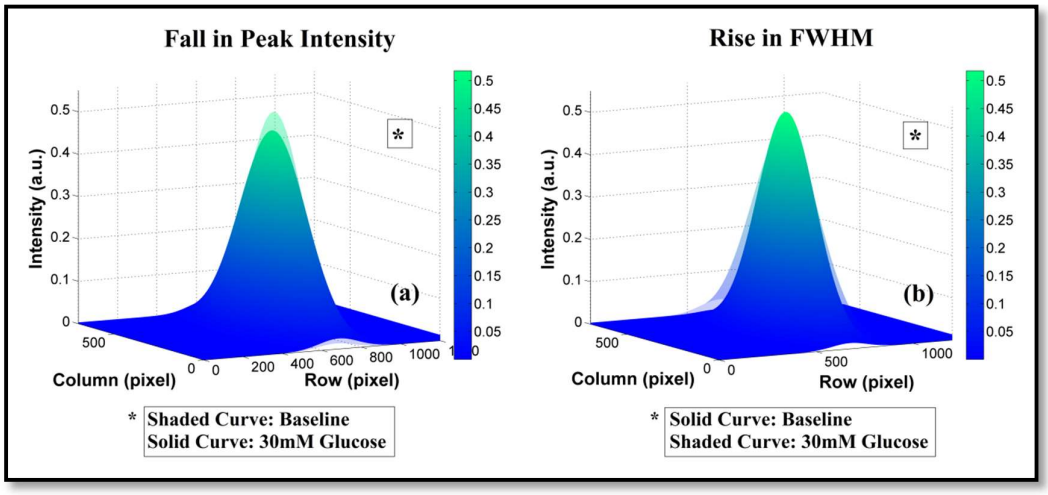

Figure 5.19. 3D Gaussian model for understanding (a) peak intensity fall and (b) FWHM rise of reflected spot after 30mM glucose introduction.

Change in different parameters due to glucose introduction is listed in table I. Rise and fall of actual data from baseline value is denoted with '↑' and '↓' signs respectively. Also, for samples with and without GOX functionalization, the parameter change pattern was found to be same.

Table I: Actual change in parameter readings with glucose introduction

Transmittance (T)	Internal Scattering (IS)	Reflectance (R)	Surface Scattering (SS)	Output Power (OP)	Absorption
↑	↓	↓	↑	↑	↓

5.5.3. Sensitivity

From the response curve for surface functionalized (SF) and non-functionalized (WSF) samples in figure 5.20, it is quite clear that all the five parameters change significantly for SF samples, while for WSF samples only two parameters (T and IS) are significant. When glucose solution is sprayed on WSF samples, glucose molecules are evenly deposited on the top surface. As R and SS are mainly surface properties, they are not affected much. Mainly the pores of WSF samples get filled up with glucose molecules, thus changing internal properties like T and IS significantly. In SF samples clustered attachment of glucose molecules on GOX sites changes R and SS along with other parameters. Pores in SF samples are partially filled with GOX molecules at the time of enzyme incubation. So, there is a limit up to which the pores can accommodate glucose molecules. After that limit is reached, T and IS will be unaffected by further increase in glucose concentration. This is observed in figure 5.20(b) i.e. after 17mM glucose concentration IS almost saturates and further deposition of glucose molecules only affects T a little which may be dominated by the effect of other three parameters. So, we can conclude that SF samples are much more reliable than WSF samples for multiparametric measurement and surface functionalization actually introduces more parameters thus more sensitivity in the system.

Sensitivity was calculated for SF samples and plotted in figure 5.21. It is observed that in the range of 1-17mM, IS is maximum sensitive among all the five parameters and maximum sensitivity of IS was found to be $1.17mM^{-1}$. For 17-30mM glucose concentration range IS sensitivity was observed to fall significantly. In this range SS was found to be the maximum

sensitive parameter with sensitivity value of $1mM^{-1}$. So, it can be concluded that scattering parameters are more sensitive than direct intensity related parameters like transmittance, reflectance, absorbance etc. which are generally measured in standard optical biosensors.

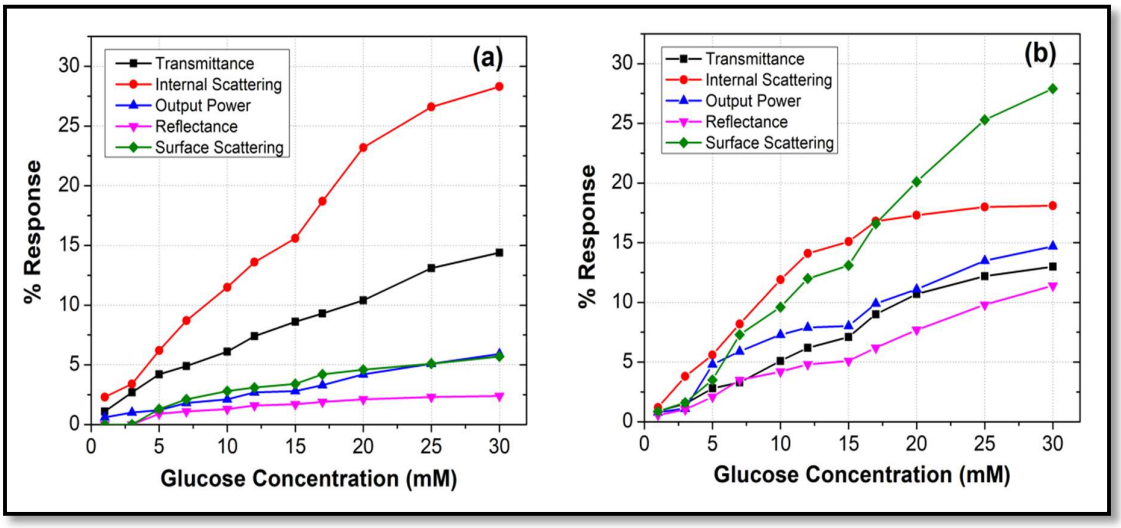

Figure 5.20. Response curve of CSNC samples (a) without surface functionalization (WSF) and (b) with surface functionalization (SF)

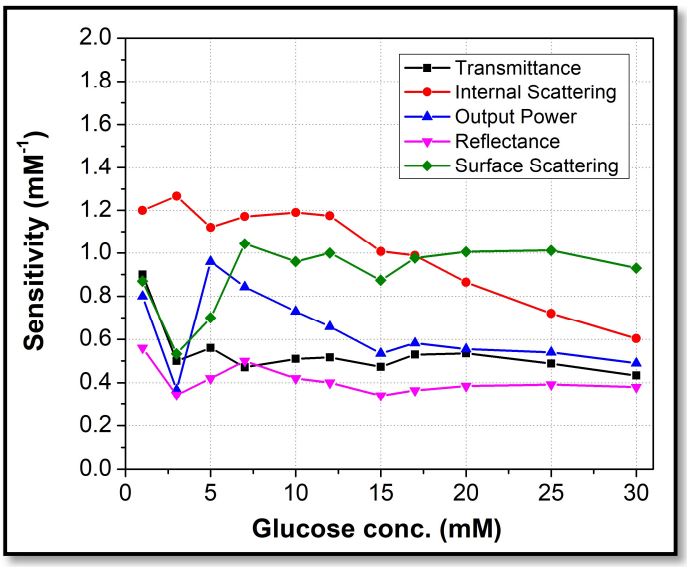

Figure 5.21. Sensitivity plot for surface functionalized (SF) samples

5.5.4. Dynamic Range and LOD

As deviation from baseline is measured to calculate %Response, blank data gets eliminated in each measurement. In this type of systems where relative output is

considered instead of absolute value, LOD becomes significantly low [18]. For the optical detection system discussed in chapter 4, cost efficiency is prioritized which resulted use of noisy components. Diode laser and CMOS sensors both have inbuilt noise which causes fluctuation in %Response due to deviation in blank data, thus increasing LOD of the system. For consecutive 10 measurements in most stable region of diode laser time response curve i.e. in between 10 to 30 minutes after initial switch on time, SD of blank (converted in %Response) was found to be ± 0.126. Thus, minimum LOD of the system was calculated to be 0.76mM (from calibration or response curve of SS) for SF samples considering S/N≥3. Detailed calculation of LOD is presented in Annexure V. By using stable laser sources like He-Ne instead of diode lasers can reduce LOD level further. The sensor was tested for 1-30mM glucose concentration and the dynamic range was determined to be 3-30mM for reliable operation.

5.5.5. Effect of GTA and GOX Concentration

GTA concentration was varied from 0.1 to 0.6% (v/v) and change in T and R for 15mM glucose solution was observed. From figure 5.23, it is evident that above 0.2% (v/v) GTA concentration, T and R value decreases which indicates reduction of GOX enzyme activity similar to the study reported by Susanto et al [23]. In figure 5.22, colour change of the CSNC films is clearly visible with increase in GTA concentration. Above 0.2% (v/v) the CSNC films becomes dark yellow and brittle. Also crack lines are formed easily and often the film gets detached from glass substrate. So, 0.1% (v/v) GTA concentration was used which produced sufficiently high response.

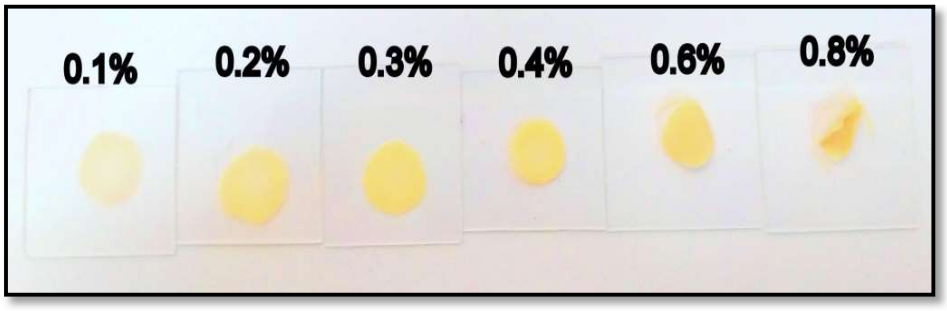

Figure 5.22. Visual effect of increased GTA concentration on CSNC thin film

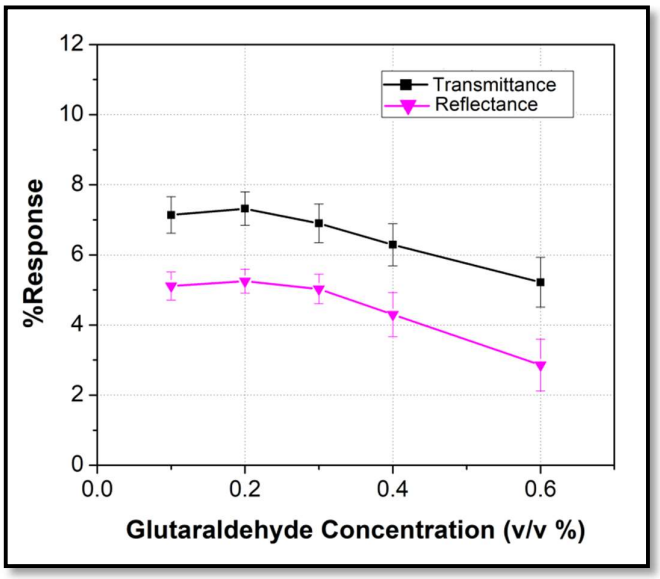

Figure 5.23. Effect of GTA concentration on sensor response (15mM glucose conc., n=3)

GOX concentration was also varied from 0.1mg/ml to 0.8mg/ml for 15mM glucose solution. It can be observed from figure 5.24 that above 0.4mg/ml T falls and R almost saturates. This may be because with higher GOX concentration the pores are almost filled with GOX molecules leaving less active site for glucose interaction inside the pores and T becomes less sensitive. On the other hand, when surface of the CSNC film is totally covered with GOX molecules number of active sites will saturate on the surface and so as R value. Thus, 0.4mg/ml GOX concentration was considered for optimum performance of the sensor.

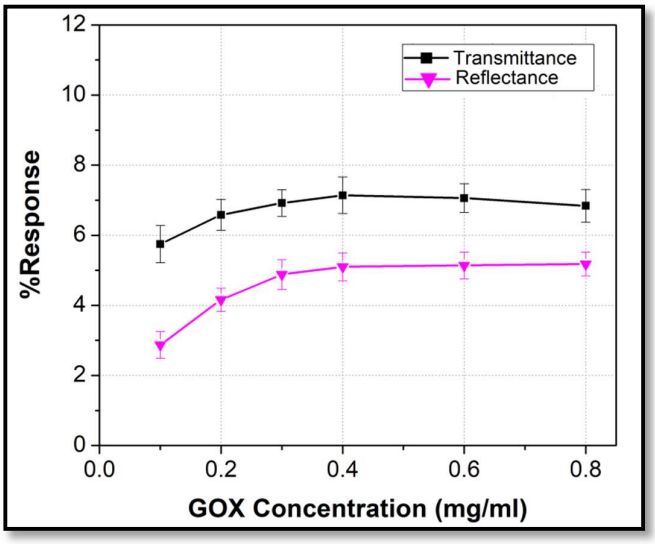

Figure 5.24. Effect of GOX concentration on sensor response (15mM glucose conc., n=3)

5.5.6. Selectivity

For selectivity study 15mM glucose, fructose, galactose, maltose and sucrose solutions were prepared. Also, phosphate buffer (PBS) was used as control. WSF and SF samples were tested for different analyte solutions. It was observed from figure 5.25(a) that WSF samples show quite high response for all the solutions except PBS control which is expected because WSF surface has no GOX enzyme present to selectively attract glucose molecules. Thus, all the analytes either gets absorbed inside the pores or attaches to the surface while solution evaporation process. There is an interesting fact to note that glucose, fructose and galactose produces almost same pattern of output response i.e. high values for T and IS and low value for R and SS. The reason behind such pattern is discussed in section 5.5.2 for WSF samples. Maltose and sucrose produce significant increase in R and SS value which may be described as the effect of their molecular weight. Maltose and sucrose are disaccharides having almost double molecular weight than glucose, fructose and galactose. So, their attachment to surface affects the surface roughness more than the monosaccharides and their tendency to penetrate deep inside the pores is also less likely. Thus, such pattern difference in WSF sensor output is observed for different analytes.

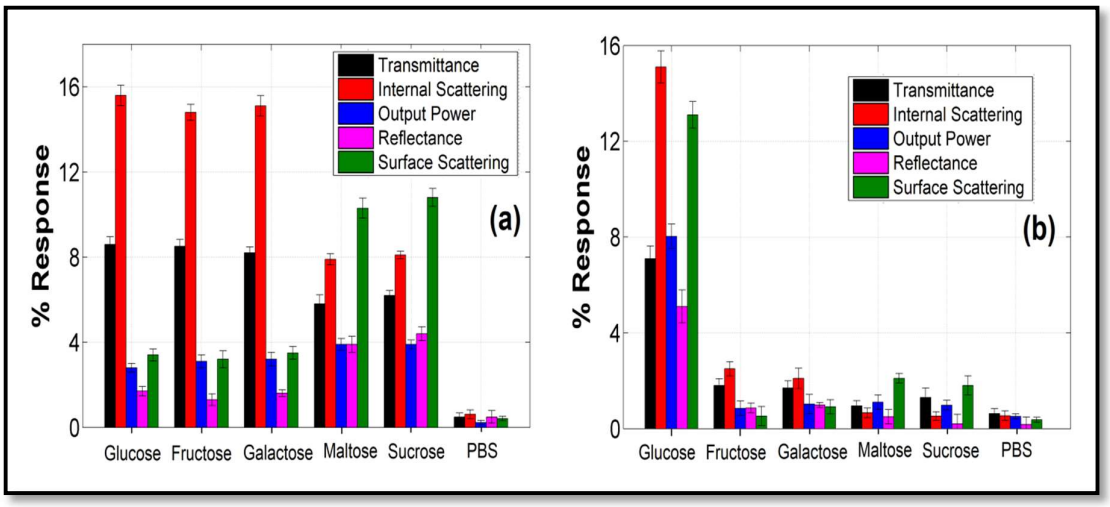

Figure 5.25. Selectivity of (a) WSF and (b) SF samples (n=3)

On the other hand, for SF samples GOX selectively binds to glucose molecules and other analytes mostly flows down the sensor surface after solution spray without significant attachment to the sensor. So, SF samples show high selectivity towards glucose molecules (figure 5.25(b)).

5.5.7. Response Time

Actual peak intensity value (PIV) of the transmitted and reflected spot is monitored for 3 minute time span to observe response time of the sensor. Initially baseline value of T and R was at ~ 0.79a.u. and ~ 0.54a.u. respectively. Baseline data fluctuation mentioned in section 5.5.4 is also visible in time response plot (figure 5.26). After 15mM glucose solution spray at 20 second, both T and R value reaches to maximum intensity saturation level of 1a.u. due to lensing effect produced by water. As the sensors were mounted vertically, excess solution quickly flows down and CSNC thin film starts drying. After 60 seconds abrupt fall in T and R value was observed and at around 80 seconds sensor output stabilises to new values indicating complete drying of the thin film. It can be observed that T has reached a higher value and R has reached a lower value compared to their baseline value which was demonstrated in table I also. From time response curve it was concluded that τ is approximately 50 seconds for the CSNC sensors.

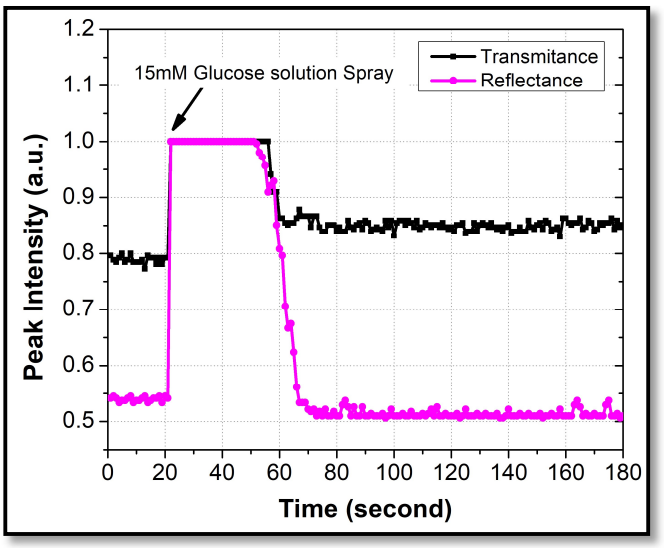

Figure 5.26. Time response curve of CSNC sensor

5.5.8. Repeatability

Repeatability study was performed on 5 CSNC sensors and after every cycle the sensors were washed in Tween20 solution followed by PBS buffer. It was found that in second cycle, T and R response drop to 68% and 83% of the first cycle response respectively (figure 5.27). Significant drop in T response indicates that gluconic acid crystals are not completely removed from complex sponge like structure of the porous film even after

vigorous washing. Also, chitosan dissolves slowly in acidic solution which can produce crater like structure shown in the FESEM image in figure 5.27(b). So, with gluconic acid production and washing, the films slowly degrade thus reducing both T and R response. In third cycle, almost no significant change in output response is observed from which it is clear that the CSNC sensors are suitable only for one time use.

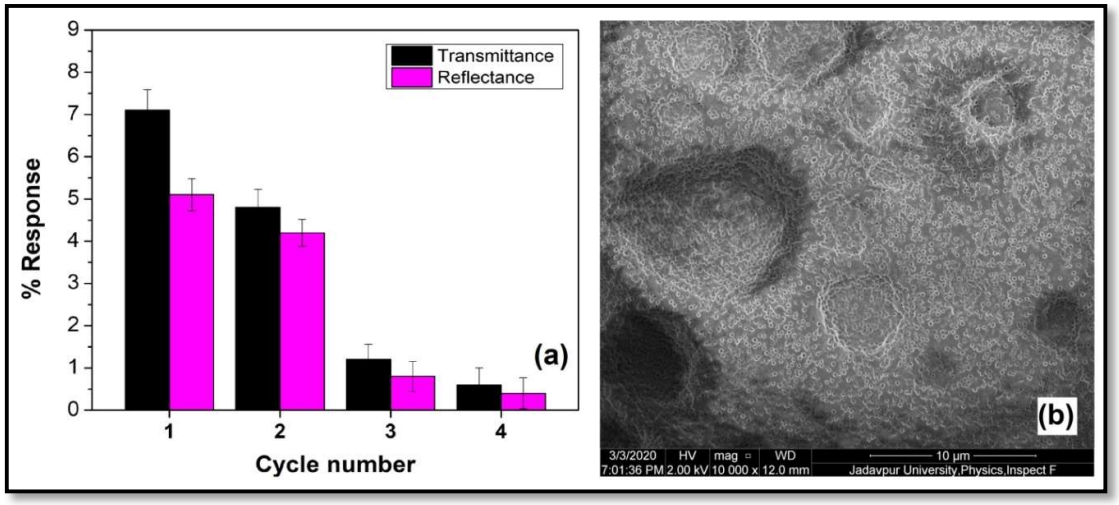

Figure 5.27. (a) Repeatability test for 15mM glucose solution (n=5), (b) FESEM micrograph after 3rd cycle

5.5.9. Stability

CSNC sensors were stored in refrigerator at 4°C and response for 15mM glucose solution was studied for every alternate day. 15mM glucose solution was freshly prepared every day and new CSNC samples were taken for every measurement as the sensors are for one time use only. It was observed that after 9th day T response falls rapidly while R response shows slow degradation for SF samples shown in figure 5.28(b). So, it can be concluded that the trapped GOX molecules inside sponge like network are affected greatly by environmental conditions compared to the surface GOX molecules. In the absence of active GOX enzyme, the sensor should act like WSF samples; but even for such samples one should get significant T response. Here it was observed that T response falls to almost blank data level which can only be described by structural degradation of CSNC membranes with time. For WSF samples such degradation was not observed and up to 30 days almost same response value was found (figure 5.28(a)). So, it can only lead to the conclusion that the

surface functionalization steps make the sensor structure prone to degradation within 10-15 days.

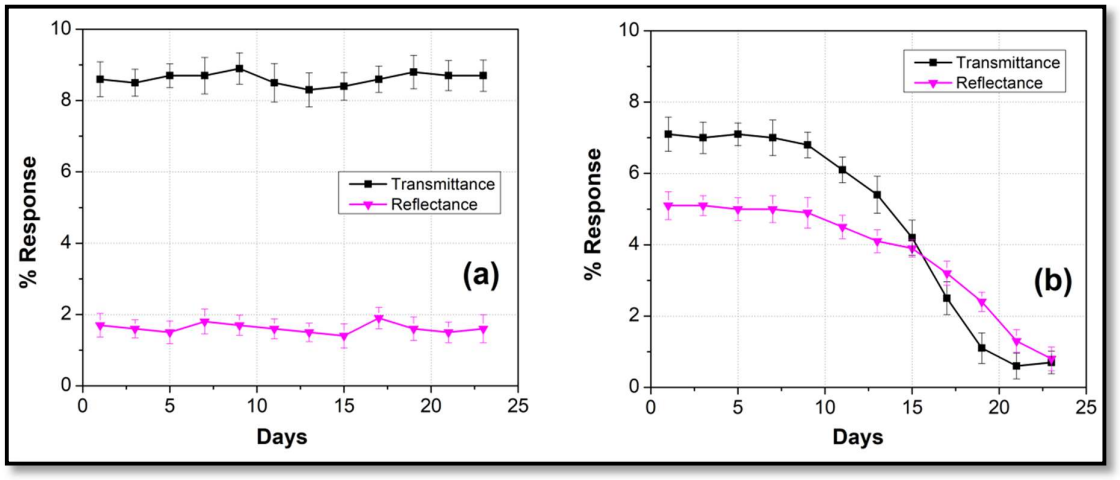

Figure 5.28. Storage stability of (a) WSF CSNC sensors and (b) SF CSNC sensor (n=3)

5.6. Comparison with Existing Literature

In Table II, recent reports on label-free optical glucose sensors have been listed and their performance comparison with present work has been demonstrated extensively.

Table II: Comparison table of label-free optical glucose sensors

Material	Transducer Type	Dynamic Range	LOD	τ (sec.)	Reference & Year
Intralipid solution	Near IR spectroscopy	0-55.55mM (0-1000mg/dl)	-	-	Jeon et al. (2006)[24]
Silver nanoparticle	LSPR	0-2.77mM (0-50mg/dl)	-	100	Serra et al. (2009) [25]
Direct serum sample	Mid IR transmittance spectroscopy	2.77-22.22mM (50-400mg/dl)	1.66mM (30mg/dl)	-	Liakat et al. (2013) [26]
Silver Halide	Optical fiber	0.27-27.77mM (5-500mg/dl)	0.21mM (3.8mg/dl)	30	Yu et al. (2013) [27]
Silver and silicon coating	Fiber optic SPR	0-14.44mM (0-260mg/dl)	-	60	Singh & Gupta (2013)[28]
ZnO nanorod	Photoluminescence	0.5-30mM (9-540mg/dl)	-	-	Sachindra et al. (2015) [10]

Ag/ZnO nanorod	Fiber optic SPR	0-10mM (0-180mg/dl)	0.012mM (0.216gm/dl)	-	Usha et al. (2016) [29]
PS thin film	Multiparametric image processing based optical detection	2-30mM (18-540mg/dl)	1.23mM (18mg/dl)	90	Present study (2018) [30]
CSNC thin film	Multiparametric image processing based optical detection	3-30mM (54-540mg)	0.76mM (13.68mg/dl)	50	Present study (2022)

5.7. Conclusion

In this chapter detailed analysis of PS and CSNC thin film glucose sensor was performed. Merits of the sensors were determined by measurement of different biosensor characteristics. The sensors were functionalized with GOX enzyme for selective attachment of glucose molecules. For PS sensors, physisorption of GOX was possible due to pore size comparable to GOX molecule size; but CSNC sensors had to go through chemisorption process of enzyme attachment due to their large pore diameter. Characterization of the sensors before and after enzyme immobilization was performed to understand change in physiochemical properties of the sensors induced by enzyme attachment.

As PS sensors were not transparent in visual spectral range, only three parameters were available for analysis solely obtained from reflected spot. Reflectance and scattering response curve were found linear in nature while absorption response curve shows distinct nonlinearity in the range of 2-30mM. On the other hand, CSNC sensor analysis was performed with total five parameters obtained from both transmitted and reflected spots; thus, the analysis was more reliable and accurate. CSNC sensor response curve was observed for both WSF and SF samples; and it was observed that response patterns were quite different for the two types of samples. Surface functionalized samples were found to have 5 accessible parameters while non-functionalised samples only provided 3 (T, IS & OP).

While PS sensors were found suitable for multi-time use and long storage time; CSNC sensor showed better sensitivity, response time and LOD. Comparison of surface functionalised PS and CSNC sensor performance is demonstrated in Table III. From the table

it can be concluded that developed thin film multiparametric sensors are very much effective for glucose detection in pathological range.

Table III: Comparison of surface functionalized PS and CSNC sensor

Sensor Characteristics	PS Sensor	CSNC Sensor
Interlinked Parameters Available	3 (R, SS, OP)	5 (T, IS, R, SS, OP)
RGB Analysis	Possible	Further study required
Maximum Sensitive Parameter	SS	IS / SS
Sensitivity	0.42 mM^{-1}	1.17 mM^{-1} / 1 mM^{-1}
Selectivity	✓	✓
Response Time	~ 90 sec.	~ 50 sec.
Dynamic Range	2-30 mM	3-30 mM
LOD	1.23 mM	0.76 mM
Repeatability	✓	×
Reproducibility	✓	✓
Stability (4^oC storage)	~ 20 days	~ 10 days

References

[1] American Diabetes Association, “Diagnosis and classification of diabetes mellitus,” Diabetes Care, vol. 37, no. 1, pp. S81-S90, Jan. 2014

[2] Jingpeng Wang, Dan F. Thomas, and Aicheng Chen. "Nonenzymatic electrochemical glucose sensor based on nanoporous PtPb networks." Analytical Chemistry 80, no. 4 (2008): 997-1004. https://doi.org/10.1021/ac701790z

[3] Mohammed Marie, Sanghamitra Mandal, and Omar Manasreh. "An electrochemical glucose sensor based on zinc oxide nanorods." Sensors 15, no. 8 (2015): 18714-18723. https://doi.org/10.3390/s150818714

[4] Hazhir Teymourian, Abbas Barfidokht, and Joseph Wang. "Electrochemical glucose sensors in diabetes management: an updated review (2010–2020)." Chemical Society Reviews (2020). https://doi.org/10.1039/D0CS00304B

[5] Duan Feng, Fang Wang, and Zilin Chen. "Electrochemical glucose sensor based on one-step construction of gold nanoparticle–chitosan composite film." Sensors and Actuators B: Chemical 138, no. 2 (2009): 539-544. https://doi.org/10.1016/j.snb.2009.02.048

[6] Shabi Abbas Zaidi, and Jae Ho Shin. "Recent developments in nanostructure based electrochemical glucose sensors." Talanta 149 (2016): 30-42. https://doi.org/10.1016/j.talanta.2015.11.033

[7] Chao Chen, Qingji Xie, Dawei Yang, Hualing Xiao, Yingchun Fu, Yueming Tan, and Shouzhuo Yao. "Recent advances in electrochemical glucose biosensors: a review." Rsc Advances 3, no. 14 (2013): 4473-4491. DOI: 10.1039/C2RA22351A

[8] Xing Xuan, Hyo S. Yoon, and Jae Y. Park. "A wearable electrochemical glucose sensor based on simple and low-cost fabrication supported micro-patterned reduced graphene oxide nanocomposite electrode on flexible substrate." Biosensors and Bioelectronics 109 (2018): 75-82. https://doi.org/10.1016/j.bios.2018.02.054

[9] J. Quincy Brown, Rohit Srivastava, and Michael J. McShane. "Encapsulation of glucose oxidase and an oxygen-quenched fluorophore in polyelectrolyte-coated calcium alginate microspheres as optical glucose sensor systems." Biosensors and Bioelectronics 21, no. 1 (2005): 212-216. https://doi.org/10.1016/j.bios.2004.08.020

[10] Sachindra Nath Sarangi, Shinji Nozaki, and Surendra Nath Sahu. "ZnO nanorod-based non-enzymatic optical glucose biosensor." Journal of biomedical nanotechnology 11, no. 6 (2015): 988-996. https://doi.org/10.1166/jbn.2015.2048

[11] Xu-dong Wang, Hai-xu Chen, Ting-yao Zhou, Zhi-jie Lin, Jing-bin Zeng, Zhao-xiong Xie, Xi Chen, Kwok-yin Wong, Guo-nan Chen, and Xiao-ru Wang. "Optical colorimetric sensor strip for direct readout glucose measurement." Biosensors and Bioelectronics 24, no. 12 (2009): 3702-3705. https://doi.org/10.1016/j.bios.2009.05.018

[12] Kuan-Chieh Chen, Yu-Le Li, Chao-Wei Wu, and Chia-Chin Chiang. "Glucose sensor using U-shaped optical fiber probe with gold nanoparticles and glucose oxidase." Sensors 18, no. 4 (2018): 1217. https://doi.org/10.3390/s18041217

[13] Mona Shehab, Shaker Ebrahim, and Moataz Soliman. "Graphene quantum dots prepared from glucose as optical sensor for glucose." Journal of Luminescence 184 (2017): 110-116. https://doi.org/10.1016/j.jlumin.2016.12.006

[14] Achim Josef Müller, Monika Knuth, Katharina Sibylle Nikolaus, Roland Krivánek, Frank Küster, and Christoph Hasslacher. "First clinical evaluation of a new percutaneous optical fiber glucose sensor for continuous glucose monitoring in diabetes." (2013): 13-23.

[15] Mark-Steven Steiner, Axel Duerkop, and Otto S. Wolfbeis. "Optical methods for sensing glucose." Chemical Society Reviews 40, no. 9 (2011): 4805-4839. https://doi.org/10.1039/C1CS15063D

[16] Dong Geon Jung, Daewoong Jung, and Seong Ho Kong. "A lab-on-a-chip-based non-invasive optical sensor for measuring glucose in saliva." Sensors 17, no. 11 (2017): 2607. https://doi.org/10.3390/s17112607

[17] Bhalla Nikhil, Jolly Pawan, Formisano Nello, and Estrela Pedro. "Introduction to biosensors." Essays Biochem 60, no. 1 (2016): 1-8.

[18] David A. Armbruster, and Terry Pry. "Limit of blank, limit of detection and limit of quantitation." The clinical biochemist reviews 29, no. Suppl 1 (2008): S49.

[19] Ximing Zhang, Priya Murria, Yuan Jiang, Weihua Xiao, Hilkka I. Kenttämaa, Mahdi M. Abu-Omar, and Nathan S. Mosier. "Maleic acid and aluminum chloride catalyzed conversion of glucose to 5-(hydroxymethyl) furfural and levulinic acid in aqueous media." Green Chemistry 18, no. 19 (2016): 5219-5229. https://doi.org/10.1039/C6GC01395C

[20] Sandip B. Bankar, Mahesh V. Bule, Rekha S. Singhal, and Laxmi Ananthanarayan. "Glucose oxidase—an overview." Biotechnology advances 27, no. 4 (2009): 489-501. DOI:10.1016/j.biotechadv.2009.04.003

[21] Aldona Beganskienė, Valdas Sirutkaitis, Marytė Kurtinaitienė, Remigijus Juškėnas, and Aivaras Kareiva. "FTIR, TEM and NMR investigations of Stöber silica nanoparticles." Mater Sci (Medžiagotyra) 10 (2004): 287-290. https://doi.org/10.5755/j01.ms.10.4.26643

[22] Chun Ming Wong, Kwun Hei Wong, and Xiao Dong Chen. "Glucose oxidase: natural occurrence, function, properties and industrial applications." Applied microbiology and biotechnology 78, no. 6 (2008): 927-938. https://doi.org/10.1007/s00253-008-1407-4

[23] Heru Susanto, A. M. Samsudin, Nur Rokhati, and I. N. Widiasa. "Immobilization of glucose oxidase on chitosan-based porous composite membranes and their potential use in biosensors." Enzyme and microbial technology 52, no. 6-7 (2013): 386-392. https://doi.org/10.1016/j.enzmictec.2013.02.005

[24] KJ. Jeon, ID. Hwang, S. Hahn, G. Yoon, “Comparison between transmittance and reflectance measurements in glucose determination using near infrared spectroscopy,” Journal of Biomedical Optics, vol. 11, no. 1, pp. 014022, Jan./Feb. 2006

[25] A. Serra, E. Filippo, M. Re, M. Palmisano, M. Vittori-Antisari, A. Buccolieri, D. Manno, “Non-functionalized silver nanoparticles for a localized surface plasmon resonance-based glucose sensor,” Nanotechnology, vol. 20, pp. 165501, 2009

[26] S. Liakat, KA. Bors, TY. Huang, APM. Michel, E. Zanghi, CF. Gmachl, “In vitro measurements of physiological glucose concentrations in biological fluids using mid-infrared light,” Biomedical Optics Express, vol. 4, no. 7, pp. 1083-1090, Jul. 2013

[27] S. Yu, D. Li, H. Chong, C. Sun, H. Yu, K. Xu, “In vitro glucose measurement using tunable mid-infrared laser spectroscopy combined with fiber-optic sensor,” Biomedical Optics Express, vol. 5, no. 1, pp. 275-286, Dec. 2013

[28] S. Singh, B. D. Gupta, “Fabrication and characterization of surface plasmon resonanace based fiber optic sensor using gel entrapment technique for the detection of low glucose concentration,” Sens. Actuators B Chem., vol. 177, pp. 589-595, 2013

[29] S. P. Usha, A. M. Shrivastav, B. D. Gupta, “FO-SPR based dextrose sensor using Ag/ZnO nanorods/GOx for insulinoma detection,” Biosens. Bioelectron., vol. 85, pp. 986-995, May 2016

[30] Deeparati Basu, Tanusree Sarkar, Kaustav Sen, Syed Minhaz Hossain, and Jayoti Das. "Multi-Parametric optical glucose sensor based on surface functionalized nano-porous silicon." IEEE Sensors Journal 18, no. 24 (2018): 9940-9947. DOI: 10.1109/JSEN.2018.2872846

Chapter 6

Conclusion & Future Scope

6.1. Conclusion

The presented work in the thesis is focussed on developing a porous thin film based multiparametric optical biosensor system for effective detection of glucose in pathological range.

Porous Silicon (PS) thin films were fabricated on silicon wafer substrate by electrochemical etching procedure to evaluate their performance in biosensing application. Effect of different preparation parameters i.e., wafer resistivity, etching time and choice of

electrolyte solution was observed on morphological and structural properties of the PS thin films. It was seen that with increased etching time surface roughness of the films increases due to formation of loosely attached agglomerated nanoparticles on the thin film surface. Such unstable structures were not suitable for surface functionalization process and thus response of the nano PS samples was observed to drop significantly for higher etching time. Also, macro PS samples showed poor performance in glucose sensing application though their response was found even greater than nano PS samples. In terms of reproducibility, repeatability and response time, the macro PS failed to compete with nano PS sample. Optimum etching time was found to be 5 minutes for best glucose sensing performance of nano PS thin film sensors.

Chitosan-Silica nanocomposite (CSNC) thin films are semi-transparent in nature inside visible spectra. Thus, compared to PS thin films which utilises only reflected spot for sensor measurements, CSNC thin films can provide more parameters for reliable multiparametric sensing. CSNC thin films of different pore size were prepared by hot etching of Silica nanoparticles (SiNp) in NaOH solution. The main advantage of CSNC was found to be that they are extremely easy to fabricate and batch production is very much possible which makes them a great choice for cost effective biosensor platform. CSNC thin films of different pore diameters were compared in terms of morphological, structural and optical properties. It was found that SiNp diameter ~ 300nm was optimum for sensing application due to their capability to produce uniform pore distribution, surface pore density and optimum optical properties in CSNC films. The effect of SiNp agglomeration and sedimentation for lower and higher particle diameter respectively, was found responsible for uneven pore distribution in CSNC thin films. CSNC thin films with ~300nm SiNp size were found to produce maximum sensitivity towards all the parameters, thus it was found to be an ideal choice for multiparametric measurements.

Both PS and CSNC thin films were surface functionalised with Glucose Oxidase (GOX) enzyme which selectively attaches glucose molecules on sensor surface and catalyses the production of gluconic acid crystals which further clusters around GOX sites. As nano PS sensors have pore diameter comparable to GOX dimension, physisorption process of surface functionalization was adequate for them. On the other hand, CSNC sensors have pore diameter almost ten times compared to nano PS sensors. So physisorption process is not

enough to prevent removal of GOX molecules in washing steps after surface functionalization. Thus, CSNC surface had to be activated with Glutaraldehyde (GTA) chains to attach GOX molecules via chemisorption process.

Images of reflected and transmitted spots from thin film sensors were taken as optical inputs to obtain different parameters using MATLAB image processing. The use of simple optical components and image processing has made the sensing system very much cost effective. Though initially there was significant amount of output fluctuation present due to noisy components like laser diodes and CMOS camera, introducing mean value method of data acquisition reduced system noise in tolerable range. The developed system can monitor total five interlinked optical parameters i.e., transmittance, internal scattering, reflectance, surface scattering and output power simultaneously. The novel technique of automated image acquisition and analysis in MATLAB GUI environment has been tested with PS thin film as non-transparent and CSNC thin film as semi-transparent core sensor materials.

The merit of a biosensor can be determined by different characteristics like sensitivity, selectivity, response time, repeatability and many more. Performance of both PS and CSNC thin film sensors were analysed in glucose sensing application based on these characteristics. PS thin films due to their non transparent nature in visible spectra can utilise only three parameters obtained from the reflected spot image. On the other hand, CSNC thin films are semitransparent and can utilise all the five optical parameters obtained from reflected and transmitted spot image. Change in the reflectance and surface scattering are mainly governed by change in surface roughness of the thin films due to clustered attachment of gluconic acid crystals around GOX sites present on sensor surface. While change in transmittance and internal scattering are mainly due to blockage of internal channels of the porous structure with gluconic acid crystal production.

Both PS and CSNC thin film sensors were found to have some merits as well as some demerits. PS thin film sensors were found to have better storage stability and they were found ideal for multi-time use due to their good repeatability. On the other hand, CSNC thin film sensors were better in terms of sensitivity, response time and LOD. CSNC sensors were found ideal for one time use as they cannot withstand repeated washing procedures before new measurement. Both PS and CSNC sensors along with the multiparametric optical

measurement system can prove to be a good choice for sensitive, selective and cost efficient glucose measurement.

6.2. Future Scope

Based on the limitations of the sensor system, further work can be initiated to improve the technology and sensing materials of the system for better performance in biosensor application.

1. A major drawback of the system is high LOD value which limits its application in measurement of small molecules or lower concentration of analytes. More stable optical sources, low noise CCD camera and use of noise reduction algorithms can improve output noise levels significantly. Though system cost may increase in the process, still investigation and optimization based on these improvements can be an extended field of study.
2. The basic of RGB histogram analysis is presented in the thesis. Detailed investigation on RGB noise and study of feasibility of these new parameters in precision sensing application may increase the reliability of the system further.
3. Storage stability of any sensor is an important factor. Maximum storage for PS sensor was found to be only 20 days at 4^{o}C. Also, CSNC thin films were found prone to degradation in extreme humidity. So, surface modification techniques to improve storage stability in room temperature needs further investigation.
4. Though the system presented in this thesis was sufficiently sensitive for glucose sensing application, there is still scope of study on new porous thin film structures which can provide more sensitive and accurate results even for lower concentrations and small molecules or ion measurement.
5. There was not much scope of testing the sensor system with actual serum or whole blood samples. Such measurements are required for pathological application.
6. Finally, a miniaturized point-of-care device or real time blood glucose monitoring device can be developed from the base work in this thesis which may prove to be quite significant contribution in multiparametric optical sensing field.

Annexure

Annexure I

MATLAB code for instantaneous snapshot analysis

Annexure II

MATLAB code for 3D Gaussian fit of IDM

Annexure III

MATLAB code for GUI development and automated data acquisition and analysis

Annexure IV

MATLAB code for RGB histogram analysis

Annexure V

LOD Calculation

Annexure I

MATLAB code for instantaneous snapshot analysis

```
%...Baseline image acquisition and analysis....%
I1=imread('baseline_30.jpg');
figure; imshow('baseline_30.jpg');
i1=rgb2gray(I1);
[x,y]=size(i1)
X1=1:x;
Y1=1:y;
Z1=im2double(i1);

disp('Baseline data');
mx_val1=max(Z1(:))
a1=find(Z1(:)>=mx_val1/2);
fwhm1=size(a1)
vol1=trapz(X1,trapz(Y1,Z1,2))


%.....Data image acquisition and analysis......%
I2=imread('sensordata_30.jpg');
figure; imshow('sensordata_30.jpg');
i2=rgb2gray(I2);
[x,y]=size(i2)
X2=1:x;
Y2=1:y;
Z2=im2double(i2);

disp('Sensor data');
mx_val2=max(Z2(:))
a2=find(Z2(:)>=mx_val2/2);
fwhm2=size(a2)
vol2=trapz(X2,trapz(Y2,Z2,2))



%..............Image IDM plot.................%
figure;h1=surf(Y1,X1,Z1);
set(h1,'LineStyle','none');
colorbar

figure;h2=surf(Y2,X2,Z2);
set(h2,'LineStyle','none');
colorbar
```

Original Images (captured by camera)

Baseline image: baseline_30.jpg

Sensor data image: sensordata_30.jpg

Program Output

```
>> newresponseprog

    Baseline data:

    mx_val1 =
       0.8353

    fwhm1 =
          59140           1

    vol1 =
       1.4955e+05
```

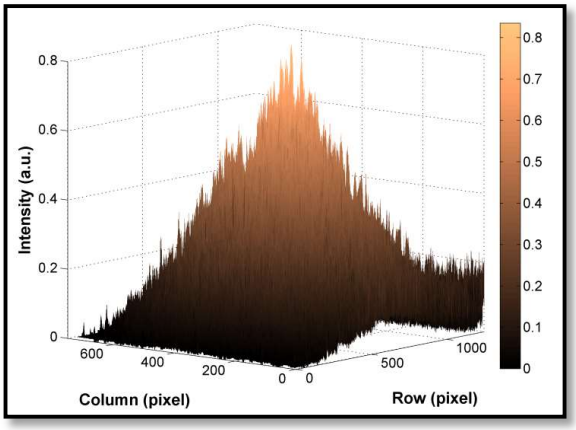

IDM of baseline_30.jpg

```
    Sensor data:

    mx_val2 =
       0.7490

    fwhm2 =
          72989           1

    vol2 =
       1.4610e+05
```

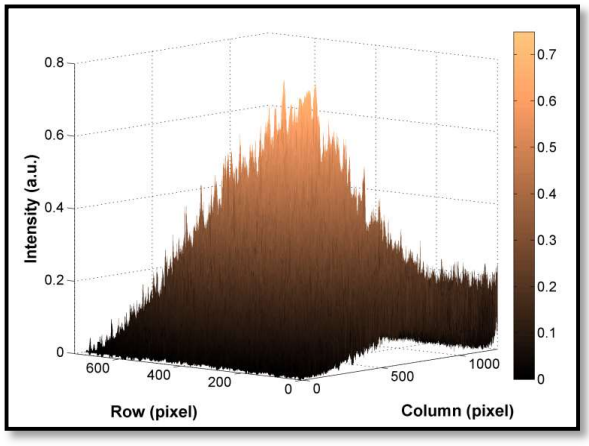

IDM of sensordata_30.jpg

Annexure II

MATLAB code for 3D Gaussian fit of IDM

```
%..............Baseline image..................%
I1=imread('baseline_30.jpg');
i1=rgb2gray(I1);
[x,y]=size(i1)
X1=1:x;
Y1=1:y;
Z1=im2double(i1);

disp('Baseline data');
[mx_val1, mx_ind1]=max(Z1(:))
[r1,c1]=ind2sub(size(Z1), mx_ind1)

max_row=Z1(r1,:);
max_col=Z1(:,c1);
fwhm_r=find(max_row>=mx_val1/2);
fwhm_c=find(max_col>=mx_val1/2);
fwhmx=size(fwhm_r);
fwhmy=size(fwhm_c);

sigmax1=fwhmx(1,2)/2.3548
sigmay1=fwhmy(1,1)/2.3548

for j=1:x
    for k=1:y
        expdata1=(((j-r1)^2)/(2*sigmax1^2))+(((k-
c1)^2)/(2*sigmay1^2));
        gauss_3d(j,k)=mx_val1*exp(-expdata1);
    end
end

figure;h1=surf(Y1,X1,gauss_3d);
xlabel('Row (pixel)');
ylabel('Column (pixel)');
zlabel('Intensity (a.u.)');
set(h1,'LineStyle','none');
colorbar
hold on;
```

```
%.................Sensor data image...................%
I1=imread('sensordata_30.jpg');
i1=rgb2gray(I1);
[x,y]=size(i1)
X1=1:x;
Y1=1:y;
Z1=im2double(i1);

disp('final data');
[mx_val1, mx_ind1]=max(Z1(:))
[r1,c1]=ind2sub(size(Z1), mx_ind1)

max_row=Z1(r1,:);
max_col=Z1(:,c1);
fwhm_r=find(max_row>=mx_val1/2);
fwhm_c=find(max_col>=mx_val1/2);
fwhmx=size(fwhm_r);
fwhmy=size(fwhm_c);

sigmax1=fwhmx(1,2)/2.3548
sigmay1=fwhmy(1,1)/2.3548

for j=1:x
    for k=1:y
        expdata1=(((j-r1)^2)/(2*sigmax1^2))+(((k-
c1)^2)/(2*sigmay1^2));
        gauss_3d(j,k)=mx_val1*exp(-expdata1);
    end
end

h2=surf(Y1,X1,gauss_3d);
set(h2,'LineStyle','none');
colorbar
hold off;
alpha(h2,0.2);
```

Note: alpha command in MATLAB makes the selected curve semi-transparent and using alpha command, peak intensity and FWHM change can be monitored for overlapping baseline and sensor data IDM.

Program Output

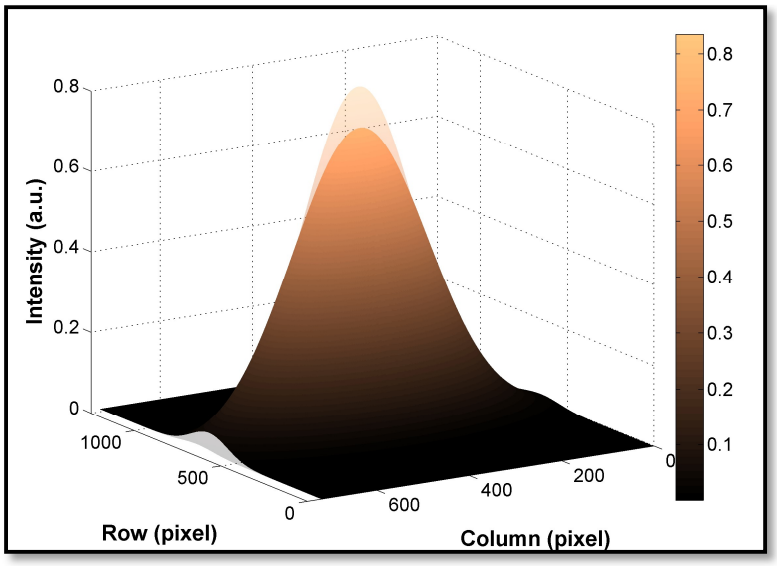

For **alpha (h1,0.2)** i.e., baseline IDM as shaded curve

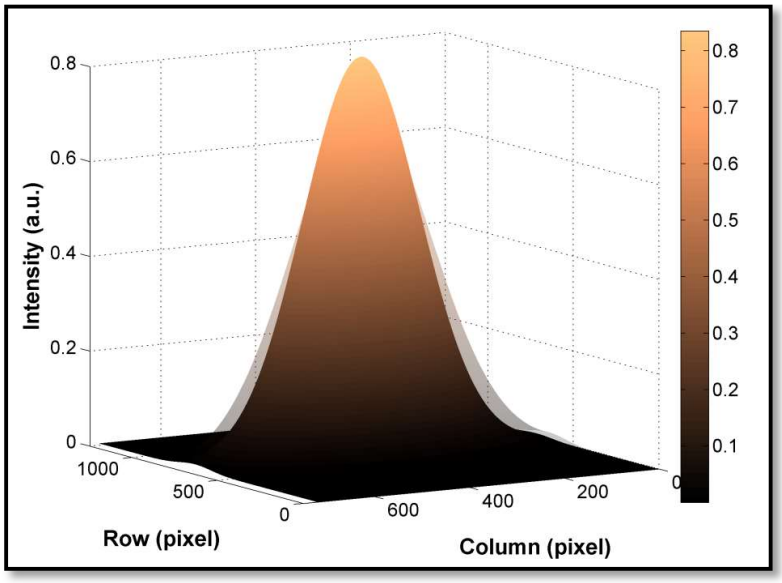

For **alpha (h2,0.2)** i.e., sensor data IDM as shaded curve

Annexure III

MATLAB code for GUI development and automated data acquisition and analysis

```
function varargout = Final_sensorprog(varargin)
% FINAL_SENSORPROG MATLAB code for Final_sensorprog.fig
%      FINAL_SENSORPROG, by itself, creates a new
FINAL_SENSORPROG or raises the existing
%      singleton*.
%
%      H = FINAL_SENSORPROG returns the handle to a new
FINAL_SENSORPROG or the handle to
%      the existing singleton*.
%
%
FINAL_SENSORPROG('CALLBACK',hObject,eventData,handles,...)
calls the local
%      function named CALLBACK in FINAL_SENSORPROG.M with the
given input arguments.
%
%      FINAL_SENSORPROG('Property','Value',...) creates a new
FINAL_SENSORPROG or raises the
%      existing singleton*.  Starting from the left, property
value pairs are
%      applied to the GUI before Final_sensorprog_OpeningFcn
gets called.  An
%      unrecognized property name or invalid value makes
property application
%      stop.  All inputs are passed to
Final_sensorprog_OpeningFcn via varargin.
%
%      *See GUI Options on GUIDE's Tools menu.  Choose "GUI
allows only one
%      instance to run (singleton)".
%
% See also: GUIDE, GUIDATA, GUIHANDLES

% Edit the above text to modify the response to help
Final_sensorprog

% Last Modified by GUIDE v2.5 29-Jul-2021 16:55:06

% Begin initialization code - DO NOT EDIT
```

```
gui_Singleton = 1;
gui_State = struct('gui_Name',       mfilename, ...
                   'gui_Singleton',  gui_Singleton, ...
                   'gui_OpeningFcn',
@Final_sensorprog_OpeningFcn, ...
                   'gui_OutputFcn',
@Final_sensorprog_OutputFcn, ...
                   'gui_LayoutFcn',  [] , ...
                   'gui_Callback',   []);
if nargin && ischar(varargin{1})
    gui_State.gui_Callback = str2func(varargin{1});
end

if nargout
    [varargout{1:nargout}] = gui_mainfcn(gui_State,
varargin{:});
else
    gui_mainfcn(gui_State, varargin{:});
end
% End initialization code - DO NOT EDIT


% --- Executes just before Final_sensorprog is made visible.
function Final_sensorprog_OpeningFcn(hObject, eventdata,
handles, varargin)
% This function has no output args, see OutputFcn.
% hObject    handle to figure
% eventdata  reserved - to be defined in a future version of
MATLAB
% handles    structure with handles and user data (see
GUIDATA)
% varargin   command line arguments to Final_sensorprog (see
VARARGIN)

% Choose default command line output for Final_sensorprog
handles.output = hObject;

% Update handles structure
guidata(hObject, handles);

% UIWAIT makes Final_sensorprog wait for user response (see
UIRESUME)
% uiwait(handles.figure1);


%.........Webcam Initialization.................
global cam1 cam2                % cam1=tr_camera,
cam2=rf_camera
cam1=videoinput('winvideo',2);
cam2=videoinput('winvideo',3);
set(cam1,'ReturnedColorSpace','RGB');
```

```
set(cam2,'ReturnedColorSpace','RGB');
%.....................................................


% --- Outputs from this function are returned to the command
line.
function varargout = Final_sensorprog_OutputFcn(hObject,
eventdata, handles)
% varargout  cell array for returning output args (see
VARARGOUT);
% hObject    handle to figure
% eventdata  reserved - to be defined in a future version of
MATLAB
% handles    structure with handles and user data (see
GUIDATA)

% Get default command line output from handles structure
varargout{1} = handles.output;


% --- Executes on button press in Tr_Camcheck.
function Tr_Camcheck_Callback(hObject, eventdata, handles)
% hObject    handle to Tr_Camcheck (see GCBO)
% eventdata  reserved - to be defined in a future version of
MATLAB
% handles    structure with handles and user data (see
GUIDATA)
global cam1
imaqhwinfo(cam1)
preview(cam1)

% --- Executes on button press in Rf_Camcheck.
function Rf_Camcheck_Callback(hObject, eventdata, handles)
% hObject    handle to Rf_Camcheck (see GCBO)
% eventdata  reserved - to be defined in a future version of
MATLAB
% handles    structure with handles and user data (see
GUIDATA)
global cam2
imaqhwinfo(cam2)
preview(cam2)

% --- Executes on button press in RadioBut_TrCam.
function RadioBut_TrCam_Callback(hObject, eventdata, handles)
% hObject    handle to RadioBut_TrCam (see GCBO)
% eventdata  reserved - to be defined in a future version of
MATLAB
% handles    structure with handles and user data (see
GUIDATA)
```

```
% Hint: get(hObject,'Value') returns toggle state of
RadioBut_TrCam
global Tr_cam
Tr_cam=get(hObject,'Value');

% --- Executes on button press in RadioBut_Rfcam.
function RadioBut_Rfcam_Callback(hObject, eventdata, handles)
% hObject    handle to RadioBut_Rfcam (see GCBO)
% eventdata  reserved - to be defined in a future version of
MATLAB
% handles    structure with handles and user data (see
GUIDATA)

% Hint: get(hObject,'Value') returns toggle state of
RadioBut_Rfcam
global Rf_cam
Rf_cam=get(hObject,'Value');



function Interval_noise_Callback(hObject, eventdata, handles)
% hObject    handle to Interval_noise (see GCBO)
% eventdata  reserved - to be defined in a future version of
MATLAB
% handles    structure with handles and user data (see
GUIDATA)

% Hints: get(hObject,'String') returns contents of
Interval_noise as text
%        str2double(get(hObject,'String')) returns contents of
Interval_noise as a double
global noise_interval
noise_interval=str2double(get(hObject,'String'));

% --- Executes during object creation, after setting all
properties.
function Interval_noise_CreateFcn(hObject, eventdata, handles)
% hObject    handle to Interval_noise (see GCBO)
% eventdata  reserved - to be defined in a future version of
MATLAB
% handles    empty - handles not created until after all
CreateFcns called

% Hint: edit controls usually have a white background on
Windows.
%       See ISPC and COMPUTER.
if ispc && isequal(get(hObject,'BackgroundColor'),
get(0,'defaultUicontrolBackgroundColor'))
    set(hObject,'BackgroundColor','white');
end
```

```
function Time_noise_Callback(hObject, eventdata, handles)
% hObject    handle to Time_noise (see GCBO)
% eventdata  reserved - to be defined in a future version of
MATLAB
% handles    structure with handles and user data (see
GUIDATA)

% Hints: get(hObject,'String') returns contents of Time_noise
as text
%        str2double(get(hObject,'String')) returns contents of
Time_noise as a double
global noise_time noise_snapnum noise_interval
noise_time=str2double(get(hObject,'String'));
noise_snapnum= (noise_time*60)/noise_interval

% --- Executes during object creation, after setting all
properties.
function Time_noise_CreateFcn(hObject, eventdata, handles)
% hObject    handle to Time_noise (see GCBO)
% eventdata  reserved - to be defined in a future version of
MATLAB
% handles    empty - handles not created until after all
CreateFcns called

% Hint: edit controls usually have a white background on
Windows.
%       See ISPC and COMPUTER.
if ispc && isequal(get(hObject,'BackgroundColor'),
get(0,'defaultUicontrolBackgroundColor'))
    set(hObject,'BackgroundColor','white');
end



function Sensor_interval_Callback(hObject, eventdata, handles)
% hObject    handle to Sensor_interval (see GCBO)
% eventdata  reserved - to be defined in a future version of
MATLAB
% handles    structure with handles and user data (see
GUIDATA)

% Hints: get(hObject,'String') returns contents of
Sensor_interval as text
%        str2double(get(hObject,'String')) returns contents of
Sensor_interval as a double
global sensor_interval sensor_snapnum
sensor_interval=str2double(get(hObject,'String'));
sensor_snapnum=(10*60)/sensor_interval
```

```
% --- Executes during object creation, after setting all
properties.
function Sensor_interval_CreateFcn(hObject, eventdata,
handles)
% hObject    handle to Sensor_interval (see GCBO)
% eventdata  reserved - to be defined in a future version of
MATLAB
% handles    empty - handles not created until after all
CreateFcns called

% Hint: edit controls usually have a white background on
Windows.
%       See ISPC and COMPUTER.
if ispc && isequal(get(hObject,'BackgroundColor'),
get(0,'defaultUicontrolBackgroundColor'))
    set(hObject,'BackgroundColor','white');
end


% --- Executes on button press in Start_sensor.
function Start_sensor_Callback(hObject, eventdata, handles)
% hObject    handle to Start_sensor (see GCBO)
% eventdata  reserved - to be defined in a future version of
MATLAB
% handles    structure with handles and user data (see
GUIDATA)
global cam1 cam2 sensor_snapnum sensor_interval true

true=1;
disp('Capture in progress......');
disp('Snapshot number:')
delay_time=sensor_interval-1;

for i=1:sensor_snapnum

    if true==1

        disp(i);

        %......Transmission camera in action..........

        img1=getsnapshot(cam1);
        baseFileName=sprintf('TransFrame %3.3d.jpg',i);
        fullFileName=fullfile('Transdata', baseFileName);
        imwrite(img1,fullFileName);
        img1_mod=rgb2gray(img1);

        [x,y]=size(img1_mod);
        X1=1:x;
        Y1=1:y;
```

```
        Z1=im2double(img1_mod);

        mx_val1=max(Z1(:));
        a1=find(Z1(:)>=mx_val1/2);
        b1=find(Z1(:)>=(mx_val1*3/4));
        fwhm1=size(a1);
        fwqm1=size(b1);
        vol1=trapz(Y1,trapz(X1,Z1));

        trans_arry(i)=mx_val1;
        trFWHM_arry(i)=fwhm1(1);
        trFWQM_arry(i)=fwqm1(1);
        tr_abs_arry(i)=vol1;
        %.................................................


        %.......Reflection camera in action..............

        img2=getsnapshot(cam2);
        baseFileName=sprintf('RefFrame %3.3d.jpg',i);
        fullFileName=fullfile('Refdata', baseFileName);
        imwrite(img1,fullFileName);
        img2_mod=rgb2gray(img2);

        [x,y]=size(img2_mod);
        X2=1:x;
        Y2=1:y;
        Z2=im2double(img2_mod);

        mx_val2=max(Z2(:));
        a2=find(Z2(:)>=mx_val2/2);
        b2=find(Z2(:)>=(mx_val2*3/4));
        fwhm2=size(a2);
        fwqm2=size(b2);
        vol2=trapz(Y2,trapz(X2,Z2));

        ref_arry(i)=mx_val2;
        rfFWHM_arry(i)=fwhm2(1);
        rfFWQM_arry(i)=fwqm2(1);
        rf_abs_arry(i)=vol2;
        %.................................................

        pause(delay_time);
    else
        disp('Capturing has been successfully stopped');
        break
    end

end

 disp('Capture complete.....');
```

```
%...Finding absorption value and setting edit box.....

abs_arry=tr_abs_arry+rf_abs_arry;
abs_mean=mean(abs_arry);
set(handles.Abs,'String',abs_mean);
%.....................................................


%......Finding mean value from transmission data and setting
edit box.....

tr_mean=mean(trans_arry);
trFWHM_mean=mean(trFWHM_arry);
trFWQM_mean=mean(trFWQM_arry);

set(handles.Trans,'String',tr_mean);
set(handles.Tr_FWHM,'String',trFWHM_mean);
set(handles.Tr_FWQM,'String',trFWQM_mean);
%.....................................................



%......Finding mean value from reflection data and setting
edit box......

ref_mean=mean(ref_arry);
rfFWHM_mean=mean(rfFWHM_arry);
rfFWQM_mean=mean(rfFWQM_arry);

set(handles.Refl,'String',ref_mean);
set(handles.Rf_FWHM,'String',rfFWHM_mean);
set(handles.Rf_FWQM,'String',rfFWQM_mean);
%.....................................................



%..........Write transmission data to excel file..........

filename='Sensordata_transmission.xlsx';
sheet=1;
xlswrite(filename,trans_arry.')
xlRange='B1';
xlswrite(filename,trFWHM_arry.',sheet,xlRange);
xlRange='C1';
xlswrite(filename,trFWQM_arry.',sheet,xlRange);
xlRange='D1';
xlswrite(filename,tr_abs_arry.',sheet,xlRange);
%.....................................................
```

```
%...........Write reflection data to excel file.............

filename='Sensordata_reflection.xlsx';
sheet=1;
xlswrite(filename,ref_arry.')
xlRange='B1';
xlswrite(filename,rfFWHM_arry.',sheet,xlRange);
xlRange='C1';
xlswrite(filename,rfFWQM_arry.',sheet,xlRange);
xlRange='D1';
xlswrite(filename,rf_abs_arry.',sheet,xlRange);
%.............................................................




% --- Executes on button press in Stop_sensor.
function Stop_sensor_Callback(hObject, eventdata, handles)
% hObject    handle to Stop_sensor (see GCBO)
% eventdata  reserved - to be defined in a future version of
MATLAB
% handles    structure with handles and user data (see
GUIDATA)
global true
disp('Stop callback executing....')
true=0;




% --- Executes on button press in Start_noise.
function Start_noise_Callback(hObject, eventdata, handles)
% hObject    handle to Start_noise (see GCBO)
% eventdata  reserved - to be defined in a future version of
MATLAB
% handles    structure with handles and user data (see
GUIDATA)
global cam1 cam2 Tr_cam Rf_cam noise_time noise_interval
noise_snapnum true

true=1;
disp('Capture initialysing.....')
disp('Total time:')
disp(noise_time)
disp('Interval:')
disp(noise_interval)
disp('Snapshot number:')
disp(noise_snapnum)
```

```
delay_time=noise_interval-1;

if Tr_cam==1

    for i=1:noise_snapnum

        if true==1

            img1=getsnapshot(cam1);
            baseFileName=sprintf('TransFrame %3.3d.jpg',i);
            fullFileName=fullfile('Transnoise', baseFileName);
            imwrite(img1,fullFileName);

            img1_mod=rgb2gray(img1);

            [x,y]=size(img1_mod);
            X1=1:x;
            Y1=1:y;
            Z1=im2double(img1_mod);

            mx_val1=max(Z1(:));
            a1=find(Z1(:)>=mx_val1/2);
            b1=find(Z1(:)>=(mx_val1*3/4));
            fwhm1=size(a1);
            fwqm1=size(b1);

            trans_arry(i)=mx_val1;
            trFWHM_arry(i)=fwhm1(1);
            trFWQM_arry(i)=fwqm1(1);
            pause(delay_time);

        end
    end


     disp('Capture complete....')

     xdata=0:noise_interval:((noise_time*60)-noise_interval);
     size(xdata)
     figure;plot(xdata,trans_arry);

     filename='Transmission_noisedata.xlsx';
     xlswrite(filename,trans_arry.')
     xlRange='B1';
     xlswrite(filename,trFWHM_arry.',xlRange);
     xlRange='C1';
     xlswrite(filename,trFWQM_arry.',xlRange);

else

    if Rf_cam==1
```

```
        for i=1:noise_snapnum

            if true==1

                img1=getsnapshot(cam2);
                baseFileName=sprintf('RefFrame %3.3d.jpg',i);
                fullFileName=fullfile('Refnoise',
baseFileName);
                imwrite(img1,fullFileName);
                img1_mod=rgb2gray(img1);

                [x,y]=size(img1_mod);
                X1=1:x;
                Y1=1:y;
                Z1=im2double(img1_mod);

                mx_val1=max(Z1(:));
                a1=find(Z1(:)>=mx_val1/2);
                b1=find(Z1(:)>=(mx_val1*3/4));
                fwhm1=size(a1);
                fwqm1=size(b1);

                ref_arry(i)=mx_val1;
                rfFWHM_arry(i)=fwhm1(1);
                rfFWQM_arry(i)=fwqm1(1);
                pause(delay_time);

            end

        end


        disp('Capture complete....')

        filename='Reflection_noisedata.xlsx';
        xlswrite(filename,ref_arry.')
        xlRange='B1';
        xlswrite(filename,rfFWHM_arry.',xlRange);
        xlRange='C1';
        xlswrite(filename,rfFWQM_arry.',xlRange);

    end
end


% --- Executes on button press in Stop_noise.
function Stop_noise_Callback(hObject, eventdata, handles)
% hObject    handle to Stop_noise (see GCBO)
% eventdata  reserved - to be defined in a future version of
MATLAB
```

```
% handles    structure with handles and user data (see
GUIDATA)
global true
true=0;



function Trans_Callback(hObject, eventdata, handles)
% hObject    handle to Trans (see GCBO)
% eventdata  reserved - to be defined in a future version of
MATLAB
% handles    structure with handles and user data (see
GUIDATA)

% Hints: get(hObject,'String') returns contents of Trans as
text
%        str2double(get(hObject,'String')) returns contents of
Trans as a double


% --- Executes during object creation, after setting all
properties.
function Trans_CreateFcn(hObject, eventdata, handles)
% hObject    handle to Trans (see GCBO)
% eventdata  reserved - to be defined in a future version of
MATLAB
% handles    empty - handles not created until after all
CreateFcns called

% Hint: edit controls usually have a white background on
Windows.
%       See ISPC and COMPUTER.
if ispc && isequal(get(hObject,'BackgroundColor'),
get(0,'defaultUicontrolBackgroundColor'))
    set(hObject,'BackgroundColor','white');
end



function Refl_Callback(hObject, eventdata, handles)
% hObject    handle to Refl (see GCBO)
% eventdata  reserved - to be defined in a future version of
MATLAB
% handles    structure with handles and user data (see
GUIDATA)

% Hints: get(hObject,'String') returns contents of Refl as
text
%        str2double(get(hObject,'String')) returns contents of
Refl as a double
```

```
% --- Executes during object creation, after setting all
properties.
function Refl_CreateFcn(hObject, eventdata, handles)
% hObject    handle to Refl (see GCBO)
% eventdata  reserved - to be defined in a future version of
MATLAB
% handles    empty - handles not created until after all
CreateFcns called

% Hint: edit controls usually have a white background on
Windows.
%       See ISPC and COMPUTER.
if ispc && isequal(get(hObject,'BackgroundColor'),
get(0,'defaultUicontrolBackgroundColor'))
    set(hObject,'BackgroundColor','white');
end



function Tr_FWHM_Callback(hObject, eventdata, handles)
% hObject    handle to Tr_FWHM (see GCBO)
% eventdata  reserved - to be defined in a future version of
MATLAB
% handles    structure with handles and user data (see
GUIDATA)

% Hints: get(hObject,'String') returns contents of Tr_FWHM as
text
%        str2double(get(hObject,'String')) returns contents of
Tr_FWHM as a double


% --- Executes during object creation, after setting all
properties.
function Tr_FWHM_CreateFcn(hObject, eventdata, handles)
% hObject    handle to Tr_FWHM (see GCBO)
% eventdata  reserved - to be defined in a future version of
MATLAB
% handles    empty - handles not created until after all
CreateFcns called

% Hint: edit controls usually have a white background on
Windows.
%       See ISPC and COMPUTER.
if ispc && isequal(get(hObject,'BackgroundColor'),
get(0,'defaultUicontrolBackgroundColor'))
    set(hObject,'BackgroundColor','white');
end
```

```
function Tr_FWQM_Callback(hObject, eventdata, handles)
% hObject    handle to Tr_FWQM (see GCBO)
% eventdata  reserved - to be defined in a future version of
MATLAB
% handles    structure with handles and user data (see
GUIDATA)

% Hints: get(hObject,'String') returns contents of Tr_FWQM as
text
%        str2double(get(hObject,'String')) returns contents of
Tr_FWQM as a double


% --- Executes during object creation, after setting all
properties.
function Tr_FWQM_CreateFcn(hObject, eventdata, handles)
% hObject    handle to Tr_FWQM (see GCBO)
% eventdata  reserved - to be defined in a future version of
MATLAB
% handles    empty - handles not created until after all
CreateFcns called

% Hint: edit controls usually have a white background on
Windows.
%       See ISPC and COMPUTER.
if ispc && isequal(get(hObject,'BackgroundColor'),
get(0,'defaultUicontrolBackgroundColor'))
    set(hObject,'BackgroundColor','white');
end



function Rf_FWHM_Callback(hObject, eventdata, handles)
% hObject    handle to Rf_FWHM (see GCBO)
% eventdata  reserved - to be defined in a future version of
MATLAB
% handles    structure with handles and user data (see
GUIDATA)

% Hints: get(hObject,'String') returns contents of Rf_FWHM as
text
%        str2double(get(hObject,'String')) returns contents of
Rf_FWHM as a double


% --- Executes during object creation, after setting all
properties.
function Rf_FWHM_CreateFcn(hObject, eventdata, handles)
% hObject    handle to Rf_FWHM (see GCBO)
```

```
% eventdata  reserved - to be defined in a future version of
MATLAB
% handles    empty - handles not created until after all
CreateFcns called

% Hint: edit controls usually have a white background on
Windows.
%       See ISPC and COMPUTER.
if ispc && isequal(get(hObject,'BackgroundColor'),
get(0,'defaultUicontrolBackgroundColor'))
    set(hObject,'BackgroundColor','white');
end



function Rf_FWQM_Callback(hObject, eventdata, handles)
% hObject    handle to Rf_FWQM (see GCBO)
% eventdata  reserved - to be defined in a future version of
MATLAB
% handles    structure with handles and user data (see
GUIDATA)

% Hints: get(hObject,'String') returns contents of Rf_FWQM as
text
%        str2double(get(hObject,'String')) returns contents of
Rf_FWQM as a double


% --- Executes during object creation, after setting all
properties.
function Rf_FWQM_CreateFcn(hObject, eventdata, handles)
% hObject    handle to Rf_FWQM (see GCBO)
% eventdata  reserved - to be defined in a future version of
MATLAB
% handles    empty - handles not created until after all
CreateFcns called

% Hint: edit controls usually have a white background on
Windows.
%       See ISPC and COMPUTER.
if ispc && isequal(get(hObject,'BackgroundColor'),
get(0,'defaultUicontrolBackgroundColor'))
    set(hObject,'BackgroundColor','white');
end



function Abs_Callback(hObject, eventdata, handles)
% hObject    handle to Abs (see GCBO)
% eventdata  reserved - to be defined in a future version of
MATLAB
```

```
% handles    structure with handles and user data (see
GUIDATA)

% Hints: get(hObject,'String') returns contents of Abs as text
%        str2double(get(hObject,'String')) returns contents of
Abs as a double


% --- Executes during object creation, after setting all
properties.
function Abs_CreateFcn(hObject, eventdata, handles)
% hObject    handle to Abs (see GCBO)
% eventdata  reserved - to be defined in a future version of
MATLAB
% handles    empty - handles not created until after all
CreateFcns called

% Hint: edit controls usually have a white background on
Windows.
%       See ISPC and COMPUTER.
if ispc && isequal(get(hObject,'BackgroundColor'),
get(0,'defaultUicontrolBackgroundColor'))
    set(hObject,'BackgroundColor','white');
end


% --- Executes on button press in Analyser.
function Analyser_Callback(hObject, eventdata, handles)
% hObject    handle to Analyser (see GCBO)
% eventdata  reserved - to be defined in a future version of
MATLAB
% handles    structure with handles and user data (see
GUIDATA)
```

Note: While operating image acquisition cycle, code for saving image file after every capture needs to be omitted. Otherwise, image capture cycle might get delayed greater than 1second for slower systems.

Program Output

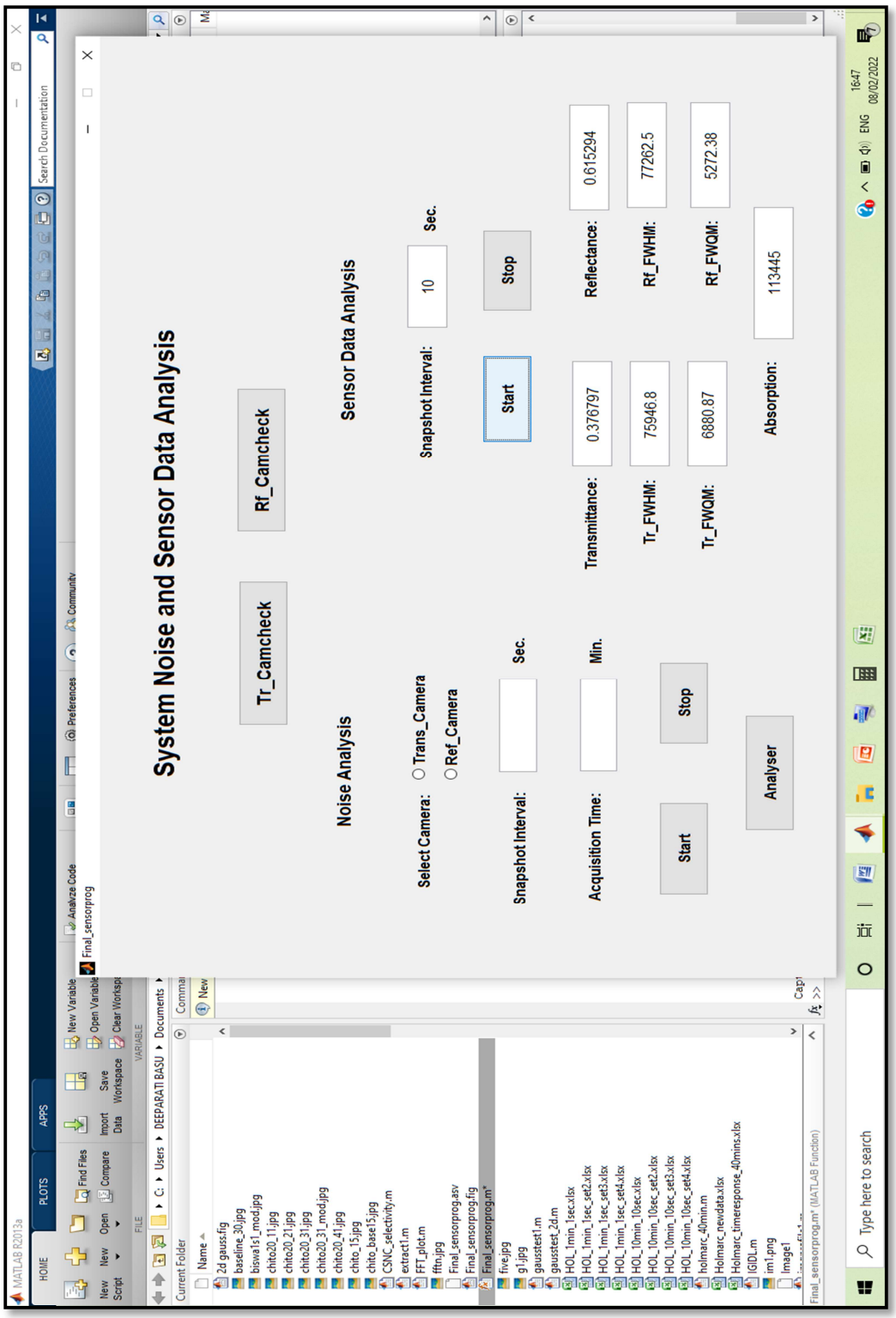

Annexure IV

MATLAB code for RGB histogram analysis

```
%.....................RGB histogram plot of IDM.............
i = imread('z30.jpg'); % imshow(im);

    [row_size, col_size, rgb] = size(i);
    nshds = 256;
    histo = zeros(rgb, nshds);

    figure;
    RGB   = ['r', 'g', 'b'];
    names = [{'Red Channel'}, {'Green Channel'}, {'Blue
Channel'}];
    x     = 0 : 255;

    for colour = 1 : rgb
        for k = 1 : row_size
            for m = 1 : col_size
                for n = 0 : (nshds - 1)          % 0 - 255
                    if i(k, m, colour) == n
                        histo(colour, n + 1) = histo(colour, n
+ 1) + 1;
                    end
                end
            end
        end

        subplot(3, 1, colour)
        bar(x, histo(colour, :), RGB(colour));
title(names(colour));
    end

    size(histo)
    rd=histo(1,:);
    maxima_rd=max(rd)
    gr=histo(2,:);
    maxima_gr=max(gr)
    bl=histo(3,:);
    maxima_bl=max(bl)
```

Program Output

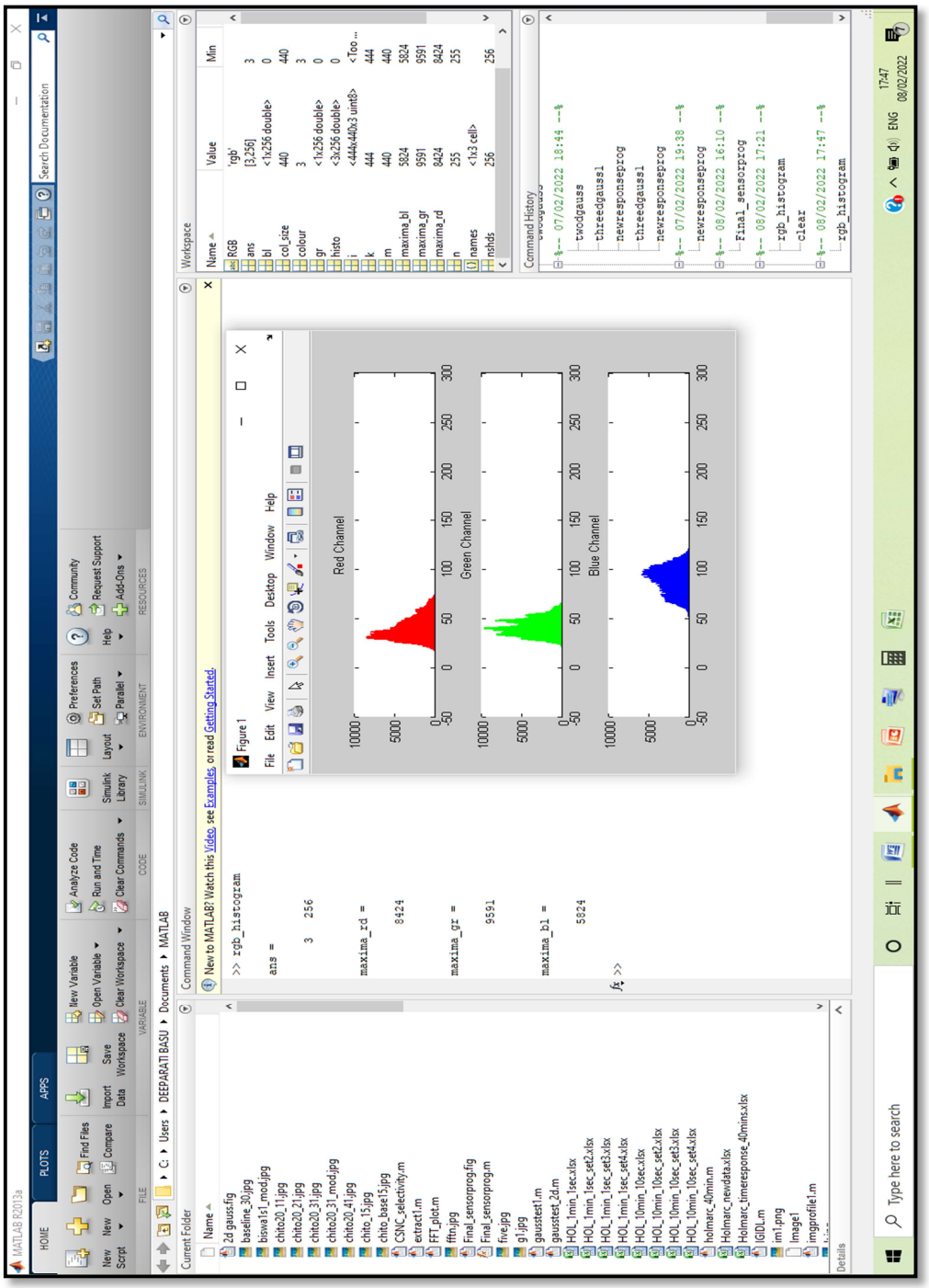

Annexure V

LOD calculation

At the time of measurement first blank data is monitored for 10 sets. Blank data is the PIV (peak intensity value) mean value of 60 snapshots taken in 1 second interval for samples before glucose solution spray. Then SD (standard deviation) of the blank is calculated and converted in equivalent %Response which is denoted as σ_{blank}. Next, system LOD is calculated using the following equation as mentioned in chapter 5: section 5.2.

$$\text{LOD} = [3 \times \sigma_{blank}]/\text{m} \;\; ; \quad \text{(considering S/N} \geq 3\text{)}$$

Here, m = slope of calibration curve or sensitivity

PS sensor LOD calculation

Reflectance parameter was considered for LOD calculation in PS sensors.

Set no.	Reflectance blank data (a.u.)	Blank data mean (μ_{blank})	Blank data SD
1	0.3031	0.3025 a.u.	0.0005 a.u.
2	0.3017		
3	0.3024		
4	0.3024		
5	0.3019		
6	0.3028		
7	0.3031		
8	0.3019		
9	0.3025		
10	0.303		

$$\sigma_{blank} = \frac{SD}{\mu_{blank}} \times 100\,\% = 0.16\,\%$$

From Reflectance calibration curve shown in figure A1, m = 0.4044 (%/mM^{-1})

LOD = 1.23 mM

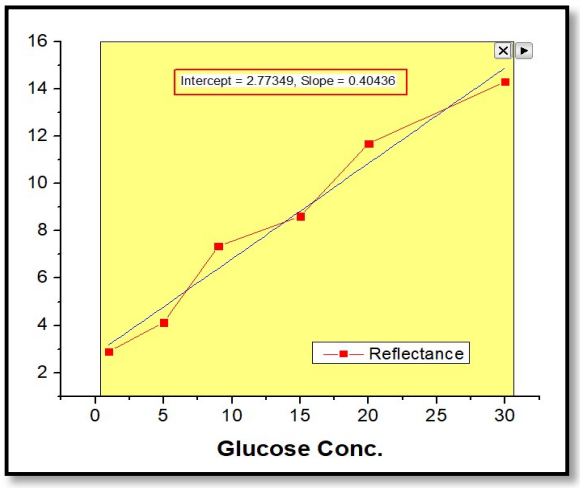

Figure A1: Linear fit of Reflectance response curve for slope calculation

Scattering calibration curve has slope or sensitivity value a bit higher than reflectance sensitivity; m = 0.4245. Due to the presence of higher magnitude of fluctuation in FWHM value, σ_{blank} of scattering parameter is also larger. LOD in term of scattering parameter is thus higher than reflectance parameter and it was not considered as minimum value of LOD.

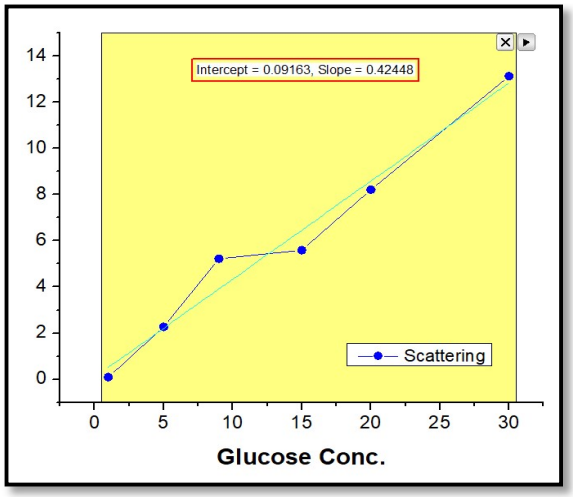

Figure A2: Linear fit of scattering response curve for slope calculation

Also absorption parameter has nonlinear calibration curve. Thus, sensitivity or slope of the curve is not constant. So LOD cannot be calculated for absorption parameter.

CSNC sensor LOD calculation

Maximum sensitive parameters in CSNC sensors are IS and SS. As IS has nonlinear calibration curve it is not considered for LOD calculation.

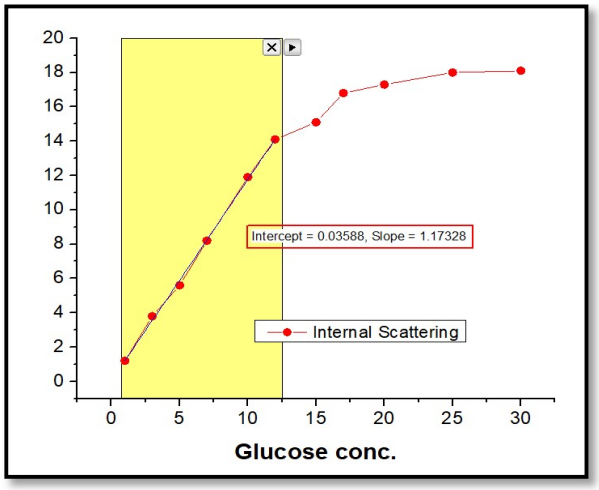

Figure A3: Nonlinear calibration curve of IS. Slope of linear section m = 1.1733

As sensitivity of other parameters (T, R, and OP) are quite low compared to SS, surface scattering is considered for LOD calculation.

Set no.	SS blank data (pixel)	Blank data mean (μ_{blank})	Blank data SD
1	25142	25044 pixels	63 pixels
2	25045		
3	25022		
4	25089		
5	24998		
6	25067		
7	24987		
8	24941		
9	25128		
10	25026		

$$\sigma_{blank} = \frac{SD}{\mu_{blank}} \times 100\ \% = 0.25\ \%$$

From SS calibration curve shown in figure A4, m = 0.99 (%/mM^{-1})

LOD = 0.76 mM

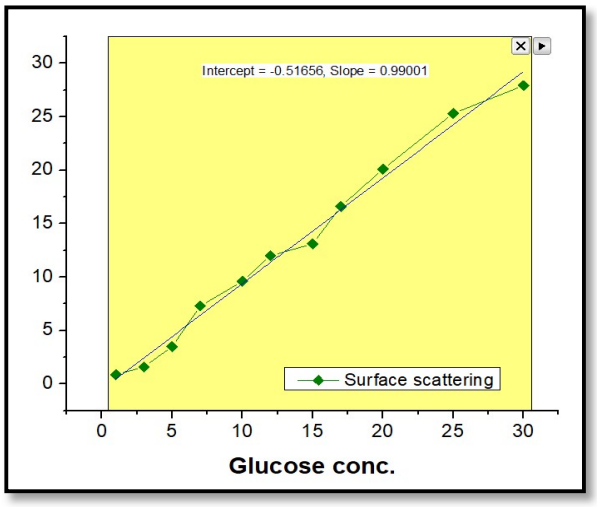

Figure A4: Linear calibration curve of SS with m = 0.99